Nuclear Factor I/A Controls A-fiber Nociceptor Development

CONTENTS

Neuroscience Bulletin

About the Cover

Nociceptive mechanical stimuli are mediated by molecularly distinct nociceptors, and their regulatory pathways are not fully understood. In the current issue, Qi *et al*. reveal a new transcription factor controlling the development of myelinated nociceptors. The cover image represents segregated genetic programs controlling the emergence of functionally distinct mechanoreceptor subtypes among TrkA-lineage neurons. See pages 685–695. (Cover image provided by Lu Qi).

Editorial

Original Articles

p 692

www.neurosci.cn

CONTENTS

Letters to the Editor

CONTENTS

Neuroscience Bulletin

◼ Research Highlight

p 822

◼ Insight

www.neurosci.cn
www.springer.com/12264

EDITORIAL

Transcriptional Control of the Development of Myelinated Mechano-nociceptors

Wen Chen[1] · Ming Yi[2,3,4] · Fei Yang[1]

The ability to perceive and respond to diverse noxious environmental stimuli, such as temperature (heat, cold), mechanical force (pinprick, pinch), and chemicals, is essential for keeping animals and humans away from damage. These stimuli are detected and encoded by nociceptors, a specialized group of somatosensory neurons with primary afferent fibers innervating the skin and with cell bodies located in the trigeminal and dorsal root ganglia (DRG) [1]. Mounting evidence indicates that various nociceptors have distinct morphological, physiological, and molecular properties. In the past decades, basic understanding of how diverse nociceptive information is sensed and transmitted has been greatly expanded with the extensive identification and functional interpretation of primary sensory neuronal categories. In contrast to noxious heat and cold information, which is almost exclusively detected and conveyed by transient receptor potential channels (TRPV1 and TRPM8) and unmyelinated C-fibers [2], mechano-nociceptors exhibit more complicated characteristics and include at least a subset of unmyelinated C-fibers (Mas-related G-protein-coupled receptor type D-positive) which transmit light punctuate pressure, and myelinated A-fibers [neurons of the neuropeptide Y receptor 2 (Npy2r$^+$) lineage], which transmit sharp pinprick information [3]. While Npy2r has been associated with A-fiber mechano-nociceptors, the precise distribution of Npy2r in DRG neurons is still obscure, given the contradictory results from different studies [4–6]. In addition, the differentiation and segregation of mechano-nociceptors during development are still not fully understood. The transcription factors involved in the genetic control of mechano-nociceptors from different linages also need to be identified.

In the current issue of *Neuroscience Bulletin*, Qi and colleagues first clarified the expression of Npy2r in developing DRG neurons at different stages [7]. Based on the results of combining Npy2r *in situ* hybridization with NF200 immunostaining, they demonstrated that Npy2r$^+$ neurons show two expression patterns: (1) myelinated NF200$^+$ neurons express Npy2r transiently, as the expression level gradually decreases from 40% on postnatal day 0 (P0) to zero on P30, and (2) unmyelinated NF200$^-$ neurons persistently expressing Npy2r along with co-expression of the pruriceptor marker Nppb (natriuretic peptide type B). Their findings provide evidence to support the stage-dependent expression of Npy2r during development in mouse DRG neurons. Although Npy2r$^+$-lineage neurons have been shown to respond to sharp, noxious mechanical stimuli, it is necessary to discriminate the possible functional discrepancy between neurons that transiently or persistently express Npy2r. Meanwhile, even though a previous study has proposed that activity of the proneural factors Neurogenin2 (Ngn2) and Ngn1 directs neural crest cells to the DRG sensory lineage during development [8], the specific neurogenetic control of mechano-nociceptors remains unclear.

✉ Fei Yang
   feiyang@ccmu.edu.cn

1   Department of Neurobiology, School of Basic Medical Sciences, Advanced Innovation Center for Human Brain Protection, Capital Medical University, Beijing 100069, China

2   Department of Neurobiology, School of Basic Medical Sciences, Peking University, Beijing 100083, China

3   Neuroscience Research Institute, Peking University, Beijing 100083, China

4   Key Laboratory for Neuroscience, Ministry of Education/National Health Commission of China, Peking University, Beijing 100083, China

Subsequently, the authors explored whether the development of these two subpopulations of Npy2r$^+$-lineage DRG neurons were regulated by the same or different transcription factors. Interestingly, they found that nuclear factor I/A (NFIA) was required for the development of neurons that expressed Npy2r both transiently and persistently, as the conditional knockout (CKO) of NFIA in DRG neurons led to the complete elimination of Npy2r expression after birth (P0, P7, and P30). Consistent with previous reports, the other transcription factor, runt-related transcription factor 1 (Runx1), was only necessary for the development of neurons that persistently express Npy2r and Nppb$^+$ [9], but was dispensable for the myelinated neurons transiently expressing Npy2r, since the percentage of Npy2r and NF200 was unaffected at P7 in Runx1-CKO mice compared with wild-type mice.

More importantly, the pinprick-evoked response of NFIA CKO mice was impaired, while other somatic sensations like light touch, heat and cold were intact. Nonetheless, acute sharp mechanical stimuli still induced c-Fos in the dorsal horn of Runx1-CKO mice, suggesting unaffected responses to pinprick in these mice. As noted above, NFIA controlled the development of the entire Npy2r lineage, and Runx1 controlled the development of neurons that persistently expressed Npy2r. The behavioral results from transgenic mice indicated that subcategories of Npy2r lineage neurons played distinct roles in the transmission of mechanical nociceptive and pruritic information. In contrast to the unmyelinated Npy2r$^+$ NF200$^-$ group, the myelinated NF200$^+$ group transiently expressing Npy2r before maturation exclusively participated in the perception and conduction of mechanical nociceptive information (Fig. 1).

The molecular mechanism underlying cell fate specification in the neuronal lineage is an important issue in developmental neurobiology. Several transcription factors have been identified that regulate the development of peripheral nociceptors. Here, Qi and colleagues establish

that NFIA plays an essential role in the emergence of A-fiber mechano-nociceptors in sensory ganglia. This finding improves the understanding of the neurogenetic control of somatosensory neuronal development. Mechanistically, the distinct regulation during development in neurons transiently and persistently expressing Npy2r by NFIA and Runx1 will allow further dissection of the molecular and functional properties of these two genetically-defined subpopulations. Given that other mechanotransducers such as Piezo2 also contribute to the sensitivity of myelinated mechano-nociceptors, whether Piezo2 channels are expressed on Npy2r lineage mechano-nociceptors and regulated by NFIA deserve further investigation. Since recent studies suggest that Npy2r signaling controls the transmission of mechanical pain under physiological conditions [10], the roles of Npy2r and NFIA in chronic pain need to be addressed as well. Finally, the findings also raise the question as to which molecules downstream of Npy2r associated with A-fiber mechano-nociceptors are engaged in sensing and processing mechanical pain, which will provide a more comprehensive map of the mechanical pain pathway.

Fig. 1 The NF200$^+$ DRG neurons that transiently express Npy2r respond to pinprick stimulation and are controlled by transcription factor NFIA during development.

References

1. Ma QF. Population coding of somatic sensations. Neurosci Bull 2012, 28: 91–99.
2. Moore C, Gupta R, Jordt SE, Chen Y, Liedtke WB. Regulation of pain and itch by TRP channels. Neurosci Bull 2018, 34: 120–142.
3. Hill RZ, Bautista DM. Getting in Touch With Mechanical Pain Mechanisms. Trends Neurosci 2020, 43: 311–325.
4. Arcourt A, Gorham L, Dhandapani R, Prato V, Taberner FJ, Wende H, et al. Touch receptor-derived sensory information alleviates acute pain signaling and fine-tunes nociceptive reflex coordination. Neuron 2017, 93: 179–193.
5. Li L, Rutlin M, Abraira VE, Cassidy C, Kus L, Gong S, et al. The functional organization of cutaneous low-threshold mechanosensoryneurons. Cell 2011, 147: 1615–1627.
6. Li C, Wang S, Chen Y, Zhang X. Somatosensory neuron typing with high-coverage single-cell RNA sequencing and functional analysis. Neurosci Bull 2018, 34: 200–207.
7. Qi L, Yin G, Zhang Y, Tao Y, Wu X, Gronostajski RM, et al. Nuclear factor I/A controls A-fiber nociceptor development. Neurosci Bull 2020, https://doi.org/10.1007/s12264-020-00486-7.
8. Lallemend F, Ernfors P. Molecular interactions underlying the specification of sensory neurons. Trends Neurosci 2012, 35: 373–381.
9. Qi L, Huang C, Wu X, Tao Y, Yan J, Shi T, et al. Hierarchical specification of pruriceptors by Runt-domain transcription factor Runx1. J Neurosci 2017, 37: 5549–5561.
10. Chen S, Liu X, Jiao Y, Chen Z, Yu W. NPY2R signaling gates spontaneous and mechanical, but not thermal, pain transmission. Mol Pain 2019, 15:1744806919887830.

ORIGINAL ARTICLE

Nuclear Factor I/A Controls A-fiber Nociceptor Development

Lu Qi[1,2] · Guangjuan Yin[2] · Yongchao Zhang[2] · Yeqi Tao[2] · Xiaohua Wu[2] ·
Richard M. Gronostajski[3] · Mengsheng Qiu[1,2] · Yang Liu[2]

Abstract Noxious mechanical information is transmitted through molecularly distinct nociceptors, with pinprick-evoked sharp sensitivity *via* A-fiber nociceptors marked by developmental expression of the neuropeptide Y receptor 2 (Npy2r) and von Frey filament-evoked punctate pressure information *via* unmyelinated C fiber nociceptors marked by MrgprD. However, the molecular programs controlling their development are only beginning to be understood. Here we demonstrate that Npy2r-expressing sensory neurons are in fact divided into two groups, based on transient or persistent Npy2r expression. Npy2r-transient neurons are myelinated, likely including A-fiber nociceptors, whereas Npy2r-persistent ones belong to unmyelinated pruriceptors that co-express Nppb. We then showed that the transcription factors NFIA and Runx1 are necessary for the development of Npy2r-transient A-fiber nociceptors and MrgprD$^+$ C-fiber nociceptors, respectively. Behaviorally, mice with conditional knockout of *Nfia*, but not *Runx1* showed a marked attenuation of pinprick-evoked nocifensive responses. Our studies therefore identify a transcription factor controlling the development of myelinated nociceptors.

✉ Mengsheng Qiu
  m0qiu001@yahoo.com

✉ Yang Liu
  yang_liu@idrbio.org

1   College of Life Sciences, Zhejiang University, Hangzhou 310058, China

2   Zhejiang Key Laboratory of Organ Development and Regeneration, Institute of Life Sciences, Hangzhou Normal University, Hangzhou 310036, China

3   Department of Biochemistry, Program in Genetics, Genomics and Bioinformatics, Center of Excellence in Bioinformatics and Life Sciences, State University of New York at Buffalo, Buffalo, NY 14203, USA

Introduction

The past decade has seen the characterization of a cohort of molecularly distinct somatosensory neurons transmitting noxious or innocuous mechanical information, three of which were addressed in this study. Firstly, a large group of unmyelinated mechanical nociceptors in dorsal root ganglia (DRG), which are marked with the expression of the mas-related G protein coupled receptor (MrgprD), exclusively innervate the skin epidermis and transmit light punctate pressure information [1–3]. Secondly, another group of unmyelinated mechanoreceptors respond to gentle stroking across the skin, and these neurons are marked by the expression of the vesicular glutamate transporter 3 (Vglut3), tyrosine hydroxylase (TH), and the cytokine TAFA4 [4–7]. Notably, although TH$^+$ neurons are called C-fiber low threshold mechanoreceptors (C-LTMRs), they can nonetheless positively and negatively modulate the transmission of noxious mechanical information [7]. Thirdly, in humans pinprick-evoked sharp mechanical pain percepts are mediated *via* myelinated nociceptors, referred here to as A-fiber nociceptors, and in mice they can be genetically marked by *Npy2r-Cre* [8]. In *Npy2r-Cre* transgenic mice, the Cre DNA recombinase is driven from the promoter of the gene encoding the neuropeptide Y receptor 2 (Npy2r) [8]. Npy2r-Cre-marked DRG neurons include a subset of nociceptors that express the nerve

growth factor receptor TrkA and the calcitonin gene-related peptide (CGRP), and ablation of these neurons leads to marked attenuation of pinprick-evoked mechanical sensitivity [8].

To date, the genetic programs controlling the development of different classes of mechanical nociceptors are still not fully understood. All nociceptors and unmyelinated sensory neurons are derived from sensory neurons whose embryonic survival is dependent on the nerve growth factor receptor TrkA [9, 10]. TrkA lineage neurons are formed in two waves in thoracic and lumbar DRGs, the early one forming A-fiber nociceptors dependent on the proneural gene *Neurog2*, and the later one forming unmyelinated neurons dependent on the proneural gene *Neurog1* [9–12]. A number of studies then showed that the runt domain transcription factor Runx1 is mainly associated with the Neurog1-dependent later wave of sensory neurons, and Runx1 is necessary for the specification of MrgprD$^+$ nociceptors [6, 13, 14], and both Runx1 and the transcription factor Zfp521 are required for establishing the molecular features of TH/Vglut3$^+$ C-LTMRs [15]. However, the transcription factor controlling the development of A-fiber nociceptors remains unknown. In this study, we set out to reveal separate genetic programs controlling the development of myelinated nociceptors *versus* unmyelinated nociceptors/LTMRs.

Materials and Methods

Animals

The generation of mice carrying the floxed *Runx1* allele (RRID:MGI:4358522), *Wnt1-Cre* and *Nav1.8-Cre* transgenic mice has been described previously [16–18]. *Nfia$^{F/F}$* mice were provided by Dr. Richard M. Gronostajski [19]. The morning that vaginal plugs were observed was considered E0.5. For immunohistochemical studies, we used mice at E11.5–E16.5 and P0–P30. For behavioral analyses, 6–10 week-old mutant and control littermates of either sex were used, and behavioral measurements were conducted with genotypes blinded for the investigators. All behavioral test protocols were approved by the Institutional Animal Care and Use Committee at Hangzhou Normal University.

In Situ Hybridization (ISH) and Immunofluorescence (IF)

Mice were anesthetized with CO_2 and perfused with 4% paraformaldehyde in phosphate buffered saline (pH 7.4) at 4 °C. The spinal cord and DRG were dissected and post-fixed at 4 °C overnight. Tissues were cryo-protected in 25% sucrose, embedded with O.C.T., and stored at − 80 °C before use. The procedures for ISH and probe preparation have been described previously [13]. The primer information for preparing all probes was from http://www.brain-map.org. The primary antibodies used in IF staining were mouse anti-NF200 monoclonal antibody (Abcam Cat# ab82259, RRID:AB_1658500, 1:500), rabbit anti-c-Fos (Millipore Cat# ABE457 RRID:AB_2631318, 1:1000), rabbit anti-NF1A (Active Motif Cat# 39036, RRID:AB_2335600), 1:1000), and mouse anti-CGRP (Abcam Cat# ab81887, RRID: AB_1658411, 1:800). FITC-conjugated IB4 was from Sigma-Aldrich (Cat#: L2895). The secondary antibodies were from Life Technologies. The ISH/IF double staining was performed as previously described [14]. We performed double ISH of Nppb mRNA labeling with DIG-AP and Npy2r mRNA labeling with botin-488. After ISH, each section was re-photographed and the *in situ* signals were pseudo-colored and superposed onto the GFP signal with Adobe Photoshop software. Quantitative analysis was determined by analyzing lumbar-level DRGs from at least three groups of mice. Only cells with clearly visible nuclei were counted.

Behavioral Studies

All animals were acclimatized to the behavioral testing apparatus in 3–5 'habituation' sessions. All acute pain behavioral tests were performed as previously described with minor modifications [8, 20, 21]. In the rotarod test, mice were first trained on the accelerating rotarod. Training sessions consisted of mice being placed on a rotarod moving at 5 rpm for 10 min so that they could stay on the rotarod for the entire 10 min. After 3–5 training sessions, mice were subjected to a full rotarod test, with the rotorod accelerating from 5 rpm to 40 rpm over 5 min. The time to fall was automatically recorded. The rotarod latency was determined as the average of 3 trials per animal performed at 30-min intervals. To measure light touch sensitivity, mice were placed on an elevated wire grid and habituated for 30 min. The plantar surface of the hindpaw was stimulated by light stroking with a paintbrush, from heel to toe. In each test, no evoked movement was scored as 0, and walking movement or brief paw lifting (< 1 s) was scored as 1. For each mouse, the cumulative score from three tests was used as a measure of the touch response. To measure radiant heat pain by the Hargreaves test, mice were placed on glass plate and habituated in plastic chambers. The plantar surface was exposed to 20% beam intensity of radiant light. The latency to paw withdrawal was calculated for 3 trials per animal, with a 10-min interval between trials. The cut-off latency to avoid tissue damage was 20 s. To measure cold pain, mice were placed on a plastic plate (0.5 mm thick) and the place beneath the hindpaw was

contacted with dry ice. The latency to hindpaw withdraw was measured. All animals were tested 3 times sequentially with a minimum of 10 min between tests. In von Frey assays, mice were placed on an elevated wire grid and the plantar surface of the hindpaw was stimulated with calibrated von Frey filaments with 2 s of bending duration. The hindpaw withdrawal threshold was determined by Dixon's up-down method [22]. For the pinprick response, a sharp steel needle (FST, 10130-10) was glued to the tip of a 1.0-g von Frey filament and gently applied to the plantar surface of the hindpaw without penetrating the skin. A scoring system was used according to the extent of the response: 0, no response; 1, quick move, look around to see what happened; 2, brief quick lift or withdrawal or removal of hindpaw; 3, brief quick shakes of hindpaw, or jumps; 4, based on score 3, 1–2 extra high-frequency shakes of hindpaw; 5, based on score 3, 3–4 extra high frequency shakes of hind paw; and 6, based on score 3, 5–7 extra high frequency shakes of hind paw. In the pinch test, an alligator clip was applied to the ventral skin surface between the footpad and the heel of the hindpaw. The cut-off threshold was set at 60 s to avoid tissue damage. Each mouse was confined in a plexiglas chamber, with video recording from below to calculate the licking duration [23]. Both males and females were used. Investigators performed these behavioral analyses blinded to genotypes.

c-Fos Induced by Pinprick

Two-month-old $Nfia^{F/F}$;Wnt1-Cre, $Runx1^{F/F}$;Wnt1-Cre mice and their littermates were anesthetized with 2% isoflurane. A sharp steel needle glued to the tip of a 1.0-g von Frey filament was poked into the left planta ~ 1200 times in a 20-min period (frequency, 1 Hz). One and a half hours later, the L4–L5 spinal segments were dissected and treated as previously described [24]. Frozen spinal cord sections (14 μm) were immuno-stained for c-Fos according to the manufacture's instructions.

Cell Counting and Statistical Analysis

The L4 or L5 lumbar DRG was dissected from at least three pairs of mutant and control mice. Three to four mutant or control DRGs were used to prepare eight sets of adjacent sections at 12 μm thickness. Only cells containing nuclei and showing levels of expression or staining clearly above background were counted. Representative data are from experiments that were replicated biologically at least three times with similar results. All data are presented as the mean and its standard error (mean ± SEM), and the difference between control and mutant samples was subjected to a two-tailed, unpaired Student's t test. Differences among multiple groups were analyzed using one-way ANOVA followed by the Bonferroni *post-hoc* analysis. Differences with $P < 0.05$ were considered statistically significant.

Results

Dynamic Expression of Npy2r Marks Two Groups of DRG Neurons

We first set out to clarify the expression of Npy2r in the developing DRG, due to conflicting results from different approaches. One study showed that DRG neurons labeled by green fluorescent protein (GFP) in transgenic $Npy2r^{GFP}$ mice are Aβ-fiber rapid-adapting low threshold mechanoreceptors or RA-LTMRs [5]. In another study, the Npy2r lineage neurons marked by transgenic $Npy2r$-Cre were shown to be peptidergic A-fiber nociceptors that are required to sense pinprick-evoked mechanical stimuli [8]. However, single-cell RNA-seq studies revealed that high-level Npy2r expression is restricted to unmyelinated pruriceptors marked by expression of the natriuretic peptide type B or Nppb [25–27]. With these controversies, we therefore decided to examine Npy2r expression in developing DRGs by performing ISH on DRG sections from different stages (from E14.5 to P30). We found that the Npy2r expression was initiated at E16.5 in lumbar DRGs (Fig. 1A, B), and that expression was still detected at the young adult stage (P30) (Fig. 1F). To assess the identity of these Npy2r-expressing neurons, we performed double staining that combined Npy2r ISH with immunostaining against the neurofilament protein NF200, which is a marker for myelinated neurons. We found that a subpopulation of Npy2r-expressing neurons were myelinated (40.6% ± 3.2% of all Npy2r$^+$ neurons) at P0 (Fig. 1C), as indicated by co-expression with NF200. This co-staining was reduced to 31.6% ± 3.2% at P7, 16.4% ± 1.3% at P10, and virtually none (1/189) at the young adult stage (P30) (Fig. 1D–F). Thus, Npy2r-expressing neurons comprise at least two groups: (1) the NF200$^+$ myelinated group expressing Npy2r transiently (or the expression is down-regulated to levels not detected by ISH at P30), and (2) the NF200-negative unmyelinated group persistently expressing Npy2r. Consistent with single-cell RNA-seq data [25–27], we further found that all Npy2r-persistent neurons co-expressed Nppb in P30 DRGs (Fig. 1G–I). It should be noted that DRG neurons marked by $Npy2r$-Cre, which have been reported to be A-fiber mechanoreceptors [8], most likely represent the Npy2r-transient population characterized here, and in that study, those investigators did not determine if $Npy2r$-Cre actually also marks unmyelinated Npy2r-persistent Nppb$^+$ pruriceptors [28, 29]. Regardless, our results suggested that the Npy2r lineage DRG neurons
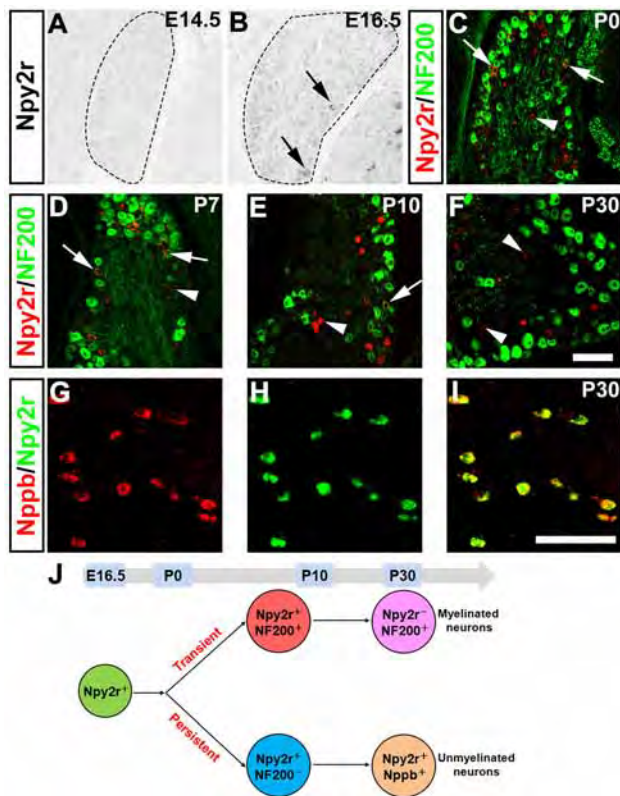
Fig. 1 Dynamic Npy2r expression in developing DRGs. A–F *In situ* hybridization (ISH) with the Npy2r probe in sections through lumbar DRGs from wild-type mice at E14.5 (A), E16.5 (B), P0 (C), P7 (D), P10 (E) and P30 (F) developmental stages (P0–P30 sections co-stained with NF200; arrowheads, Npy2r$^+$;NF200$^-$ neurons; arrows, Npy2r$^+$;NF200$^+$ neurons). G–I Double stained ISH showing that Nppb and Npy2r are completely co-labeled. J Schematic of dynamic Npy2r expression that reveals two subsets of Npy2r lineage neurons. Scale bars, 100 μm.

include Npy2r-transient myelinated A fiber sensory neurons, plus Npy2r-persistent unmyelinated pruriceptors (Fig. 1J). Next, we investigated the roles of two transcription factors, nuclear factor I/A (NFIA) and Runx1, in controlling the development of these Npy2r-lineage DRG neurons.

Detection of NFIA Expression in Npy2r-transient Myelinated Neurons

Using immunostaining, we discovered that NFIA is expressed in a subset of DRG neurons (Fig. 2A). Expression was first detected at ~E12.5–E13.5 and persisted to young adult ages (Fig. 2A). The fidelity of this NFIA antibody was indicated by the high co-labelling rate of the immunostaining signal and the *Nfia* mRNA in P7 DRGs (Fig. 2B), as well as by the loss of immunostaining signals in mice with conditional knockout (see below, Fig. 3B). Double staining showed that by P7, NFIA was mainly expressed in myelinated neurons, with 92.3% ± 0.9% of
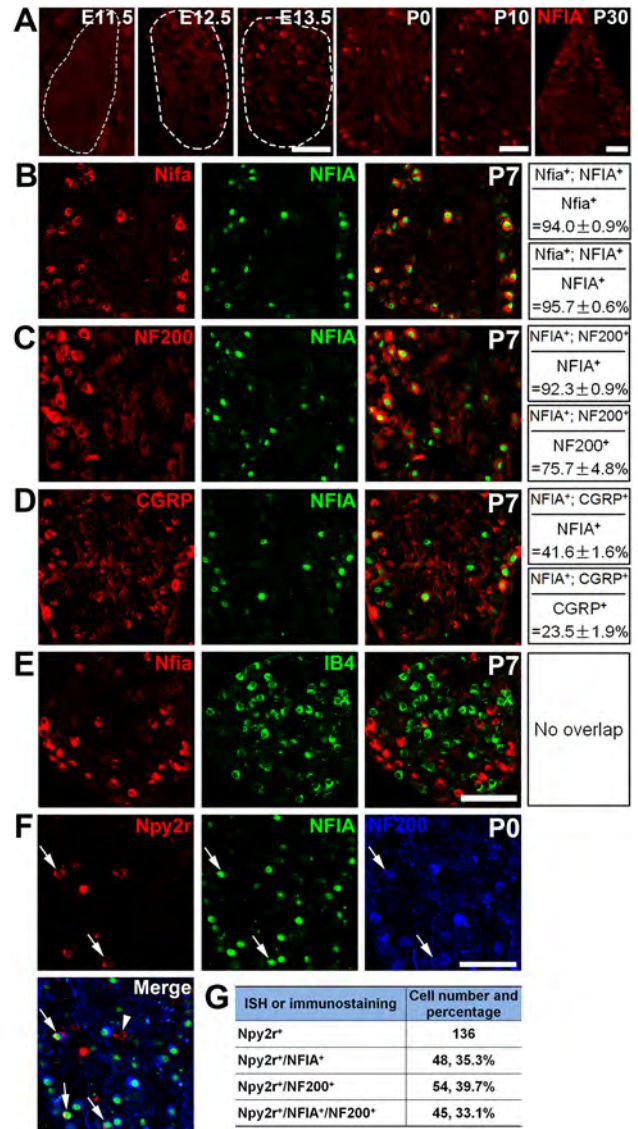
Fig. 2 NFIA expression in developing DRG neurons and its association with Npy2r-transient neurons. A Representative images of anti-NFIA immunostaining showing its expression in a subset of DRG neurons at indicated stages. B Images of *Nfia* mRNA revealed by ISH combined with NFIA immunostaining (green) in DRG sections from P7 wild-type mice. C, D Double staining of NFIA and indicated molecular markers in DRG sections from P7 wild-type mice. E Double staining of *Nfia* mRNA by ISH plus IB4 labeling. F Images showing *Npy2r* mRNA by ISH combined with immunostaining against NFIA (green) and NF200 (blue) in DRG sections from P0 wild-type mice (arrowhead, an Npy2r$^+$;NF200$^-$ neuron; arrows, Npy2r$^+$ cells co-expressing NFIA and NF200). G Tabular representation of various neuronal populations (18 sections from 3 mice). Scale bars, 100 μm.

NFIA$^+$ cells co-expressing NF200 (Fig. 2C), and NFIA$^+$ cells accounting for 75.7% ± 4.8% of NF200$^+$ cells. Previous studies have shown that NPY2R-lineage A-fiber nociceptors co-express CGRP [8]. Consistent with this, 41.6% ± 1.6% of NFIA$^+$ neurons co-expressed CGRP (Fig. 2D), and 23.5% ± 1.9% of CGRP$^+$ neurons co-

Fig. 3 Selective impairment of Npy2r neuron development in $Nfia^{F/F}$;$Wnt1$-Cre mutants. **A, B** Nfia knockout confirmed by loss of $Nfia$ mRNA by ISH (**A**) and NFIA protein by immunostaining (**B**). **C** The numbers of MrgprD$^+$ neurons in $Nfia^{F/F}$;$Wnt1$-Cre mutants (36.0% ± 1.1%, $n = 7$) were comparable to those in control mice (35.2% ± 1.0%, $n = 6$) (Student's unpaired t-test, $P = 0.6064$, $t_{(11)} = 0.5303$). **D** The numbers of TH$^+$ neuron in $Nfia^{F/F}$;$Wnt1$-Cre mutants (11.0% ± 0.4%) were comparable to those in control mice (10.4% ± 0.4%) ($n = 6$/group; Student's unpaired t-test, $P = 0.3516$, $t_{(10)} = 0.9769$). **E–H** Complete loss of Npy2r expression in P7 and P30 $Nfia^{F/F}$;$Wnt1$-Cre mutant mice (arrows, Npy2r$^+$;NF200$^+$ neurons; arrowheads, persistent Npy2r$^+$;NF200$^-$ neurons). Scale bars, 100 µm.
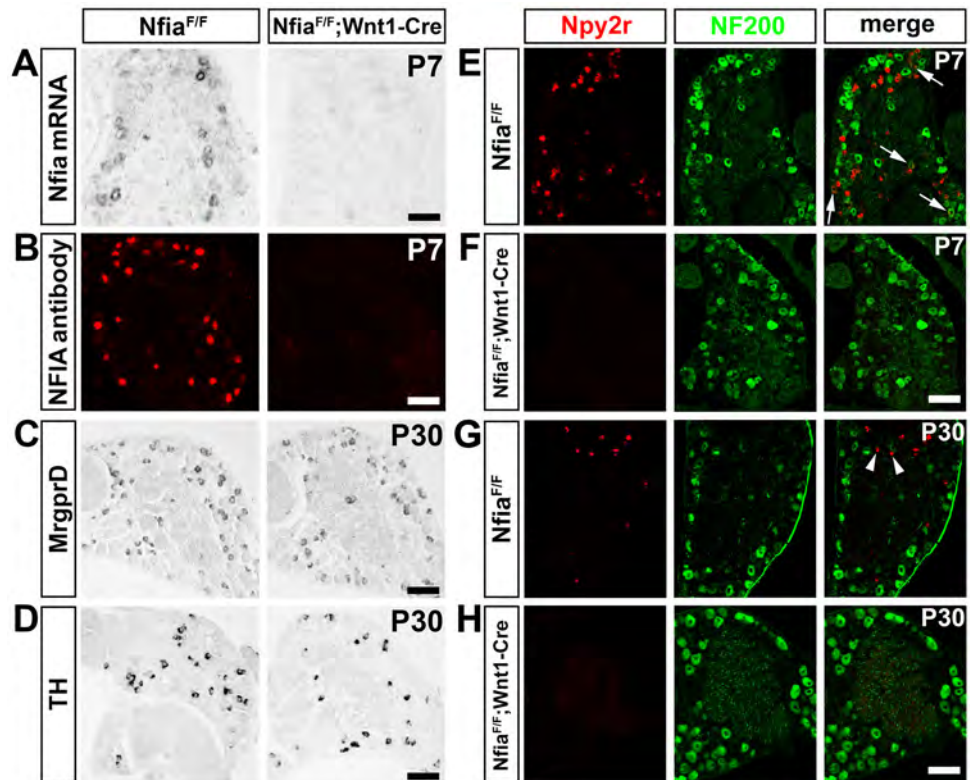
expressed NFIA. In contrast, $Nfia$ mRNA was not detected in a large group of non-peptidergic, unmyelinated neurons marked by co-staining with isolectin B4 (IB4) (Fig. 2E).

With predominant expression of NFIA in NF200$^+$ neurons at P7, we next determined whether NFIA is expressed in Npy2r-transient NF200$^+$ neuron at neonatal stages, before Npy2r is downregulated in NF200$^+$ neurons at young adult stages. We co-stained sections of P0 DRGs, and found that 33.1% of Npy2r$^+$/NF200$^+$ cells showed detectable NFIA expression (Fig. 2F, G), indicating that NFIA is at least expressed in a subset of Npy2r-transient A-fiber sensory neurons. As described below, NFIA is necessary for Npy2r expression, raising the possibility that the remaining 67% of Npy2r$^+$ neurons (including the NF200$^+$ and NF200$^-$ subsets) might have switched off NFIA expression during embryonic development.

NFIA is Necessary for Npy2r Lineage Neuron Development

To determine the role of NFIA in controlling sensory neuron development, we generated $Nfia$ conditional knockout (CKO) mice by crossing $Nfia^{F/F}$ mice [19] with $Wnt1$-Cre, in which the Cre recombinase is expressed in the neural crest stem cells that give rise to all peripheral neurons and in spinal cord neurons [16]. In the resulting $Nfia^{F/F}$;$Wnt1$-Cre mice, NFIA expression in the DRG, detected by ISH and immunostaining, was completely eliminated (Fig. 3A, B). As described above, NFIA is not expressed in non-myelinated IB4$^+$ neurons, most of which are MrgprD$^+$ polymodal nociceptors [2, 3]. Consistent with this, the percentages of DRG neurons expressing MrgprD were not different between $Nfia^{F/F}$; $Wnt1$-Cre mice (36.0% ± 1.1%, $n = 7$) and control littermates (35.2% ± 1.0%, $n = 6$; t-test, $P = 0.6064$, $t_{(11)} = 0.5303$) (Fig. 3C). The percentage of DRG neurons expressing TH was also unaffected (control: 10.4% ± 0.4%, $n = 6$; CKO: 11.0% ± 0.4%; $n = 6$; t-test, $P = 0.3516$, $t_{(10)} = 0.9769$) (Fig. 3D), suggesting that NFIA is dispensable for the development of MrgprD$^+$ polymodal nociceptors and TH$^+$ C-LTMRs. In marked contrast, the expression of Npy2r was completely eliminated in DRGs of $Nfia^{F/F}$;$Wnt1$-Cre mutant mice at all stages tested, including P0 (data not shown), P7 (Fig. 3E, F), and P30 (Fig. 3G, H), indicating that NFIA is necessary for the development of the whole lineage of Npy2r neurons, including both the Npy2r-transient myelinated and Npy2r-persistent unmyelinated subsets.

Pinprick-evoked Mechanical Sensitivity is Markedly Attenuated in *Nfia* Conditional Knockout Mice

We next examined behavioral phenotypes in $Nfia^{F/F}$;*Wnt1-Cre* mice, using littermates as blinded controls. We found that sensori-motor coordination was not affected in $Nfia^{F/F}$;*Wnt1-Cre* mice (Fig. 4A), suggesting that NFIA is likely dispensable for proprioceptor development. We found that $Nfia^{F/F}$ control mice and $Nfia^{F/F}$;*Wnt1-Cre* mice showed comparable light touch responses using the dynamic brush assay (Fig. 4B). Reflexive responses to noxious heat or cold were also unaffected, as indicated by normal withdrawal latencies (Fig. 4C, D). We then found that the responses to light punctate pressure evoked by von Frey filaments were attenuated, with the withdrawal threshold increased from 0.29 ± 0.03 g in control mice to 0.46 ± 0.04 g in $Nfia^{F/F}$;*Wnt1-Cre* mice (Fig. 4E). However, the net increase of average thresholds in CKO *versus* control mice (0.46 g – 0.29 g = 0.17 g) was modest compared with a much larger increase following the ablation of MrgprD$^+$ neurons (0.99 g – 0.41 g = 0.58 g). This is consistent with a lack of change of MrgprD expression in $Nfia^{F/F}$;*Wnt1-Cre* mice. As noted above, the Npy2r lineage neurons marked by transgenic *Npy2r-Cre*

include the A-fiber nociceptors required to sense pinprick-evoked mechanical pain [8]. Consistent with a complete loss of Npy2r expression in $Nfia^{F/F}$;*Wnt1-Cre* mice, pinprick-evoked responses were indeed markedly attenuated in CKO mice in comparison with control mice (Fig. 4F). In contrast, the licking responses evoked by skin-pinching stimuli, which produce sustained pain in humans [23], were unchanged (Fig. 4G).

To further confirm that the mutants had a deficit in transmitting pinprick-evoked sharp mechanical information, we examined the induction of c-Fos, an immediate-early protein induced by neural activity [30], in the dorsal spinal cord. To do this, a sharp needle glued to the tip of a 1.0-g von Frey filament was used to stimulate the left planta, and the c-Fos expression in the spinal segment innervated by L4 and L5 DRG neurons was assessed. We found a significant reduction in c-Fos expression in the ipsilateral dorsal horn from $Nfia^{F/F}$;*Wnt1-Cre* mice (82.0 ± 5.1), in comparison with $Nfia^{F/F}$ control mice (184.5 ± 5.3, $n = 6$/group, one-way ANOVA with Bonferroni *post-hoc* analysis, $F_{2,\ 15} = 420.2$, $P < 0.0001$; Fig. 5A–C). No significant c-Fos induction in the contralateral dorsal horn was observed in either $Nfia^{F/F}$ control or $Nfia^{F/F}$;*Wnt1-Cre* mice ($n = 6$/group, one-way ANOVA
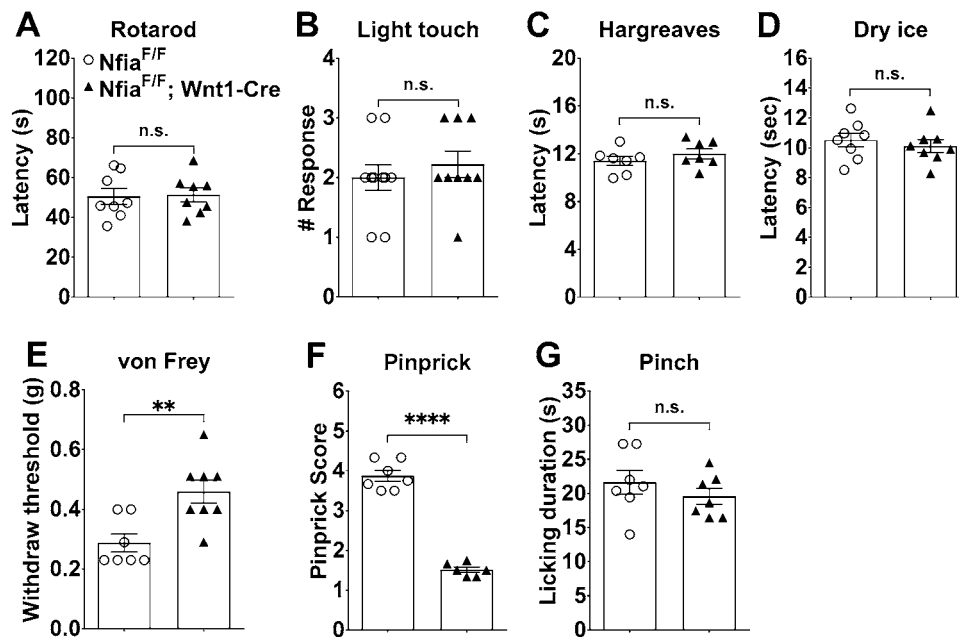
Fig. 4 Attenuated pinprick-evoked responses in conditional *Nfia* null mice. **A** General motor coordination, assessed by the accelerating rotarod test, in $Nfia^{F/F}$;*Wnt1-Cre* and $Nfia^{F/F}$ control mice ($n = 8$/group, Student's unpaired *t*-test, $P = 0.8812$, $t_{(14)} = 0.1521$). **B** Normal reflex responses to light touch in the dynamic brush assay in $Nfia^{F/F}$ control ($n = 10$) and $Nfia^{F/F}$;*Wnt1-Cre* CKO mice ($n = 9$) (Student's unpaired *t*-test, $P = 0.478$, $t_{(17)} = 0.7255$). **C** Normal reflex responses to radiant heat in the Hargreaves assay ($n = 7$/group, Student's unpaired *t*-test, $P = 0.318$, $t_{(12)} = 1.042$). **D** Normal reflex responses to noxious cold in the dry ice assay ($n = 8$/group, Student's

unpaired *t*-test, $P = 0.5403$, $t_{(14)} = 0.6277$). **E** Withdrawal thresholds in response to von Frey filament stimulation in $Nfia^{F/F}$;*Wnt1-Cre* CKO ($n = 8$) and $Nfia^{F/F}$ control mice ($n = 7$) (Student's unpaired *t*-test, $P = 0.0045$, $t_{(13)} = 3.425$). **F** Pinprick scores evoked by a sharp steel pin glued to the tip of a 1.0-g von Frey filament in $Nfia^{F/F}$;*Wnt1-Cre* ($n = 6$) and $Nfia^{F/F}$ control mice ($n = 7$) (Student's unpaired *t*-test, $P < 0.0001$, $t_{(11)} = 14.63$). **G** Noxious pinch-evoked licking responses in $Nfia^{F/F}$ control and $Nfia^{F/F}$;*Wnt1-Cre* mice ($n = 7$/group, Student's unpaired *t*-test, $P = 0.3472$, $t_{(12)} = 0.9783$).
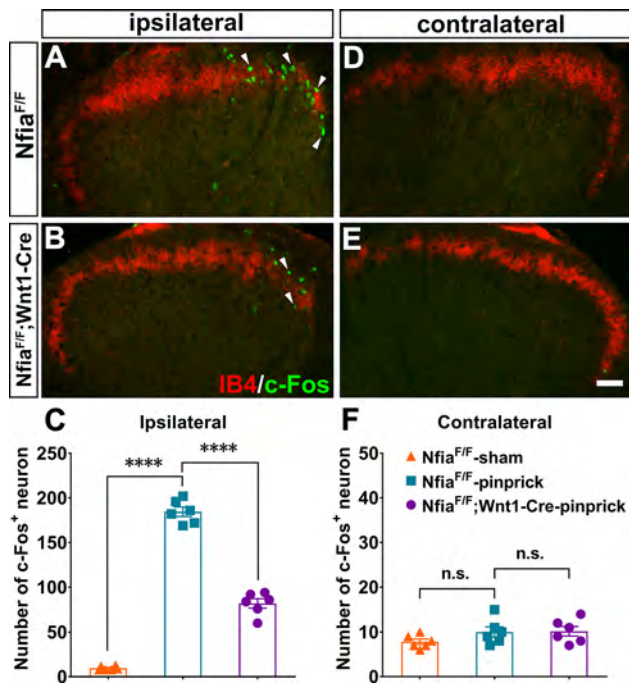
Fig. 5 Impairment of pinprick-evoked information transmission in conditional *Nfia* null mice. **A, B, D, E** Representative images of pinprick-induced c-Fos expression in the ipsilateral and contralateral dorsal horn of adult control (**A, D**) and *Nfia^F/F^;Wnt1-Cre* mice (**B, E**) (scale bar, 100 μm). **C** Numbers of c-Fos^+^ neurons in the ipsilateral and contralateral dorsal horns from mice with indicated genotypes and conditions ($n = 6$/group, one-way ANOVA with Tukey's *post-hoc* analysis, $F_{2, 15} = 420.2$, ****$P < 0.0001$). **F** Numbers of c-Fos^+^ neurons in the contralateral dorsal horns from mice with indicated genotypes and conditions ($n = 6$/group, one-way ANOVA with Tukey's *post-hoc* analysis, $F_{2, 15} = 1.78$, $P = 0.2024$).

with Bonferroni *post-hoc* analysis, $F_{2, 15} = 1.78$, $P = 0.2024$; Fig. 5D–F). Thus, transmission of pinprick-evoked mechanical information from the plantar skin to the dorsal spinal cord is compromised in *Nfia^F/F^;Wnt1-Cre* mice.

It should be noted that in *Nfia^F/F^;Wnt1-Cre* mice, NFIA expression would have been eliminated in both DRGs and in the dorsal spinal cord [16]. However, the same loss of Npy2r expression and impairment of pinprick-evoked responses were found in *Nfia^F/F^;Nav1.8-Cre* mice (Fig. 6A–D), in which the Cre recombinase is confined to DRG neurons, not in spinal neurons [18, 31].

Thus, NFIA-dependent DRG neurons, which include the Npy2r lineage neurons, play a prominent role in the transmission of pinprick-evoked sharp mechanical stimuli. These neurons only play a minor role in the transmission of von Frey filament punctate pressure information and are dispensable for the processing of pinch-evoked sustained licking responses.
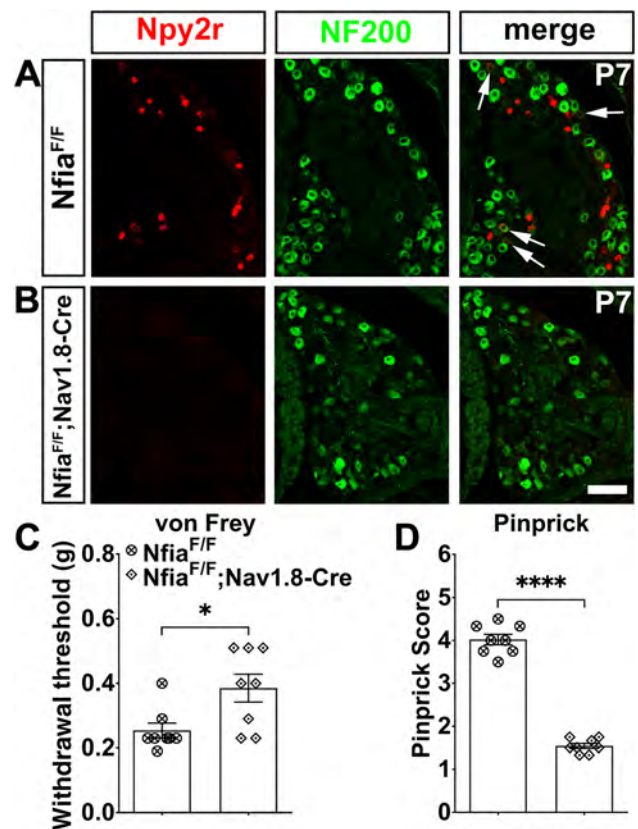
Fig. 6 Requirement of NFIA for the induction of pinprick-evoked pain transmission. **A, B** Representative images of ISH with the Npy2r probe plus NF200 immunostaining in sections through lumbar DRGs from P7 *Nfia^F/F^* control and *Nfia^F/F^;Nav1.8-Cre* mutant mice (arrows, Npy2r^+^;NF200^+^ neurons; scale bar, 100 μm). **C** Withdrawal thresholds in response to von Frey filament stimulation in *Nfia^F/F^;Nav1.8-Cre* CKO and *Nfia^F/F^* control mice ($n = 8$/group, Student's unpaired *t*-test, $P = 0.0178$, $t_{(14)} = 2.683$). **D** Pinprick scores evoked by a sharp steel pin glued to the tip of 1.0-g von Frey filament in *Nfia^F/F^;Nav1.8-Cre* and *Nfia^F/F^* control mice ($n = 8$/group, Student's unpaired *t*-test, $P < 0.0001$, $t_{(14)} = 18.21$).

Runx1 is Dispensable for the Development of Npy2r-transient A-fiber Neurons

We have reported previously that the development of Npy2r-persistent (Nppb^+^) neurons requires the transcription factor Runx1 [24]. Hence we asked whether Runx1 is also involved in the development of Npy2r-transient myelinated sensory neurons. Using the same *Wnt1-Cre*, we generated *Runx1* CKO mice, referred to as *Runx1^F/F^; Wnt1-Cre*, and found that at P7, there was no difference between CKO and control mice in the percentages of myelinated neurons co-expressing Npy2r and NF200 (control: $5.8\% \pm 0.3\%$, $n = 7$; CKO: $6.1\% \pm 0.1\%$; $n = 12$; *t*-test, $P = 0.8246$, $t_{(34)} = 0.83$; Fig. 7A–C). In contrast, the percentages of Npy2r^+^;NF200^-^ neurons, which represent Npy2r-persistent unmyelinated Nppb^+^ pruriceptors (see above, Fig. 1J), were lower in P7

692

Neurosci. Bull. July, 2020, 36(7):685–695

Fig. 7 Requirement of Runx1 for the development of Npy2r-persistent but not Npy2r-transient neurons. **A, B** Representative images of ISH with the Npy2r probe plus NF200 immunostaining in sections through lumbar DRGs from P7 $Runx1^{F/F}$ control and $Runx1^{F/F}$; $Wnt1$-Cre mutant mice (arrows, Npy2r$^+$;NF200$^+$ neurons; scale bar, 100 μm). **C** Percentages of Npy2r$^+$;NF200$^+$ and Npy2r$^+$; NF200$^-$ among all neurons in $Runx1^{F/F}$ control and $Runx1^{F/F}$; $Wnt1$-Cre CKO mice. **D** Pinprick scores evoked by a sharp steel pin glued to the tip of 1.0 g von Frey filament in $Runx1^{F/F}$ control ($n = 10$) and $Runx1^{F/F}$; $Wnt1$-Cre mice ($n = 6$) (Student's unpaired t-test, $P = 0.2766$, $t_{(14)} = 1.132$). **E, F** Pinprick-evoked c-Fos expression in the ipsilateral dorsal horns in $Runx1^{F/F}$ control and $Runx1^{F/F}$;$Wnt1$-Cre CKO mice. **G** Statistical comparison of c-Fos$^+$ neuronal numbers in the ipsilateral dorsal horns between $Runx1^{F/F}$ control and $Runx1^{F/F}$; $Wnt1$-Cre CKO mice ($n = 6$/group, one-way ANOVA with Tukey's $post$-hoc analysis, $F_{2, 15} = 151.7$, ****$P < 0.0001$). **H, I** C-Fos in the contralateral dorsal horn in $Runx1^{F/F}$ control and $Runx1^{F/F}$;$Wnt1$-Cre CKO mice. **J** Statistical comparison of c-Fos$^+$ neuronal numbers in the contralateral dorsal horn between $Runx1^{F/F}$ control and $Runx1^{F/F}$;$Wnt1$-Cre CKO mice ($n = 6$/group, one-way ANOVA with Tukey's $post$-hoc analysis, $F_{2, 15} = 1.075$, $P = 0.366$).
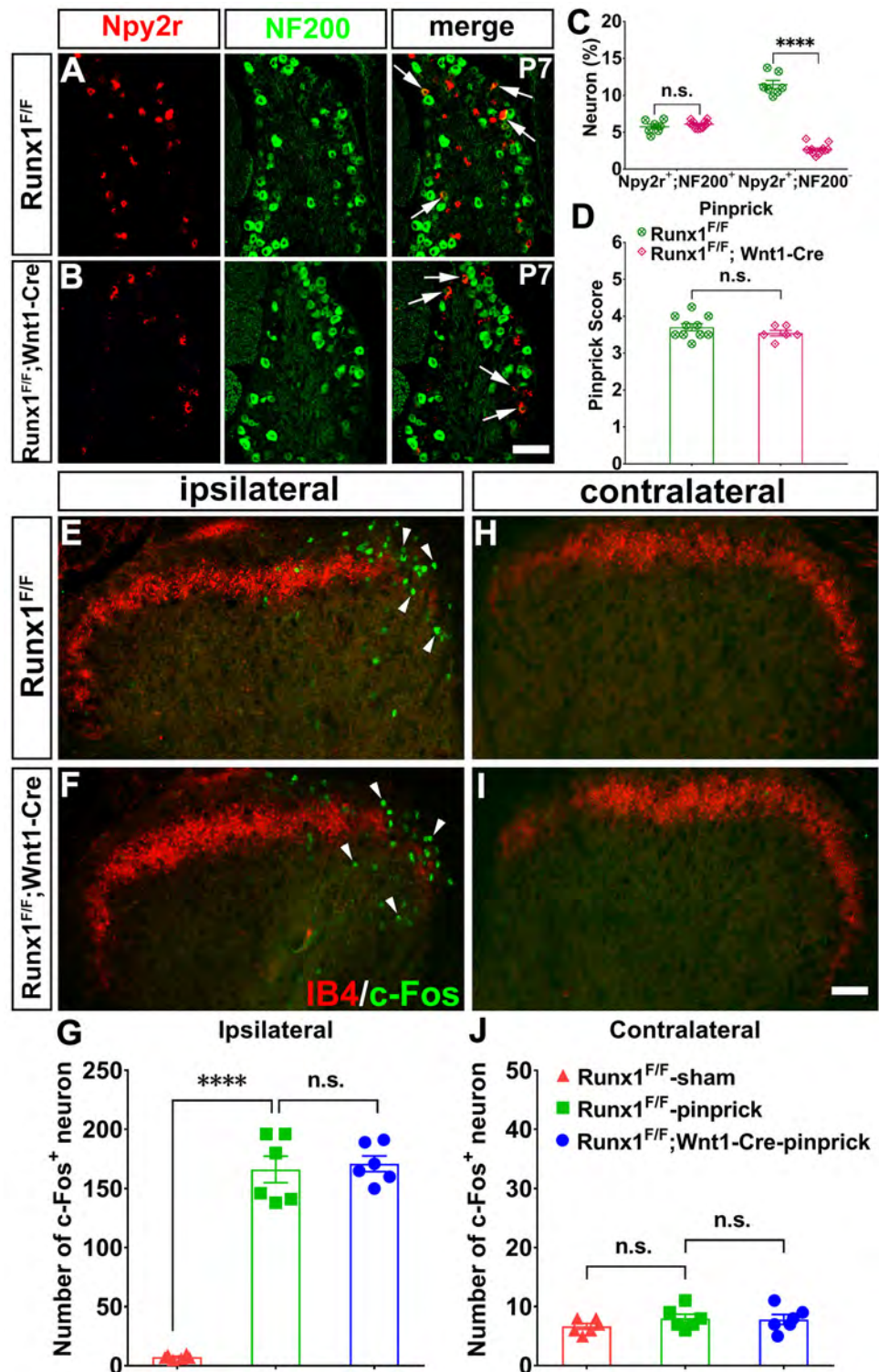
$Runx1^{F/F}$;$Wnt1$-Cre mice than in control littermates (control: 11.5% ± 0.5%, $n = 7$; CKO: 2.7% ± 0.2%; $n = 12$; t-test, $P < 0.0001$, $t_{(34)} = 21.77$; Fig. 7A–C), and we reported previously that by P30, persistent Npy2r expression is completely eliminated in these mutants [24]. Thus,

Runx1 is required for the development of Npy2r-persistent unmyelinated pruriceptors, but is apparently dispensable for that of Npy2r-transient myelinated sensory neurons. We then found that pinprick-evoked responses remained unchanged in $Runx1^{F/F}$;$Wnt1$-Cre mice compared with

controls (control: 3.7 ± 0.1, $n = 10$; CKO: 3.5 ± 0.1; $n = 6$; t-test, $P = 0.2766$, $t_{(14)} = 1.132$; Fig. 7D). Furthermore, the pinprick-evoked c-Fos induction in the dorsal spinal cord was not affected in these mutants (control: 166.2 ± 11.3, $n = 6$; CKO: 171.0 ± 6.6; $n = 6$; one-way ANOVA with Bonferroni *post-hoc* analysis, $F_{2, 15} = 151.7$, $P > 0.99$; Fig. 7E–G), in contrast with the marked reduction in $Nfia^{F/F}$;*Wnt1-Cre* mice. Our studies therefore suggested that Nfia and Runx1 control the development of different groups of mechanoreceptors (summarized in Fig. 8).

Discussion

NFIA Controls A-fiber Nociceptor Development

In humans, pinprick-evoked sharp pain percepts are mediated by myelinated A-fiber mechanoreceptors [32]. In both humans and animals, the transmission of noxious sensory information is dependent on TrkA-lineage neurons (TrkA is the receptor for nerve growth factor), since patients with loss-of-function *TrkA* mutations show congenital insensitivity to pain [33]. Earlier studies have shown that the genesis of TrkA neurons is entirely dependent on the proneural gene Neurog1 in the trigeminal and most rostral cervical DRGs [11]. Subsequent studies have shown that in thoracic and caudal DRGs, TrkA linages are formed in two waves, the early one giving rise to myelinated neurons and dependent on Neurog2, and the late one forming unmyelinated neurons and dependent on Neurog1 [9, 10], providing the first evidence for the existence of separate genetic programs controlling the development of myelinated *versus* unmyelinated nociceptors. Most recently, it has been reported that a subset of TrkA$^+$ A-fiber nociceptors can be genetically marked by *Npy2r-Cre*, and ablation of these neurons leads to impaired responses to pinprick stimuli [8]. It should, however, be noted that *Npy2r-Cre*-marked neurons include those with persistent or transient *Npy2r* expression. Our studies

Fig. 8 Separate genetic programs controlling different mechanoreceptors.

suggested that Npy2r is expressed transiently in A-fiber sensory neurons, and persistent high level of Npy2r expression is confined to Nppb$^+$ pruriceptors, consistent with single-cell RNA-seq results [25–27] and with an earlier report showing that Npy2r is predominantly expressed in small CGRP-positive DRG neurons [34]. Our subsequent studies showed that the transcription factor NFIA is required for the proper development of both Npy2r-transient and Npy2r-persistent neurons, as indicated by the complete elimination of Npy2r expression in $Nfia^{F/F}$;*Wnt1-Cre* mice at both neonatal and young adult stages. Two potential mechanisms, peripheral sensitization and central disinhibition, are responsible for the development of pinprick-evoked pain [8]. The spinal neurons marked by SOM^{Cre} are critical for the transmission of both pinprick and von Frey hair stimuli [20, 35]. Conditional knock-out of *Nfia* confined to peripheral DRG neurons results in the same loss of Npy2r expression and impairment of pinprick-evoked responses, which indicates that NFIA is mainly responsible for the induction of pinprick-evoked mechanical pain. All together, the above findings suggest that NFIA-dependent Npy2r-transient DRG neurons represent A-fiber nociceptors that transmit noxious sharp mechanical information. In other words, our studies identify NFIA as the first post-mitotic transcription factor controlling the development of A-fiber nociceptors. The complete loss of Npy2r also suggests a requirement of NFIA for the proper development of Nppb$^+$ neurons, which function as pruriceptors [28, 29]. Indeed, marked itch deficits were found in $Nfia^{F/F}$;*Wnt1-Cre* mice (unpublished results to be described elsewhere).

Separate Genetic Programs Controlling Myelinated *Versus* Unmyelinated Mechanical Nociceptors, as well as C-LTMRs

We found that while NFIA is necessary for the development of Npy2r-transient A-fiber nociceptors, it is dispensable for the expression of MrgprD, a marker for polymodal nociceptors, and TH, a marker for C-LTMRs, both of which are unmyelinated C-fiber sensory neurons [1–3, 5, 7]. Interestingly, the phenotypes are exactly opposite in mice with *Runx1* knockout, with complete loss of MrgprD and TH [6, 13] and without loss of Npy2r$^+$; NF200$^+$ myelinated sensory neurons, even though both transcription factors are required for the development of Npy2r-persistent Nppb$^+$ pruriceptors. Earlier studies have shown that Runx1 expression is confined to the Neurog1-dependent late-born TrkA neurons, as indicated by complete loss of Runx1 in *Neurog1$^{-/-}$* mice [9, 13, 36]. This explains why Runx1 is dispensable for the development of Npy2r-transient A-fiber nociceptors, which are likely formed during the Neurog2-dependent first wave of
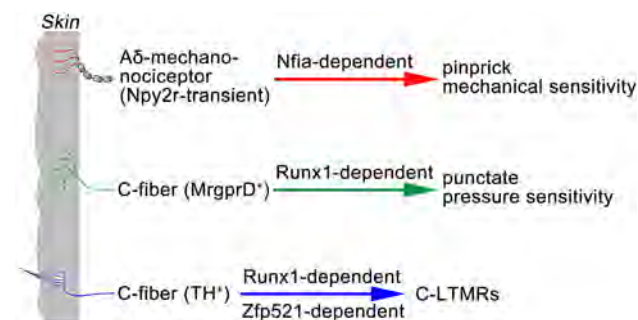
neurogenesis [9]. It should be noted that another transcription factor, Zfp521, is expressed selectively in TH$^+$ C-LTMRs, and it acts to promote and suppress molecular features associated with TH$^+$ C-LTMRs and MrgprD$^+$ nociceptors, respectively [15], leading to further segregation of Runx1-dependent neurons. All together, these studies reveal separate genetic programs controlling the emergence of functionally distinct mechanoreceptor subtypes among TrkA-lineage neurons (summarized in Fig. 8).

Conflict of interest The authors declare no competing financial interests.

References

1. Cavanaugh DJ, Lee H, Lo L, Shields SD, Zylka MJ, Basbaum AI, *et al.* Distinct subsets of unmyelinated primary sensory fibers mediate behavioral responses to noxious thermal and mechanical stimuli. Proc Natl Acad Sci U S A 2009, 106: 9075–9080.

2. Zylka MJ, Rice FL, Anderson DJ. Topographically distinct epidermal nociceptive circuits revealed by axonal tracers targeted to Mrgprd. Neuron 2005, 45: 17–25.

3. Rau KK, Mcilwrath SL, Wang H, Lawson JJ, Jankowski MP, Zylka MJ, *et al.* Mrgprd enhances excitability in specific populations of cutaneous murine polymodal nociceptors. J Neurosci 2009, 29: 8612–8619.

4. Seal RP, Wang X, Guan Y, Raja SN, Woodbury CJ, Basbaum AI, *et al.* Injury-induced mechanical hypersensitivity requires C-low threshold mechanoreceptors. Nature 2009, 462: 651–655.

5. Li L, Rutlin M, Abraira VE, Cassidy C, Kus L, Gong S, *et al.* The functional organization of cutaneous low-threshold mechanosensory neurons. Cell 2011, 147: 1615–1627.

6. Lou S, Duan B, Vong L, Lowell BB, Ma Q. Runx1 controls terminal morphology and mechanosensitivity of VGLUT3-expressing C-mechanoreceptors. J Neurosci 2013, 33: 870–882.

7. Delfini MC, Mantilleri A, Gaillard S, Hao J, Reynders A, Malapert P, *et al.* TAFA4, a chemokine-like protein, modulates injury-induced mechanical and chemical pain hypersensitivity in mice. Cell Reports 2013, 5: 378–388.

8. Arcourt A, Gorham L, Dhandapani R, Prato V, Taberner FJ, Wende H, *et al.* Touch receptor-derived sensory information alleviates acute pain signaling and fine-tunes nociceptive reflex coordination. Neuron 2017, 93: 179–193.

9. Lallemend F, Ernfors P. Molecular interactions underlying the specification of sensory neurons. Trends Neurosci 2012, 35: 373–381.

10. Liu Y, Ma Q. Generation of somatic sensory neuron diversity and implications on sensory coding. Curr Opin Neurobiol 2011, 21: 52–60.

11. Ma Q, Fode C, Guillemot F, Anderson DJ. Neurogenin1 and neurogenin2 control two distinct waves of neurogenesis in developing dorsal root ganglia. Genes Dev 1999, 13: 1717–1728.

12. Bachy I, Franck MCM, Li L, Abdo H, Pattyn A, Ernfors P. The transcription factor Cux2 marks development of an A-delta sublineage of TrkA sensory neurons. Dev Biol 2011, 360: 77–86.

13. Chen CL, Broom DC, Liu Y, de Nooij JC, Li Z, Cen C, *et al.* Runx1 determines nociceptive sensory neuron phenotype and is required for thermal and neuropathic pain. Neuron 2006, 49: 365–377.

14. Liu Y, Yang FC, Okuda T, Dong X, Zylka MJ, Chen CL, *et al.* Mechanisms of compartmentalized expression of Mrg class G-protein-coupled sensory receptors. J Neurosci 2008, 28: 125–132.

15. Lou S, Pan X, Huang T, Duan B, Yang F-C, Yang J, *et al.* Incoherent feed-forward regulatory loops control segregation of C-mechanoreceptors, nociceptors, and pruriceptors. J Neurosci 2015, 35: 5317–5329.

16. Jiang X, Rowitch DH, Soriano P, Mcmahon AP, Sucov HM. Fate of the mammalian cardiac neural crest. Development 2000, 127: 1607–1616.

17. Growney JD, Shigematsu H, Li Z, Lee BH, Adelsperger J, Rowan R, *et al.* Loss of Runx1 perturbs adult hematopoiesis and is associated with a myeloproliferative phenotype. Blood 2005, 106: 494–504.

18. Agarwal N, Offermanns S, Kuner R. Conditional gene deletion in primary nociceptive neurons of trigeminal ganglia and dorsal root ganglia. Genesis 2004, 38: 122–129.

19. Clark BS, Stein-O'Brien GL, Shiau F, Cannon GH, Davis-Marcisak E, Sherman T, *et al.* Single-cell RNA-Seq analysis of retinal development identifies NFI factors as regulating mitotic exit and late-born cell specification. Neuron 2019, 102: 1111–1126.

20. Duan B, Cheng L, Bourane S, Britz O, Padilla C, Garcia-Campmany L, *et al.* Identification of spinal circuits transmitting and gating mechanical pain. Cell 2014, 159: 1417–1432.

21. Peng C, Li L, Zhang MD, Gonzales CB, Parisien M, Belfer I, *et al.* MiR-183 cluster scales mechanical pain sensitivity by regulating basal and neuropathic pain genes. Science 2017, 356: 1168–1171.

22. Chaplan SR, Bach FW, Pogrel JW, Chung JM, Yaksh TL. Quantitative assessment of tactile allodynia in the rat paw. J Neurosci Methods 1994, 53: 55–63.

23. Huang T, Lin S, Malewicz NM, Zhang Y, Zhang Y, Goulding M, *et al.* Identifying the pathways required for coping behaviours associated with sustained pain. Nature 2019, 565: 86–90.

24. Qi L, Huang C, Wu X, Tao Y, Yan J, Shi T, *et al.* Hierarchical specification of pruriceptors by Runt-domain transcription factor Runx1. J Neurosci 2017, 37: 5549–5561.

25. Usoskin D, Furlan A, Islam S, Abdo H, Lönnerberg P, Lou D, *et al.* Unbiased classification of sensory neuron types by large-scale single-cell RNA sequencing. Nat Neurosci 2015, 18: 145–153.

26. Li CL, Li KC, Wu D, Chen Y, Luo H, Zhao JR, *et al.* Somatosensory neuron types identified by high-coverage single-cell RNA-sequencing and functional heterogeneity. Cell Res 2016, 26: 83–102.
27. Li C, Wang S, Chen Y, Zhang X. Somatosensory neuron typing with high-coverage single-cell RNA sequencing and functional analysis. Neurosci Bull 2018, 34: 200–207.
28. Mishra SK, Hoon MA. The cells and circuitry for itch responses in mice. Science 2013, 340: 968–971.
29. Huang J, Polgã RE, Solinski HJ, Mishra SK, Tseng PY, Iwagaki N, *et al.* Circuit dissection of the role of somatostatin in itch and pain. Nat Neurosci 2018, 21: 707–716.
30. Gao YJ, Ji RR. c-Fos and pERK, which is a better marker for neuronal activation and central sensitization after noxious stimulation and tissue injury? Open Pain Journal 2009, 2: 11–17.
31. Shields SD, Ahn H, Yang Y, Han C, Seal RP, Wood JN, *et al.* Nav1.8 expression is not restricted to nociceptors in mouse peripheral nervous system. Pain 2012, 153: 2017–2030.
32. Haggard P, Iannetti GD, Longo MR. Spatial sensory organization and body representation in pain perception. Curr Biol 2013, 23: R164–R176.
33. Indo Y. NGF-dependent neurons and neurobiology of emotions and feelings: Lessons from congenital insensitivity to pain with anhidrosis. Neurosci Biobehav Revi 2018, 87: 1–16.
34. Brumovsky P, Stanic D, Shuster S, Herzog H, Villar M, Hökfelt T. Neuropeptide Y2 receptor protein is present in peptidergic and nonpeptidergic primary sensory neurons of the mouse. J Comp Neurol 2005, 489: 328–348.
35. Duan B, Cheng L, Ma Q. Spinal circuits transmitting mechanical pain and itch. Neurosci Bull 2018, 34: 186–193.
36. Kramer I, Sigrist M, De Nooij JC, Taniuchi I, Jessell TM, Arber S. A role for Runx transcription factor signaling in dorsal root ganglion sensory neuron diversification. Neuron 2006, 49: 379–393.

ORIGINAL ARTICLE

Association of Polygenic Risk Score with Age at Onset and Cerebrospinal Fluid Biomarkers of Alzheimer's Disease in a Chinese Cohort

Wei-Wei Li[1] · Zhen Wang[2] · Dong-Yu Fan[1] · Ying-Ying Shen[1] · Dong-Wan Chen[1] ·
Hui-Yun Li[1] · Ling Li[1] · Heng Yang[1] · Yu-Hui Liu[1] · Xian-Le Bu[1] ·
Wang-Sheng Jin[1] · Fan Zeng[1] · Zhi-Qiang Xu[1] · Jin-Tai Yu[5] · Li-Yong Chen[2] ·
Yan-Jiang Wang[1,3,4]

Abstract To evaluate whether the polygenic profile modifies the development of sporadic Alzheimer's disease (sAD) and pathological biomarkers in cerebrospinal fluid (CSF), 462 sAD patients and 463 age-matched cognitively normal (CN) controls were genotyped for 35 single-nucleotide polymorphisms (SNPs) that are significantly associated with sAD. Then, the alleles found to be associated with sAD were used to build polygenic risk score (PRS) models to represent the genetic risk. Receiver operating characteristic (ROC) analyses and the Cox proportional hazards model were used to evaluate the predictive value of PRS for the sAD risk and age at onset. We measured the CSF levels of Aβ42, Aβ42/Aβ40, total tau (T-tau), and phosphorylated tau (P-tau) in a subgroup (60 sAD and 200 CN participants), and analyzed their relationships with the PRSs. We found that 14 SNPs, including SNPs in the *APOE, BIN1, CD33, EPHA1, SORL1*, and *TOMM40* genes, were associated with sAD risk in our cohort. The PRS models built with these SNPs showed potential for discriminating sAD patients from CN controls, and were able to predict the incidence rate of sAD and age at onset. Furthermore, the PRSs were correlated with the CSF levels of Aβ42, Aβ42/Aβ40, T-tau, and P-tau. Our study suggests that PRS models hold promise for assessing the genetic risk and development of AD. As genetic risk profiles vary among populations, large-scale genome-wide sequencing studies are urgently needed to identify the genetic risk loci of sAD in Chinese populations to build accurate PRS models for clinical practice.

Keywords Alzheimer's disease · Single nucleotide polymorphism · Polygenic risk score · Cerebrospinal fluid · Biomarker · Amyloid-beta · Tau

Wei-Wei Li and Zhen Wang have contributed equally to this work.

✉ Li-Yong Chen
mzkcly@aliyun.com

✉ Yan-Jiang Wang
yanjiang_wang@tmmu.edu.cn

1 Department of Neurology and Centre for Clinical Neuroscience, Daping Hospital, Third Military Medical University, Chongqing 400042, China

2 Department of Anaesthesiology, Daping Hospital, Third Military Medical University, Chongqing 400042, China

3 Chongqing Key Laboratory of Aging and Diseases, Chongqing 400042, China

4 Centre for Excellence in Brain Science and Intelligence Technology, Chinese Academy of Sciences, Shanghai 200031, China

5 Department of Neurology, Huashan Hospital, Fudan University, Shanghai 200040, China

Introduction

Alzheimer's disease (AD) is the most common neurodegenerative disorder and is closely related to the complex interaction among genes and environmental/lifestyle factors, among which heritability accounts for 58%–79% of the attribution for AD [1]. Apart from the apolipoprotein E (*APOE*) ε4 allele, which is the major susceptibility gene for sporadic AD (sAD) [2], a series of genome-wide association studies (GWASs) on AD dementia have identified a large number of single nucleotide polymorphisms (SNPs) with already known or hypothesized relationships to AD [3–11]. Most of these risk SNPs only exert minor effects on

the susceptibility to AD. The polygenic risk score (PRS) determines the genetic risk for a disease by combining the effects of multiple genetic loci and has proved to be a promising strategy for identifying the genetic risk for sAD [12, 13].

Previous studies have demonstrated the value of PRS models for sAD risk prediction, and the age at onset has also been found to correlate with the PRS [14–16]. Because disease-risk genetic loci vary according to ethnicity, PRSs must be established for different ethnicities. Here, we hypothesized that if an individual's PRS is associated with their disease liability, individuals having the highest PRSs may be the most likely to develop sAD, even at a young age. We built several PRS models to determine the contribution of the polygenic profile to the incidence risk and the age at onset of sAD in a Chinese cohort. Meanwhile, we analyzed the relationships between PRS and core cerebrospinal fluid (CSF) biomarkers of AD in an amyloid-beta (Aβ) deposition, pathologic tau, and neurodegeneration [AT(N)] scheme [17], with Aβ42, Aβ42/Aβ40, T-tau, and P-tau, to explore the impact of genetic risk on the pathology of AD.

Methods

Participants

A total of 462 sAD patients and 463 age-matched cognitively normal (CN) controls were recruited from Chongqing Daping Hospital from January 2015 to January 2019. Eligible participants were required (1) to have been diagnosed with sAD; (2) to be age-matched CN participants; and (3) to be willing to participate in the study. Participants were excluded for the following reasons: (1) a family history of dementia; (2) a concomitant neurologic disorder like head trauma or brain lesions that could potentially affect cognitive function, or other types of dementia; (3) severe cardiac, pulmonary, hepatic, or renal disease; and (4) mental illness (e.g., schizophrenia). The study was approved by the Institutional Review Board of Daping Hospital, and all participants and their caregivers provided informed consent.

Clinical Assessment and Diagnosis of sAD

Clinical assessment and diagnosis of sAD were performed following our previous protocol [18, 19]. All participants underwent clinical assessments that included medical history, physical examination, laboratory tests, *APOE* genotyping, and neuropsychological tests. Participants with abnormal cognition were further subjected to a brain CT/MRI investigation and blood tests for thyroxine, vitamin

B12, folic acid, and HIV/syphilis to rule out metabolic and infectious reasons for cognitive decline.

The diagnosis of AD was made according to the criteria of the National Institute of Neurological and Communicative Diseases and Stroke and the Alzheimer's Disease and Related Disorders Association (NINCDS–ADRDA) [20]; they included (1) insidious onset of symptoms, (2) a clear-cut history of worsening of cognition, and (3) prominent cognitive deficits in at least one of the following categories: amnestic presentation, language presentation, visuospatial presentation, or executive dysfunction. Patients were identified as having sAD if none of their first-degree relatives had dementia. CN participants had no memory complaints and performed within the normal range in the Mini-Mental State Examination (MMSE) [21] or the Montreal Cognitive Assessment [22].

SNP Selection and Genotyping

The SNPs reported in published GWASs and meta-analysis studies [5, 6, 9, 23, 24, 14] were initially included in the selection process. The alleles were excluded if (1) the minor allele frequency of the SNPs in the Chinese population was <0.05 (http://asia.ensembl.org/) or (2) the SNPs had been verified not to be associated with sAD risk in Chinese cohorts [25–29]. Detailed data for the selection and exclusion processes are provided in Table S1. Finally, a total of 35 SNPs in 18 candidate genes (including rs7412 and rs429358 in the *APOE* gene) were selected (Table S2).

Genotyping

Genotyping was conducted following a previously described method [30]. Briefly, genomic DNA was extracted from venous blood leukocytes using the Wizard genomic DNA purification kit (Promega, Madison, WI). Genotyping of the 35 SNPs was carried out with the multiplex polymerase chain reaction-ligase detection reaction method. For each SNP, the alleles were distinguished by the different fluorescent labels of allele-specific oligonucleotide probe pairs. Different SNPs were distinguished by different extended lengths at the 3' end. All SNPs in the study had an overall call rate of >95%.

CSF Sampling and Analyses

A subgroup of 60 sAD and 200 CN participants underwent CSF sampling and analyses. In detail, in the sAD patients, CSF was sampled by the standard procedure [31]. In CN participants who had diseases of the urinary system, the CSF samples were collected during lumbar anesthesia before surgery for their diseases. Specifically, CSF samples free from any blood contamination were collected in

698

Neurosci. Bull. July, 2020, 36(7):696–704

polypropylene tubes by lumbar puncture, centrifuged at 1800 g at 4°C for 10 min within 1 h, and stored frozen at −80°C until analysis.

The levels of Aβ42, Aβ40, T-tau, and P-tau were determined using commercially available ELISA kits (Innotest, Fujirebio Europe, Ghent, Belgium), which have been widely used and validated in multiple studies and show good assay sensitivity and intra- and inter-assay precision. All measurements were made in one round of analysis with one batch of reagents by an experienced laboratory technician who was blinded to the clinical information. Our laboratory is a center of the Alzheimer's Association quality control program [32] and is experienced in the examination of CSF biomarkers.

Statistical Analyses

Differences between groups were assessed by the two-sample independent t-test, the Mann-Whitney U test, the χ^2 test, Fisher's exact test, or analysis of variance according to the characteristics of the data. The data are expressed as the mean $\pm$ standard deviation (SD) for numerical variables or as the count (%) for categorical variables. All hypothesis-testing was two-sided, and statistical significance was defined as $P < 0.05$. All statistical computations were performed using SPSS version 19.0 (SPSS, Inc., Chicago, IL) or PLINK version 1.09 (http://www.cog-genomics.org/plink2), and all figures were created using a graphics package (GraphPad Software, Inc., San Diego, CA).

Single SNP Analyses

The allele and genotype distributions of the SNPs between the sAD patients and CN participants were analyzed using χ^2 statistics [33]. The odds ratios (ORs; calculated relative to the common genotype) and 95% confidence intervals (CIs) were corrected for age (age at onset for sAD patients and age at inclusion for CN participants), sex, and APOE ε4 status (presence of one or two APOE ε4 alleles *versus* absence of the APOE ε4 allele) using logistic regression models (correction for APOE ε4 status was performed for all SNPs except those on the APOE gene).

Computation of PRSs

The SNPs associated with sAD ($P < 0.05$) in our cohort were selected to generate a PRS model (Model 1). For each participant, the PRS was calculated by summing the risk allele counts of the SNPs weighted by the natural logarithms of their respective ORs (calculated based on the present study). Given the strong effect of APOE genotypes on sAD and a recent systematic review, which

suggested that including APOE in the PRS increased the AD prediction accuracy [13], APOE ε2/3/4 genotypes were incorporated into the PRS as special covariates with standard effects, namely, ε2/ε2 = 0.6, ε2/ε3 = 0.6, ε2/ε4 = 2.6, ε3/ε3 = 1.0, ε3/ε4 = 3.2, and ε4/ε4 = 14.9, as previously reported [34]. To build a more rigorous PRS model, only SNPs with a P-value threshold of 0.01 in the logistic regression analysis were included in Model 2. Because APOE is a critical gene for sAD, we also constructed Model 3 with APOE genotypes only.

The association of the PRS with sAD risk was tested by logistic regression, with age and sex as covariates. To evaluate the ability of PRS for case/control discrimination, receiver operating characteristic (ROC) analyses were performed by plotting the true positive rate against the false-positive rate. The area under the curve (AUC), sensitivity, and specificity with 95% CIs were calculated. Moreover, participants were partitioned into tertiles (two points at 33.33% and 66.67% divided the ordered distribution of PRSs into three parts, each containing a third of the population); the associations of the PRS with the age at onset and the cumulative incidence rate of sAD were reflected by a Cox proportional hazard model. Relationships between the PRSs and CSF biomarkers were assessed by Spearman correlation analyses. And the relationships were also evaluated with general linear models. Specifically, the PRS was used as the independent variable and the CSF biomarkers were used as dependent variables; the confounders age, sex, and APOE genotype were taken as covariates.

Results

Characteristics of the Study Participants and SNP Distributions

The characteristics of the participants are shown in Table 1. There were no significant differences in age ($P = 0.17$) between sAD patients and CN controls. sAD patients consisted of a higher proportion of females and APOE ε4 carriers and had lower MMSE scores. The CSF levels of Aβ42, Aβ40, and Aβ42/Aβ40 in the sAD group were lower than those in the control group (Aβ42: 632.60 $\pm$ 233.16 pg/mL *vs* 1265.39 $\pm$ 437.02 pg/mL, $P < 0.001$; Aβ40: 8519.27 $\pm$ 3846.22 pg/mL *vs* 11276.15 $\pm$ 4502.05 pg/mL, $P < 0.001$; Aβ42/Aβ40: 0.092 $\pm$ 0.092 *vs* 0.13 $\pm$ 0.088, $P < 0.001$). The CSF levels of T-tau and P-tau in the sAD group were higher than those in the control group (T-tau: 527.62 $\pm$ 443.62 pg/mL *vs* 219.74 $\pm$ 112.09 pg/mL, $P < 0.001$; P-tau: 70.03 $\pm$ 39.19 pg/mL *vs* 47.82 $\pm$ 16.72 pg/mL, $P < 0.001$).

Table 1 Characteristics of the study participants.

Characteristics	sAD (*n* = 462)	Control (*n* = 463)	*P* value
Age, mean (SD), years	69.75 (9.84)	68.85 (10.12)	0.17
Female, *n* (%)	243 (52.6)	193 (41.7)	0.001
MMSE score, mean (SD)	14.41 (7.55)	24.84 (3.97)	<0.001
APOE ε4 carriers, *n* (%)	191 (41.3)	101 (21.8)	<0.001
CSF Aβ42, pg/mL, mean (SD)	632.60 (233.16)	1265.39 (437.02)	<0.001
CSF Aβ40, pg/mL, mean (SD)	8519.27 (3846.22)	11276.15 (4502.05)	<0.001
CSF Aβ42/Aβ40, mean (SD)	0.092 (0.092)	0.13 (0.088)	<0.001
CSF T-tau, pg/mL, mean (SD)	527.62 (443.62)	219.74 (112.09)	<0.001
CSF P-tau, pg/mL, mean (SD)	70.03 (39.19)	47.82 (16.72)	<0.001

Differences between groups were assessed using Mann–Whitney U tests (for numerical variables) or χ^2 tests (for categorical variables); sAD, sporadic Alzheimer's disease; MMSE Mini-Mental State Examination; *APOE,* apolipoprotein E; CSF, cerebrospinal fluid.

Fourteen of the 35 SNPs were significantly associated with the risk of sAD ($P < 0.05$, Table 2): two (rs429358 and rs7412) on the *APOE* gene, two (rs6733839 and rs7561528) on the *BIN1* gene, two (rs3865444 and rs3826656) on the *CD33* gene, one (rs11771145) on the *EPHA1* gene, four (rs561655, rs541458, rs10792832, and rs3851179) on the *PICALM* gene, two (rs11218343 and rs3781834) on the *SORL1* gene, and one (rs2075650) on the *TOMM40* gene. Only rs2075650 on the *TOMM40* gene and rs429358 on the *APOE* gene remained significant after Bonferroni correction ($P < 0.001$). Information on the included SNPs (neighboring genes, chromosomes, minor alleles, minor allele frequencies, Hardy-Weinberg equilibrium values, and positions) and their allele and genotype frequencies are summarized in Tables S2–S4.

Discriminative Performance of PRSs for sAD Patients and CN Controls

Three PRS models were developed (Table 3). As expected, the average PRSs in sAD patients were significantly higher than those in controls based on all three models (Mann-Whitney test, $P < 0.0001$, Fig. 1). Logistic regression analyses with adjustment for age and sex showed a positive relationship between sAD risk and PRS (OR > 1, Table 3). When we compared the discriminative ability of each PRS model by ROC curve analyses (Fig. 2), Model 1 had a sensitivity of 0.68 and a specificity of 0.57 (AUC = 0.66) and Model 2 had a sensitivity of 0.72 and a specificity of 0.49 (AUC = 0.65) (there was no significant difference between the two models). The sensitivity of Model 3 (0.61)

Table 2 Allele distribution of the significant SNPs.

SNP	Neighboring Gene	Risk allele	Risk allele frequency		OR (95% CI)	*P* value
			sAD	Control		
rs429358	*APOE*	C	0.25	0.12	2.55 (1.99–3.28)	<0.001
rs7412	*APOE*	T	0.05	0.07	0.62 (0.42–0.92)	0.02
rs6733839	*BIN1*	T	0.45	0.38	1.30 (1.08–1.57)	0.007
rs7561528	*BIN1*	A	0.13	0.10	1.38 (1.03–1.85)	0.032
rs3865444	*CD33*	A	0.17	0.22	0.72 (0.57–0.91)	0.006
rs3826656	*CD33*	A	0.30	0.34	0.81 (0.66–0.98)	0.03
rs11771145	*EPHA1*	G	0.48	0.43	1.25 (1.04–1.50)	0.02
rs561655	*PICALM*	G	0.43	0.49	0.78 (0.65–0.94)	0.01
rs541458	*PICALM*	T	0.47	0.53	0.79 (0.65–0.95)	0.01
rs10792832	*PICALM*	A	0.35	0.40	0.81 (0.67–0.98)	0.03
rs3851179	*PICALM*	T	0.35	0.39	0.81 (0.67–0.99)	0.04
rs11218343	*SORL1*	C	0.26	0.31	0.78 (0.64–0.96)	0.02
rs3781834	*SORL1*	G	0.19	0.23	0.79 (0.63–0.99)	0.04
rs2075650	*TOMM40*	G	0.23	0.11	2.32 (1.79–3.00)	<0.001

The ORs and 95% CIs were adjusted for age, sex, and *APOE* ε4 status; SNP, single-nucleotide polymorphism; OR, odds ratio; CI, confidence interval.

Table 3 Logistic regressions for the associations of PRSs with sAD risk in the different PRS models.

PRS models	P thresholds of SNPs	Logistic regressions		ROC curve analyses		
		OR (95% CI)	P	AUC (95% CI)	Sensitivity	Specificity
Model 1	0.05	1.58 (1.41–1.76)	<0.001	0.66 (0.63–0.70)	0.68	0.57
Model 2	0.01	1.56 (1.39–1.76)	<0.001	0.65 (0.61–0.68)	0.72	0.49
Model 3	*APOE* genotype only	1.20 (1.12–1.28)	<0.001	0.61 (0.58–0.65)	0.42	0.78

The associations of the PRSs with sAD risk were tested by logistic regression adjusted by age and sex. PRS, polygenic risk score; SNP, single nucleotide polymorphism; sAD, sporadic Alzheimer's disease.

Fig. 1 PRSs in sAD patients and controls based on models 1 (**A**), 2 (**B**) and 3 (**C**). Differences between groups were assessed using Mann–Whitney U tests (error bars, SD; ****$P < 0.0001$; PRS, polygenic risk score; sAD, sporadic Alzheimer's disease).
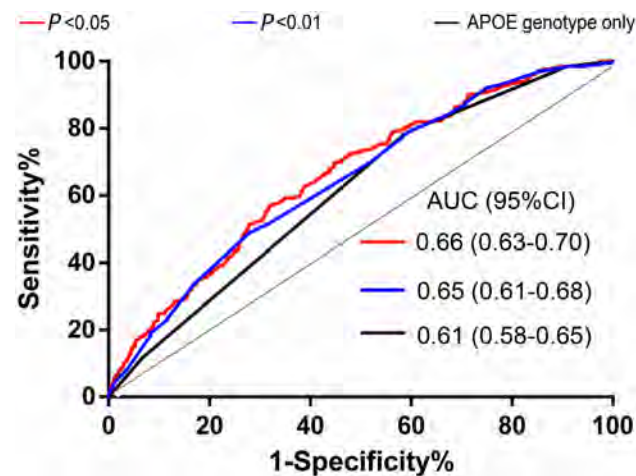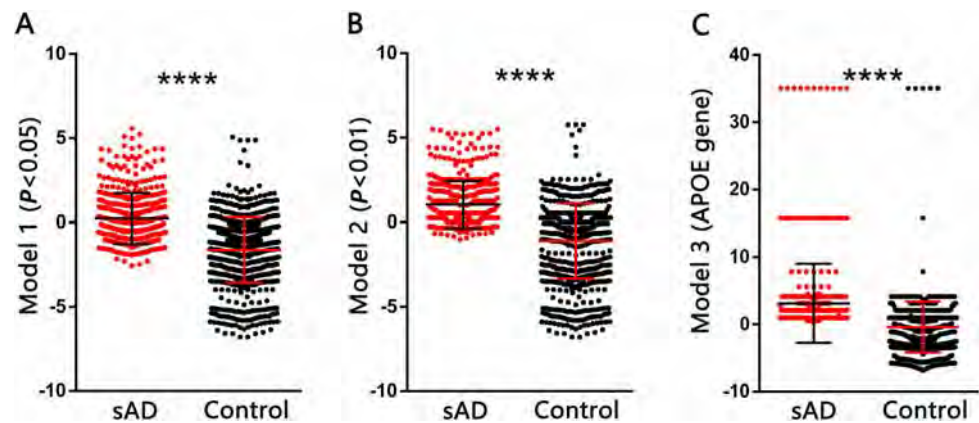
Fig. 2 Discriminative ability (ROC curves) of different PRS models for sAD. PRSs were built with SNPs with $P < 0.05$ (red), $P < 0.01$ (blue), and *APOE* genotype only (black) (AUC, area under the curve; ROC, receiver operating characteristic curve; sAD, sporadic Alzheimer's disease).

Predictive Ability of PRS Models for the Incidence Rate of sAD and Age at Onset

The modulation of PRS with the occurrence of sAD was evaluated using a Cox proportional hazards model (Fig. 3). The PRSs from Model 1 were chosen for the analysis. Participants were classified into three risk groups based on the PRS tertiles. The Log-Rank test revealed that a higher PRS was significantly associated with an earlier age at onset (high-PRS *vs* low-PRS, OR = 1.56, $P = 0.0001$, 95% CI: 1.26–1.97; intermediate-PRS *vs* low-PRS, OR = 1.39, $P = 0.0076$, 95% CI: 1.10–1.81). For example, in a cohort with a high-PRS, the expected age for 50% to develop sAD was ~75 years, earlier than in individuals with a low-PRS (the expected age for developing sAD in 50% was ~80 years). Moreover, the cumulative incidence rates in the high-PRS group were higher than those in the low-PRS group. For example, among two groups of 70-year-old individuals (with high-PRS or low-PRS), the percentage of sAD patients in the high-PRS group was higher than that in the low-PRS group (30% *vs* 20%).

Correlations Between PRS and AD Biomarkers in CSF

We analyzed the correlations between PRSs and the CSF levels of Aβ42, Aβ42/Aβ40, T-tau, and P-tau in the total

based on the *APOE* gene alone was lower than that of the other models, but the specificity (0.78) was higher.

Fig. 3 Cumulative incidence rates of sAD in three genetic risk groups. Participants were partitioned into tertiles (low *vs* intermediate *vs* high PRS), with PRS cut-offs at 33.33% and 66.67% (PRS, polygenic risk score; sAD, sporadic Alzheimer's disease).
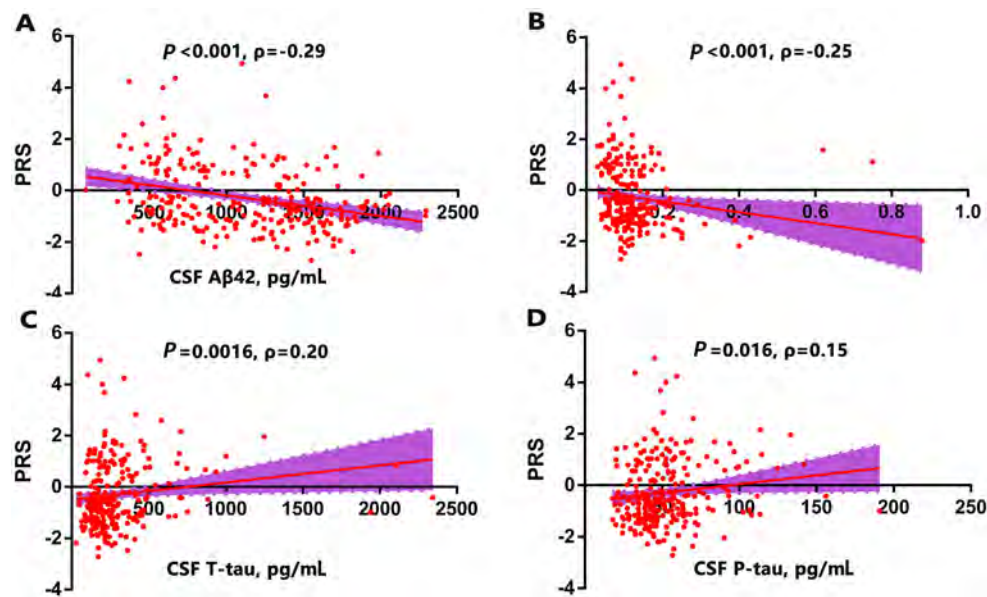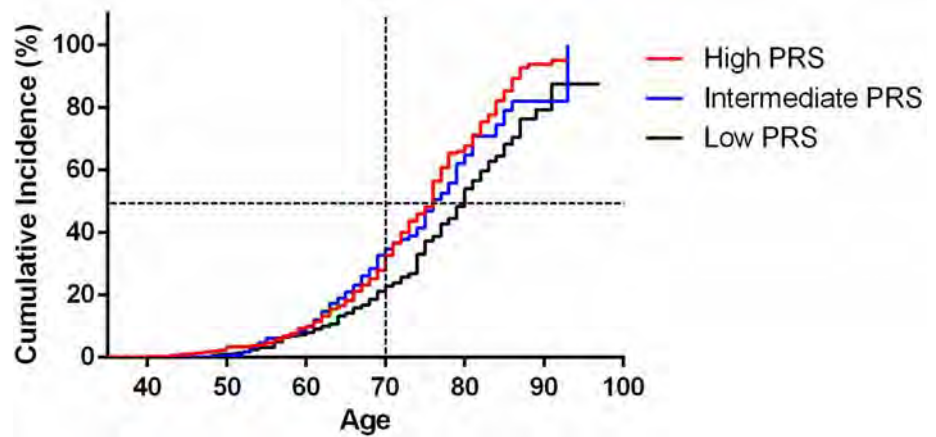
Fig. 4 Correlations between PRSs and CSF biomarkers. **A–D** Scatterplots of PRS with (**A**) Aβ42, (**B**) Aβ42/Aβ40 ratio, (**C**) T-tau, and (**D**) P-tau (Spearman correlation coefficients (ρ) were used to assess the correlations; PRS, polygenic risk score; CSF, cerebrospinal fluid).

cohort (Fig. 4), and used the PRSs from Model 1 for analysis. The CSF levels of Aβ42 and the Aβ42/Aβ40 ratio were inversely associated with the PRS (Aβ42: $P < 0.001$, Spearman $\rho = -0.29$; Aβ42/Aβ40 ratio: $P < 0.001$, Spearman $\rho = -0.25$), T-tau and P-tau were positively associated with the PRS (T-tau: $P = 0.0016$, Spearman $\rho = 0.20$; P-tau: $P = 0.016$, Spearman $\rho = 0.15$). The correlations remained similar for Aβ42 and T-tau (Aβ42, $\beta = -0.31$, $P < 0.001$; Aβ42/Aβ40 ratio, $\beta = -0.13$, $P = 0.10$; T-tau, $\beta = 0.16$, $P = 0.032$; P-tau, $\beta = 0.13$, $P = 0.08$) after adjusting for age, sex and *APOE* genotype with a general linear regression. The correlations in the CN control group were consistent with the total cohort (Table S5). Further, we partitioned the participants into three groups based on the tertiles of CSF Aβ42 level. The PRSs from Model 1

were used to differentiate individuals with the highest (third tertile) and lowest (first tertile) Aβ42 levels. The ability of PRS to determine the CSF level of Aβ42 was ∼0.61 (AUC of the ROC curve) (Fig. 5), and increased to 0.69 when taking age and sex into account.

Discussion

In this study, we explored the effects of genes on sAD development and the pathological process by screening and integrating AD-associated SNPs identified from large GWASs and building polygenic risk models. Only 14 of the 35 SNPs identified in other populations had significant correlations with sAD, and the PRSs based on the 14 SNPs
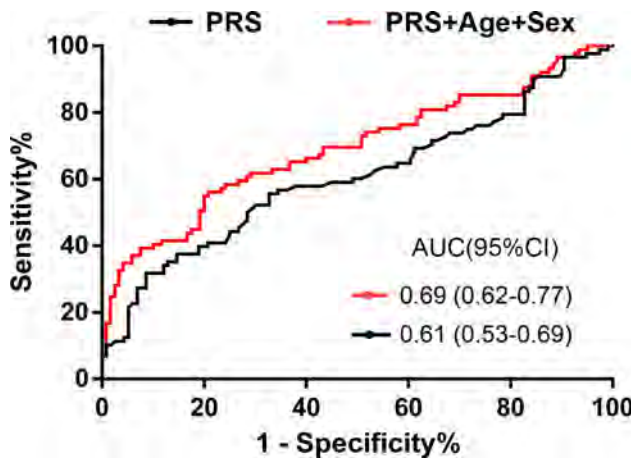
Fig. 5 Discriminative ability of PRS model for CSF Aβ42 level. The AUC of the ROC curve was improved when taking age and sex into account (PRS, polygenic risk score; ROC, receiver operating characteristic curve; AUC, area under the curve; CI, confidence interval; CSF, cerebrospinal fluid).

were associated with the risk of sAD, age at onset, and CSF biomarkers in our Chinese cohort.

Three PRS models containing different numbers or categories of SNPs were built for case/control discrimination. We found no improvement in the discrimination when more SNPs were included in the PRS model. Thus, considering the expense of genotype sequencing, a PRS model based on fewer SNPs (SNPs with a P threshold of 0.01 in our study) would be more accessible. The PRS model built on the *APOE* genotype, which is associated with amyloid pathology in Chinese AD patients [35], had relatively higher specificity and lower sensitivity in case/control discrimination, confirming the hypothesis that sAD can be attributed to multiple genetic profiles rather than a single gene.

We used a Cox regression survival model for the age at onset analysis because it provides more power than a simple linear regression model. Consistent with previous findings [14–16], individuals with a high genetic risk (high-PRS) were more likely to develop sAD, and the time of onset was earlier than that in individuals with a low genetic risk (low-PRS), which suggests that the incidence risk of sAD and age at onset are modified by the polygenic profile. From a clinical perspective, although not ready for use in clinical practice, our PRS model has the potential to serve as a predictor for identifying seniors at risk for developing sAD at a given age and provides potential sAD patients with access to early diagnosis and treatment. Of course, additional studies with SNPs from Chinese GWASs are needed to strengthen the predictive power of PRS models.

The impact of genetic risk on the biomarkers of sAD can provide deep insight into the pathogenesis of the disease. We found a significant relationship between an increased

PRS and decreased CSF levels of Aβ42 or the Aβ42/Aβ40 ratio as well as increased CSF levels of T-tau and P-tau, suggesting that the genetic profile modulates the pathogenesis of sAD. Because the pathological changes of AD begin 15–20 years before clinical presentation [36] and clinical trials of disease-modifying therapy at the preclinical stage are promising [37], the use of a polygenic model to identify individuals with abnormal level of CSF biomarkers seems valuable. In this study, we identified individuals with an extremely abnormal level of CSF Aβ42 using the PRS model we built. However, the model was not accurate enough to determine the sAD risk and its related pathology, which is reasonable because complex factors, including the environment and lifestyle, also contribute to the pathogenesis of AD [1]. Future studies elucidating these non-hereditary factors in individuals with genetic risk information may offer more valuable insight into the relationship between genes and AD pathology. Nevertheless, individuals who exhibit a 'positive' result from a genomic examination can apply for more accurate clinical, CSF, or imaging examinations, which will provide more accurate probabilistic assessments as to whether AD development is likely to occur.

The present study has three major limitations. First, the case/control approach assumes that controls do not develop sAD and considers the disease process to be a dichotomous variable; errors may exist because some controls may be at the preclinical stage of AD. Second, our AD participants were actually probable AD because the diagnosis was made based on the NINCDS–ADRDA criteria; results can be more accurate if AD is diagnosed with the assistance of biomarkers [18]. Third, the PRSs were based on SNPs identified in other ethnicities. Because the risk loci of sAD may differ among ethnicities, a PRS model built on SNPs identified in the Chinese population would provide more accurate prediction of the genetic risk of sAD in Chinese participants.

Conclusions

In the present study, several SNPs had significant correlations with sAD risk, age at onset, and its CSF biomarkers in our cohort, suggesting that PRS models hold promise for assessing the genetic risk of the development of AD. As genetic risk profiles vary among populations, large-scale genome-wide sequencing studies are urgently needed to identify the genetic risk loci of sAD in Chinese populations to build accurate PRS models for clinical practice.

References

1. Gatz M, Reynolds CA, Fratiglioni L, Johansson B, Mortimer JA, Berg S, *et al*. Role of genes and environments for explaining Alzheimer disease. Arch Gen Psychiatry 2006, 63: 168–174.

2. Saunders AM, Strittmatter WJ, Schmechel D, George-Hyslop PH, Pericak-Vance MA, Joo SH, *et al*. Association of apolipoprotein E allele epsilon 4 with late-onset familial and sporadic Alzheimer's disease. Neurology 1993, 43: 1467–1472.

3. Lambert JC, Ibrahim-Verbaas CA, Harold D, Naj AC, Sims R, Bellenguez C, *et al*. Meta-analysis of 74,046 individuals identifies 11 new susceptibility loci for Alzheimer's disease. Nat Genet 2013, 45: 1452–1458.

4. Hollingworth P, Harold D, Sims R, Gerrish A, Lambert JC, Carrasquillo MM, *et al*. Common variants at *ABCA7, MS4A6A/MS4A4E, EPHA1, CD33* and *CD2AP* are associated with Alzheimer's disease. Nat Genet 2011, 43: 429–435.

5. Harold D, Abraham R, Hollingworth P, Sims R, Gerrish A, Hamshere ML, *et al*. Genome-wide association study identifies variants at CLU and PICALM associated with Alzheimer's disease. Nat Genet 2009, 41: 1088–1093.

6. Naj AC, Jun G, Beecham GW, Wang LS, Vardarajan BN, Buros J, *et al*. Common variants at *MS4A4/MS4A6E, CD2AP, CD33* and *EPHA1* are associated with late-onset Alzheimer's disease. Nat Genet 2011, 43: 436–441.

7. Lambert JC, Heath S, Even G, Campion D, Sleegers K, Hiltunen M, *et al*. Genome-wide association study identifies variants at CLU and CR1 associated with Alzheimer's disease. Nat Genet 2009, 41: 1094–1099.

8. Chouraki V, Seshadri S. Genetics of Alzheimer's disease. Adv Genet 2014, 87: 245–294.

9. Miyashita A, Koike A, Jun G, Wang LS, Takahashi S, Matsubara E, *et al*. SORL1 is genetically associated with late-onset Alzheimer's disease in Japanese, Koreans and Caucasians. PLoS One 2013, 8: e58618.

10. Lacour A, Espinosa A, Louwersheimer E, Heilmann S, Hernandez I, Wolfsgruber S, *et al*. Genome-wide significant risk factors for Alzheimer's disease: role in progression to dementia due to Alzheimer's disease among subjects with mild cognitive impairment. Mol Psychiatry 2017, 22: 153–160.

11. Jansen IE, Savage JE, Watanabe K, Bryois J, Williams DM, Steinberg S, *et al*. Genome-wide meta-analysis identifies new loci and functional pathways influencing Alzheimer's disease risk. Nat Genet 2019, 51: 404–413.

12. Sun BL, Li WW, Zhu C, Jin WS, Zeng F, Liu YH, *et al*. Clinical research on Alzheimer's disease: progress and perspectives. Neurosci Bull 2018, 34: 1111–1118.

13. Stocker H, Mollers T, Perna L, Brenner H. The genetic risk of Alzheimer's disease beyond APOE epsilon4: systematic review of Alzheimer's genetic risk scores. Transl Psychiatry 2018, 8: 166.

14. Karch CM, Goate AM. Alzheimer's disease risk genes and mechanisms of disease pathogenesis. Biol Psychiatry 2015, 77: 43–51.

15. Desikan RS, Fan CC, Wang Y, Schork AJ, Cabral HJ, Cupples LA, *et al*. Genetic assessment of age-associated Alzheimer disease risk: Development and validation of a polygenic hazard score. PLoS Med 2017, 14: e1002258.

16. Sleegers K, Bettens K, De Roeck A, Van Cauwenberghe C, Cuyvers E, Verheijen J, *et al*. A 22-single nucleotide polymorphism Alzheimer's disease risk score correlates with family history, onset age, and cerebrospinal fluid Abeta42. Alzheimers Dement 2015, 11: 1452–1460.

17. Jack CR, Jr., Bennett DA, Blennow K, Carrillo MC, Dunn B, Haeberlein SB, *et al*. NIA-AA Research Framework: Toward a biological definition of Alzheimer's disease. Alzheimers Dement 2018, 14: 535–562.

18. Li WW, Shen YY, Tian DY, Bu XL, Zeng F, Liu YH, *et al*. Brain amyloid-beta deposition and blood biomarkers in patients with clinically diagnosed Alzheimer's disease. J Alzheimers Dis 2019, 69: 169–178.

19. Bu XL, Yao XQ, Jiao SS, Zeng F, Liu YH, Xiang Y, *et al*. A study on the association between infectious burden and Alzheimer's disease. Eur J Neurol 2015, 22: 1519–1525.

20. McKhann G, Drachman D, Folstein M, Katzman R, Price D, Stadlan EM. Clinical diagnosis of Alzheimer's disease: report of the NINCDS-ADRDA Work Group under the auspices of Department of Health and Human Services Task Force on Alzheimer's Disease. Neurology 1984, 34: 939–944.

21. Folstein MF, Folstein SE, McHugh PR. "Mini-mental state". A practical method for grading the cognitive state of patients for the clinician. J Psychiatr Res 1975, 12: 189–198.

22. Nasreddine ZS, Phillips NA, Bedirian V, Charbonneau S, Whitehead V, Collin I, *et al*. The Montreal Cognitive Assessment, MoCA: a brief screening tool for mild cognitive impairment. J Am Geriatr Soc 2005, 53: 695–699.

23. Cuyvers E, Sleegers K. Genetic variations underlying Alzheimer's disease: evidence from genome-wide association studies and beyond. Lancet Neurol 2016, 15: 857–868.

24. Lambert JC, Ibrahim-Verbaas CA, Harold D, Naj AC, Sims R, Bellenguez C, *et al*. Meta-analysis of 74,046 individuals identifies 11 new susceptibility loci for Alzheimer's disease. Nature Genetics 2013, 45: 1452–1458.

25. Zhang S, Li X, Ma G, Jiang Y, Liao M, Feng R, *et al*. *CLU* rs9331888 polymorphism contributes to Alzheimer's disease susceptibility in Caucasian but not East Asian populations. Mol Neurobiol 2016, 53: 1446–1451.

26. Yu JT, Li L, Zhu QX, Zhang Q, Zhang W, Wu ZC, *et al*. Implication of CLU gene polymorphisms in Chinese patients with Alzheimer's disease. Clin Chim Acta 2010, 411: 1516–1519.

27. Xiao Q, Liu ZJ, Tao S, Sun YM, Jiang D, Li HL, *et al*. Risk prediction for sporadic Alzheimer's disease using genetic risk score in the Han Chinese population. Oncotarget 2015, 6: 36955–36964.

28. Liu Y, Yu JT, Wang HF, Hao XK, Yang YF, Jiang T, *et al*. Association between NME8 locus polymorphism and cognitive decline, cerebrospinal fluid and neuroimaging biomarkers in Alzheimer's disease. PLoS One 2014, 9: e114777.

29. Lu H, Zhu XC, Wang HF, Cao L, Tan MS, Tan CC, *et al*. Lack of Association between SLC24A4 polymorphism and late-onset Alzheimer's disease in Han Chinese. Curr Neurovasc Res 2016, 13: 239–243.

30. Zeng F, Shen C, Liu YH, Li J, Zhu J, Wang YR, *et al*. Genetic association between APP, *ADAM10* gene polymorphism, and sporadic Alzheimer's disease in the Chinese population. Neurotox Res 2015, 27: 284–291.

31. Blennow K, Hampel H, Weiner M, Zetterberg H. Cerebrospinal fluid and plasma biomarkers in Alzheimer disease. Nat Rev Neurol 2010, 6: 131–144.

32. Mattsson N, Andreasson U, Persson S, Arai H, Batish SD, Bernardini S, *et al*. The Alzheimer's Association external quality

control program for cerebrospinal fluid biomarkers. Alzheimers Dement 2011, 7: 386–395 e386.

33. Yuan L, Song Z, Deng X, Yang Z, Yang Y, Guo Y, *et al.* Genetic analysis of *FBXO2, FBXO6, FBXO12*, and *FBXO41* variants in Han Chinese patients with sporadic Parkinson's disease. Neurosci Bull 2017, 33: 510–514.

34. Farrer LA, Cupples LA, Haines JL, Hyman B, Kukull WA, Mayeux R, *et al.* Effects of age, sex, and ethnicity on the association between apolipoprotein E genotype and Alzheimer disease. A meta-analysis. APOE and Alzheimer Disease Meta Analysis Consortium. JAMA 1997, 278: 1349–1356.

35. Yang Q, Chen K, Zhang H, Zhang W, Gong C, Zhang Q, *et al.* Correlations between single nucleotide polymorphisms, cognitive dysfunction, and postmortem brain pathology in Alzheimer's disease among Han Chinese. Neurosci Bull 2019, 35: 193–204.

36. Mormino EC, Papp KV, Rentz DM, Schultz AP, LaPoint M, Amariglio R, *et al.* Heterogeneity in suspected non-Alzheimer disease pathophysiology among clinically normal older individuals. JAMA Neurol 2016, 73: 1185–1191.

37. Scheltens P, Blennow K, Breteler MM, de Strooper B, Frisoni GB, Salloway S, *et al.* Alzheimer's disease. Lancet 2016, 388: 505–517.

www.neurosci.cn
www.springer.com/12264

ORIGINAL ARTICLE

Astrocytic GABA$_B$ Receptors in Mouse Hippocampus Control Responses to Behavioral Challenges through Astrocytic BDNF

Ji-Hong Liu[1] · Ze-Lin Li[1] · Yi-Si Liu[1] · Huai-De Chu[1] · Neng-Yuan Hu[1] ·
Ding-Yu Wu[1] · Lang Huang[1] · Shu-Ji Li[1] · Xiao-Wen Li[1] · Jian-Ming Yang[1] ·
Tian-Ming Gao[1]

Abstract Major depressive disorder (MDD) is a common mood disorder that affects almost 20% of the global population. In addition, much evidence has implicated altered function of the gamma-aminobutyric acid (GABAergic) system in the pathophysiology of depression. Recent research has indicated that GABA$_B$ receptors (GABA$_B$Rs) are an emerging therapeutic target in the treatment of stress-related disorders such as MDD. However, which cell types with GABA$_B$Rs are involved in this process is unknown. As hippocampal dysfunction is implicated in MDD, we knocked down GABA$_B$Rs in the hippocampus and found that knocking down these receptors in astrocytes, but not in GABAergic or pyramidal neurons, caused a decrease in immobility in the forced swimming test (FST) without affecting other anxiety- and depression-related behaviors. We also generated astrocyte-specific GABA$_B$R-knockout mice and found decreased immobility in the FST in these mice. Furthermore, the conditional knockout of GABA$_B$Rs in astrocytes selectively increased the levels of brain-derived neurotrophic factor protein in hippocampal astrocytes, which controlled the decrease in immobility in the FST. Taken together, our findings contribute to the current understanding of which cell types expressing GABA$_B$Rs modulate antidepressant activity in the FST, and they may provide new insights into the pathological mechanisms and potential targets for the treatment of depression.

Keywords Depression · Astrocyte · Gamma-aminobutyric acid receptor · Forced swimming test · Brain-derived neurotrophic factor

Introduction

Major depressive disorder (MDD) is a common chronic mental disorder that is estimated to be the most prevalent and costly brain disease and the leading cause of disability worldwide [1]. Current antidepressants used to treat MDD exert their therapeutic effects through the serotonin and/or norepinephrine systems [2]. However, not all depressed patients respond to these antidepressants and only ∼35%–40% of patients treated with antidepressants recover to premorbid levels of functioning [3]. Most seriously, some antidepressants do not work until 3−5 weeks after the initiation of treatment in the vast majority of patients [4]. Nevertheless, some newer types of antidepressant are better tolerated and are safer, in terms of potential overdose, than the older tricyclic compounds. However, these new antidepressants also have troublesome side-effects such as sleepiness, weight gain, and changes in sexual functioning [3]. Thus, finding better antidepressants or methods with better efficacy and fewer side-effects is extremely urgent.

Recently, growing evidence from pre-clinical and clinical data has implicated gamma aminobutyric acid (GABA) as an emerging therapeutic target in the pathophysiology and treatment of depression [5]. For example, some investigators found reduced GABA levels in the plasma and corticospinal

Ji-Hong Liu and Ze-Lin Li have contributed equally to this work.

✉ Tian-Ming Gao
tgao@smu.edu.cn

1   State Key Laboratory of Organ Failure Research, Key Laboratory of Mental Health of the Ministry of Education, Guangdong–Hong Kong–Macao Greater Bay Area Center for Brain Science and Brain-Inspired Intelligence, Guangdong Key Laboratory of Psychiatric Disorders, Collaborative Innovation Center for Brain Science, Department of Neurobiology, School of Basic Medical Sciences, Southern Medical University, Guangzhou 510515, China

706

Neurosci. Bull. July, 2020, 36(7):705–718

fluid from patients with MDD [6]. In addition, the administration of selective serotonin-reuptake inhibitors increases the GABA levels in corticospinal fluid [7]. Furthermore, treatment with the $GABA_A$ receptor ($GABA_AR$) agonist benzodiazepines alprazolam and adinazolam has antidepressant effects in depressed patients similar to widely-prescribed antidepressants [8, 9]. $GABA_BRs$ are G protein-coupled receptors and are heterodimers composed of two subunits, $GABA_{B(1)}$ and $GABA_{B(2)}$ [10]. Growing evidence suggests that $GABA_BRs$ are emerging therapeutic targets in the treatment of stress-related psychiatric disorders such as MDD. For example, pharmacological studies have demonstrated that $GABA_B$ agonists have anxiolytic effects, while $GABA_B$ antagonists have antidepressant-like effects [11–13]. Genetic inactivation of the $GABA_{B(1)}$ subunit induces anxiogenic and antidepressant-like phenotypes in different behavioral paradigms [10, 12, 14]. These results suggest that GABAergic systems and their receptors play a role in the treatment of depression [15].

$GABA_BRs$ are G protein-coupled receptors that are expressed by almost all cell types, such as neurons and glial cells in the central nervous system (CNS) [16, 17]. However, the investigations described above do not mention which cell-types with $GABA_BRs$ are involved in modulating MDD. The hippocampus is an important region implicated in the pathogenesis of MDD, as shown by convergent lines of research. In the clinic, MDD is considered a highly stress-sensitive illness [18], and the hippocampus is recognized as a highly stress-sensitive region [19]. Hippocampal volume is reduced before the clinical onset of illness in individuals at risk for MDD [20–22]. Furthermore, these stress-associated changes in the hippocampus can be ameliorated by antidepressant treatment [23]. From the pre-clinical data, we can predict the relationship between the molecular and cellular effects of chronic stress and antidepressant treatment on the hippocampus [24], which suggests that MDD might be associated with hippocampal dysfunction.

Therefore, the aim of this study was to evaluate which cell-types containing $GABA_BRs$ in the hippocampus are involved in modulating emotional responses. Moreover, since some investigations have indicated an intimate relationship between the levels of brain-derived neurotrophic factor (BDNF) and depression, we also explored whether BDNF is involved in this phenomenon.

Materials and Methods

Mice

The mice housed in standard laboratory cages at 24 ± 1°C were maintained on a 12-h light/dark cycle with lights on at 08:00 and provided standard food and water *ad libitum*. All procedures were conducted with the approval of the Southern Medical University Animal Ethics Committee [25], and efforts were made to minimize animal suffering and to reduce the number of animals used.

Aldh1l1-CreER^{T2} mice were generated at the Model Animal Research Center of Nanjing University (Nanjing, China). Briefly, Aldh1l1-CreER^{T2} knock-in mice were generated *via* a CRISPR/Cas9 system [26, 27] using Cas9 mRNA, single guide RNA (sgRNA; CCAGGTCTTGTCCCCAATACTGG), and a donor, which were co-injected into C57BL/6J zygotes by microinjection. Then, these zygotes were transplanted into pseudopregnant mice [28]. The sgRNA-directed Cas9 endonuclease cleavage occurred near the termination codon and created a double-strand break. This break was subsequently repaired and resulted in a T2A-CreER^{T2} insertion before the stop codon of the Aldh1l1 gene. The mice were screened using PCR analysis with specific primers and the following amplification program: one cycle of 5 min at 95 °C followed by 10 cycles (−1 °C/cycle) of 30 s at 95 °C, 30 s at 65 °C, and 2 min at 72 °C; 20 cycles of 30 s at 95 °C, 30 s at 55 °C, and 2 min at 72 °C; and 5 min at 72 °C. The reaction was then held at 4 °C and submitted to sequencing validation.

$GABA_{B(1)}$-loxp mice were a kind gift from Prof. B. Bettler (University of Basel, Switzerland) [29]. Aldh1l1-CreER^{T2} mice were crossed with $GABA_{B(1)}$-loxp mice to generate Aldh1l1-CreER^{T2}; $GABA_{B(1)}^{-/-}$ ($GABA_{B(1)}$-cKO) mice. $GABA_{B(1)}^{loxP/loxP}$ mice were used as controls.

Virus Generation and Stereotaxic Injections

The recombinant adeno-associated viral (AAV) vectors were generated by Shanghai Sunbio Medical Biotechnology (Shanghai, China) and were ligated into an AAV5 vector expressing EGFP with viral titers of 2×10^{12} particles/mL. The micropipette was brought to the correct x and y coordinates and lower to the desired z coordinate of the injection site. A 33-gauge needle fitted to a Hamilton syringe was lowered to the hippocampal CA1 region (AP, −2.0 mm; ML, ±1.6 mm; DV, −1.5 mm), and 0.25 µL (0.1 µL/min) of the virus was delivered over 3 min. The needle was withdrawn 10 min after the end of injection. Mice were used 3 weeks after AAV injection.

Immunofluorescence

Tissue slices were washed in PBS and then incubated while shaking for 2 h in PBS containing 5% BSA and 1% Triton X-100 at room temperature. They were then washed three times for 5 min each in PBS, incubated in primary antibodies overnight at 4 °C, washed three times for 5 min

each in PBS, incubated in secondary antibodies for 2 h at room temperature, and finally washed three times for 5 min each in PBS. They were then sealed in place for imaging, which was performed using a laser confocal microscope (Nikon C2, Japan). We used the following primary antibodies: rabbit anti-GABA$_{B(1)}$R (1:1500; ab55051, Abcam, Cambridge, MA), mouse anti-GFAP (1:500; 3670S, Cell Signaling Technology, Beverly, MA), mouse anti-NeuN (1:500; 24307, Cell Signaling Technology), and mouse anti-GAD67 (1:500; MAB5406, Millipore, Billerica, MA)]; and the following secondary antibodies: goat anti-mouse IgG with Alexa Fluor 594 or 488 (1:2000; #A11005 or #A11001, Life Technologies). Fluoroshield mounting medium (ab104139; Abcam) was used to seal the tissues in place.

Cell Counting

Five to eight slices containing each brain area were obtained from each mouse, and three or five mice were used in each experiment. The image allocations were blinded for analysis. The cells were counted to determine how many were single-positive for NeuN, GAD-67, GFAP, and tdTomato or double-positive for tdTomato. The "Cell Counter" plug-in in ImageJ 1.50i software (NIH) was used for cell counting. The presence of DAPI labeling was required to identify each cell. The specificity of the virus injected into Cre mice was defined as merger cells/the total number of GFP+ cells. The specificity of Cre recombinase expression in the transgenic mouse line was defined as the merger cells/the total number of tdTomato+ cells. The number of merger cells/the total number of marker+ cells was used to define the mean efficiency of Cre recombinase expression.

Western Blots

Western blots were performed as previously described [30]. The tissue from Cre mice injected with virus included only the GFP-infected areas in CA1, while tissue from GABA$_B$R-cKO mice included the whole hippocampus. Then, the tissue was lysed in ice-cold lysis buffer (11836170001, Roche, Switzerland) containing 1 mmol/L of the protease inhibitor PMSF. Samples were then centrifuged for 30 min at 16,000 g at 4 °C, and the supernatant was collected for quantification using the Microplate BCA Protein Assay Kit (#23227, Thermo, MA). The proteins were separated by SDS-PAGE (10% for IP3R2 or 12% for P2X2 polyacrylamide gels) and transferred to a PVDF membrane (Millipore). The membrane was blocked with 5% defatted milk powder at room temperature for 1 h and then incubated overnight with the primary antibody [rabbit polyclonal anti-GABA$_{B(1)}$R (1:1500; ab55051, Abcam, Cambridge, MA) and rabbit polyclonal anti-BDNF (1:1000; ab108319, Abcam, Cambridge, MA)] at 4 °C. Antibody binding was detected with an HRP-conjugated secondary antibody [monoclonal mouse anti-β-actin (1:1000; Bostor, China) and monoclonal mouse anti-GAPDH (1:1,000; 3683S, Cell Signaling)] at room temperature for 1 h. The protein expression levels were evaluated by quantifying the gray density of the western blot bands with FluorChem SP software (ProteinSimple, USA). All samples were normalized to internal controls.

Open Field Test

The open field apparatus was a rectangular chamber (40 × 40 × 30 cm^3) made of gray polyvinyl chloride. As previously described [25], each mouse was gently placed in the center of the chamber and left for 5 min to record free movement, which was monitored by an automated video tracking system. The digitized image of the path was mapped and analyzed using EthoVision 11.0 software (EthoVision, Noldus, USA).

Elevated Plus Maze (EPM) Test

The EPM consisted of four arms (30 × 5 cm^2): two open arms without walls and two closed arms with 15.25-cm-high walls. Each mouse was placed in the center of the elevated plus maze, facing an open arm. In the 5-min test, the time spent in each arm was recorded using EthoVision 11.0. The maze was cleaned between sessions with 20% ethanol.

Light-Dark Box Test

This test was performed as previously described [31]. The box apparatus contained two similar opaque compartments connected by a central opening (18 × 10 × 13 cm^3; light compartment illuminated by a 60 W desk lamp). Each mouse was placed in the center of the dark compartment, facing the opening. Then, the mouse was tracked for 5 min after first crossing the opening threshold. The total number of entries into the dark side and time spent in the dark compartment were recorded.

Social Interaction Test

This behavioral test was performed in a dark room as previously described [25]. A mouse was placed in the center of the testing chamber, and baseline movement was tracked for 2.5 min, followed by another 2.5 min in the presence of a caged male aggressor mouse. The times that the mice spent in the interaction zone and the corner zone

were recorded using Ethovision XT software (EthoVision, Noldus, USA). The chamber was cleaned between sessions with 20% ethanol.

Sucrose Preference Test

Mice were singly housed 3 days before the test, and then we replaced the normal water bottles with two 50-mL bottles (A and B), the positions of which were switched daily to avoid a side bias. The mice were habituated with water for the first 2 days (w/w) followed by a 1% sucrose solution for the next 2 days. Then, sucrose preference tests were performed on days 5–8, with bottle A containing 1% sucrose and bottle B containing water. We measured the volume of fluid consumed from each bottle daily. The sucrose preference was calculated as $v_A / (v_A + v_B)$ [32].

Forced Swimming Test (FST)

The FST apparatus was a clear glass cylinder (height 45 cm, diameter 19 cm) filled with water (22 °C–25 °C) to 23 cm. In the 6-min test, the duration of immobility was measured during the final 4 min using Ethovision XT software.

Contextual Fear Conditioning Test

The contextual fear conditioning test was conducted as reported previously [25]. Each mouse was first habituated to the room, and then allowed to freely explore the apparatus for 3 min (EthoVision, Noldus, USA). During training, each mouse was placed in conditioning chamber A, and exposed to tone-foot-shock pairings (tone, 30 s, 80 dB; foot shock, 1 s, 0.4 mA) at an interval of 80 s. Twenty-four hours after training, each mouse was returned to chamber A to evaluate contextual fear learning. Freezing during training and testing was scored using Med Associates Video-Tracking and Scoring software.

ELISA

The mice were anesthetized with pentobarbital and then decapitated; the brain was quickly removed and the medial prefrontal cortex (mPFC), nucleus accumbens (NAc), habenula (Hb), hippocampus, and ventral tegmental area (VTA) were dissected. BDNF levels were assessed with the Emax ImmunoAssay System ELISA kit (BDNF-ELISA E-max, Promega, USA) following the manufacturer's instructions.

Cell Cultures

We isolated primary astrocytes from the hippocampus of mice on postnatal day 1 and used a modified established protocol [33]. We isolated primary hippocampal neurons using a protocol that is routinely performed in our laboratory [32, 34].

Statistical Analyses

In the experimental data, t-tests were used to compare the means of two independent samples, and one-way ANOVA was used to compare the means of multiple groups of samples using SPSS 22.0 software (SPSS, Chicago, IL). The mean values shown in the text and figures are expressed as the mean ± standard error of the mean (SEM), unless otherwise stated. $P < 0.05$ was considered statistically significant, and GraphPad Prism 6.0 (La Jolla, CA) was used to draw the graphs.

Results

Conditional Knock-Down of Neuronal GABA$_B$Rs in the Hippocampal CA1 Region Has No Effect on Emotional Responses

GABA$_B$Rs have been reported to be expressed in neurons, such as pyramidal and GABAergic neurons [10]. To investigate whether neuronal GABA$_B$Rs have an effect on emotional responses, we used adeno-associated virus (AAV)–DIO-GABA$_B$ short-hairpin RNAs (shRNAs) and first injected the AAV–GABA$_B$ shRNA virus into the CA1 region in CamKII-Cre mice to knock down the receptor in pyramidal neurons (Fig. 1A), then we did the behavioral tests (Fig. 1B). Immunofluorescence results showed that the virus was correctly injected into CA1 and that most of the pyramidal neurons were infected (Fig. 1C, D). Western blot results verified that the receptor was knocked down ($t_{(8)} = 6.998$, $P = 0.003$; Fig. 1E, F).

We first investigated anxiety-related behaviors. In the open field test, there was no significant difference between groups in locomotor activity ($t_{(16)} = -1.360$, $P = 0.732$; Fig. 1G) or exploration time in the center ($t_{(17)} = 0.342$, $P = 0.284$; Fig. 1H). Mice with GABA$_B$Rs knocked out in pyramidal neurons spent an amount of time similar to normal mice in the open arms ($t_{(17)} = 2.235$, $P = 0.764$; Fig. 1I) and closed arms ($t_{(17)} = 1.678$, $P = 0.665$; Fig. 1J) in the EPM. In the light/dark test, the number of entries into the light compartment ($t_{(17)} = 4.679$, $P = 0.154$; Fig. 1K) and time spent in the light compartment ($t_{(17)} = 3.626$, $P = 0.202$; Fig. 1L) were similar in mice injected with control or GABA$_B$Rs shRNA. Similar results were obtained in the
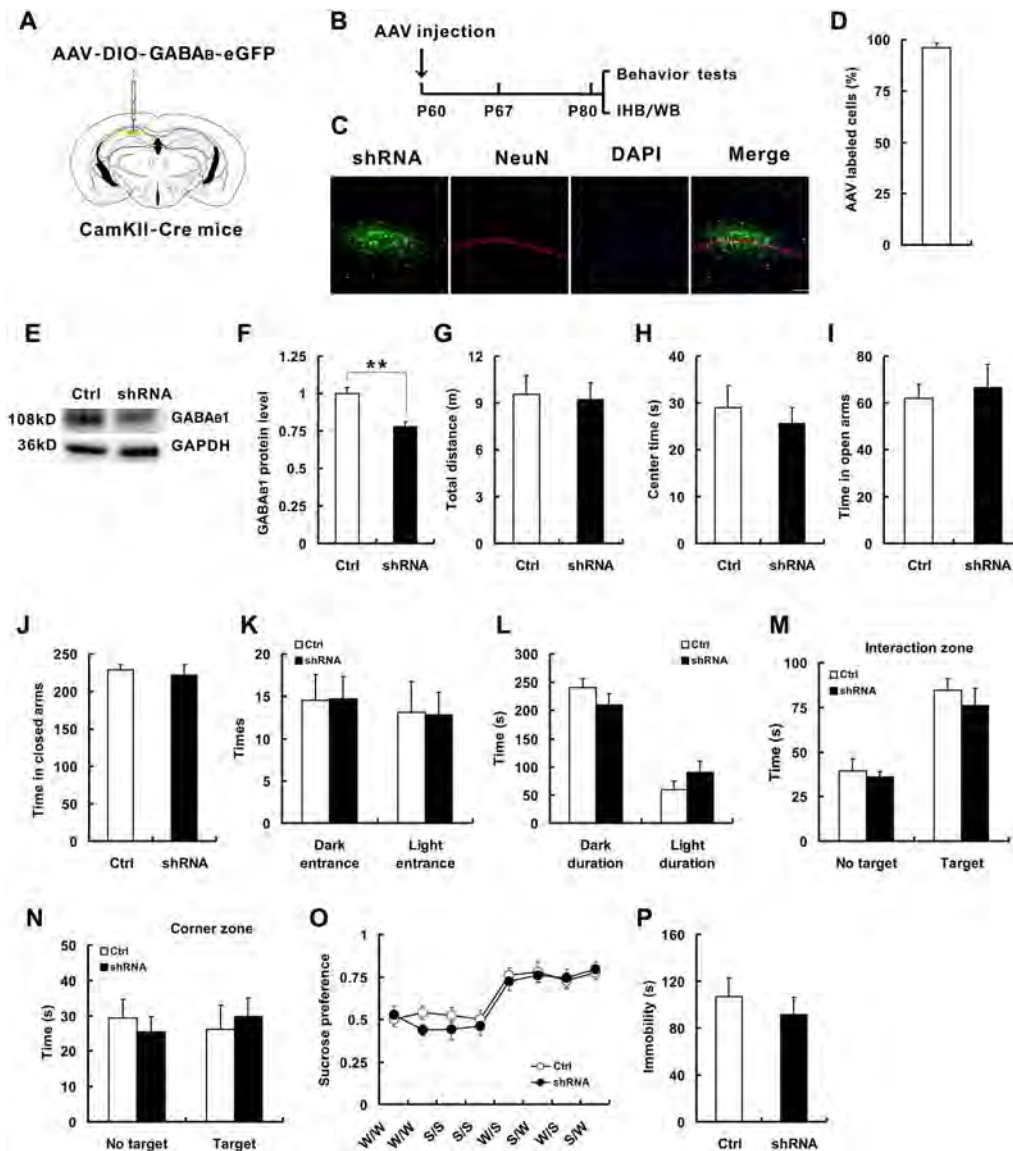
Fig. 1 Hippocampal GABA$_B$Rs in pyramidal neurons are not necessary for response to behavioral challenge. **A** Schematic of the delivery of AAV-DIO- GABA$_B$-eGFP into the CA1 region of CamKII-Cre mice. **B** Schematic of the experiments. **C** Representative fluorescence images showing that most of the cells infected with AAV-DIO-GABA$_B$-eGFP (shRNA) vectors were pyramidal neurons in CA1 of CamKII-Cre mice (scale bar, 100 μm). **D** Average percentage of cells infected with AAV-DIO-GABA$_B$-eGFP (shRNA) vectors that were positive among pyramidal neurons. **E** Representative blots showing that GABA$_{B1}$ levels were decreased in the hippocampus of CamKII-Cre mice injected with GABA$_B$ shRNA. **F** Quantitative analysis of data as in **E** (*n* = 4 pairs of mice, two-tailed Student's *t*-test; GABA$_{B1}$ band density was normalized to the loading control GAPDH; values from control mice were taken as 100%). **G, H** Mice with GABA$_B$R-knockdown in pyramidal neurons in CA1 travelled the same total distance (**G**) and spent the same time in the central arena (**H**) in the open field test (Ctrl: *n* = 9 mice; shRNA: *n* = 10; two-tailed

Student's *t*-test). **I, J** In the elevated plus maze test, CamKII-Cre mice injected with GABA$_B$ shRNA spent the same amount of time in the open (**I**) and closed (**J**) arms (Ctrl: *n* = 9; shRNA: *n* = 10; two-tailed Student's *t*-test). **K, L** There was no difference in the number of entries (**K**) or time spent (**L**) in the light/dark sides of the light/dark box test (Ctrl: *n* = 9; shRNA: *n* = 10; two-tailed Student's *t*-test). **M, N** There was no difference between the two groups in the time spent in the interaction zone and corner zone in the presence/absence of a target mouse (Ctrl: *n* = 9; shRNA: *n* = 10; two-tailed Student's *t*-test). **O** Knockdown of GABA$_B$Rs in pyramidal neurons in CA1 did not change the preferences in the sucrose preference test (Ctrl: *n* = 9; shRNA: *n* = 10; repeated measures two-way ANOVA). **P** Immobility time was not changed in the FST after knockdown of GABA$_B$Rs in pyramidal neurons in CA1 (Ctrl: *n* = 9; shRNA: *n* = 10; two-tailed Student's *t*-test). Data are presented as the mean ± SEM; *P < 0.05 *vs* controls.

time spent interacting with other mice in the social interaction test in knocked-down mice compared to control mice ($t_{(17)}$ = −2.646, *P* = 0.423; Fig. 1M, N). These results

indicate that knocking out GABA$_B$Rs in pyramidal neurons has no effect on anxiety-like behaviors. We next investigated depressive-like behaviors. The sucrose preference

test was used to assess anhedonia, a core symptom of depression [35]. No differences were found between the two groups in consuming sucrose solution ($F_{(1,136)}$ = 10.138; P = 0.461; Fig. 1O). The FST is widely considered to test depression-related responses in rodents [36]. We found that the total duration of immobility in the FST was also not affected after knocking out $GABA_BRs$ in pyramidal neurons ($t_{(17)}$ = 2.021, P = 0.46; Fig. 1P), suggesting no effect of pyramidal neuronal $GABA_BRs$ on depressive-like behaviors.

We then injected the virus into the CA1 region in the GAD-Cre mice to knock down the receptors in GABAergic neurons (Fig. 2A) and tested the behaviors (Fig. 2B). Immunofluorescence (Fig. 2C, D) and western blot results ($t_{(8)}$ = 3.087, P = 0.037; Fig. 2E, F) verified the effectiveness of the $GABA_BR$ shRNA virus in GAD-Cre mice. We found that knocking out $GABA_BRs$ in GABAergic neurons in CA1 did not affect the behaviors (Fig. 2G–N), confirming the lack of an effect of GABAergic neuronal $GABA_BRs$ on emotion-related behaviors.

Conditional Knockdown of Astrocytic $GABA_BRs$ in the CA1 Region Decreases Immobility in the FST

To investigate whether astrocytic $GABA_BRs$ in the hippocampus are critical in modulating emotional responses, we used aldehyde dehydrogenase 1 family member L1 (aldh1l1)::CreER^{T2} mice. First, to assess the specificity of the expression in astrocytes of aldh1l1::CreER^{T2} mice, we crossed this line with Ai14 reporter mice to create the double transgenic mouse line aldh1l1::CreER^{T2}:Ai14. Then, these mice were treated with 75 mg/kg tamoxifen for seven days at P60–66, and CreER^{T2}-mediated recombination was assessed in the hippocampus two weeks after the last dose of tamoxifen (Fig. 3A). We found a high level of specificity in CA1 in the aldh1l1::CreER^{T2}:Ai14 mice (GFAP co-expression: 97.18% ± 0.58%; Fig. 3B–D). This inducible system allowed us to delete $GABA_BRs$ specifically in the astrocytes of adult animals. We then injected the virus into the CA1 region in aldh1l1-CreER^{T2} mice to knock down astrocytic $GABA_BRs$ in the hippocampus induced by one week of intraperitoneal injection of tamoxifen (75 mg/kg; Fig. 4A) and then we investigated the emotional responses in the behavioral tests (Fig. 4B). The viral expression indicated by green fluorescence demonstrated that the virus was correctly injected into CA1, and most of the astrocytes were infected (Fig. 4C, D). In addition, the results of western blots verified that the receptor was knocked down ($t_{(8)}$ = 6.880, P = 0.028; Fig. 4E, F). We then tested these mice for anxiety- and depression-related behavior. We found that knocking out the astrocytic $GABA_BRs$ in CA1 did not affect behavior in the open field test (Fig. 4G, H), EPM (Fig. 4I, J), light/dark

box (Fig. 4K, L), social interaction test (Fig. 4M, N), or sucrose preference test (Fig. 4O). However, in the FST, aldh1l1-CreER^{T2} mice that had the shRNA virus injected into CA1 exhibited decreased immobility, which is considered a state of passive coping or behavioral despair and represents an active escape behavior [37, 38], compared with that in mice injected with control virus ($t_{(15)}$ = 7.781, P = 0.012; Fig. 4P). These results confirmed a positive role of astrocytic $GABA_BR$ deletion in response to behavioral challenge.

Conditional Knockout of $GABA_BRs$ in Astrocytes Leads to Decreased Immobility Time in the FST

To further determine whether astrocytic $GABA_BRs$ have an effect on emotional responses, we generated conditional $GABA_{B(1)}R$ mutant mice by crossing $GABA_B^{loxP/loxP}$ mice with aldh1l1::CreER^{T2} mice (Figs. 3 and 5A), in which Cre expression was under the control of the human aldh1l1 promoter. After one week of daily intra-peritoneal injection of tamoxifen (75 mg/kg), we used the behavioral tests to evaluate the emotional responses of mice (Fig. 5B). Western blot analysis revealed that $GABA_BRs$ were decreased in the hippocampus in aldh1l1-$GABA_BR^{-/-}$ mice (cKO), compared with the levels in the control wild-type (WT) mice ($t_{(6)}$ = 7.740, P = 0.017; Fig. 5C, D). In evaluating the emotion-related behaviors, we found that knocking out $GABA_BRs$ in astrocytes had no effect (Fig. 5E–M), except for a decrease in the total duration of immobility in the FST ($t_{(16)}$ = 8.311, P = 0.002; Fig. 5N). To explore whether the decreased immobility in the FST is a result of the impairment of learning and memory caused by knocking out $GABA_BRs$ in astrocytes, we next assessed contextual fear conditioning in cKO and WT mice and found that this did not affect the learning and memory process (Fig. 5O, P). These results further indicate that mice with astrocytic $GABA_BR$ deletion exhibit an active behavioral response to challenge.

Conditional Knockout of Astrocytic $GABA_BRs$ Increases Astrocytic BDNF Levels in the Hippocampus

Neurotrophic factors, such as BDNF, are critical regulators of mood disorders [39], and some investigations have highlighted the relationship between BDNF and depression, as well as its role in the antidepressant treatment [40–42]. For example, reduced brain BDNF levels have been found in postmortem samples from depressed patients [43], whereas BDNF infusion into the brain can induce antidepressant-like behaviors [44, 45]. In addition, mice exposed to stress exhibit decreased levels of BDNF that are associated with depression [46, 47], while antidepressant
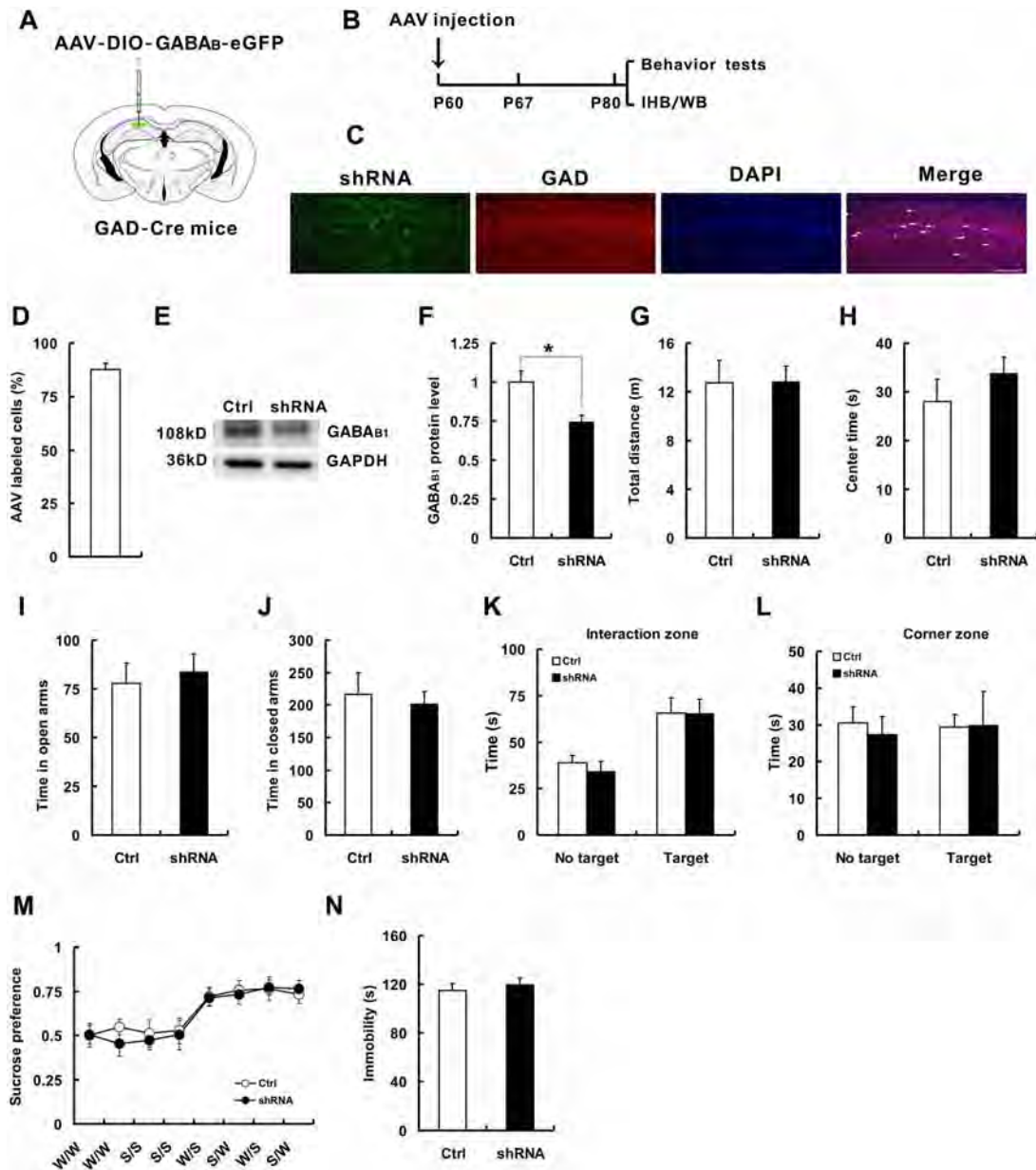
Fig. 2 Hippocampal GABA$_B$Rs in GABAergic neurons are not critical for responses to behavioral challenge. **A** Schematic of the delivery of AAV-DIO-GABA$_B$-eGFP into CA1 in GAD-Cre mice. **B** Schematic of the experiments. **C** Representative fluorescence images showing that most of the cells infected with AAV-DIO-GABA$_B$-eGFP (shRNA) vectors were GABAergic neurons in CA1 of GAD-Cre mice (scale bar, 100 μm). **D** Average percentage of cells infected with AAV-DIO-GABA$_B$-eGFP (shRNA) vectors that were GABAergic neurons. **E** Representative blots showing GABA$_{B1}$ was decreased in the hippocampus of GAD-Cre mice injected with GABA$_B$ shRNA. **F** Quantitative analysis of data as in **E** ($n = 4$ pairs of mice, two-tailed Student's t-test). GABA$_{B1}$ band density was normalized to the loading control GAPDH; values from control mice were taken as 100%. **G, H** Mice with GABA$_B$Rs knocked down in GABAergic neurons in CA1 travelled the same total distance (**G**) and spent the same amount of time in the central arena (**H**) in the open field test (Ctrl: $n = 10$ mice; shRNA: $n = 11$; two-tailed Student's t-test). **I, J** In the EPM test, GAD-Cre mice injected with GABA$_B$ shRNA spent the same amount of time in the open (**I**) and closed (**J**) arms (Ctrl: $n = 10$; shRNA: $n = 11$; two-tailed Student's t-test). **K, L** No difference was found between the two groups in the time spent in the interaction zone or corner zone in the presence/absence of a target mouse (Ctrl: $n = 10$; shRNA: $n = 11$; two-tailed Student's t-test). **M** Knocking down GABA$_B$Rs in GABAergic neurons in CA1 did not change preferences in the sucrose preference test (Ctrl: $n = 10$; shRNA: $n = 11$; repeated measures two-way ANOVA). **N** In the FST, immobility time was similar in the two groups (Ctrl: $n = 10$ mice; shRNA: $n = 11$ mice; two-tailed Student's t-test). Data are presented as the mean ± SEM; *$P < 0.05$ *vs* controls.
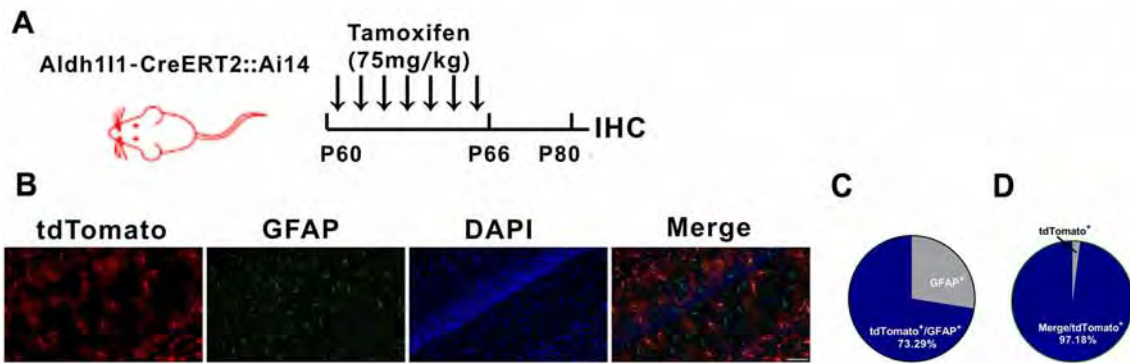
Fig. 3 Characterization of the Aldh1l1-CreER^{T2} transgenic line. **A** Schematic of the experiments. **B** Representative high-magnification images of CA1 astrocytes in Aldh1l1-CreER^{T2} transgenic mice showing co-staining with GFAP (scale bar, 50 μm). **C** Pie-chart showing the specificity (percentage of tdTomato-positive cells that express GFAP) of Cre-mediated recombination in CA1 of Aldh1l1-CreER^{T2}

transgenic mice with tamoxifen (75 mg/kg; $n = 7$ slices from 4 mice). **D** Pie-chart showing the efficiency (percentage of GFAP-positive cells that express tdTomato) of Cre-mediated recombination in CA1 of Aldh1l1-CreER^{T2} transgenic mice ($n = 7$ slices from 4 mice). Data show the mean ± SEM.

treatment can block the effects of stress through BDNF [48, 49]. These studies collectively indicate the significant role of BDNF in depression.

To test whether the decreased immobility in the FST with astrocytic GABA$_B$R deletion is due to changes in BDNF, we measured the BDNF protein levels in depression-related brain regions (the mPFC, NAc, Hb, hippocampus, and VTA) in WT and GABA$_B$R-cKO mice and found significantly higher levels in the hippocampus of GABA$_B$-R-cKO mice (80.26 ± 2.43 pg/mL) than in WT mice (57.97 ± 2.49 pg/mL) ($t_{(4)} = 5.141$, $P = 0.004$; Fig. 6A). No significant difference was detected in the BDNF protein levels between the two groups in the mPFC (WT, 39.29 ± 0.87 pg/mL *versus* cKO, 35.22 ± 3.03 pg/mL, $t_{(4)} = 0.148$, $P = 0.384$); NAc (WT, 24.24 ± 4.95 pg/mL *vs* cKO, 28.74 ± 4.03 pg/mL, $t_{(4)} = 2.987$, $P = 0.844$); Hb (WT, 19.40 ± 3.77 pg/mL *vs* cKO, 22.90 ± 0.54 pg/mL, $t_{(4)} = 1.241$, $P = 0.644$); and VTA (WT, 49.18 ± 3.86 pg/mL *vs* cKO, 49.90 ± 8.89 pg/mL, $t_{(4)} = 2.151$, $P = 0.594$). Furthermore, western blot analysis confirmed an increase in BDNF protein level in the hippocampus of cKO mice ($t_{(6)} = 7.081$, $P = 0.044$; Fig. 6B, C). Moreover, BDNF concentrations were markedly increased in the culture medium of astrocytes isolated from the hippocampus of cKO mice ($t_{(10)} = 8.054$, $P = 0.007$; Fig. 6D). However, neuronal BDNF release was undisturbed by the lack of astrocytic GABA$_B$Rs ($t_{(10)} = 3.646$, $P = 0.361$; Fig. 6D), indicating that BDNF release specifically from astrocytes is increased in cKO mice. These results suggest that the conditional knockout of GABA$_B$Rs in astrocytes selectively increases the level of BDNF from astrocytes in the hippocampus, and that this increase may contribute to the active behavioral response to challenge.

Decreasing BDNF Levels Restore Changes in GABA$_B$R-cKO Mice

To further test the involvement of astrocytic BDNF in modulating the response to behavioral challenge, we injected AAV-DIO-BDNF shRNAs into the CA1 region of GABA$_B$R-cKO mice to knock down astrocytic BDNF (Fig. 7A), then we carried out the behavioral tests (Fig. 7B). Immunofluorescence results indicated that the virus was correctly injected into CA1 and that most of the astrocytes were infected with the virus (Fig. 7C, D). Western blot results ($t_{(6)} = 5.576$, $P = 0.041$; Fig. 7E, F) and ELISA ($t_{(4)} = 5.386$, $P = 0.011$; Fig. 7G) showed that the BDNF levels were almost restored to normal in the hippocampus of knockdown animals compared with those in control mice. In the behavioral tests, we found that decreased BDNF levels rescued the abnormal performance in the FST, while GABA$_B$R-cKO mice injected with control shRNA still showed decreased immobility ($t_{(17)} = 6.416$, $P = 0.023$; Fig. 7Q). However, the injection of shRNA had no effect on the performance in the open field test (Fig. 7H, I), EPM (Fig. 7J, K), light/dark box test (Fig. 7L, M), social interaction test (Fig. 7N, O), or sucrose preference test (Fig. 7P). These data suggested that enhanced astrocytic BDNF contributes to controlling the response to behavioral challenge caused by deleting astrocytic GABA$_B$Rs.

Discussion

The major findings of this study are as follows. First, knocking down GABA$_B$Rs in astrocytes in the hippocampus, but not in GABAergic or pyramidal neurons, caused a decrease in immobility time in the FST. Second,
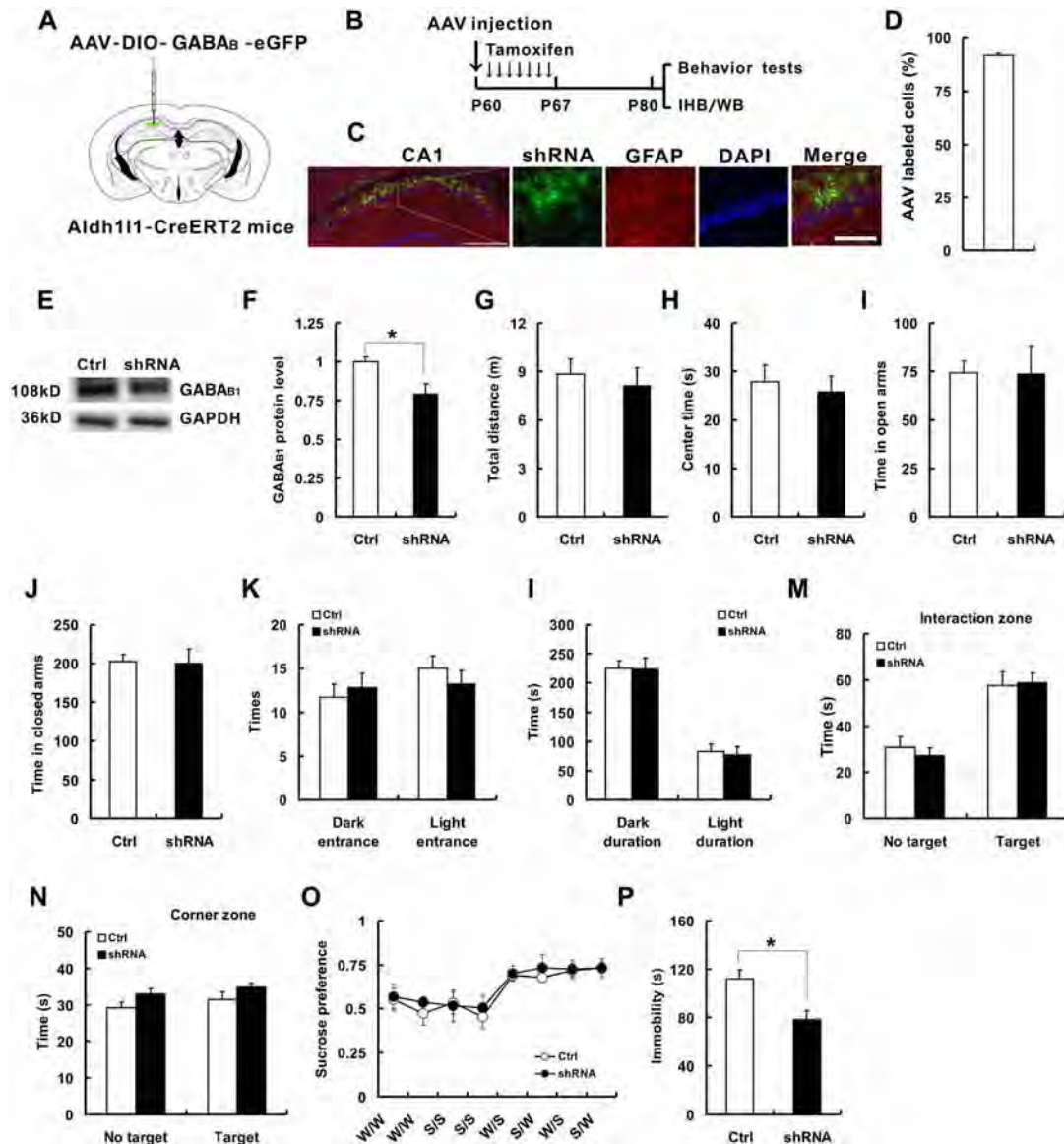
Fig. 4 Conditional knockdown of astrocytic GABA$_B$Rs in the CA1 region decreases immobility in the FST. **A** Schematic of the delivery of AAV-DIO-GABA$_B$-eGFP into CA1 in Aldh1l1-CreER^{T2} mice. **B** Schematic of the experiments. **C** Representative location of the GABA$_B$ shRNA virus (green) injected into the CA1 region (left; scale bar, 500 μm), and representative fluorescence images showing that most of the cells infected with AAV-DIO-GABA$_B$-eGFP (shRNA) vectors were astrocytes in CA1 of aldh1l1-CreER^{T2} mice (right; scale bar, 125 μm). **D** Average percentage of cells infected with AAV-DIO-GABA$_B$-eGFP (shRNA) vectors that were positive for astrocytes. **E** Representative blots showing that GABA$_{B1}$ was decreased in the hippocampus of aldh1l1-CreER^{T2} mice injected with GABA$_B$ shRNA. **F** Quantitative analysis of data as in **E** ($n = 4$ pairs of mice, two-tailed Student's *t*-test). GABA$_{B1}$ band density was normalized to the loading control GAPDH; values from control mice are taken as 100%. **G, H** Mice with knockdown of astrocytic GABA$_B$Rs in the CA1 region travelled the same total distance (**G**) and spent the same amount of time in the central arena (**H**) in the open field test (Ctrl: $n = 8$ mice; shRNA: $n = 9$; two-tailed Student's *t*-test). **I, J** In the EPM test, Aldh1l1-CreER^{T2} mice injected with GABA$_B$ shRNA spent the same time in the open (**I**) and closed (**J**) arms (Ctrl: $n = 8$; shRNA: $n = 9$; two-tailed Student's *t*-test). **K, L** There was no difference between the two groups in the time spent in the interaction zone or corner zone in the presence/absence of a target mouse (Ctrl: $n = 8$; shRNA: $n = 9$; two-tailed Student's *t*-test). **M, N** There was no difference in the number of entries (**M**) or time spent (**N**) in the light/dark side in the light/dark box test (Ctrl: $n = 8$; shRNA: $n = 9$; two-tailed Student's *t*-test). **O** Knocking down the GABA$_B$Rs in CA1 did not change preferences in the sucrose preference test (Ctrl: $n = 8$; shRNA: $n = 9$; repeated measures two-way ANOVA). **P** In the FST, Aldh1l1-CreER^{T2} mice injected with GABA$_B$ shRNA exhibited decreased immobility compared with that of wild-type mice (Ctrl: $n = 8$; shRNA: $n = 9$; two-tailed Student's *t*-test). Data are presented as the mean ± SEM; *$P < 0.05$ *vs* controls.
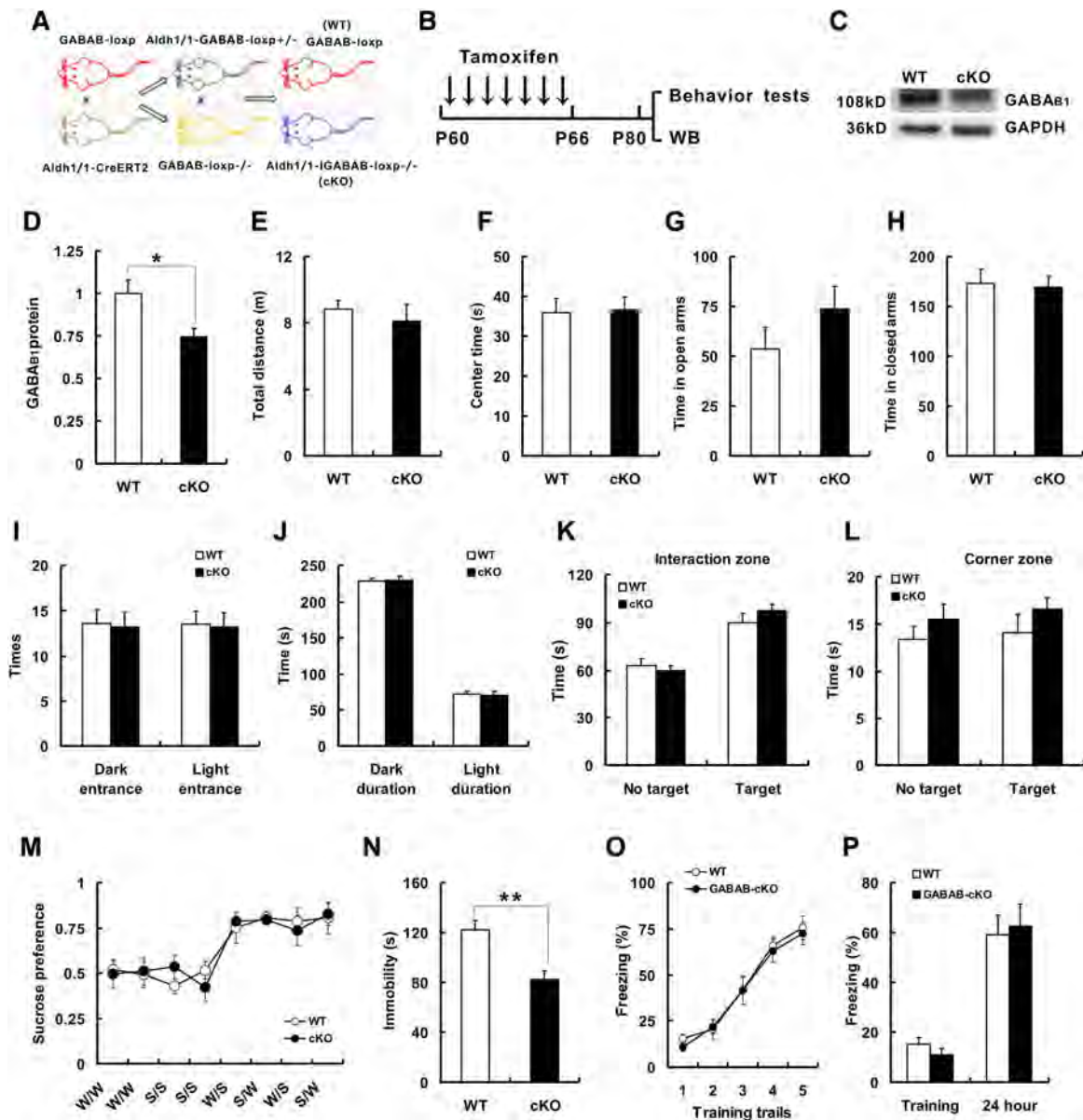
Fig. 5 Conditional knockout of GABA$_B$Rs in astrocytes leads to decreased immobility in the FST. **A** GABA$_B^{loxP/loxP}$ mice were crossed with aldh1l1::CreER^{T2} mice; the resulting aldh1l1::CreER^{T2}; GABA$_B^{loxP/loxP/+}$ mice were crossed with GABA$_B^{loxP/loxP/+}$ mice to generate aldh1l1::CreER^{T2}; GABA$_B^{loxP/loxP}$ (cKO) and GABA$_B^{loxP/loxP}$ (WT) mice. **B** Schematic of the experiments on cKO and WT mice. **C** Representative blots showing that GABA$_{B1}$ levels were decreased in the hippocampus of cKO mice. **D** Quantitative analysis of data as in (**C**) ($n = 4$ mice/group, two-tailed Student's t-test). GABA$_{B1}$ band density was normalized to the loading control GAPDH. **E, F** Mice with knocked out astrocytic GABA$_B$Rs travelled the same total distance (**E**) and spent the same amount of time in the central arena (**F**) in the open field test (WT: $n = 8$ mice; cKO: $n = 10$; two-tailed Student's t-test). **G, H** In the EPM test, cKO mice spent the same time in the open (**G**) and closed (**H**) arms

(WT: $n = 8$; cKO: $n = 10$; two-tailed Student's t-test). **I, J** There was no difference in the number of entries (**I**) or time spent (**J**) in the light/dark side in the light/dark box test (WT: $n = 8$; cKO: $n = 10$; two-tailed Student's t-test). **K, L** There is no difference between cKO and WT mice in the time spent in the interaction zone or corner zone in the presence/absence of a target mouse (WT: $n = 8$; cKO: $n = 10$; two-tailed Student's t-test). **M** cKO mice did not exhibit preferences in the sucrose preference test (WT: $n = 8$; cKO: $n = 10$; repeated measures two-way ANOVA). **N** In the FST, cKO mice exhibited decreased immobility compared with WT mice (WT: $n = 8$; cKO: $n = 10$; two-tailed Student's t-test). **O, P** Conditional knockout of GABA$_B$Rs in astrocytes does not affect learning and memory (WT: $n = 10$; cKO: $n = 12$; repeated two-way ANOVA in **O**; two-tailed Student's t-test in **P**). Data are presented as the mean ± SEM; *$P < 0.05$; **$P < 0.01$ vs controls.

conditional knockout of GABA$_B$Rs in astrocytes led to decreased immobility time in the FST. Third, the conditional knockout of GABA$_B$Rs in astrocytes selectively

increased hippocampal astrocytic BDNF protein levels, which controlled the decrease in immobility time in the FST. Together, our results suggest that astrocytic
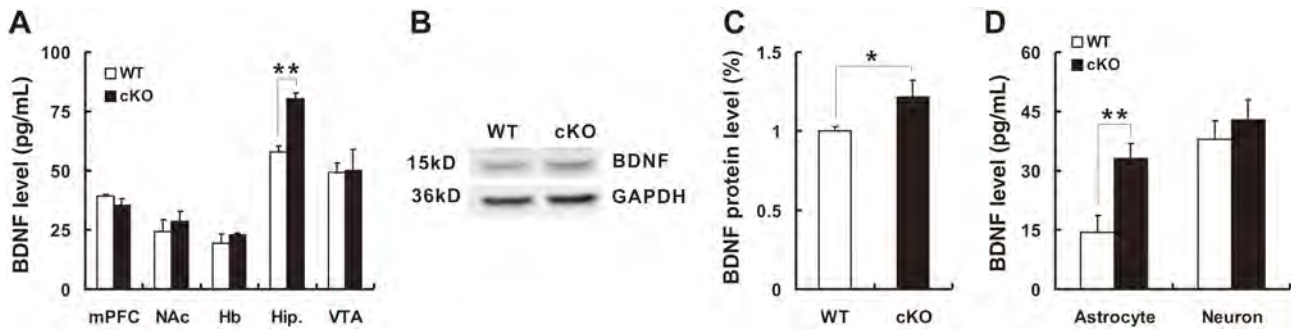
Fig. 6 The lack of GABA$_B$Rs in astrocytes increases the astrocytic BDNF level in the hippocampus. **A** Histogram showing BDNF protein levels assessed by ELISA in the mPFC, NAc, Hb, hippocampus, and VTA of aldh1l1::CreER^{T2}; GABA$_B^{loxP/loxP}$ (cKO), and GABA$_B^{loxP/loxP}$ (WT) mice. There was a difference only in the hippocampus of cKO *vs* WT mice ($n = 3$ mice/group; two-tailed Student's *t*-test). **B** Representative blots showing that BDNF protein levels were increased in the hippocampus of cKO mice. **C** Quantitative analysis of data as in (**B**) ($n = 4$ pairs of mice, two-tailed Student's *t*-test). BDNF band density was normalized to the loading control GAPDH; values of control mice are taken as 100%. **D** BDNF levels in cultured astrocytes and neurons isolated from the hippocampus of cKO and WT mice. Astrocytic BDNF levels were significantly higher in the cKO mice ($n = 6$; two-tailed Student's *t*-test). Data are presented as the mean $\pm$ SEM; *$P < 0.05$; **$P < 0.01$ *vs* controls.

GABA$_B$Rs in the hippocampus control the response to behavioral challenge, and this may result from increased astrocytic BDNF levels in the hippocampus.

Depression is a common, disabling mental illness [50]. Although it is widely considered to be due to a dysfunction in monoamine neurotransmission and this is the focus of all antidepressant strategies [51], growing numbers of clinical and preclinical studies indicate that there is a GABA system dysfunction in depression [5, 6]. More recently, growing evidence suggests that GABA$_B$Rs are important targets in the treatment of psychiatric disorders such as MDD. For example, increasing emphasis has been placed on GABA$_B$R antagonism as a potential therapeutic strategy for depression [11, 12]. GABA$_{B(1)}$R-knockout mice display antidepressant-like behaviors in the FST model of depression [10, 12, 14]. However, thus far, there is no evidence to demonstrate which cell type expressing GABA$_B$Rs modulates this antidepressant-like activity, as this receptor type has been reported to be present on almost all neurons and glial cells in the CNS [16, 17].

As the most abundant cell type in the CNS, astrocytes are thought to play important roles in mediating brain function [52]. In addition, astrocytes regulate neuronal excitability and synaptic transmission by releasing glutamate, adenosine triphosphate, and D-serine, a process termed gliotransmission [53, 54]. Furthermore, many neurotransmitter receptors are expressed on astrocytes, including those activated by glutamate, GABA, adenosine, and adenosine triphosphate [53, 54]. Although the roles of glutamatergic receptors in regulating astrocyte activity have already been described, the role of GABARs in mediating these processes is not as well understood. Our results support an active role of GABA$_B$Rs in response to behavioral challenge and further confirm the modulation of

this activity by astrocytic GABA$_B$Rs. It is worth noting that, although GABA$_B$Rs are also expressed by progenitor cells [55, 56], the specificity of Aldh1l1-CreER^{T2}-mediated recombination used in our study was high in astrocytes (Fig. 3). These results support the hypothesis that astrocytic GABA$_B$Rs modulate antidepressant activity in the FST.

It is well known that antidepressants increase serotonin and/or norepinephrine levels by preventing the reuptake of serotonin and/or norepinephrine into presynaptic terminals [57]. Although monoamine levels increase soon after drug administration, antidepressants work gradually over several weeks of continuous application; thus, it is possible that in addition to an increase in monoamine levels, other molecules may be responsible for their effects [58]. Our findings also showed that conditional knockout of GABA$_B$-Rs in astrocytes significantly increased the BDNF protein levels in the hippocampus; this finding is supported by previous studies demonstrating that GABA$_B$R antagonists increase BDNF levels in the hippocampus [59], while the GABA$_B$R agonist baclofen decreases these levels [60]. Meanwhile, studies have also suggested that BDNF-TrkB receptor signaling is necessary and sufficient to reduce depression [39, 46]. BDNF-mediated signaling is also involved in responses to stress and antidepressant activity [61]. Reduced brain BDNF levels have been shown to lead to depression [43], whereas increased BDNF levels can have antidepressant effects [44]. The direct infusion of BDNF into the hippocampus, acutely and chronically, mimics the behavioral responses induced by antidepressants in animal models of depression [45]. Therefore, our study supports an active role of BDNF in antidepressant activity. In addition, BDNF is also released from astrocytes [62, 63]. Our study further indicated that the increase in
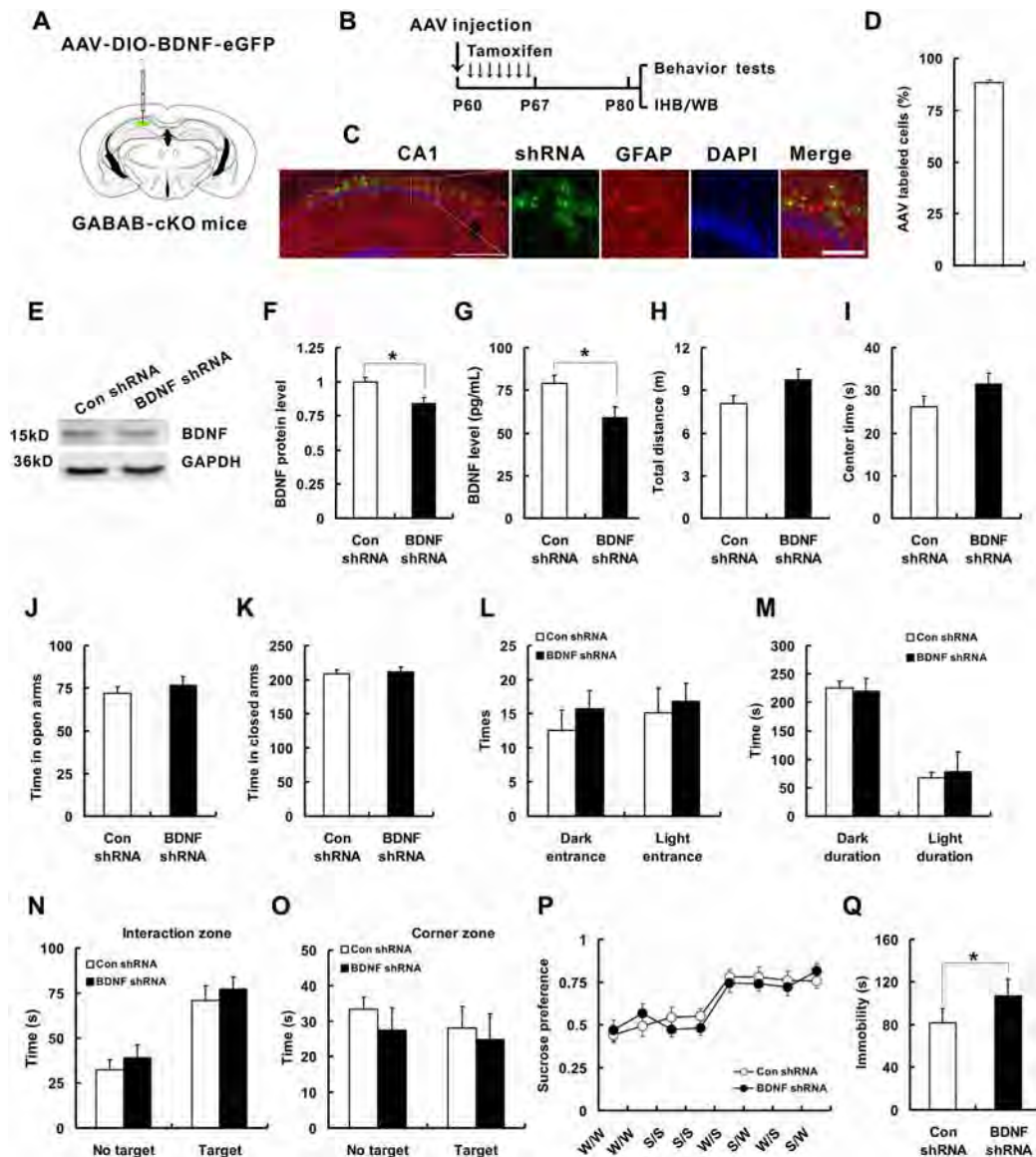
Fig. 7 Conditional knockdown of astrocytic BDNF restores the behavioral changes in cKO mice. **A** Schematic of the delivery of AAV-DIO-BDNF-eGFP into the CA1 region of cKO mice. **B** Schematic of the experiments. **C** Representative location of the BDNF shRNA virus (green) injected into the CA1 region (left; scale bar, 500 μm), and representative fluorescence images showing that most of the cells infected with AAV-DIO-BDNF-eGFP (shRNA) vector were astrocytes in the CA1 region of cKO mice (right; scale bar, 100 μm). **D** Average percentage of cells infected with AAV-DIO-BDNF-eGFP (shRNA) vectors that were positive for astrocytes. **E** Representative blots showing that the BDNF protein levels were restored in the hippocampus of cKO mice. **F** Quantitative analysis of data as in **E** ($n = 4$ pairs of mice, two-tailed Student's t-test). BDNF band density was normalized to the loading control GAPDH. **G** BDNF protein levels were restored to normal levels in the hippocampus of cKO mice after BDNF shRNA injection ($n = 3$ mice/group, two-tailed Student's t-test). **H, I** Knockdown of astrocytic BDNF in CA1 did not affect the total distance travelled (**H**) or the time spent in the central arena (**I**) in the open field test (Ctrl: $n = 9$ mice; shRNA: $n = 10$ mice; two-tailed Student's t-test). **J, K** In the EPM test, cKO mice injected with BDNF shRNA spent the same amount of time in the open (**J**) and closed (**K**) arms (Ctrl: $n = 9$; shRNA: $n = 10$; two-tailed Student's t-test). **L, M** There was no difference in the number of entries (**L**) or time spent (**M**) in the light/dark side in the light/dark box test (Ctrl: $n = 9$; shRNA: $n = 10$; two-tailed Student's t-test). **N, O** There was no difference between the two groups in the time spent in the interaction zone or corner zone in the presence/absence of a target mouse (Ctrl: $n = 9$; shRNA: $n = 10$; two-tailed Student's t-test). **P** Knockdown of BDNF in CA1 in cKO mice did not change preferences in the sucrose preference test (Ctrl: $n = 9$; shRNA: $n = 10$; repeated measures two-way ANOVA). **Q** Immobility time was restored in the FST after knocking down BDNF in CA1 in cKO mice (Ctrl: $n = 9$; shRNA: $n = 10$; two-tailed Student's t-test). Data are presented as the mean ± SEM; *$P < 0.05$ vs controls.

BDNF from astrocytes caused by deleting astrocytic GABA_BRs plays an important role in controlling the response to behavioral challenge.

In conclusion, these results demonstrate that conditional knockout of GABA_BRs in astrocytes positively affects the response to behavioral challenge. Moreover, it is conceivable that increased astrocytic BDNF protein levels in the hippocampus might be involved in this process. Taken together, our findings contribute to the current understanding of the cell types expressing GABA_BRs that modulate antidepressant activity in the FST model, which may provide new insight into the pathological mechanisms and potential targets in MDD.

Conflict of interest The authors declare no competing interests.

References

1. Hasin DS, Sarvet AL, Meyers JL, Saha TD, Ruan WJ, Stohl M, et al. Epidemiology of adult DSM-5 major depressive disorder and its specifiers in the United States. JAMA Psychiatry 2018, 75: 336–346.
2. Disner SG, Beevers CG, Haigh EAP, Beck AT. Neural mechanisms of the cognitive model of depression. Nat Rev Neurosci 2011, 12: 467–477.
3. Cassano P, Fava M. Tolerability issues during long-term treatment with antidepressants. Ann Clin Psychiatry 2004, 16: 15–25.
4. Wong ML, Licinio J. Research and treatment approaches to depression. Nat Rev Neurosci 2001, 2: 343–351.
5. Brambilla P, Perez J, Barale F, Schettini G, Soares JC. GABAergic dysfunction in mood disorders. Mol Psychiatry 2003, 8: 721–737, 715.
6. Sanacora G, Saricicek A. GABAergic contributions to the pathophysiology of depression and the mechanism of antidepressant action. CNS Neurol Disord Drug Targets 2007, 6: 127–140.
7. Bhagwagar Z, Wylezinska M, Taylor M, Jezzard P, Matthews PM, Cowen PJ. Increased brain GABA concentrations following acute administration of a selective serotonin reuptake inhibitor. Am J Psychiatry 2004, 161: 368–370.
8. Amsterdam JD, Kaplan M, Potter L, Bloom L, Rickels K. Adinazolam, a new triazolobenzodiazepine, and imipramine in the treatment of major depressive disorder. Psychopharmacology (Berl) 1986, 88: 484–488.
9. Petty F, Trivedi MH, Fulton M, Rush AJ. Benzodiazepines as antidepressants: does GABA play a role in depression? Biol Psychiatry 1995, 38: 578–591.
10. Gassmann M, Bettler B. Regulation of neuronal GABAB receptor functions by subunit composition. Nat Rev Neurosci 2012, 13: 380–394.
11. Felice D, O'Leary OF, Pizzo RC, Cryan JF. Blockade of the GABAB receptor increases neurogenesis in the ventral but not dorsal adult hippocampus: Relevance to antidepressant action. Neuropharmacology 2012, 63: 1380–1388.
12. Mombereau C, Kaupmann K, Froestl W, Sansig G, van der Putten H, Cryan JF. Genetic and pharmacological evidence of a role for GABAB receptors in the modulation of anxiety- and antidepressant-like behavior. Neuropsychopharmacology 2004, 29: 1050–1062.
13. Cryan JF, Kaupmann K. Don't worry 'B' happy!: a role for GABAB receptors in anxiety and depression. Trends Pharmacol Sci 2005, 26: 36–43.
14. Mombereau C, Kaupmann K, van der Putten H, Cryan JF. Altered response to benzodiazepine anxiolytics in mice lacking GABA B(1) receptors. Eur J Pharmacol 2004, 497: 119–120.
15. Mohler H. The GABA system in anxiety and depression and its therapeutic potential. Neuropharmacology 2012, 62: 42–53.
16. Perea G, Gómez R, Mederos S, Covelo A, Ballesteros JJ, Schlosser L, et al. Activity-dependent switch of GABAergic inhibition into glutamatergic excitation in astrocyte-neuron networks. eLife 2016, 5: e20362.
17. Oka M, Wada M, Wu Q, Yamamoto A, Fujita T. Functional expression of metabotropic GABAB receptors in primary cultures of astrocytes from rat cerebral cortex. Biochem Biophys Res Commun 2006, 341: 874–881.
18. Kessler RC. The effects of stressful life events on depression. Annu Rev Psychol 1997, 48: 191–214.
19. Thomas RM, Hotsenpiller G, Peterson DA. Acute psychosocial stress reduces cell survival in adult hippocampal neurogenesis without altering proliferation. J Neurosci 2007, 27: 2734–2743.
20. Frodl T, Koutsouleris N, Bottlender R, Born C, Jager M, Morgenthaler M, et al. Reduced gray matter brain volumes are associated with variants of the serotonin transporter gene in major depression. Mol Psychiatry 2008, 13: 1093–1101.
21. Treadway MT, Waskom ML, Dillon DG, Holmes AJ, Park M, Chakravarty MM, et al. Illness progression, recent stress, and morphometry of hippocampal subfields and medial prefrontal cortex in major depression. Biol Psychiatry 2015, 77: 285–294.
22. Campbell S, Marriott M, Nahmias C, MacQueen GM. Lower hippocampal volume in patients suffering from depression: a meta-analysis. Am J Psychiatry 2004, 161: 598–607.
23. Santarelli L, Saxe M, Gross C, Surget A, Battaglia F, Dulawa S, et al. Requirement of hippocampal neurogenesis for the behavioral effects of antidepressants. Science 2003, 301: 805–809.
24. MacQueen G, Frodl T. The hippocampus in major depression: evidence for the convergence of the bench and bedside in psychiatric research? Mol Psychiatry 2011, 16: 252–264.
25. Liu JH, You QL, Wei MD, Wang Q, Luo ZY, Lin S, et al. Social isolation during adolescence strengthens retention of fear memories and facilitates induction of late-phase long-term potentiation. Mol Neurobiol 2015, 52: 1421–1429.
26. Shen B, Zhang J, Wu H, Wang J, Ma K, Li Z, et al. Generation of gene-modified mice via Cas9/RNA-mediated gene targeting. Cell Res 2013, 23: 720–723.
27. Ma Y, Zhang X, Shen B, Lu Y, Chen W, Ma J, et al. Generating rats with conditional alleles using CRISPR/Cas9. Cell Res 2014, 24: 122–125.
28. Cui L, Zhang Z, Sun F, Duan X, Wang M, Di K, et al. Transcervical embryo transfer in mice. J Am Assoc Lab Anim Sci 2014, 53: 228–231.
29. Haller C, Casanova E, Müller M, Vacher C, Vigot R, Doll T, et al. Floxed allele for conditional inactivation of the GABAB(1) gene. Genesis 2004, 40: 125–130.
30. Li B, Jie W, Huang L, Wei P, Li S, Luo Z, et al. Nuclear BK channels regulate gene expression via the control of nuclear calcium signaling. Nat Neurosci 2014, 17: 1055–1063.
31. Mineur YS, Taylor SR, Picciotto MR. Calcineurin downregulation in the amygdala is sufficient to induce anxiety-like and

718

Neurosci. Bull. July, 2020, 36(7):705–718

depression-like behaviors in C57BL/6J male mice. Biol Psychiatry 2014, 75: 991–998.

32. Cao X, Li L, Wang Q, Wu Q, Hu H, Zhang M, et al. Astrocyte-derived ATP modulates depressive-like behaviors. Nat Med 2013, 19: 773–777.

33. McCarthy KD, de Vellis J. Preparation of separate astroglial and oligodendroglial cell cultures from rat cerebral tissue. J Cell Biol 1980, 85: 890–902.

34. Li XM, Yang JM, Hu DH, Hou FQ, Zhao M, Zhu XH, et al. Contribution of downregulation of L-type calcium currents to delayed neuronal death in rat hippocampus after global cerebral ischemia and reperfusion. J Neurosci 2007, 27: 5249–5259.

35. Willner P. Chronic mild stress (CMS) revisited: consistency and behavioural-neurobiological concordance in the effects of CMS. Neuropsychobiology 2005, 52: 90–110.

36. Porsolt RD, Le Pichon M, Jalfre M. Depression: a new animal model sensitive to antidepressant treatments. Nature 1977, 266: 730–732.

37. Warden MR, Selimbeyoglu A, Mirzabekov JJ, Lo M, Thompson KR, Kim S, et al. A prefrontal cortex–brainstem neuronal projection that controls response to behavioural challenge. Nature 2012, 492: 428–432.

38. Seo C, Guru A, Jin M, Ito B, Sleezer BJ, Ho YY, et al. Intense threat switches dorsal raphe serotonin neurons to a paradoxical operational mode. Science 2019, 363: 538–542.

39. Castren E, Voikar V, Rantamaki T. Role of neurotrophic factors in depression. Curr Opin Pharmacol 2007, 7: 18–21.

40. Lewin GR, Barde YA. Physiology of the neurotrophins. Annu Rev Neurosci 1996, 19: 289–317.

41. Li Y, Liu J, Liu X, Su C, Zhang Q, Wang Z, et al. Antidepressant-like action of single facial injection of botulinum neurotoxin a is associated with augmented 5-HT levels and BDNF/ERK/CREB pathways in mouse brain. Neurosci Bull 2019, 35: 661–672.

42. Li K, Shen S, Ji Y, Li X, Zhang L, Wang X. Melatonin augments the effects of fluoxetine on depression-like behavior and hippocampal BDNF–TrkB signaling. Neurosci Bull 2018, 34: 303–311.

43. Karege F, Perret G, Bondolfi G, Schwald M, Bertschy G, Aubry JM. Decreased serum brain-derived neurotrophic factor levels in major depressed patients. Psychiatry Res 2002, 109: 143–148.

44. Shirayama Y, Chen AC, Nakagawa S, Russell DS, Duman RS. Brain-derived neurotrophic factor produces antidepressant effects in behavioral models of depression. J Neurosci 2002, 22: 3251–3261.

45. Siuciak JA, Lewis DR, Wiegand SJ, Lindsay RM. Antidepressant-like effect of brain-derived neurotrophic factor (BDNF). Pharmacol Biochem Behav 1997, 56: 131–137.

46. Kozisek ME, Middlemas D, Bylund DB. Brain-derived neurotrophic factor and its receptor tropomyosin-related kinase B in the mechanism of action of antidepressant therapies. Pharmacol Ther 2008, 117: 30–51.

47. Duman RS, Monteggia LM. A neurotrophic model for stress-related mood disorders. Biol Psychiatry 2006, 59: 1116–1127.

48. De Foubert G, Carney SL, Robinson CS, Destexhe EJ, Tomlinson R, Hicks CA, et al. Fluoxetine-induced change in rat brain expression of brain-derived neurotrophic factor varies depending on length of treatment. Neuroscience 2004, 128: 597–604.

49. Nibuya M, Nestler EJ, Duman RS. Chronic antidepressant administration increases the expression of cAMP response element binding protein (CREB) in rat hippocampus. J Neurosci 1996, 16: 2365–2372.

50. Nestler EJ, Barrot M, DiLeone RJ, Eisch AJ, Gold SJ, Monteggia LM. Neurobiology of depression. Neuron 2002, 34: 13–25.

51. Schratt G. Neurobiology: a molecular knife to dice depression. Nature 2014, 516: 45–46.

52. Attwell D, Buchan AM, Charpak S, Lauritzen M, Macvicar BA, Newman EA. Glial and neuronal control of brain blood flow. Nature 2010, 468: 232–243.

53. Haydon PG, Carmignoto G. Astrocyte control of synaptic transmission and neurovascular coupling. Physiol Rev 2006, 86: 1009–1031.

54. Wang Q, Jie W, Liu J, Yang J, Gao T. An astroglial basis of major depressive disorder? An overview. Glia 2017, 65: 1227–1250.

55. Giachino C, Barz M, Tchorz JS, Tome M, Gassmann M, Bischofberger J, et al. GABA suppresses neurogenesis in the adult hippocampus through GABAB receptors. Development 2014, 141: 83–90.

56. Codega P, Silva-Vargas V, Paul A, Maldonado-Soto AR, Deleo AM, Pastrana E, et al. Prospective identification and purification of quiescent adult neural stem cells from their in vivo niche. Neuron 2014, 82: 545–559.

57. Malinow R. Depression: Ketamine steps out of the darkness. Nature 2016, 533: 477–478.

58. Yagasaki Y, Numakawa T, Kumamaru E, Hayashi T, Su TP, Kunugi H. Chronic antidepressants potentiate via sigma-1 receptors the brain-derived neurotrophic factor-induced signaling for glutamate release. J Biol Chem 2006, 281: 12941–12949.

59. Heese K, Otten U, Mathivet P, Raiteri M, Marescaux C, Bernasconi R. GABA(B) receptor antagonists elevate both mRNA and protein levels of the neurotrophins nerve growth factor (NGF) and brain-derived neurotrophic factor (BDNF) but not neurotrophin-3 (NT-3) in brain and spinal cord of rats. Neuropharmacology 2000, 39: 449–462.

60. Pedron VT, Varani AP, Balerio GN. Baclofen prevents the elevated plus maze behavior and BDNF expression during naloxone precipitated morphine withdrawal in male and female mice. Synapse 2016, 70: 187–197.

61. Krishnan V, Nestler EJ. The molecular neurobiology of depression. Nature 2008, 455: 894–902.

62. Giralt A, Carreton O, Lao-Peregrin C, Martin ED, Alberch J. Conditional BDNF release under pathological conditions improves Huntington's disease pathology by delaying neuronal dysfunction. Mol Neurodegener 2011, 6: 71.

63. Parpura V, Zorec R. Gliotransmission: Exocytotic release from astrocytes. Brain Res Rev 2010, 63: 83–92.

www.neurosci.cn
www.springer.com/12264

ORIGINAL ARTICLE

Overexpression of Purinergic P2X4 Receptors in Hippocampus Rescues Memory Impairment in Rats with Type 2 Diabetes

Ping-An Zhang[1,2] · Qian Sun[1] · Yong-Chang Li[1] · Rui-Xia Weng[3] ·
Rui Wu[1] · Hong-Hong Zhang[3] · Guang-Yin Xu[1,2]

Abstract Purinergic receptors have been reported to be involved in brain disorders. In this study, we explored their roles and mechanisms underlying the memory impairment in rats with type 2 diabetes mellitus (T2DM). T2DM rats exhibited a worse performance in the T-maze and Morris water maze (MWM) than controls. Microglia positive for P2X purinoceptor 4 (P2X4R) in the hippocampus were reduced and activated microglia were increased in T2DM rats. Long Amplicon PCR (LA-PCR) showed that DNA amplification of the *p2x4r* gene in the hippocampus was lower in T2DM rats. Minocycline significantly reduced the number of activated microglia and the mean distance traveled by T2DM rats in the MWM. Most importantly, P2X4R overexpression suppressed the activated microglia and rescued the memory impairment of T2DM rats. Overall, T2DM led to excessive activation of microglia in the hippocampus, partly through the DNA damage-mediated downregulation of P2X4Rs, thus contributing to memory impairment.

✉ Guang-Yin Xu
guangyinxu@suda.edu.cn

1   Jiangsu Key Laboratory of Neuropsychiatric Diseases and Institute of Neuroscience, Soochow University, Suzhou 215123, China

2   Center for Translational Medicine, The Affiliated Zhangjia-gang Hospital of Soochow University, Suzhou 215600, China

3   The Second Affiliated Hospital of Soochow University, Suzhou 215004, China

Introduction

Diabetes mellitus (DM) is one of the most common metabolic disorders and its prevalence in adults has been increasing rapidly in the last decade [1]. Its prevalence is predicted to increase to 642 million people (1 in 10 adults) by 2040 [2]. The rapid transition in lifestyle to urbanization has been accompanied by increases in the risk factors for non-communicable diseases like type 2 DM (T2DM) [3]. DM has been associated with an increased risk of developing Alzheimer disease (AD) and can affect cognitive systems [4, 5]. Specifically, people with T2DM often (but not invariably) do poorly on measures of learning and memory, whereas deficits in these domains are rarely seen in people with type 1 diabetes [6]. Despite the increased risk of AD in patients with T2DM [7], emerging evidence shows that such patients do not show the accumulation of amyloid plaques and neurofibrillary tangles that are the core neuropathological features of AD [8, 9]. Studies of brain tissue have even suggested that T2DM is associated with decreases in amyloid plaques and neurofibrillary tangles [10, 11]. So, the link between T2DM and the risk of cognitive impairment may involve other mechanisms.

The role of inflammation in the pathogenesis of T2DM and its associated complications is now well established [12–14]. Recently, a study reported the central role of interleukin (IL-1)-mediated neuroinflammation as a mechanism underlying the cognitive deficits in obesity and diabetes [15]. Microglia are the primary immune effector cells in the brain [16]. In response to brain damage or injury, microglia are activated and undergo morphological

as well as functional transformations [17]. Excessive activation of microglia contributes to the progression of chronic neurodegenerative diseases [18], but the underlying mechanisms are still unclear. Recent reports have revealed profound synaptic changes (long-term potentiation and depression) caused by a mirror microglia-mediated inflammatory response in the hippocampus during peripheral organ inflammation [19]. Furthermore, microglia stimulated with lipopolysaccharide phagocytose viable neurons [20]. Studies have shown that the time taken to remove activated microglia determines the severity and duration of central nervous system inflammation.

ATP that supplies energy for cellular metabolism can be released into the extracellular space and play an important role *via* purinergic 2 receptors (P2Rs) in mediating neurotransmission as well as Ca^{2+} waves between astrocytic glial cells [21, 22]. In addition, ATP released locally from damaged tissue induces microgliosis, and activated microglial cells migrate to the site of injury, proliferate, and phagocytose cells and cellular components [23]. Microglial processes in the hippocampal dentate gyrus retract as early as 2 h after injection of lipopolysaccharide and die ∼24 h later. These processes are prevented by blocking P2X4 receptors (P2X4Rs), suggesting that P2X4Rs contribute to controlling the fate of activated microglia and their survival [24]. So, early microglial activation mediated by P2X4Rs during neuroinflammation provides a new means of understanding the memory impairment in T2DM.

Taking these findings together, we hypothesized that downregulation of P2X4Rs in the hippocampus leads to the over-activation of microglia and the release of inflammatory mediators, eventually contributing to memory impairment in T2DM rats. Here, we investigated the expression of P2X4Rs in the hippocampus of T2DM rats.

Materials and Methods

Animals

Male Sprague-Dawley rats (∼250 g) were purchased from the Laboratory Animal Center of Soochow University, China, and housed in a temperature-controlled room at ∼23°C with a 12-h day/night cycle (lights on at 08:00 and off at 20:00). The rats were given free access to tap water and food. Relevant studies have shown that a high-fat diet (HFD) followed by a low dose of streptozotocin (STZ) successfully induces T2DM, and the symptoms in this animal model are close to those in patients with T2DM [25], so we used this combination to induce T2DM. Briefly, rats were fed an HFD (20% carbohydrate, 20% protein, and 60% fat) for 2 weeks, followed by one intraperitoneal

injection of STZ (30 mg/kg; Sigma, St Louis, MO). Age-matched control rats were fed a normal diet (ND; 60% carbohydrate, 22% protein, and 18% fat), and intraperitoneally injected with citrate buffer. One week after the injection, blood glucose measurements were performed in the morning using blood samples from the tail vein with a glucometer (Johnson & Johnson Medical Co., New Brunswick, NJ). Rats with blood glucose levels ≥16.7 mmol/L were considered diabetic. All experimental procedures were approved by the Animal Care and Use Committee of Soochow University.

Drug Administration

For insulin tolerance tests, rats were intraperitoneally injected with regular human insulin (Novolin R; Novo Nordisk, Copenhagen, Denmark) at 0.75 U/kg body weight after a 6-h fasting period. The blood glucose level was measured at 0 min, 20 min, 40 min, 60 min, 120 min, and 240 min after the injection.

In the behavioral and molecular experiments, minocycline (Mino, inhibitor of activated microglia, 45 mg/kg body weight) dissolved in normal saline (NS) was intraperitoneally injected daily from 54 days to 61 days after STZ injection [26]. T2DM rats receiving NS injection served as controls.

Microinjection of Adeno-Associated Virus (AAV)

For behavioral tests and molecular measurements, AAV-NC or AAV-P2X4R from Genechem Co. Ltd (Shanghai, China) was stereotaxically microinjected into the hippocampus of T2DM rats as described in our previous study [22]. Briefly, after the rat was anesthetized by intraperitoneal injection of 4% chloral hydrate, a microinjector was fixed unilaterally to the left side of the skull and aimed at the hippocampus (coordinates with respect to bregma: AP − 4.8 mm, ML 3.2 mm, DV 3.5 mm, angle 0°) or at the right hippocampus. The AAV-NC (8.44×10^{12} viral genomes (vg)/mL, 800 nL) or AAV-P2X4R (1.74×10^{12} vg/mL, 800 nL) was injected into both the left and right hippocampus 28 days after the STZ injection. After four weeks, rats infected with AAV were assessed in the MWM or sacrificed for further molecular tests.

Delayed Alternation T-Maze (DAT) Task

Rats were trained on the DAT task using a T-maze device with minor modifications [27]. Behavioral testing was conducted in the daytime between 08:00 and 17:00. Each daily session included one initial trial and nine formal trials. In the initial trial, both arms were baited so that rats would get a food reward by choosing either arm. During

the formal trials, rats had to learn to avoid the arm visited in the previous trial and choose the opposite arm to get a reward. If rats made the wrong choice, they would receive a correction procedure to make the correct choice by keeping the baited arm still baited and the procedure would not stop until they visited the baited arm. The errors were counted and divided into two types: a Win-shift failure was defined as wrong choice following a correct choice in the previous trial; and a Lose-shift failure was counted when the rat continued to enter the previously wrong arm. The maze was wiped with alcohol to remove any smell between trials.

Morris Water Maze (MWM)

This test was carried out with minor modifications as described previously [28]. The training trials were carried out for 5 consecutive days (4 trials daily starting from each quadrant). Each rat was allowed to swim for 60 s. In addition, the rats that failed to locate the platform within the criterion period were placed on it for 5 s. In the probe test trial on day 6, the platform was removed to measure spatial memory. The number of entries into and time spent in the target quadrant where the platform was previously located, and the mean distance from the previous platform position for each rat were recorded by Anymaze video tracking system software (Global Biotech Inc., Shanghai, China).

Immunofluorescence Assay

Rats were deeply anesthetized by intraperitoneal injection of 4% chloral hydrate, then perfused transcardially with 300 mL NS followed by precooled 4% paraformaldehyde (PFA). The brain was rapidly removed, post-fixed in PFA for 3 h, and then immersed in phosphate-buffered sucrose to dehydrate gradiently. For double labeling, 14-μm sections were simultaneously incubated with antibodies against P2X4Rs (1:100, Alomone Labs, Jerusalem, Israel; APR-002) and NeuN (1:50, Merk Millpore, Darmstadt, Germany; MAB377) or GFAP (1:300, Cell Signaling Technology, Danvers, MA; 3670S) or CD11b (1:100, Bio-Rad, Berkeley, CA; MCA275R) at 4°C overnight and then with Alexa Fluor 488 (1:500, Molecular Probes, Shanghai, China; A21206) and 555 (1:100, Molecular Probes, A31570) for 2 h at room temperature (RT). The primary antibodies were omitted for negative controls. After staining, images were captured on an Axioscope A1 microscope (Zeiss, Jena, Thuringian, Germany). The fluorescent cells were counted and analyzed using ImageJ software (Rawak Software Inc., Stuttgart, Baden-Württemberg, Germany).

Western Blotting

Each rat was guillotined and the brain was quickly dissected out and lysed by ultrasonication in an ice bath. Twenty micrograms of total protein was fractionated on 10% polyacrylamide gel. Proteins were then transferred to PVDF membranes for 2 h at 200 mA in an ice bath. The membranes were blocked in 5% non-fat milk powder at RT for 2 h and then incubated with primary antibodies (GAPDH, 1:1000, Hangzhou Goodhere Biotechnology, AB-P-R001; P2X4Rs, 1:500, Alomone Labs, APR-002; and ATM, 1:100, Santa Cruz, CA; sc-23921) at 4°C overnight. Then, the membranes were incubated with HRP-conjugated secondary antibodies (GAR0072 or GAM0072, 1:2000, Multi Science, Hangzhou, China) at RT. Bands were visualized using an enhanced chemiluminescence detection kit for HRP (EZ-ECL, Biological Industries, Kibbutz Beit Haemek, Israel; 20-500-120) and appropriately exposed in a chemiluminescence imaging system (ChemiDoc XRS, Bio-Rad, Hercules, CA). Band intensities were measured using ImageJ. Protein expression was normalized to GAPDH.

Real-Time Quantitative Polymerase Chain Reaction (qPCR)

Total RNA was exacted from the hippocampus using the TRIzol method. cDNA was synthesized from total RNA using the EasyScript First-Strand cDNA Synthesis Super-Mix kit (Transgen Biotech, Beijing, China) following the manufacturer's instructions. The primer of *p2x4r* used in qPCR was: Forward 5′-GGCTACCAGGAAACGGACTC-3′ and Reverse 5′-ATCACATAGTCCGCCACGTC-3′. Negative control reactions were performed by omitting the cDNA template. The relative expression level for each target gene was normalized using the $2^{-\Delta\Delta Ct}$ method.

Long Amplicon PCR (LA-PCR)

Genomic DNA was extracted from the hippocampus of T2DM and control rats using the QIAamp DNA Mini kit according to the manufacturer's instructions (Qiagen, Dusseldorf, Germany). Briefly, ground hippocampal tissue was digested in proteinase K at 56°C for 3 h, then total DNA was purified using the QIAamp procedures. NCBI GenBank showed that the *p2x4r* gene contains 17,652 base pairs. Long- and short-PCR were separately performed using Phanta Max Master Mix (Vazyme Biotech Co., Ltd, Nanjing, China). The primers were as follows: *Long-p2x4r* F: 5′-GAGCCTGCCGGAGCTGGTGGGTGGA-3′, R: 5′-TGCTTGGGCAACCCTGAGTATTTGTGGAGT-3′; *Short-p2x4r* F: 5′-GACGAGCAAATAACTAAGCC-3′, R: 5′-TGTTTCCCTGTAATCCACT-3′. The long PCR procedure

was conducted as follows: 95°C, 10 min; 95°C, 15 s, 76°C, 18 min for 3 cycles; 95°C, 15 s, 75°C, 18 min for 3 cycles; 95°C, 15 s, 74°C, 18 min for 3 cycles; 95°C, 15 s, 73.6°C, 18 min for 24 cycles; 72°C, 10 min. Agarose gel electrophoresis was carried out after long- and short-PCR. The densitometry of bands was determined using ImageJ, and the long-PCR/ short-PCR ratio was used for statistical analyses.

Statistical Analysis

All values are shown as the mean ± SEM. Data were analyzed using OriginPro 8 (OriginLab, Northampton, MA) and Prism 6 (Graph Pad, San Diego, CA) softwares. Gaussian distribution tests were conducted before analysis.

The two-sample t-test or Mann-Whitney test was used to determine the significance of differences between two groups. Two-way ANOVA followed by Tukey's post hoc test was performed when appropriate. $P < 0.05$ was considered statistically significant.

Results

T2DM Rats Exhibit Memory Impairment

To induce T2DM, rats were fed the HFD for 2 weeks followed by an intraperitoneal injection of a low dose of STZ. Rats fed the normal diet and intraperitoneally injected
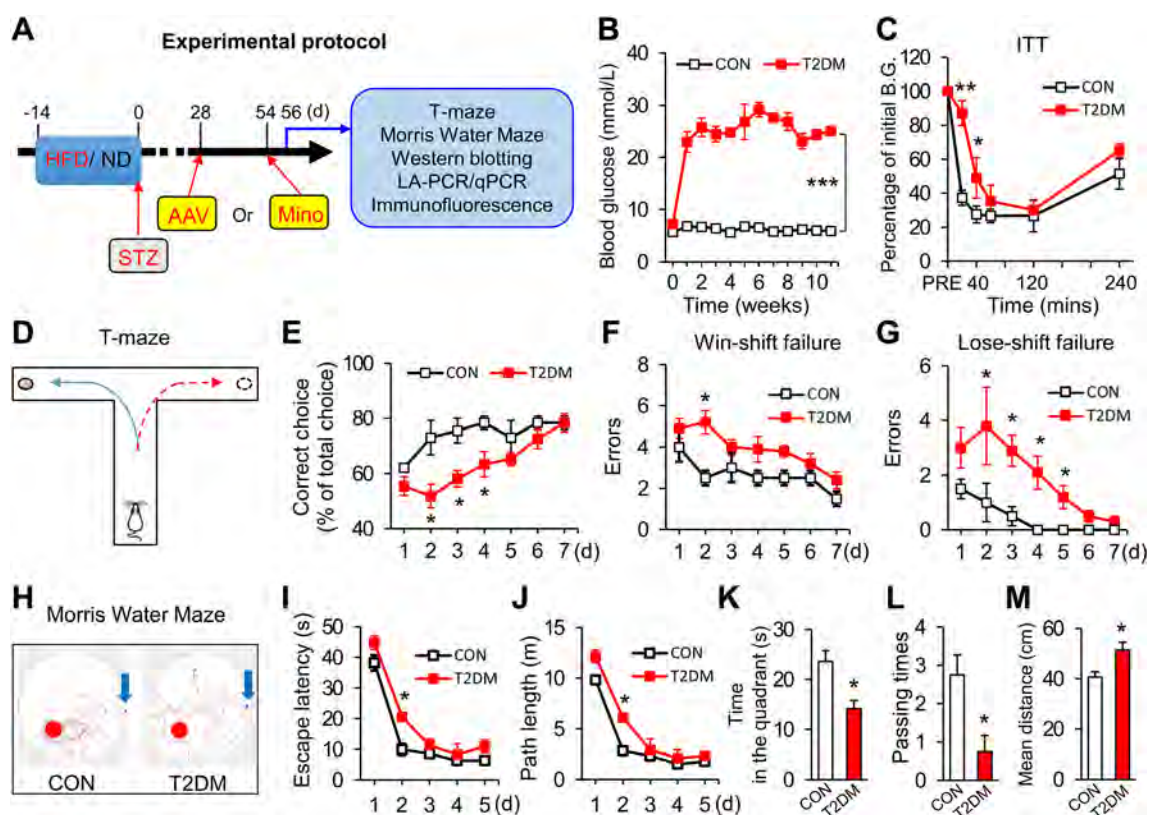
Fig. 1 T2DM rats show memory impairment. A Experimental protocol. Rats were fed an HFD or ND for two weeks then intraperitoneally injected with STZ or NS. AAV-NC or AAV-P2X4R was microinjected into the hippocampus on day 28. Minocycline or NS was injected daily for one week from day 54. On day 56, behavioral tests and molecular determinations were conducted (HFD, high-fat diet; ND, normal diet; STZ, streptozotocin; AAV, adeno-associated virus; Mino, minocycline). B Blood glucose levels in T2DM rats and controls (CON) ($n = 8$/group; ***$P < 0.001$ vs CON, two-way ANOVA). C Insulin tolerance test (ITT) results showing the percentage of initial blood glucose (B.G.) in T2DM and CON rats after intraperitoneal insulin injection ($n = 8$/group; *$P < 0.05$, **$P < 0.01$ vs CON, two-way ANOVA followed by Tukey's post hoc test). D The T-maze consisted of a stem (50 cm × 10 cm) and two arms (40 cm × 10 cm) with walls 20 cm high. E Correct choices

of T2DM and CON rats in the T-maze ($n = 8$/group; *$P < 0.05$ vs CON, two-way ANOVA followed by Tukey's post hoc test). F Errors using the Win-shift strategy by T2DM and CON rats ($n = 8$/group; *$P < 0.05$ vs CON, two-way ANOVA followed by Tukey's post hoc test). G Errors using the Lose-shift strategy by T2DM and CON rats ($n = 8$/group; *$P < 0.05$ vs CON, two-way ANOVA followed by Tukey's post hoc test). H Representative tracking of T2DM and CON rats in the MWM test on day 6. I, J Escape latency and path length of T2DM and CON rats in training trials of the MWM ($n = 16$/group; *$P < 0.05$ vs CON, two-way ANOVA followed by Tukey's post hoc test). K–M Time in the target quadrant, passing times, and mean distance from the platform of T2DM and CON rats in the probe test on day 6 ($n = 16$/group; *$P < 0.05$, two-sample t-test for K and M, Mann-Whitney test for L).

with NS were used as controls (Fig. 1A). One week after STZ injection, the blood glucose levels of T2DM rats were >16.7 mmol/L and lasted to the 11th week while they were normal in control rats (Fig. 1B). Confirming the induction of T2DM, insulin tolerance tests showed that the blood glucose levels of T2DM rats were significantly higher than those of controls 20 min and 40 min after intraperitoneal injection of insulin (0.75 U/kg), which means that these rats were insulin tolerant (Fig. 1C).

Then we investigated how T2DM rats performed in the DAT task (Fig. 1D). In a week of trials, the correct choice rate of T2DM rats was significantly lower than that of control rats on days 2–4, but there was no significant difference on days 5–7 (Fig. 1E). Interestingly, analysis of error types revealed that T2DM rats showed more errors using the Win-shift strategy on day 2, and they made many more errors using the Lose-shift strategy on days 2–5 than

controls (Fig. 1F, G). T2DM rats failed to use the Win-shift and Lose-shift strategies in the DAT task, which led to their low correct choice rate. These results indicated that T2DM rats have a deficit in spatial working memory.

To further confirm the memory impairment of T2DM rats, we applied the MWM test and there was no significant difference between T2DM rats and controls in the learning procedure from day 1 to day 5, except for day 2 (Fig. 1I, J). However, in the probe test on day 6, the time that T2DM rats remained in the quadrant where the platform had been located was greatly reduced compared with controls (Fig. 1K). Similarly, the passing times of T2DM rats were markedly fewer than in controls (Fig. 1L). Furthermore, the mean distance from the platform was remarkably greater in T2DM rats than in controls (Fig. 1M). These data confirmed that T2DM rats exhibit memory impairment.
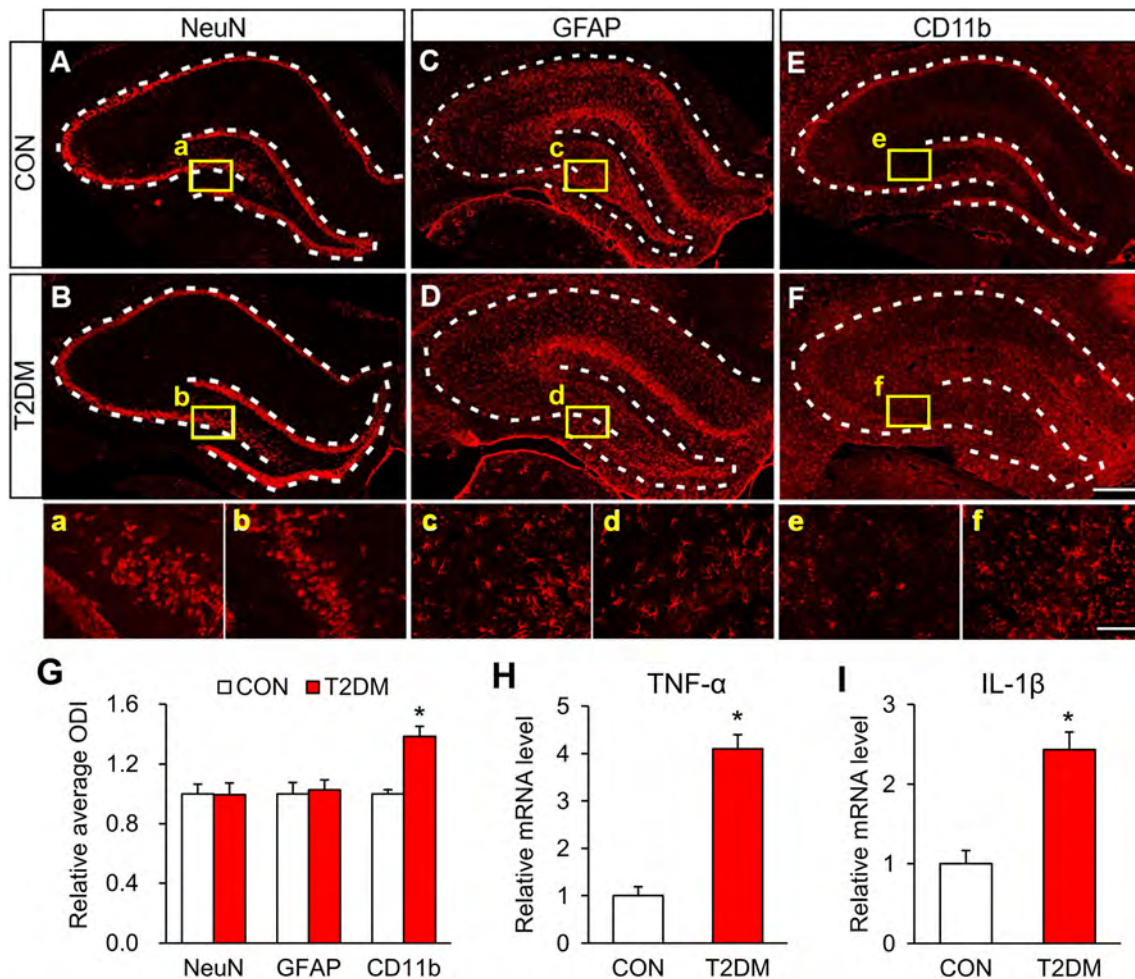

Fig. 2 Microglia are activated in the hippocampus of T2DM rats. **A–F** In the hippocampus of T2DM and control (CON) rats: NeuN-labeled neurons (**A, B, a, b**); GFAP-labeled astrocytes (**C, D, c, d**); and CD11b-labeled microglia (**E, F, e, f**) (scale bars, 500 μm in **F**; 100 μm in **f**). Dashed lines outline the hippocampus. **G** Relative numbers of NeuN-, GFAP-, and CD11b-positive cells in the hippocampus of T2DM and CON rats ($n = 4$/group; *$P < 0.05$ *vs* CON, two-sample *t*-test). **H, I** The mRNA levels of TNF-α (**H**) and IL-1β (**I**) in the hippocampus of T2DM and CON rats ($n = 4$/group; *$P < 0.05$ *vs* CON, two-sample *t*-test).

724

Neurosci. Bull. July, 2020, 36(7):719–732

Microglia are Activated in the Hippocampus of T2DM Rats

We next investigated whether the functions of cell types in the hippocampus were altered in T2DM rats. Immunofluorescence assays showed that the number of neurons labeled by NeuN in the hippocampus of T2DM rats did not differ from controls (Fig. 2A, B). Similarly, the number and appearance of astrocytes marked by GFAP did not differ in the hippocampus of T2DM rats (Fig. 2C, D). However, and interestingly, the number of CD11b-stained microglia was dramatically higher in T2DM rats than in controls (Fig. 2E–G). And these microglia in T2DM rats were amoeboid in shape (Fig. 2F). Since activated microglia synthesize and secrete inflammatory mediators [29], we assessed the expression of TNF-α and IL-1β in the hippocampus using qPCR. The results showed that their mRNA levels were significantly higher in T2DM rats than in controls (Fig. 2H, I). These data demonstrated that microglia are clearly activated in the hippocampus of T2DM rats.

Minocycline Treatment Inhibits Activated Microglia and Improves the MWM Performance of T2DM Rats

Minocycline is an effective inhibitor of activated microglia [30]. Using immunofluorescence assays, we showed that activated microglia in the hippocampus of T2DM rats were markedly reduced by daily intraperitoneal injections of minocycline for a week from day 54 (Fig. 3A–C). In addition, the mRNA levels of TNF-α and IL-1β in the
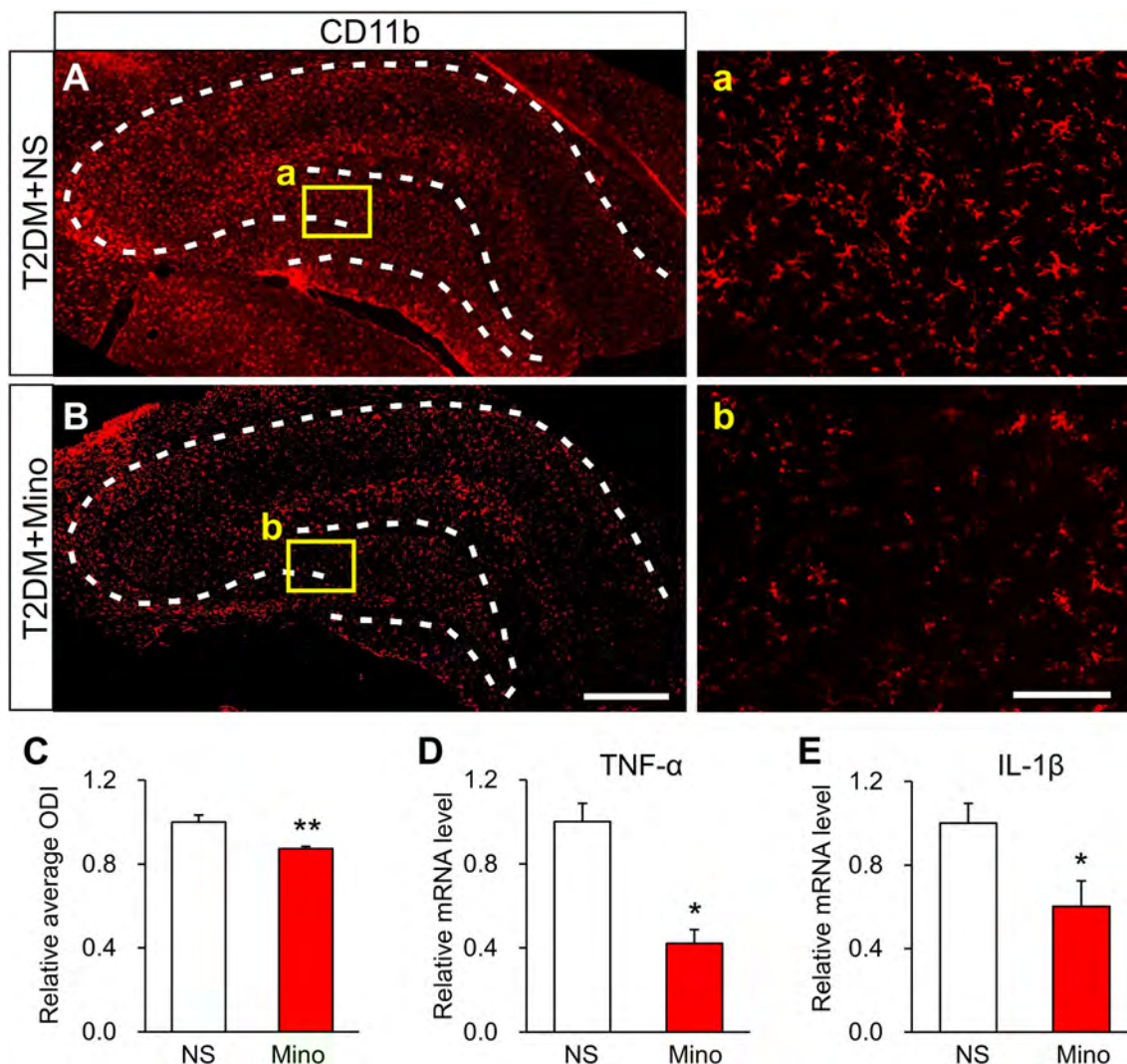
Fig. 3 Minocycline treatment inhibits activated microglia. **A–C** Representative images and statistics for the number of activated microglia labeled by CD11b in the hippocampus of T2DM rats injected with minocycline (Mino) or normal saline (NS) (scale bars, 500 μm in **B**; 100 μm in **b**; $n = 4$/group; **$P < 0.01$ vs NS, two-sample t-test). Dashed lines outline the hippocampus. **D**, **E** TNF-α and IL-1β levels after Mino or NS injection ($n = 4$/group; *$P < 0.05$ vs NS, two-sample t-test).

hippocampus of T2DM rats were significantly decreased compared with NS injection (Fig. 3D, E). These data indicated that minocycline effectively inhibits the activated microglia in T2DM rats.

We then determined the effect of minocycline on the performance of T2DM rats in the MWM. There was no difference between T2DM rats treated with minocycline and NS during the learning period (Fig. 4B, C). In the probe test on day 6, we found that minocycline significantly reduced the mean distance traveled by T2DM rats compared with the NS group (Fig. 4D), although the time spent in the target quadrant and crossing times did not differ (Fig. 4E, F). Besides, T2DM rats with minocycline appeared to better memorize the target position than the NS group (Fig. 4A). These results indicated that minocycline rescues the spatial memory impairment in T2DM rats.

P2X4Rs are Down-Regulated in the Hippocampus of T2DM Rats

Here we showed that P2X4R expression was significantly decreased at both the protein and mRNA levels in the hippocampus of T2DM rats when compared with control rats (Fig. 5A, D), while the protein levels of P2X3Rs and P2X7Rs were not altered (Fig. 5B, C). In addition, P2X4R expression in the basolateral amygdaloid nucleus (BLA) and anterior cingulate cortex (ACC) did not significantly differ between T2DM rats and controls (Fig. 5E, F).

P2X4Rs are Mainly Expressed in Microglia of the Hippocampus

Since previous studies have shown that P2X4Rs are predominantly expressed in microglia in the spinal cord [31], we performed an immunofluorescence study to determine the location of P2X4Rs in the hippocampus of control rats. We found that P2X4Rs were mainly co-expressed with CD11b, the marker of microglia, but not with GFAP or NeuN (Fig. 6A). In addition, we analyzed P2X4R expression in the hippocampal microglia of both T2DM and control rats. The immunofluorescence results showed that the co-expression of P2X4Rs and CD11b was dramatically lower in T2DM rats than in controls (Fig. 6B). These results implied that P2X4R expression is decreased in the microglia of the hippocampus in T2DM rats.
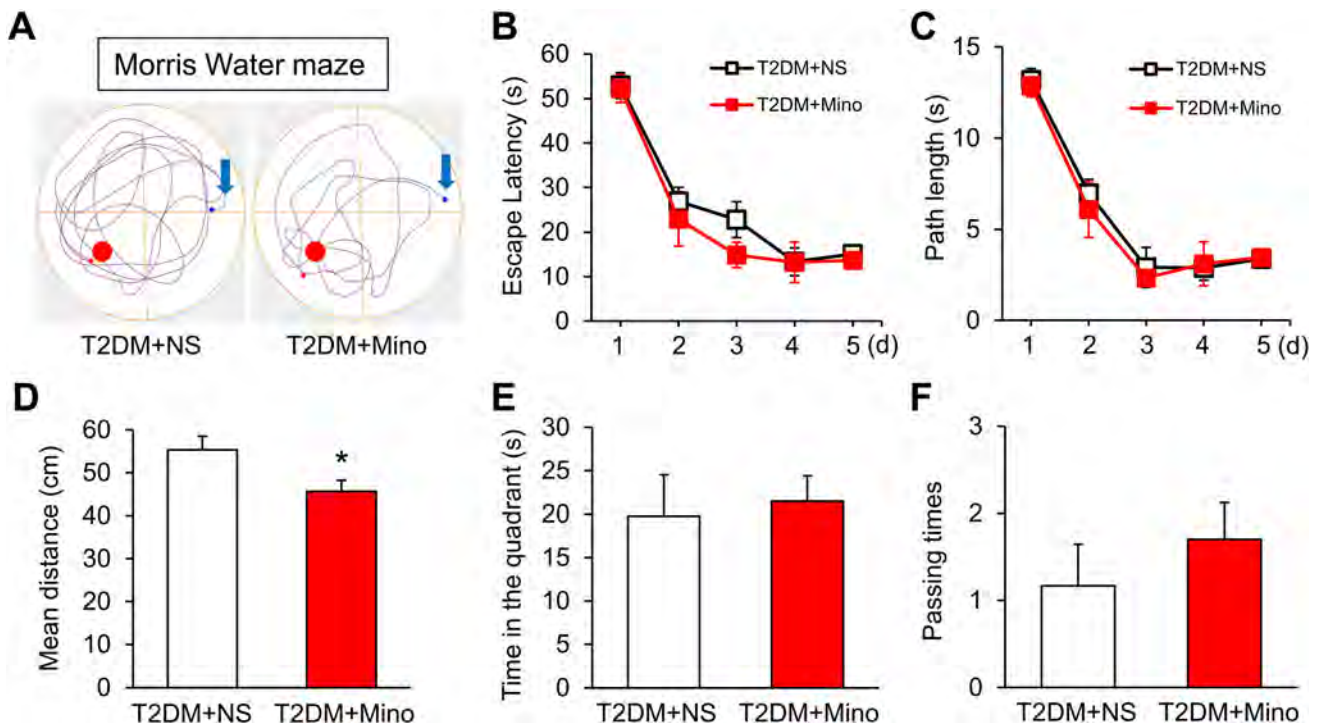

Fig. 4 Minocycline improves the MWM performance of T2DM rats. **A** Tracking of T2DM rats after injection of normal saline (NS) or minocycline (Mino) on day 6. **B**, **C** Escape latency and path length of T2DM rats injected with minocycline or NS ($n = 4$/group; no significant difference, two-way ANOVA followed by Tukey's *post hoc* test). **D** Average distance from the platform of T2DM rats injected with minocycline or NS ($n = 8$/group; *$P < 0.05$ *vs* T2DM+NS, two-sample *t*-test). **E**, **F** Time in the platform quadrant and passing times of T2DM rats injected with minocycline or NS ($n = 8$/group; no significant difference, two-sample *t*-test for **E** and Mann–Whitney test for **F**).

726

Neurosci. Bull. July, 2020, 36(7):719–732

Fig. 5 P2X4R expression is down-regulated in the hippocampus of T2DM rats. **A** Protein expression of P2X4Rs in the hippocampus of T2DM and control (CON) rats ($n = 4$; *$P < 0.05$ vs CON, two-sample t-test). **B**, **C** Protein expression of P2X3Rs and P2X7Rs in the hippocampus of T2DM and CON rats ($n = 4$/group; no significant difference, two sample t-test). **D** mRNA levels of P2X4Rs in the hippocampus of T2DM and CON rats ($n = 4$/group; *$P < 0.05$ vs CON, two-sample t-test). **E**, **F** Protein expression of P2X4Rs in the basolateral amygdaloid nucleus (BLA) and anterior cingulate cortex (ACC) of T2DM and CON rats ($n = 4$/group, no significant difference, two-sample t-test).
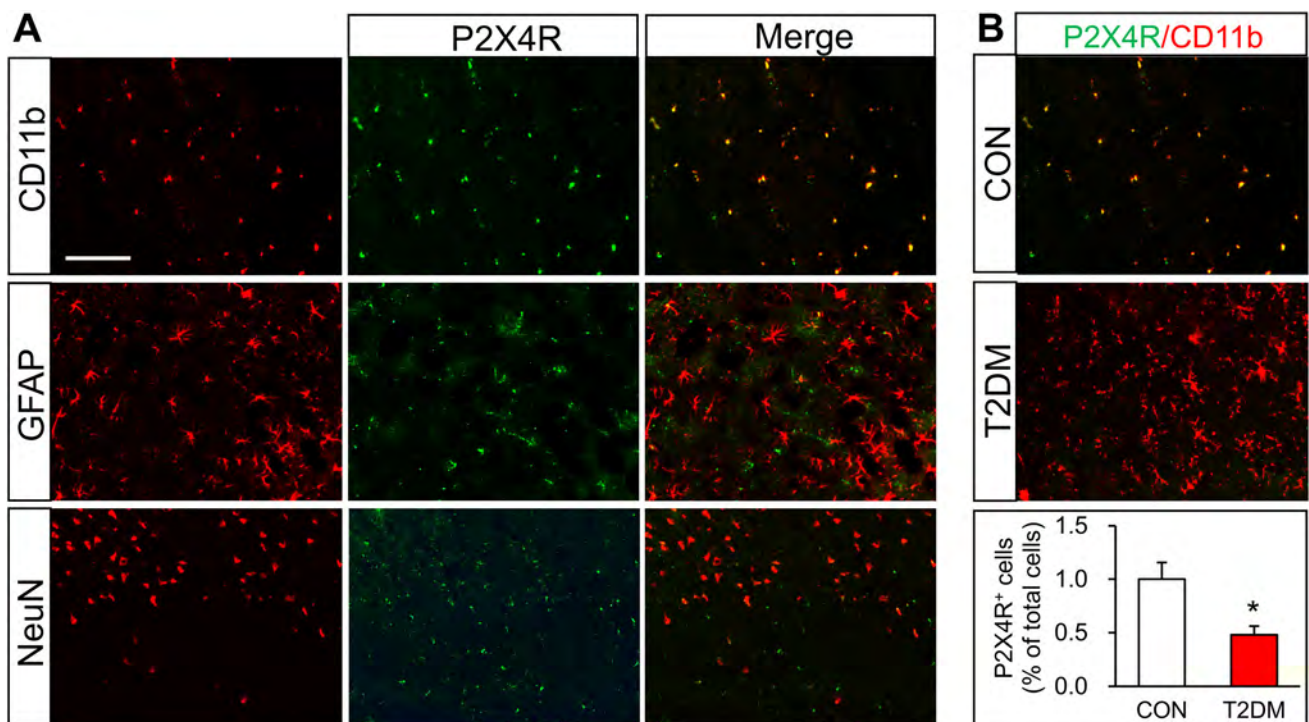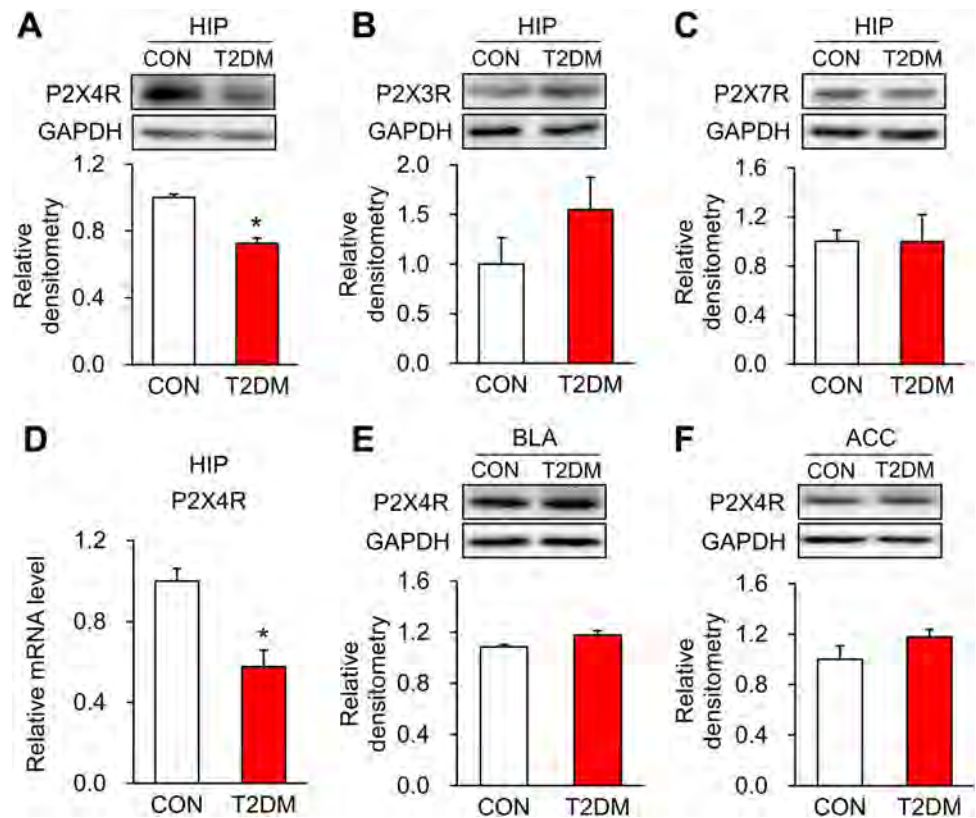
Fig. 6 P2X4Rs are mainly expressed in microglia in the hippocampus. **A** Representative images of P2X4Rs (green) co-expressed with CD11b (red), but not with GFAP (red) or NeuN (red) (scale bar, 100 μm). **B** Representative images and statistics showing the percentages of P2X4R-positive cells in T2DM and control (CON) rats ($n = 4$/group; *$P < 0.05$ vs CON, two-sample t-test).

Fig. 7 T2DM results in DNA damage of the *p2x4r* gene. **A** Expression of ATM in the hippocampus of T2DM and control (CON) rats (*n* = 3/group; *******P* < 0.01 *vs* CON, two-sample *t*-test). **B** Diagram showing that Long Amplicon PCR (LA-PCR) contains the Long-PCR product and the Short-PCR product. **C** L-PCR/S-PCR ratio of *p2x4r* gene in the hippocampus of T2DM and CON rats (*n* = 4/group; **P* < 0.05 *vs* CON, two-sample *t*-test). **D** Protein expression of P2X4R after minocycline (Mino) and normal saline (NS) treatment (*n* = 4 for NS group, *n* = 3 for Mino group; *P* > 0.05, two-sample *t*-test).
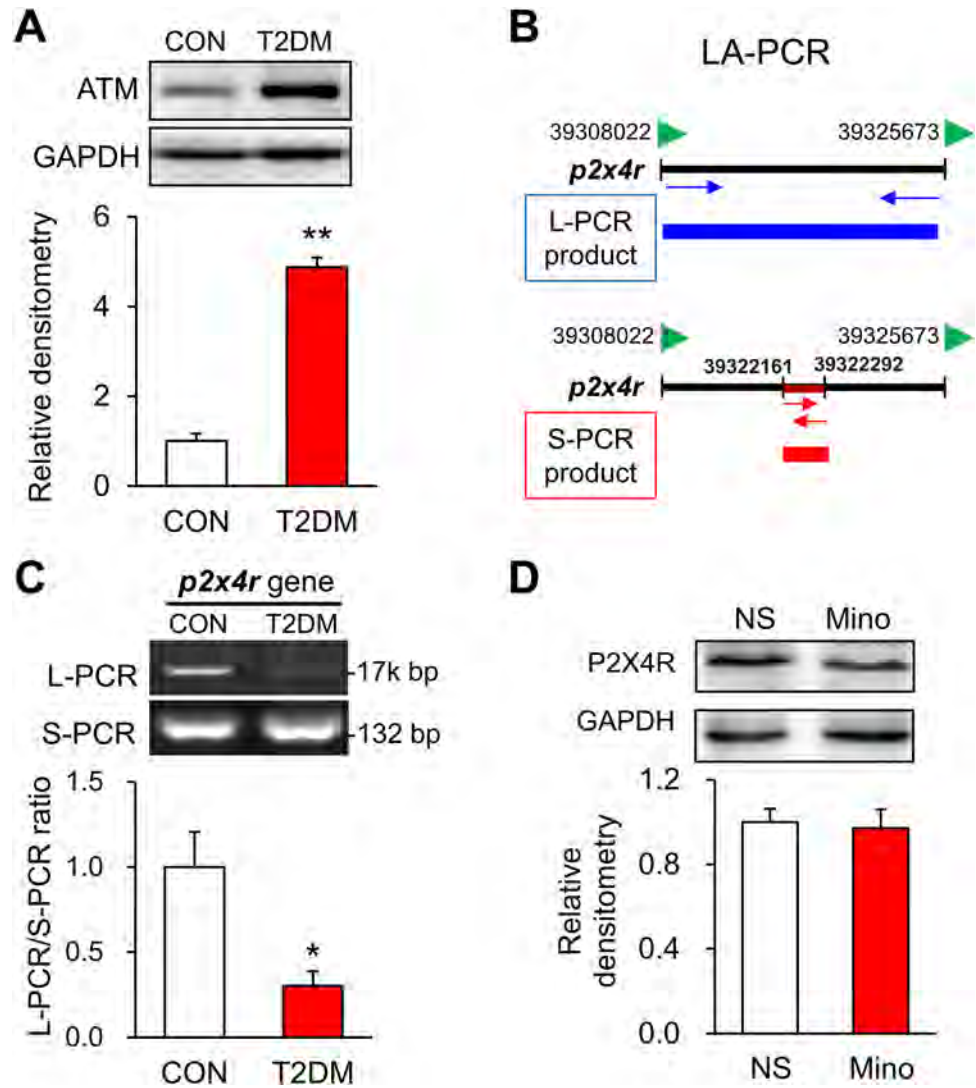
DNA Damage Contributes to the Down-Regulation of P2X4Rs

We next investigated the mechanisms by which P2X4R expression is down-regulated. Since DNA damage is involved in patients with T2DM [32], we determined whether DNA damage contributes to the downregulation of P2X4R expression. Western blotting showed that ATM (ataxia telangiectasia mutated), a marker of DNA damage, was significantly up-regulated in the hippocampus of T2DM rats (Fig. 7A). LA-PCR technology was used to further detect DNA damage in specific genes (Fig. 7B). The Long-chain PCR/Short-chain PCR ratio of the *p2x4r* gene was significantly reduced in the hippocampus of T2DM rats when compared with control rats (Fig. 7C). These data indicated that DNA damage of the *p2x4r* gene contributes to the decreased P2X4R expression. In addition, minocycline injection did not affect P2X4R expression in the hippocampus of T2DM rats compared with NS injection (Fig. 7D), suggesting that decreased P2X4Rs might be an upstream signal of activated microglia.

Overexpression of P2X4Rs Reduces the Activation of Microglia

To further investigate the involvement of P2X4Rs in microglial activation in T2DM rats, we overexpressed P2X4Rs in the bilateral hippocampus of these rats by microinjection of AAV-P2X4R and demonstrated that P2X4Rs were successfully overexpressed in the hippocampus (Fig. 8A, B). Importantly, after overexpression of P2X4Rs, activated microglia were markedly suppressed in the hippocampus of T2DM rats (Fig. 8C–E). And the mRNA levels of TNF-α and IL-1β were also significantly reduced when P2X4Rs were overexpressed (Fig. 8F, G).
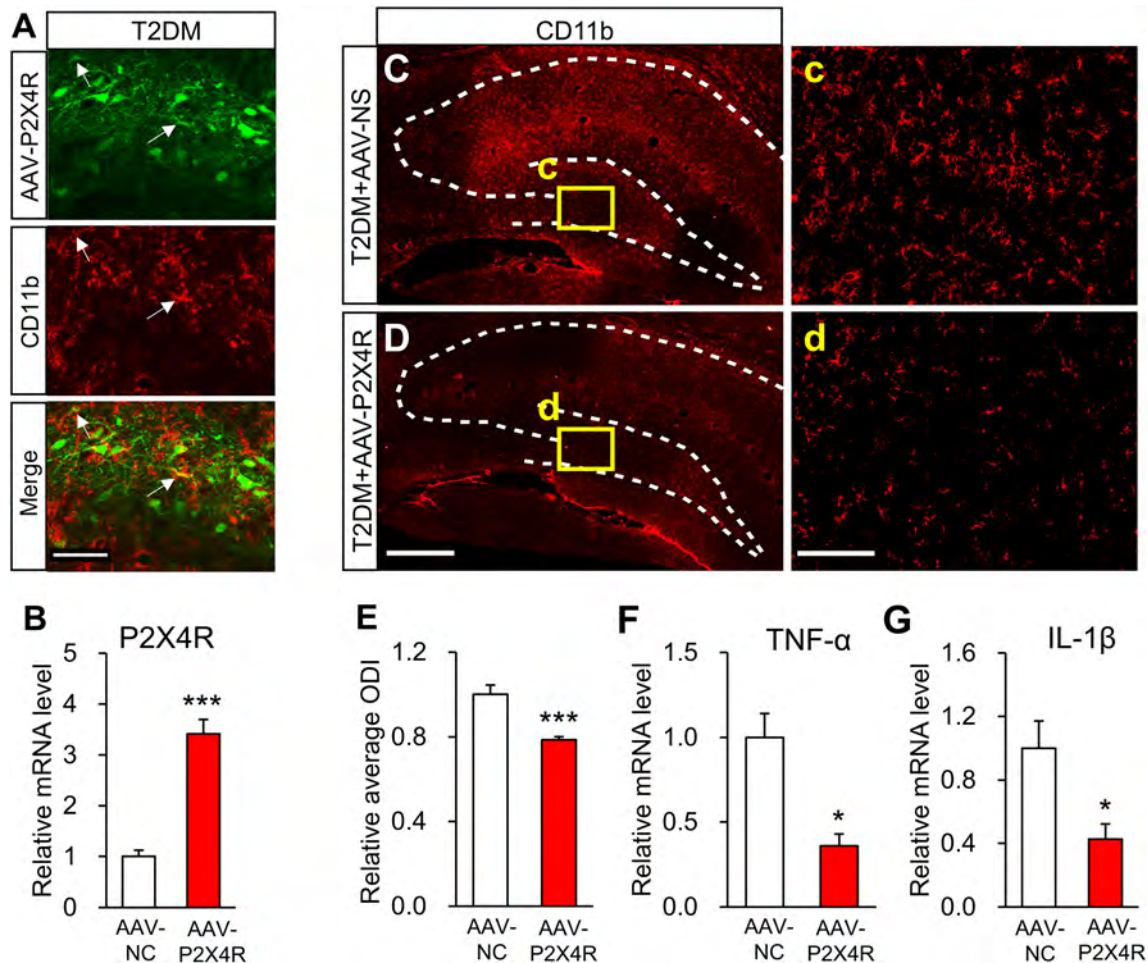
Fig. 8 Overexpression of P2X4Rs blocks the activation of microglia. **A** Representative images of AAV-P2X4R (green) and CD11b (red) staining in the hippocampus of a T2DM rat (arrows, co-localization of AAV-P2X4R and CD11b; broken lines outline the hippocampus). **B** P2X4R expression after microinjection of AAV-P2X4R or AAV-NC ($n = 4$/group; ***$P < 0.001$ *vs* AAV-NC, two-sample *t*-test). **C–** **E** Representative images and statistics of activated microglia labeled by CD11b in the hippocampus of T2DM rats injected with AAV-P2X4R or AAV-NC (scale bars, 500 μm in **D**, 100 μm in **d**; $n = 4$/group; ***$P < 0.001$ *vs* AAV-NC, two-sample *t*-test). **F**, **G** TNF-α and IL-1β mRNA levels after AAV-P2X4R injection ($n = 4$/group; *$P < 0.05$ *vs* AAV-NC, two-sample *t*-test).

Above all, these data indicated that P2X4R overexpression can effectively inhibit activated microglia.

Overexpression of P2X4Rs Rescues Memory in T2DM Rats

Four weeks after microinjection of AAV-P2X4R, we assessed rat behaviors in the MWM. Tracking showed that T2DM rats injected with AAV-P2X4R moved around the platform position, but those injected with AAV-NC did not improve (Fig. 9A). Although the two groups did not differ in the learning exercise (Fig. 9B, C), the mean distance from the platform was remarkably lower in T2DM rats injected with AAV-P2X4R than in those injected with AAV-NC (Fig. 9D). In contrast, the time T2DM rats injected with AAV-P2X4R remained in the quadrant with the platform was longer than that of those injected with

AAV-NC (Fig. 9E), while the passing times did not improve (Fig. 9F). These data demonstrated that P2X4R overexpression markedly improves the spatial memory of T2DM rats.

Discussion

T2DM is associated with an increased risk of AD and vascular dementia induced by increasing oxidative stress, inflammation, impaired insulin, and amyloid metabolism [33]. Here, we showed that T2DM rats exhibited clear spatial memory impairment in the MWM and the DAT task, because they had fewer passing times and spent less time in the platform quadrant but traveled a greater distance than controls in the MWM probe test on day 6. However, there was no significant difference between
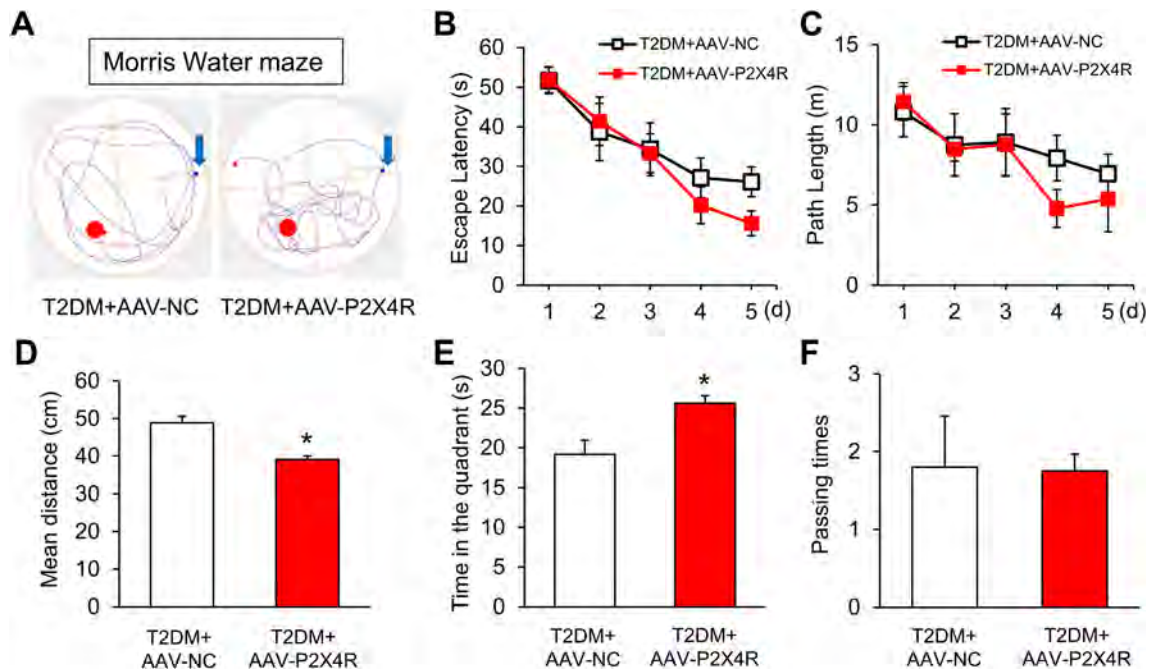
Fig. 9 P2X4R overexpression rescues memory in T2DM rats. **A** Tracking of T2DM rats injected with AAV-NC or AAV-P2X4R on day 6 in the MWM test. **B**, **C** Escape latency and path length in the MWM training trials of the two groups (n = 8/group; no significant difference, two-way ANOVA followed by Tukey's *post hoc* test). **D** Mean distance from the platform of T2DM rats injected with AAV-P2X4R or AAV-NC in the probe test on day 6 (n = 8/group; *$P < 0.05$ *vs* AAV-NC, two-sample *t*-test). **E** Time in the target quadrant of T2DM rats injected with AAV-P2X4R or AAV-NC (n = 8/group; *$P < 0.05$ *vs* AAV-NC, two-sample *t*-test). **F** Passing times of the two groups (n = 8/group; no significant difference, Mann-Whitney test).

T2DM rats and controls for finding the platform in the training period. One possible reason is that the diabetic rats might be in the early stages of cognitive dysfunction; this differs from patients who have suffered from diabetes for 10 years on average. In addition, greater learning intensity and density led to faster learning by control and T2DM rats, because the time they needed to find the platform both declined to ∼10 s on days 3–5 (Fig. 1I). It has been established that memory is strengthened in the hippocampus by the consolidation of new synaptic connections with the repeated learning of information [34]. So, it is possible that in the learning and training procedure, the hippocampus of T2DM rats produces new synaptic connections and temporary short-term memory, but these connections are not stable and long-term memory cannot be stored correctly.

In line with memory impairment, the P2X4R expression was significantly decreased at both the transcriptional and translational levels in the hippocampus of T2DM rats. The downregulation of P2X4R expression in the hippocampus seemed to be specific since there was no alteration in the expression of P2X4Rs in the BLA and ACC. These data suggested that P2X4Rs might be important in the development of the memory impairment of T2DM rats. This is consistent with other reports showing stronger long-term potentiation in the hippocampus of wild-type mice than

that in P2X4R-knockout mice [35, 36]. ATM, an important marker of DNA damage, was pronouncedly increased in the hippocampus of T2DM rats. So, we determined whether DNA damage is responsible for the P2X4R downregulation. Several methods can be used to detect DNA damage, such as the γH2AX signal [37], but they are all global tests. We used LA-PCR, a newly-developed technology, to precisely detect DNA damage on one specific gene [38]. Because a long fragment of nucleotides is more easily damaged than a short one, we designed specific primers for long and short fragments of the *p2x4r* gene. As expected, the long-PCR amplification of the *p2x4r* gene in the hippocampus of T2DM rats was significantly less than that in controls. These data strongly suggested that DNA damage of the *p2x4r* gene occurs in T2DM rats. However, how this damage happened was not clear. Accumulating studies have reported that oxidative stress can induce DNA damage [39–41]. We also found that the concentration of reactive oxygen species was dramatically increased in hippocampal neurons after 24 h of culture with high glucose (Fig. S1), indicating that diabetes may cause oxidative stress that leads to DNA damage. Above all, we demonstrated here that DNA damage is a novel regulatory mechanism of P2X4R expression in the hippocampus of T2DM rats.
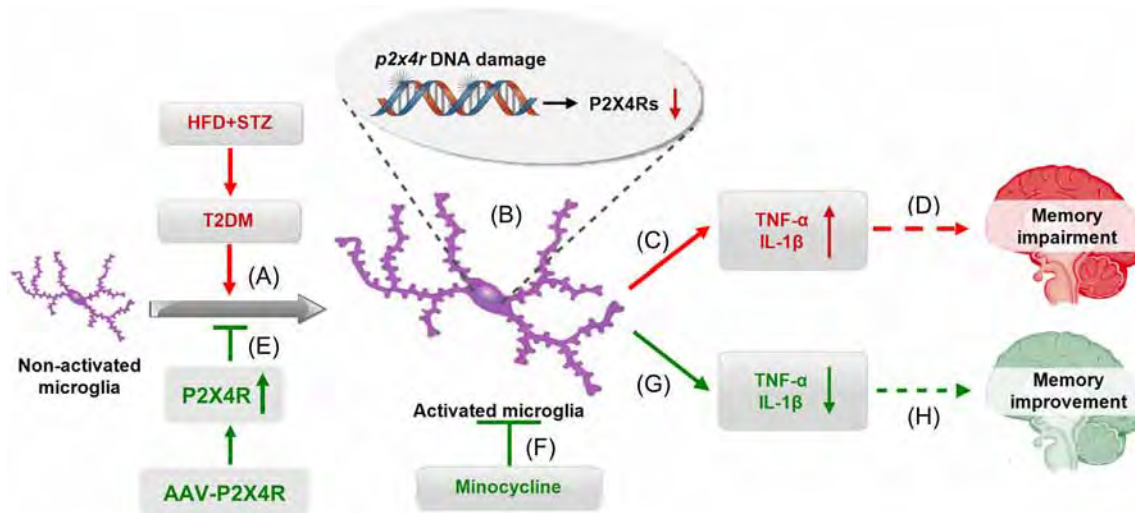
Fig. 10 Working hypothesis. **A** T2DM induces excessive activation of microglia in the hippocampus, likely mediated by downregulated P2X4R expression. **B** DNA damage of the *p2x4r* gene leads to downregulated P2X4R expression. **C** Excessive activation of microglia results in enhanced release of TNF-α and IL-1β. **D** The released inflammatory mediators eventually lead to memory impairment in T2DM rats, **E**, **G**, **H** P2X4R overexpression counteracts the microglial activation and decreases the expression of TNF-α and IL-1β, eventually rescuing the memory impairment of T2DM rats. **F**, **G**, **H** Intervention by inhibiting microglial activation with minocycline successfully improves memory in T2DM rats.

Since the mRNA level of P2X4Rs was significantly reduced in the hippocampus of T2DM rats (Fig. 5D), transcription of the *p2x4r* gene was inhibited. DNA methylation is one of the most common epigenetic mechanisms in the regulation of gene expression [42]. Our previous study showed that the expression of purinergic P2X3Rs is regulated by DNA methylation [43, 44]. Therefore, we took the methylation status of the *p2x4r* gene DNA into account. However, there were no CpG islands in the promoter of the *p2x4r* gene (Fig. S2). We therefore can exclude the involvement of DNA methylation and demethylation in the down-regulation of P2X4R expression in the hippocampus of T2DM rats. It is worth noting that other mechanisms of epigenetic regulation such as histone modification or non-coding RNAs need to be investigated in future.

Using immunofluorescence assays, we showed that P2X4Rs were specifically expressed in hippocampal microglia, indicating a role of microglia in the memory impairment of T2DM rats. Although the expression of P2X4Rs was decreased, the microglia were strongly activated in the hippocampus of T2DM rats. Once activated, microglia secrete a variety of inflammatory factors and we found that TNF-α and IL-1β were significantly increased in the hippocampus of T2DM rats (Fig. 2H, I). Treatment with minocycline, a microglia inhibitor, significantly reduced microglial activation and the expression of TNF-α and IL-1β (Fig. 3D, E), further supporting a role of microglia. More importantly, the mean distance from the platform after minocycline treatment was markedly

decreased in T2DM rats (Fig. 4D). Therefore, over-activated microglia in the hippocampus are indeed involved in the memory impairment of T2DM rats. Microglia have the capacity to release a large number of substances that can be detrimental to surrounding neurons, including glutamate, ATP, and reactive oxygen species. However, how altered neurotransmission following acute insults or chronic neurodegenerative conditions modulates neuronal functions is still poorly understood [23]. Besides, microglia have been demonstrated to play opposing roles in the regulation of synaptic plasticity in the spinal cord and hippocampus [45–47]. Indeed, microglia show a variety of different properties even in the sub-nuclei of the basal ganglia [48]. This warrants further investigation into the detailed mechanism by which over-reaction of microglia induces memory impairment in T2DM rats.

In order to investigate whether the microglial over-reaction is mediated by downregulation of P2X4R expression, we designed two crucial experiments. First, we overexpressed P2X4Rs by AAV microinjection into the hippocampus of T2DM rats, and found that AAV co-localized with some CD11b-positive microglia in addition to neurons (Fig. 8A). Although we cannot exclude an exogenous role of P2X4R in neurons, we showed for the first time that overexpression of P2X4Rs dramatically suppressed the microglial activation and the mRNA levels of TNF-α and IL-1β in the hippocampus of T2DM rats, indicating that the P2X4R is an upstream signaling molecule in the regulation of microglial activation. Encouraged, we performed the second experiment to

further confirm this by examination of P2X4R expression after administration of minocycline. Since minocycline did not affect the expression of P2X4Rs, it is reasonable to assume that downregulation of P2X4R expression might be an upstream mechanism underlying the activation of microglial cells. This is consistent with the previous report that P2X4Rs determine the fate of microglia, especially in the early stage of controlling the apoptosis of activated microglia [24]. Our findings also suggest that decreased P2X4Rs are not able to regulate the apoptosis of activated microglia, which results in their excessive activation. However, the mechanism of suppression of activated microglia by P2X4R overexpression is elusive. Conversely, overexpression of P2X4Rs remarkably improved the memory of T2DM rats. This is a very important finding that provides strong evidence for the development of novel strategies for the treatment of memory disorders. Recently, reports have shown that P2X4-deficient mice exhibit sociocommunicative and sensorimotor impairments [49], and that P2X4Rs favor remyelination in autoimmune encephalitis [50]. Taken together, our findings highlight a putative role of P2X4Rs in the regulation of memory functions in T2DM patients. In addition, P2Y12R is a microglial signature gene and participates in normal brain function and diseases [51–53]. Whether P2Y12R contributes to the memory impairment of T2DM rats deserves further investigation.

Taken together, we conclude that: T2DM causes DNA damage to the *p2x4r* gene and the downregulation of P2X4R expression, resulting in the over-activation of microglia in the hippocampus, thus contributing to memory impairment in T2DM rats induced by an HFD and STZ injection. P2X4R over-expression or minocycline treatment improves memory in T2DM rats by blocking microglial activation (Fig. 10). These findings provide promising clues for the development of new therapeutic strategies for managing memory impairment in patients with type 2 diabetes.

Conflict of interest No conflicts of interest, financial or otherwise, are declared by the authors.

References

1. Xu L, Li Y, Dai Y, Peng J. Natural products for the treatment of type 2 diabetes mellitus: Pharmacology and mechanisms. Pharmacol Res 2018, 130: 451–465.
2. Aye-Mon A, Hori K, Kozakai Y, Nakagawa T, Hiraga S, Nakamura T*, et al.* CCR2 upregulation in DRG neurons plays a crucial role in gastric hyperalgesia associated with diabetic gastropathy. Mol Pain 2018, 14: 1744806917751322.
3. Guariguata L, Whiting DR, Hambleton I, Beagley J, Linnenkamp U, Shaw JE. Global estimates of diabetes prevalence for 2013 and projections for 2035. Diabetes Res Clin Pract 2014, 103: 137–149.
4. Arvanitakis Z, Wilson RS, Bienias JL, Evans DA, Bennett DA. Diabetes mellitus and risk of Alzheimer disease and decline in cognitive function. Arch Neurol 2004, 61: 661–666.
5. Bergantin LB. Debating the "bidirectional link" between diabetes and depression through the Ca(2+)/cAMP signalling: Off-label effects of Ca(2+) channel blockers. Pharmacol Res 2019, 141: 298–302.
6. McCrimmon RJ, Ryan CM, Frier BM. Diabetes and cognitive dysfunction. Lancet 2012, 379: 2291–2299.
7. Gudala K, Bansal D, Schifano F, Bhansali A. Diabetes mellitus and risk of dementia: A meta-analysis of prospective observational studies. J Diabetes Investig 2013, 4: 640–650.
8. Biessels GJ, Reagan LP. Hippocampal insulin resistance and cognitive dysfunction. Nat Rev Neurosci 2015, 16: 660–671.
9. Wei YP, Ye JW, Wang X, Zhu LP, Hu QH, Wang Q*, et al.* Tau-induced Ca(2+)/calmodulin-dependent protein kinase-IV activation aggravates nuclear tau hyperphosphorylation. Neurosci Bull 2018, 34: 261–269.
10. Ahtiluoto S, Polvikoski T, Peltonen M, Solomon A, Tuomilehto J, Winblad B*, et al.* Diabetes, Alzheimer disease, and vascular dementia: a population-based neuropathologic study. Neurology 2010, 75: 1195–1202.
11. Nelson PT, Smith CD, Abner EA, Schmitt FA, Scheff SW, Davis GJ*, et al.* Human cerebral neuropathology of Type 2 diabetes mellitus. Biochim Biophys Acta 2009, 1792: 454–469.
12. Schneider JA, Arvanitakis Z, Bang W, Bennett DA. Mixed brain pathologies account for most dementia cases in community-dwelling older persons. Neurology 2007, 69: 2197–2204.
13. Donath MY. Targeting inflammation in the treatment of type 2 diabetes: time to start. Nat Rev Drug Discov 2014, 13: 465–476.
14. Balducci C, Forloni G. Novel targets in Alzheimer's disease: A special focus on microglia. Pharmacol Res 2018, 130: 402–413.
15. Erion JR, Wosiski-Kuhn M, Dey A, Hao S, Davis CL, Pollock NK*, et al.* Obesity elicits interleukin 1-mediated deficits in hippocampal synaptic plasticity. J Neurosci 2014, 34: 2618–2631.
16. Fang X, Sun D, Wang Z, Yu Z, Liu W, Pu Y*, et al.* MiR-30a positively regulates the inflammatory response of microglia in experimental autoimmune encephalomyelitis. Neurosci Bull 2017, 33: 603–615.
17. Nimmerjahn A, Kirchhoff F, Helmchen F. Resting microglial cells are highly dynamic surveillants of brain parenchyma *in vivo*. Science 2005, 308: 1314–1318.
18. Li D, Zhang L, Huang X, Liu L, He Y, Xu L*, et al.* WIP1 phosphatase plays a critical neuroprotective role in brain injury

induced by high-altitude hypoxic inflammation. Neurosci Bull 2017, 33: 292–298.

19. Riazi K, Galic MA, Kentner AC, Reid AY, Sharkey KA, Pittman QJ. Microglia-dependent alteration of glutamatergic synaptic transmission and plasticity in the hippocampus during peripheral inflammation. J Neurosci 2015, 35: 4942–4952.

20. Fricker M, Oliva-Martin MJ, Brown GC. Primary phagocytosis of viable neurons by microglia activated with LPS or Abeta is dependent on calreticulin/LRP phagocytic signalling. J Neuroinflammation 2012, 9: 196.

21. Guthrie PB, Knappenberger J, Segal M, Bennett MV, Charles AC, Kater SB. ATP released from astrocytes mediates glial calcium waves. J Neurosci 1999, 19: 520–528.

22. Zhang PA, Xu QY, Xue L, Zheng H, Yan J, Xiao Y, et al. Neonatal maternal deprivation enhances presynaptic p2x7 receptor transmission in insular cortex in an adult rat model of visceral hypersensitivity. CNS Neurosci Ther 2017, 23: 145–154.

23. Domercq M, Vazquez-Villoldo N, Matute C. Neurotransmitter signaling in the pathophysiology of microglia. Front Cell Neurosci 2013, 7: 49.

24. Vazquez-Villoldo N, Domercq M, Martin A, Llop J, Gomez-Vallejo V, Matute C. P2X4 receptors control the fate and survival of activated microglia. Glia 2014, 62: 171–184.

25. Mansor LS, Gonzalez ER, Cole MA, Tyler DJ, Beeson JH, Clarke K, et al. Cardiac metabolism in a new rat model of type 2 diabetes using high-fat diet with low dose streptozotocin. Cardiovasc Diabetol 2013, 12: 136.

26. Adembri C, Selmi V, Vitali L, Tani A, Margheri M, Loriga B, et al. Minocycline but not tigecycline is neuroprotective and reduces the neuroinflammatory response induced by the superimposition of sepsis upon traumatic brain injury. Crit Care Med 2014, 42: e570–582.

27. Shu H, Zheng GQ, Wang X, Sun Y, Liu Y, Weaver JM, et al. Activation of matrix metalloproteinase in dorsal hippocampus drives improvement in spatial working memory after intra-VTA nicotine infusion in rats. J Neurochem 2015, 135: 357–367.

28. Singh S, Kaur H, Sandhir R. Fractal dimensions: A new paradigm to assess spatial memory and learning using Morris water maze. Behav Brain Res 2016, 299: 141–146.

29. Fu P, Tang R, Yu Z, Li C, Chen X, Xie M, et al. Rho-associated kinase inhibitors promote microglial uptake via the erk signaling pathway. Neurosci Bull 2016, 32: 83–91.

30. Kong X, Wei J, Wang D, Zhu X, Zhou Y, Wang S, et al. Upregulation of spinal voltage-dependent anion channel 1 contributes to bone cancer pain hypersensitivity in rats. Neurosci Bull 2017, 33: 711–721.

31. Tsuda M, Shigemoto-Mogami Y, Koizumi S, Mizokoshi A, Kohsaka S, Salter MW, et al. P2X4 receptors induced in spinal microglia gate tactile allodynia after nerve injury. Nature 2003, 424: 778–783.

32. Tatsch E, De Carvalho JA, Hausen BS, Bollick YS, Torbitz VD, Duarte T, et al. Oxidative DNA damage is associated with inflammatory response, insulin resistance and microvascular complications in type 2 diabetes. Mutat Res 2015, 782: 17–22.

33. Biessels GJ, Deary IJ, Ryan CM. Cognition and diabetes: a lifespan perspective. Lancet Neurol 2008, 7: 184–190.

34. Antony JW, Paller KA. Retrieval and sleep both counteract the forgetting of spatial information. Learn Mem 2018, 25: 258–263.

35. Sim JA, Chaumont S, Jo J, Ulmann L, Young MT, Cho K, et al. Altered hippocampal synaptic potentiation in P2X4 knock-out mice. J Neurosci 2006, 26: 9006–9009.

36. Baxter AW, Choi SJ, Sim JA, North RA. Role of P2X4 receptors in synaptic strengthening in mouse CA1 hippocampal neurons. Eur J Neurosci 2011, 34: 213–220.

37. Zeng Y, Shen Y, Hong L, Chen Y, Shi X, Zeng Q, et al. Effects of single and repeated exposure to a 50-Hz 2-mT electromagnetic field on primary cultured hippocampal neurons. Neurosci Bull 2017, 33: 299–306.

38. Gonzalez-Hunt CP, Rooney JP, Ryde IT, Anbalagan C, Joglekar R, Meyer JN. PCR-based analysis of mitochondrial DNA copy number, mitochondrial DNA damage, and nuclear DNA damage. Curr Protoc Toxicol 2016, 67: 201121–201125.

39. Lindahl T. Instability and decay of the primary structure of DNA. Nature 1993, 362: 709–715.

40. Sung HJ, Ma W, Wang PY, Hynes J, O'Riordan TC, Combs CA, et al. Mitochondrial respiration protects against oxygen-associated DNA damage. Nat Commun 2010, 1: 5.

41. Cadet J, Ravanat JL, TavernaPorro M, Menoni H, Angelov D. Oxidatively generated complex DNA damage: tandem and clustered lesions. Cancer Lett 2012, 327: 5–15.

42. Tost J. Current and emerging technologies for the analysis of the genome-wide and locus-specific DNA methylation patterns. Adv Exp Med Biol 2016, 945: 343–430.

43. Zhang HH, Hu J, Zhou YL, Qin X, Song ZY, Yang PP, et al. Promoted interaction of nuclear factor-kappab with demethylated purinergic P2X3 receptor gene contributes to neuropathic pain in rats with diabetes. Diabetes 2015, 64: 4272–4284.

44. Zhou YL, Jiang GQ, Wei J, Zhang HH, Chen W, Zhu H, et al. Enhanced binding capability of nuclear factor-kappaB with demethylated P2X3 receptor gene contributes to cancer pain in rats. Pain 2015, 156: 1892–1905.

45. Liu Y, Zhou LJ, Wang J, Li D, Ren WJ, Peng J, et al. TNF-alpha differentially regulates synaptic plasticity in the hippocampus and spinal cord by microglia-dependent mechanisms after peripheral nerve injury. J Neurosci 2017, 37: 871–881.

46. Tsuda M. Modulation of pain and itch by spinal glia. Neurosci Bull 2018, 34: 178–185.

47. Lee S, Shi XQ, Fan A, West B, Zhang J. Targeting macrophage and microglia activation with colony stimulating factor 1 receptor inhibitor is an effective strategy to treat injury-triggered neuropathic pain. Mol Pain 2018, 14: 1744806918764979.

48. De Biase LM, Schuebel KE, Fusfeld ZH, Jair K, Hawes IA, Cimbro R, et al. Local cues establish and maintain region-specific phenotypes of basal ganglia microglia. Neuron 2017, 95: 341–356 e346.

49. Wyatt LR, Godar SC, Khoja S, Jakowec MW, Alkana RL, Bortolato M, et al. Sociocommunicative and sensorimotor impairments in male P2X4-deficient mice. Neuropsychopharmacology 2013, 38: 1993–2002.

50. Zabala A, Vazquez-Villoldo N, Rissiek B, Gejo J, Martin A, Palomino A, et al. P2X4 receptor controls microglia activation and favors remyelination in autoimmune encephalitis. EMBO Mol Med 2018. https://doi.org/10.15252/emmm.201708743.

51. Eyo UB, Gu N, De S, Dong H, Richardson JR, Wu LJ. Modulation of microglial process convergence toward neuronal dendrites by extracellular calcium. J Neurosci 2015, 35: 2417–2422.

52. Peng J, Liu Y, Umpierre AD, Xie M, Tian DS, Richardson JR, et al. Microglial P2Y12 receptor regulates ventral hippocampal CA1 neuronal excitability and innate fear in mice. Mol Brain 2019, 12: 71.

53. Qin C, Zhou LQ, Ma XT, Hu ZW, Yang S, Chen M, et al. Dual functions of microglia in ischemic stroke. Neurosci Bull 2019, 35: 921–933.

www.neurosci.cn
www.springer.com/12264

ORIGINAL ARTICLE

BDNF Overexpression Enhances the Preconditioning Effect of Brief Episodes of Hypoxia, Promoting Survival of GABAergic Neurons

M. V. Turovskaya[1] · S. G. Gaidin[1] · M. V. Vedunova[2] · A. A. Babaev[2] ·
E. A. Turovsky[1]

Abstract Hypoxia causes depression of synaptic plasticity, hyperexcitation of neuronal networks, and the death of specific populations of neurons. However, brief episodes of hypoxia can promote the adaptation of cells. Hypoxic preconditioning is well manifested in glutamatergic neurons, while this adaptive mechanism is virtually suppressed in GABAergic neurons. Here, we show that brain-derived neurotrophic factor (BDNF) overexpression in neurons enhances the preconditioning effect of brief episodes of hypoxia. The amplitudes of the NMDAR- and AMPAR-mediated Ca^{2+} responses of glutamatergic and GABAergic neurons gradually decreased after repetitive brief hypoxia/reoxygenation cycles in cell cultures transduced with the (AAV)-Syn-BDNF-EGFP virus construct. In contrast, the amplitudes of the responses of GABAergic neurons increased in non-transduced cultures after preconditioning. The decrease of the amplitudes in GABAergic neurons indicated the activation of mechanisms of hypoxic preconditioning. Preconditioning suppressed apoptotic or necrotic cell death. This effect was most pronounced in cultures with BDNF overexpression. Knockdown of BDNF abolished the effect of preconditioning and promoted the death of GABAergic neurons. Moreover, the expression of the anti-apoptotic genes Stat3, Socs3, and Bcl-xl substantially increased 24 h after hypoxic episodes in the transduced cultures compared to controls. The expression of genes encoding the pro-inflammatory cytokines IL-10 and IL-6 also increased. In turn, the expression of pro-apoptotic (Bax, Casp-3, and Fas) and pro-inflammatory (IL-1β and TNFα) genes decreased after hypoxic episodes in cultures with BDNF overexpression. Inhibition of vesicular BDNF release abolished its protective action targeting inhibition of the oxygen-glucose deprivation (OGD)-induced $[Ca^{2+}]_i$ increase in GABAergic and glutamatergic neurons, thus promoting their death. Bafilomycin A1, Brefeldin A, and tetanus toxin suppressed vesicular release (including BDNF) and shifted the gene expression profile towards excitotoxicity, inflammation, and apoptosis. These inhibitors of vesicular release abolished the protective effects of hypoxic preconditioning in glutamatergic neurons 24 h after hypoxia/reoxygenation cycles. This finding indicates a significant contribution of vesicular BDNF release to the development of the mechanisms of hypoxic preconditioning. Thus, our results demonstrate that BDNF plays a pivotal role in the activation and enhancement of the preconditioning effect of brief episodes of hypoxia and promotes tolerance of the most vulnerable populations of GABAergic neurons to hypoxia/ischemia.

✉ E. A. Turovsky
turovsky.84@mail.ru

[1] Institute of Cell Biophysics of the Russian Academy of Sciences, Federal Research Center "Pushchino Scientific Center for Biological Research of the Russian Academy of Sciences", Pushchino, Russia

[2] Institute of Biology and Biomedicine, Lobachevsky State University of Nizhny Novgorod, Nizhny Novgorod, Russia

Introduction

Many cardiovascular diseases such as angina, myocardial infarction, cardiac insufficiency, and peripheral arteriolar constriction are followed by hypoxia. Hypoxic conditions

Springer

and ischemia are caused by arterial occlusion and anatomical capillary rarefaction due to hypertension. Hypoxia also occurs during rapid tissue growth during organogenesis or cancer tumor formation, chronic inflammation, and altitude sickness [1].

Oxygen consumption by the mammalian brain is very high, accounting for 20% of body oxygen consumption [2]. This metabolic peculiarity makes brain cells particularly sensitive to hypoxia. Acute episodes of hypoxia depress synaptic activity, while prolonged exposure to hypoxia leads to the death of neurons [3]. Episodes of ischemia that last > 2 min can lead to the death of neurons [4], especially GABAergic neurons without Ca^{2+}-binding proteins [5, 6].

On the contrary, positive effects of brief hypoxia have also been reported. For instance, low oxygen tension promotes the proliferation of endothelial cells [7] and angiogenesis [8], thus ameliorating tissue hypoxia. Such positive effects are tightly coupled to the phenomenon of hypoxic preconditioning (HP), which is considered to be an efficient approach to reducing the vulnerability of tissues and organs to prolonged hypoxia/ischemia-reoxygenation episodes. The approach consists of a single [9] or repetitive brief episodes of hypoxia followed by reoxygenation [10, 11]. HP can be divided into two types—rapid and delayed—according to the time interval between the stimulus and the development of adaptation. Rapid HP develops in the range from minutes to some hours after sublethal hypoxia. This type of HP is mediated by changes in the conductivity of ion channels and the phosphorylation of proteins and their post-translational modification [12–15]. On the contrary, delayed HP requires gene expression and de novo protein synthesis. The effects of delayed HP can be detected some hours or days after the stimulus. Delayed HP involves the activation of genes that promote tolerance of the brain to ischemia, suppression of the mechanisms of cell damage, and enhancement of the mechanisms of cell survival [16].

HP for neuroprotection was first used in 1986 [12]. Brain slices and primary cell cultures from different brain regions are used as in vitro models of HP in brain research [17, 18]. It has been shown that a single 2-min and three repetitive 1-min episodes of anoxia (in slices of the olfactory cortex and hippocampus, respectively) increase the tolerance of cells to prolonged anoxia, inhibit the depression of evoked potentials, and suppress global Ca^{2+} increases. Interestingly, a moderate increase in intracellular Ca^{2+} concentration ($[Ca^{2+}]_i$) is necessary for the induction of HP in both models [19]. We have previously described a cellular model that includes three brief (3-min) episodes of hypoxia followed by three 10-min reoxygenation periods. This model allows detection of the development of HP in neurons by changes in the amplitudes of Ca^{2+} responses to

the application of agonists. It is also possible to detect post-hypoxic hyperexcitation by the appearance of spontaneous Ca^{2+} signals, which can promote the death of some neuronal populations during reoxygenation [20].

The role of neurotrophic factors in the protection of cells against ischemia and activation of the mechanisms of preconditioning has been studied in the past few years. Brain-derived neurotrophic factor (BDNF) is the most common neurotrophin in the brain, and its expression is affected by many external and internal factors. Altered BDNF expression occurs under ischemia, hypoxia, brain trauma, and various stresses. It regulates neurotransmission and cell survival via the activation of different receptors [21]. We have previously shown that BDNF overexpression alters the expression of genes that regulate neurotransmission, inflammation, and apoptosis, thus protecting hippocampal cells against death under oxygen-glucose deprivation (OGD) and glutamate toxicity [22].

It has been shown that preconditioning of rats with three episodes of moderate hypoxia evokes an increase in the BDNF level one day later and promotes their tolerance to traumatic injury. HP stimulates BDNF expression in a long-term manner in the neocortex and hippocampus in a model of post-traumatic stress disorder-associated anxiety [23], however, the protective effects of BDNF overexpression on different populations of neurons have not yet been investigated, while the mechanisms and signaling pathways involved in HP formation in GABAergic neurons remain unclear. Taking into account the peculiar vulnerability of GABAergic neurons to hypoxia and their role in the regulation of neuronal network activity, it can be concluded that studying the mechanisms of HP formation in this population of neurons is an important issue. Thus, the present study was designed to investigate the effects of BDNF overexpression on the activation and enhancement of HP in glutamatergic and GABAergic neurons.

Materials and Methods

Animals and Reagents

All animal studies were performed in accordance with legal requirements and were approved by the Animal Ethics Committees of the Institute of Cell Biophysics, Russian Academy of Sciences. Pregnant female Sprague-Dawley rats were housed in the animal facility of the Institute of Cell Biophysics, Russian Academy of Sciences, at 25 ± 3°C with a 12-h light/dark cycle and free access to food and water.

Reagents included 5-fluorowillardiine, N-methyl-D-aspartate (NMDA), bafilomycin A1 (BafA1), brefeldin A (BFA), sodium dithionite (Tocris Bioscience, Bristol, UK);

KCl, tetanus toxin (TeNT), paraformaldehyde, poly(ethyleneimine), adenosine 5′-triphosphate disodium salt hydrate (ATP) (Sigma-Aldrich, St. Louis, MO); Fura-2AM, Hoechst 33342, propidium iodide (Thermo Fisher Scientific, Waltham, MA); Neurobasal-A medium, B-27 supplement, trypsin (1%) (Life Technologies, Grand Island, NY); donkey serum, mouse anti-NeuN antibodies, chicken anti-BDNF antibodies, donkey anti-rabbit Alexa Fluor-488- and Alexa Fluor-555- conjugated antibodies, donkey anti-mouse Alexa Fluor-647- conjugated antibodies, and donkey anti-chicken Alexa Fluor-488- conjugated antibodies (Abcam, Cambridge, UK).

Preparation of Mixed Hippocampal Neuroglial Cell Cultures

Cell cultures were prepared as described in detail previously [5]. Briefly, 0–1 day-old pups were euthanized by halothane overdose and decapitated. The extracted hippocampus was washed with Mg^{2+}- and Ca^{2+}-free Versene solution and minced with scissors. Then, the tissue fragments were digested in 1% trypsin for 10 min at 37 °C and washed twice with cold Neurobasal-A medium. The trypsinized tissue was gently triturated with a pipette, and the debris was then carefully removed with a pipette tip. The cell suspension was seeded on polyethyleneimine-coated glass coverslips and grown for 10–12 days in Neurobasal-A medium supplemented with 2% B-27 and 0.5 mmol/L glutamine.

References [5, 25, 26] BafA1, BFA, and TeNT were added to the medium under sterile conditions in experiments with 24-h pre-incubation. Then, the cultures were washed with Hank's balanced salt solution (HBSS) containing inhibitors and used in experiments.

Induction of BDNF Overexpression in Neurons

Mixed neuroglial hippocampal cell cultures were transduced with the (AAV)-Syn-BDNF-EGFP virus vector to induce BDNF overexpression in neurons. The structure of this adeno-associated viral construct was described previously [24]. To achieve selective BDNF overexpression in neurons, the human synapsin (hSyn) promoter sequence was incorporated into the vector. The (AAV)-Syn-BDNF-EGFP construct was added to cultures at 4–5 days *in vitro* (DIV) (construct dilution 1:125). BDNF overexpression occurred mainly in hippocampal neurons 24 h after transduction (Fig. S1) and was maintained until 10–12 DIV.

Ca^{2+} Fluorescence Measurements

To assess the changes in $[Ca^{2+}]_i$, hippocampal cell cultures were loaded with Fura-2 (4 µmol/L, 40-min incubation at

37°C). The cells were stained with the probe dissolved in HBSS composed of (in mmol/L): 156 NaCl, 3 KCl, 2 $MgSO_4$, 1.25 KH_2PO_4, 2 $CaCl_2$, 10 glucose, and 10 HEPES, pH 7.4. To measure $[Ca^{2+}]_i$, we used a system based on an inverted motorized microscope (Leica Microsystems, Wetzlar, Germany; DMI6000B) with a high-speed monochrome CCD-camera Hamamatsu C9100 (Hamamatsu Photonics, Hamamatsu City, Japan). For excitation and registration of Fura-2 fluorescence, we used the FU-2 filter set (Leica Microsystems, Wetzlar, Germany) with excitation filters (BP340/30 and BP387/15), a beam-splitter (FT-410), and an emission filter (BP510/84). An illuminator with a high-pressure mercury lamp (Leica EL6000) was used as the source of excitation. To distinguish neurons from astrocytes, we briefly applied 35 mmol/L KCl and 10 µmol/L ATP before the main experiments. This method has been described in detail in our previous report References [5, 25, 26]. Briefly, KCl depolarizes excitable cells that contain a wide range of voltage-gated cation channels. The KCl-induced depolarization promotes the opening of voltage-gated Ca^{2+} channels (predominantly L-type channels) in neurons. The KCl-induced increase in $[Ca^{2+}]_i$ is easily detected with Ca^{2+}-sensitive fluorescent probes such as Fura-2 and Fluo-4. The Ca^{2+} responses of neurons were characterized by rapid rising and slow decay phases. The conductivity and density of cation channels in astrocytes are insufficient to evoke a high-amplitude Ca^{2+} response to KCl. In turn, the ATP-induced biphasic Ca^{2+} response, which is mediated by ionotropic and metabotropic purinergic receptors, occurs mainly in astrocytes due to the rich repertoire of P2X and P2Y receptors, while the response of neurons to ATP is negligible. The ratio of neurons to glial cells was determined by immunostaining with antibodies against NeuN. This ratio was 1:3 for our protocol of cell culture preparation. All the Ca^{2+} signals are presented as the 340/380 ratio of Fura-2 fluorescence.

Techniques for Modeling Brief Hypoxic Episodes and Prolonged Oxygen-glucose Deprivation (OGD)

To model hypoxic conditions, we used HBSS with a low concentration of dissolved O_2. The HBSS was purged for 15 min with argon in a special hermetic system to displace O_2. O_2 tension was measured with a Clark electrode and reached 50–60 mmHg, corresponding to moderate hypoxia. Each hypoxia/reoxygenation cycle consisted of a 3-min episode of hypoxia when the hypoxic medium was added to the experimental chamber with the hippocampal cell culture and a 10-min reoxygenation episode when the cultures were washed with HBSS containing the normal concentration of dissolved O_2. α-Amino-3-hydroxy-5-methylisoxazole-4-propionic acid receptor (AMPAR) or

736

Neurosci. Bull. July, 2020, 36(7):733–760

NMDAR agonists were applied briefly (30 s) after each hypoxia/reoxygenation cycle. The drugs were added at 10 L/min using a specially-designed perfusion system. The volume of medium in the experimental chamber was 500 μL, and excess liquid was drained with a water-jet pump. Inlet and outlet pipes were installed on the opposite sides of the experimental chamber. Using a colored solution, we determined that complete replacement of the bathing solution in the chamber occurred 20–30 s after the start of perfusion. This system allowed the short-term and long-term application of drugs. Control experiments established that the responses of cells to mechanical stimulation caused by the fluid flow during drug application were negligible or absent.

The development of the preconditioning effect was estimated by the changing amplitudes of NMDA-induced Ca^{2+} responses after hypoxia/reoxygenation cycles. The amplitudes of the Ca^{2+} responses to NMDA application before and after three episodes of hypoxia/reoxygenation were calculated for all analyzed neurons, and the values were presented in a coordinate plane (X-axis, amplitude before hypoxia; Y-axis, amplitude after hypoxia). Then the data points were approximated by linear regression. The slopes of the regression lines were used to estimate the preconditioning effect of hypoxic episodes. A decrease in the slope indicated the development of preconditioning. To investigate the protective effects of HP, the cultures were returned to a CO_2 incubator after three episodes of hypoxia/reoxygenation and then used in OGD experiments 24 h after preconditioning.

In turn, to model ischemia-like conditions, glucose was displaced by an equivalent quantity of sucrose (HBSS without glucose). O_2 tension in the medium reached 30–40 mmHg and the OGD lasted for 40 min. To prevent contact of the medium with atmospheric O_2, we used a constant argon feed into the experimental chamber during brief episodes of hypoxia or prolonged OGD. In some experiments (Fig. 4), the cultures were returned to the CO_2 incubator for 24 h after OGD, and the ischemic medium was replaced by standard culture medium.

To create OGD conditions in release experiments, complete HBSS was replaced by glucose-free HBSS (glucose replaced by an osmotically equivalent concentration of sucrose) 1.5–2 min before the experiment. Then, the O_2-scavenger sodium dithionite (30 μg/mL) was added to the medium during the measurement of EGFP fluorescence to remove dissolved O_2. This dose of sodium dithionite removes O_2 without changing the pH, which has been established using Blood Gas Electrolyte Analyzer (Siemens Healthineers, Erlangen, Germany).

Immunocytochemistry

Coverslips with hippocampal cell cultures were mounted in the experimental chamber. A marker grid was plotted on the bottom of each coverslip. The chamber was placed on the microscope stage, and a grid-bordered area was randomly selected for fluorescent Ca^{2+} imaging. Then the cells were fixed and stained with antibodies according to the previously-described protocol [22]. Briefly, the cells were rinsed with Ca^{2+}- and Mg^{2+}-free phosphate-buffered saline (PBS) and fixed for 20 min in 4% paraformaldehyde and 0.25% glutaraldehyde diluted in PBS. After that, the cells were rinsed thrice in ice-cold PBS and permeabilized with 0.1% Triton X-100. Then, the cells were incubated for 30 min with 10% donkey serum (in PBS) to block non-specific binding of the secondary antibodies and stained overnight at 4°C with primary antibodies diluted in 1% donkey serum. We used mouse anti-NeuN antibodies (1:200; Abcam) to identify neurons and rabbit anti-glutamate decarboxylase 65/67 (GAD65/67) antibodies (1:500; Abcam) to discriminate GABAergic neurons. Chicken anti-BDNF antibodies (1:150; Abcam) were used to determine the level of BDNF in cells. The cells were rinsed thrice with PBS after incubation with the primary antibodies and stained with secondary antibodies. We used secondary donkey anti-rabbit Alexa Fluor-488- or Alexa Fluor-555-conjugated (1:200; Abcam), donkey anti-mouse Alexa Fluor-647-conjugated (1:200; Abcam), and donkey anti-chicken Alexa Fluor-488-conjugated antibodies (1:200; Abcam). Fluorescence of the conjugated dyes was detected with a Leica TCS SP5 confocal microscope in the grid-bordered areas chosen for Ca^{2+} imaging. The confocal images of cell cultures stained with the antibodies were matched with the images of the same cultures captured during vital Ca^{2+} imaging. Thus, the combination of vital Ca^{2+} imaging and immunostaining allowed us to obtain data about Ca^{2+} dynamics in NeuN-positive or GAD65/67-positive cells.

Assessment of BDNF Release

BDNF release in cultures transduced with the (AAV)-BDNF-EGFP construct was assessed as a decrease of EGFP fluorescence in the processes and somata of neurons using the Leica TCS SP5 confocal microscope. EGFP fluorescence was excited with a 488-nm argon laser and detected in the 505–575 nm range. High-resolution images were captured using a Leica HCX PL APO lambda blue 63.0 × 1.40 oil objective. Time-lapse series were recorded at a rate of 1 scan per 10 s. The depth of each optical slice was ∼ 2 μm. To avoid phototoxicity, the laser power was set to the minimum (1%–4% of laser output).

Cell Viability Test

Hoechst 33342 (2 µmol/L) and propidium iodide (1 µmol/L) were used to evaluate the number of dead cells in cultures before and after OGD. The cells were stained for 5 min with the probes diluted in HBSS and then rinsed in HBSS. The fluorescence of the probes was detected with an inverted fluorescence microscope (Zeiss Axio Observer Z1) using Filter Sets 01 and 20. Early and late apoptotic cells were discriminated using a previously-described method [22, 27]. Five different areas in each culture were analyzed. Each experimental group consisted of three cultures from different passages.

Transfection with Small-interfering RNA (siRNA)

When confluence reached 40% (5 DIV), cells were transfected with siRNA against rat BDNF (Thermo Fisher Scientific) using Lipofectamine RNAiMax (Life Technologies, Grand Island, NY) according to the manufacturer's instructions. After incubating hippocampal cells with siRNA, reagent mixtures in Opti-MEM (Life Technologies) containing 50 pmol/L of shBDNF were added and incubated for 6 h. Then the medium was changed and cells were incubated for an additional 48 h. The efficiency of knockdown was at least 85%–90% as confirmed by RT-PCR and immunostaining with anti-BDNF antibodies (Fig. S2).

Extraction of RNA

The Mag Jet RNA Kit (Thermo Fisher Scientific) was used for the extraction of total RNA. The RNA quality was estimated by electrophoresis in the presence of 1 µg/mL ethidium bromide (2% agarose gel in Tris/borate/EDTA buffer). The concentration of the extracted RNA was determined with a NanoDrop 1000c spectrophotometer (Thermo Fisher Scientific, Wilmington, DE). The RevertAid H Minus First Strand cDNA Synthesis Kit (Thermo Fisher Scientific) was used for reverse transcription of total RNA.

Real-time Polymerase Chain Reaction (RT-qPCR)

Each PCR was performed in a 25-µL mixture of 5 µL of qPCRmix-HS SYBR (Evrogen, Moscow, Russia), 1 µL (0.2 µmol/L) of the primer solution, 17 µL RNase-free water, and 1 µL cDNA. The Dtlite Real-Time PCR System (DNA-technology, Moscow, Russia) was used for amplification, which consisted of an initial 5-min denaturation at 95°C, 40 cycles of 30 s denaturation at 95°C, 20 s annealing at 60–62°C, and a 20 s extension step at 72°C. The final extension was for 10 min at 72°C. The sequences

of the primers are listed in Table S1. All the sequences were designed with FAST PCR 5.4 and NCBI Primer-BLAST software. The data were analyzed with Dtlite software (DNA-technology). The expression of the studied genes was normalized to the gene encoding glyceraldehyde 3-phosphate dehydrogenase (GAPDH). Data were analyzed using Livak's method [28].

Statistical Analysis

All presented data were from at least three cultures from 2–3 different passages. n indicates the number of experiments. All values are given as the mean $\pm$ standard error (SE). The significance of differences between two groups was estimated with the paired t-test. Two-way or one-way analysis of variance (ANOVA) followed by the Tukey-Kramer *post-hoc* test was used for multiple group comparisons. The statistical tests were performed using GraphPad Prism 5 software (GraphPad Software, San Diego, CA).

Results

BDNF Overexpression Activates HP in GABAergic Hippocampal Neurons and Reduces the Amplitude of Ca^{2+} Responses by Changing the Expression of AMPAR and NMDAR Subunits

GABAergic neurons were identified by immunostaining with antibodies against glutamate GAD65/67, while GAD65/67-negative neurons were glutamatergic (Fig. 1A). It is known that GAD65/67 is expressed exclusively in neurons [29]. The Ca^{2+} responses of GABAergic and glutamatergic neurons to brief applications of NMDA (10 µmol/L in Mg^{2+}-free medium), a selective agonist of NMDARs, were found to decrease after hypoxia/reoxygenation cycles (Fig. 1C). In glutamatergic neurons, the slope of the curve approximating the ratio of the amplitude of NMDA-induced responses after a hypoxic episode to the amplitude before hypoxia was 0.57 ± 0.06 after the first episode, 0.39 ± 0.07 after the second, and 0.33 ± 0.07 after the third. This hypoxia-induced decrease of amplitudes is considered to be an expression of HP [11]. On the contrary, the amplitudes of NMDA-induced responses increased in GABAergic neurons after hypoxia-reoxygenation cycles (Fig. 1C), with a slope of 1.09 ± 0.14 after the first, 1.11 ± 0.18 after the second, and 1.14 ± 0.14 after the third cycle (Fig. 1D). These data showed a lack of HP in GABAergic neurons. The shape of the Ca^{2+} responses of glutamatergic neurons to repetitive applications of NMDA did not significantly change in experiments without hypoxia (Fig. S3A) and the slope of regression line was
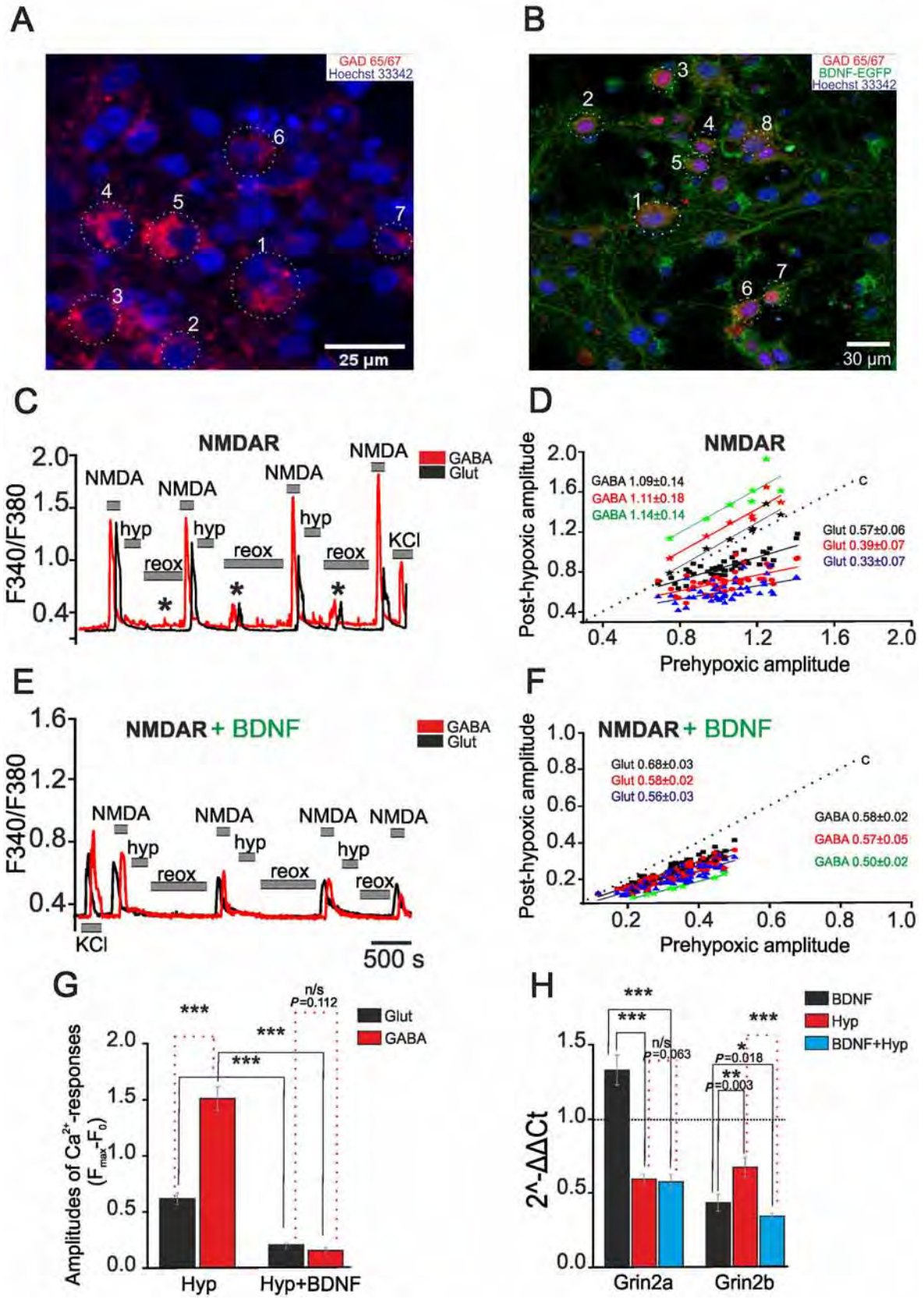
◀**Fig. 1** Effects of BDNF overexpression on the amplitude of NMDA-induced Ca^{2+} responses and expression of NMDAR subunits. **A** Identification of GABAergic neurons in a rat hippocampal culture (blue, nuclei stained with Hoechst 33342). Cells 1–7 are GABAergic neurons [averaged Ca^{2+} signal shown as the red trace in **C**, and individual amplitudes in **D** (stars)]. **B** Immunostaining of GABAergic neurons in a culture transduced with (AAV)-Syn-BDNF-EGFP (green). Cells 1–8 are GABAergic neurons [averaged Ca^{2+} signal shown as the red trace in **E**, and individual amplitudes in **F** (stars)]. **C**, **E** Averaged Ca^{2+} responses to NMDA (10 μmol/L in Mg^{2+}-free medium) in GABAergic (red trace) and glutamatergic (black trace) neurons from non-transduced cultures (**C**) and those transduced with (AAV)-Syn-BDNF-EGFP (**E**) (hyp, reox: brief episodes of hypoxia and reoxygenation; *spontaneous synchronous Ca^{2+} pulses reflecting post-hypoxic hyperexcitation). **D**, **F** Amplitude of Ca^{2+} responses (arbitrary units) of individual neurons to NMDA after hypoxia/reoxygenation cycles before preconditioning for GABAergic (stars) and glutamatergic neurons from non-transduced cultures (**D**) and those transduced with (AAV)-Syn-BDNF-EGFP (**F**) [dotted lines (c): linear function of data from control cultures (without hypoxia/reoxygenation cycles); black squares, red circles, and green triangles: responses of glutamatergic neurons after the first, second, and third cycles of hypoxia/reoxygenation, respectively; black, red and green stars: responses of GABAergic neurons after the first, second, and third hypoxia/reoxygenation cycles; solid lines in corresponding colors: linear regressions approximating the amplitudes of Ca^{2+} responses for both populations of neurons]. **G** Averaged amplitudes of Ca^{2+} responses of glutamatergic (black) and GABAergic (red) neurons to NMDA (10 μmol/L in Mg^{2+}-free medium) after three hypoxia/reoxygenation cycles in non-transduced (Hyp) and transduced cultures (Hyp + BDNF). **H** Effects of neuronal BDNF overexpression on the expression of Grin2a and Grin2b genes in transduced cultures that were not exposed to hypoxia (black) and the transduced cultures 24 h after the preconditioning with short episodes of hypoxia (blue) (red bars (Hyp), levels of Grin2a and Grin2b expression in non-transduced cultures 24 h after preconditioning with brief episodes of hypoxia). The level of expression in non-transduced cultures that were not exposed to hypoxia was set at 1 (dotted line).

0.97 ± 0.03 after the second, 0.93 ± 0.05 after the third, and 1.02 ± 0.02 after the fourth NMDA application (Fig. S3B). Similarly, the amplitudes of Ca^{2+} responses of GABAergic neurons also did not change (Fig. S3A), and the corresponding slopes were 0.93 ± 0.08, 0.89 ± 0.16, and 0.91 ± 0.06 (Fig. S3B). However, the amplitudes of Ca^{2+} responses of GABAergic neurons were, on average, higher than those of glutamatergic neurons (Fig. S3I).

BDNF overexpression was found in cultures 2–3 days after transduction with (AAV)-Syn-BDNF-EGFP (Fig. 1B). The amplitude of NMDA-induced Ca^{2+} responses in glutamatergic neurons before hypoxia was lower in cultures with BDNF overexpression than in controls (Fig. 1E). The Ca^{2+} responses of individual glutamatergic neurons both before and after hypoxic episodes was right-shifted along the X-axis (Fig. 1F), compared to the GABAergic neurons (Fig. 1D). The slope of linear regression (Fig. 1F) for glutamatergic neurons was 0.68 ± 0.03 after the first, 0.58 ± 0.02 after the second, and 0.56 ± 0.03 after the third hypoxia-

reoxygenation cycle. It should be noted that the amplitudes of NMDA-induced Ca^{2+} responses of GABAergic neurons (Fig. 1E) were lower in cultures with neuronal BDNF overexpression than in controls, indicating the induction of HP. The slope of linear regression for GABAergic neurons was 0.58 ± 0.02 after the first, 0.57 ± 0.05 after the second, and 0.50 ± 0.02 after the third hypoxia/reoxygenation cycle (Fig. 1F). The amplitudes of NMDA-induced Ca^{2+} responses of GABAergic neurons before hypoxia were also lower than in controls. We also compared the average amplitudes of the responses of GABAergic and glutamatergic neurons to NMDA application after three hypoxia/reoxygenation cycles (Fig. 1G). The amplitudes of Ca^{2+} responses of glutamatergic neurons decreased by 64% in cultures with BDNF overexpression compared to non-transduced cultures (Fig. 1G). In turn, the amplitude in GABAergic neurons decreased by 92%. Interestingly, hippocampal neurons generated spontaneous Ca^{2+} pulses during reoxygenation that can be considered post-hypoxic hyperexcitation (Fig. 1C). Such pulses can sometimes turn into irreversible $[Ca^{2+}]_i$ elevation that leads to damage and death of the most vulnerable populations of neurons, including GABAergic neurons [20]. These Ca^{2+} pulses did not occur in cultures transduced with the (AAV)-Syn-BDNF-EGFP construct. Thus, post-hypoxic hyperexcitation is suppressed by neuronal BDNF overexpression. According to the slope values (Fig. S3D), the amplitudes of the Ca^{2+} responses of GABAergic and glutamatergic neurons induced by repetitive NMDA treatment did not change in the absence of episodes of hypoxia in the transduced cultures with BDNF overexpression (Fig. S3C). Similar to non-transduced cultures, the average amplitudes of the responses of GABAergic neurons in the transduced cultures were higher than those of glutamatergic neurons (Fig. S3I). However, the amplitudes of the responses of GABAergic and glutamatergic neurons were significantly lower (GABAergic, $P = 0.021$; glutamatergic, $P = 0.012$) in the cultures with BDNF overexpression than in non-transduced cultures (Fig. S3I).

Expression of the Grin2a gene, which encodes the NR2A subunit of the NMDAR, was 48% higher in cultures with BDNF overexpression than in controls (Fig. 1H). Meanwhile, the expression of the Grin2b gene, which encodes the NR2B subunit, was 57% lower in the transduced cultures (Fig. 1H).

The expression of Grin2a decreased by 41% and that of Grin2b by 33% in non-transduced cultures 24 h after preconditioning with three episodes of hypoxia (Fig. 1H). In turn, the expression of Grin2a was 43% lower in transduced cultures 24 h after the preconditioning than in cultures without any exposure. However, the difference between the preconditioned transduced and non-transduced

740

Neurosci. Bull. July, 2020, 36(7):733–760

cultures was not significant (Fig. 1H). The expression of Grin2b in the transduced cultures decreased by 67% compared to controls (without exposure) after hypoxic preconditioning and by 52% compared to non-transduced cultures after hypoxia (Fig. 1H).

Repetitive brief application of 5-fluorowillardiine (FW), a selective AMPAR agonist (0.3 μmol/L), induced Ca^{2+} responses in GABAergic and glutamatergic neurons. These responses were similar to NMDA-induced responses, and the slopes of the linear regressions were close to 1 in cultures without hypoxia (Fig. S3E, F). Nevertheless, the amplitudes of FW-induced Ca^{2+} responses of GABAergic neurons were significantly higher than those of glutamatergic neurons ($P \leq 0.001$; Fig. S3J). Brief episodes of hypoxia decreased the amplitude of AMPAR-mediated Ca^{2+} responses in glutamatergic neurons (Fig. 2A). The slope of the linear regression decreased gradually (Fig. 2B) and was 0.64 ± 0.03 after the first, 0.51 ± 0.04 after the second, and 0.45 ± 0.05 after the third hypoxia/reoxygenation cycle. In contrast, the amplitudes of FW-induced Ca^{2+} responses of GABAergic neurons increased after the hypoxia/reoxygenation cycles (Fig. 2A); the slope of regression was 1.36 ± 0.12 after the first, 1.23 ± 0.15 after the second, and 1.22 ± 0.12 after the third cycle (Fig. 2B). Therefore, the activity of AMPARs of GABAergic neurons is not affected by brief episodes of hypoxia.

However, the amplitudes of the FW-induced Ca^{2+} responses of GABAergic neurons after episodes of hypoxia/reoxygenation decreased in cell cultures transduced with (AAV)-Syn-BDNF-EGFP (Fig. 2C). The slope of the linear regression in this case was 0.56 ± 0.04 after the first, 0.41 ± 0.02 after the second, and 0.32 ± 0.03 after the third hypoxia/reoxygenation cycle (Fig. 2D). Interestingly, neuronal BDNF overexpression dramatically enhanced the preconditioning effect of hypoxia in glutamatergic neurons. The amplitudes of FW-induced Ca^{2+} responses of these neurons substantially decreased (Fig. 2C) in (AAV)-Syn-BDNF-EGFP-transduced cultures after hypoxia-reoxygenation cycles compared to those in non-transduced cultures. The slope values were significantly lower than those in non-transduced cultures (0.66 ± 0.02 after the first, 0.48 ± 0.02 after the second, and 0.39 ± 0.01 after the third cycle) (Fig. 2D).

The averaged amplitudes of FW-induced Ca^{2+} responses of glutamatergic neurons after three hypoxia/reoxygenation cycles were 23% lower in cultures with neuronal BDNF overexpression than those in non-transduced cultures ($P = 0.002$; Fig. 2E). In addition, the averaged amplitudes of GABAergic neurons decreased by 62% ($P \leq 0.001$; Fig. 2E).

The amplitudes of repetitive FW-induced Ca^{2+} responses of GABAergic and glutamatergic neurons did not change in cultures with BDNF overexpression (Fig. S3G, H). Interestingly, BDNF overexpression promoted a decrease in the amplitudes of FW-induced responses only in GABAergic neurons (Fig. S3J), while the changes in the amplitudes of glutamatergic neurons were insignificant ($P = 0.725$). However, the amplitudes of the responses of GABAergic neurons in cultures with BDNF overexpression were higher than those of glutamatergic neurons (Fig. S3J; $P = 0.017$).

The basal expression of the Gria1 and Gria2 genes that encode the GluA1 and GluA2 subunits of AMPARs decreased by 71.3% and 38.5% respectively in (AAV)-Syn-BDNF-EGFP-transduced cultures compared to control cultures not exposed to hypoxia (Fig. 2F). Gria1 expression increased by 35% in non-transduced cell cultures 24 h after preconditioning with hypoxia/reoxygenation episodes, while Gria2 expression decreased by 80%; in contrast, Gria1 expression decreased by 53%, while Gria2 expression increased by 71% in the transduced cultures 24 h after preconditioning (Fig. 2F).

We noted that the amplitudes of the NMDAR- and AMPAR-mediated Ca^{2+} responses of GABAergic neurons were always higher than those of glutamatergic neurons. BDNF overexpression promoted the development of HP in GABAergic neurons, thus decreasing the amplitudes of NMDAR- and AMPAR-mediated Ca^{2+} responses. The amplitudes of repetitive NMDAR- and AMPAR-mediated responses did not change in GABAergic or glutamatergic neurons without episodes of hypoxia/reoxygenation. BDNF overexpression promoted the decrease in the amplitudes of NMDAR-mediated responses of both GABAergic and glutamatergic neurons, while AMPAR-mediated responses decreased only in GABAergic neurons. BDNF overexpression promoted the development of HP in GABAergic neurons. This phenomenon appeared as a decrease in Ca^{2+} response amplitudes upon activation of NMDARs and AMPARs. In addition, the preconditioning effect of hypoxia was enhanced in glutamatergic neurons from transduced cultures. The amplitudes of Ca^{2+} responses to the activation of AMPARs and NMDARs before episodes of hypoxia were lower in both GABAergic and glutamatergic neurons from cultures with BDNF overexpression. This effect can be explained by BDNF-mediated changes in the expression of the genes encoding the subunits that regulate the Ca^{2+} permeability of the receptors. Grin2a and Grin2b expression was lower 24 h after repetitive episodes of hypoxia/reoxygenation in the (AAV)-Syn-BDNF-EGFP-transduced cultures than in control cultures not exposed to hypoxia. However, we found that Gria1 expression was increased 24 h after hypoxia/reoxygenation cycles in controls, while Gria2 expression was decreased. In contrast, the decreased Gria1 and
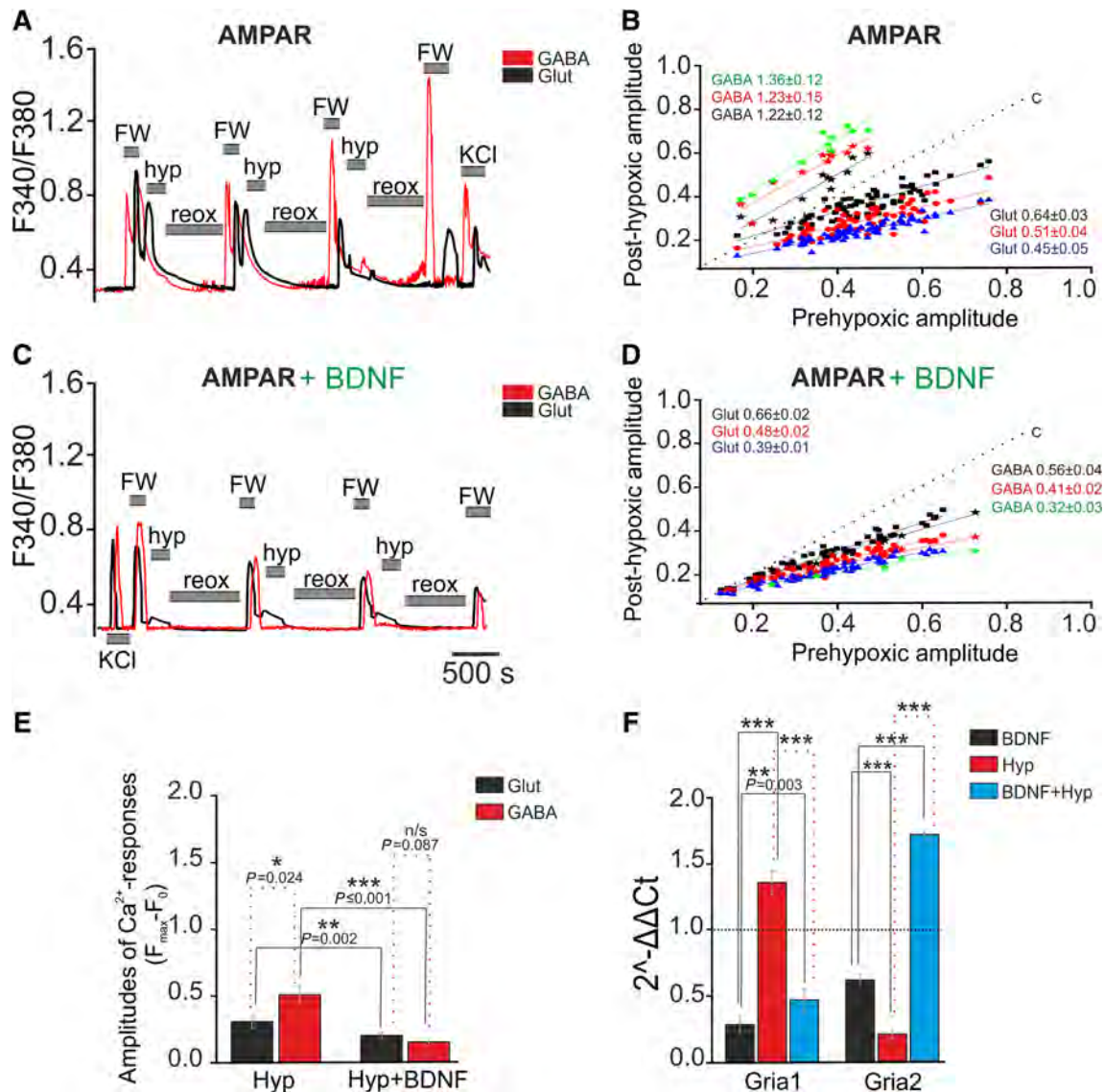
Fig. 2 Effects of BDNF overexpression on the amplitude of AMPAR-mediated Ca^{2+} responses and the expression of AMPAR subunits. **A**, **C** Averaged Ca^{2+} responses to FW application (0.3 μmol/L) in GABAergic (red traces) and glutamatergic (black traces) neurons from non-transduced cultures (**A**) and those transduced with (AAV)-Syn-BDNF-EGFP (**C**) (hyp, reox: brief episodes of hypoxia and reoxygenation). **B**, **D** Dependence of amplitudes of Ca^{2+} responses (arbitrary units) to FW after hypoxia/reoxygenation cycles on the amplitudes before preconditioning in GABAergic (stars) and glutamatergic neurons from non-transduced cultures (**B**) and those transduced with (AAV)-Syn-BDNF-EGFP (**D**) (black squares, red circles, and blue triangles: responses of glutamatergic neurons after the first, second, and third cycles of hypoxia/reoxygenation, respectively: black, red, and green stars: responses of GABAergic neurons after the first, second, and third hypoxia/reoxygenation cycles, respectively; color-coded solid lines: corresponding linear regressions; dotted line (c): linear regression for control cultures without hypoxia/reoxygenation). **E** Averaged amplitudes of Ca^{2+} responses of glutamatergic (black) and GABAergic (red) neurons to FW application after three hypoxia/reoxygenation cycles in non-transduced and transduced cultures. **F** Effects of neuronal BDNF overexpression on the expression of Gria1 and Gria2 genes in transduced cultures not exposed to hypoxia (black) and 24 h after preconditioning with short episodes of hypoxia (blue) (red bars: levels of Gria1 and Gria2 expression in non-transduced cultures 24 h after preconditioning with brief episodes of hypoxia). The level of expression in non-transduced cultures not exposed to hypoxia was set at 1 (dotted line). ***$P \leq 0.001$.

increased Gria2 expression occurred 24 h after exposure to brief episodes of hypoxia in cultures with BDNF overexpression in neurons. This finding indicates that the decreased Ca^{2+} permeability of AMPARs is due to the weak synthesis of GluA2 subunits that are known to regulate Ca^{2+} conductivity.

BDNF Overexpression Enhances the Protective Effect of Hypoxic Preconditioning Against OGD-Induced Cell Death

To investigate the contribution of BDNF to the development of the HP effect and the activation of the protective signaling cascades in GABAergic neurons, we knocked down BDNF in cultures using siRNA. The OGD experiments were performed 48 h after transfection (Fig. 3). Cultures transfected with an siRNA whose sequence differed from that of the siRNA against BDNF (Scrambled) were used as controls (Fig. 3A). We found that the process of transfection did not itself induce cell death because the percentage of early apoptotic cells in the scrambled group was similar to that in control cultures (without exposure; Fig. 7B) and accounted for $\sim 10\%$ of cells (Fig. 3F, G); only individual necrotic cells were observed (Fig. 3E). Necrotic, as well as early and late apoptotic cells were identified using PI and Hoechst 33342. A biphasic increase in $[Ca^{2+}]_i$ (Fig. 3A) was detected in glutamatergic and GABAergic neurons during 40-min OGD in the scrambled group. GABAergic neurons were characterized by higher amplitudes of Ca^{2+} signals during the first phase of the response, which was immediately followed by the second phase (irreversible $[Ca^{2+}]_i$ increase). In contrast, a small lag period between the first and second phases was found in glutamatergic neurons (Fig. 3A). The duration of this lag varied from culture to culture and may be dependent on the activity of Ca^{2+}-transporting systems in neurons. The death of $60\% \pm 18\%$ cells occurred after 40 min of OGD (Fig. 3E, H).

The cultures preconditioned with brief episodes of hypoxia following the experimental protocol presented in Fig. 1 were returned to a CO_2 incubator for 24 h, after which they were used in OGD experiments. We detected only individual necrotic cells in the preconditioned cultures (Fig. 3E), while the proportion of early apoptotic cells was $17\% \pm 4\%$ (Fig. 3F, G). In turn, the proportion of late apoptotic cells was $\sim 1\%$—lower than in the scrambled group. Therefore, it can be assumed that HP induces apoptosis in a small group of cells on the one hand, and promotes the appearance of a lag phase that may suppress the development of apoptosis on the other hand. The first phase of the OGD-induced Ca^{2+} response was virtually suppressed in the preconditioned cultures, and the amplitudes of Ca^{2+} responses during the second phase were 60% lower (Fig. 3B) than in the scrambled group (Fig. 3A). A prolonged lag period preceding the OGD-induced Ca^{2+} responses appeared in GABAergic neurons from preconditioned cultures (Fig. 3B). However, the preconditioning did not abolish the irreversible $[Ca^{2+}]_i$ increase. HP promoted a decrease in OGD-induced cell death to $15\% \pm 6\%$ (Fig. 3E, H).

Fig. 3 Protective action of brief periods of hypoxic preconditioning ▶ and BDNF overexpression against OGD-induced Ca^{2+} overload and cell death. **A–D** OGD-induced Ca^{2+} responses of glutamatergic (black traces) and GABAergic neurons (red traces) in cultures: (**A**) transfected with an siRNA whose sequence differed from that of the siRNA against BDNF (Scrambled, negative control); (**B**) preconditioned with brief episodes of hypoxia-reoxygenation (HP); (**C**) transduced with (AAV)-Syn-BDNF-EGFP and preconditioned with HP; (**D**) transfected with siRNA targeting the BDNF gene and preconditioned with HP. **E** Effects of BDNF overexpression on cell survival in preconditioned hippocampal cultures after 40-min OGD. Representative images of PI-stained cultures (white dots) before (left panels) and after OGD (right panels). 1: cultures transfected with an siRNA whose sequence differed from that of the siRNA against BDNF; 2: cultures preconditioned with HP; 3: cultures transduced with (AAV)-Syn-BDNF-EGFP and preconditioned with HP; 4: cultures transfected with siRNA targeting the BDNF gene preconditioned with HP. **F** Effects of BDNF overexpression and hypoxic preconditioning on the induction of apoptosis and necrosis in cultures before OGD. The cytogram shows the viability of hippocampal cells (X-axis, intensity of PI fluorescence; Y-axis, intensity of Hoechst 33342 fluorescence; cells were stained with probes 24 h after preconditioning). **G** Percentages of living (black), necrotic (red), and early (violet) and late (green) apoptotic cells in different experimental groups before OGD (two-way ANOVA followed by *post-hoc* Tukey-Kramer test; comparisons between experimental groups but not between individual columns; all differences were significant: ***$P \leq 0.001$, HP *vs* Scrambled, AAV-BDNF + HP *vs* Scrambled, and BDNF-KD + HP *vs* Scrambled; *$P = 0.022$, HP *vs* BDNF-KD + HP; ***$P \leq 0.001$, HP *vs* BDNF-KD + HP, AAV-BDNF + HP *vs* BDNF-KD + HP). **H** Percentages of dead cells after 40-min OGD in different experimental groups as in **E** [one-way ANOVA followed by *post-hoc* Tukey-Kramer test; ***$P \leq 0.001$, HP *vs* Scrambled, AAV-BDNF + HP *vs* Scrambled AAV-BDNF, AAV-BDNF + HP *vs* BDNF-KD + HP, and HP *vs* BDNF-KD + HP; *$P = 0.027$, BDNF-KD + HP *vs* Scrambled and HP *vs* AAV-BDNF + HP; $n = 3$ for **F** and **G**]. After preconditioning, the cultures were returned to a CO_2 incubator for 24 h.

Preconditioning of cultures with BDNF overexpression caused a decrease in the proportion of early apoptotic cells to 1% (Fig. 3F, G). Moreover, necrotic cells were not detected in this group before OGD (Fig. 3E). The second phase of the OGD-induced Ca^{2+} response was completely suppressed in glutamatergic neurons from these cultures, while the first phase was not affected, but in GABAergic neurons, the amplitudes of the responses were 59% lower than in the scrambled group (Fig. 3C). Similar to glutamatergic neurons, the first phase was also unaffected by preconditioning. The proportion of dead cells after OGD decreased to $5\% \pm 3\%$ (Fig. 3E, H).

As noted above, to suppress BDNF expression, the cells were transfected with siRNA against BDNF. The efficiency of transfection and BDNF knockdown were determined by immunostaining and RT-PCR assay 48 h later. The cells were stained with antibodies against BDNF and NeuN (Fig. S2A, B) and the fluorescence of anti-BDNF antibodies was detected in most neurons and some NeuN-negative cells from the negative control group (scrambled;

744

Neurosci. Bull. July, 2020, 36(7):733–760
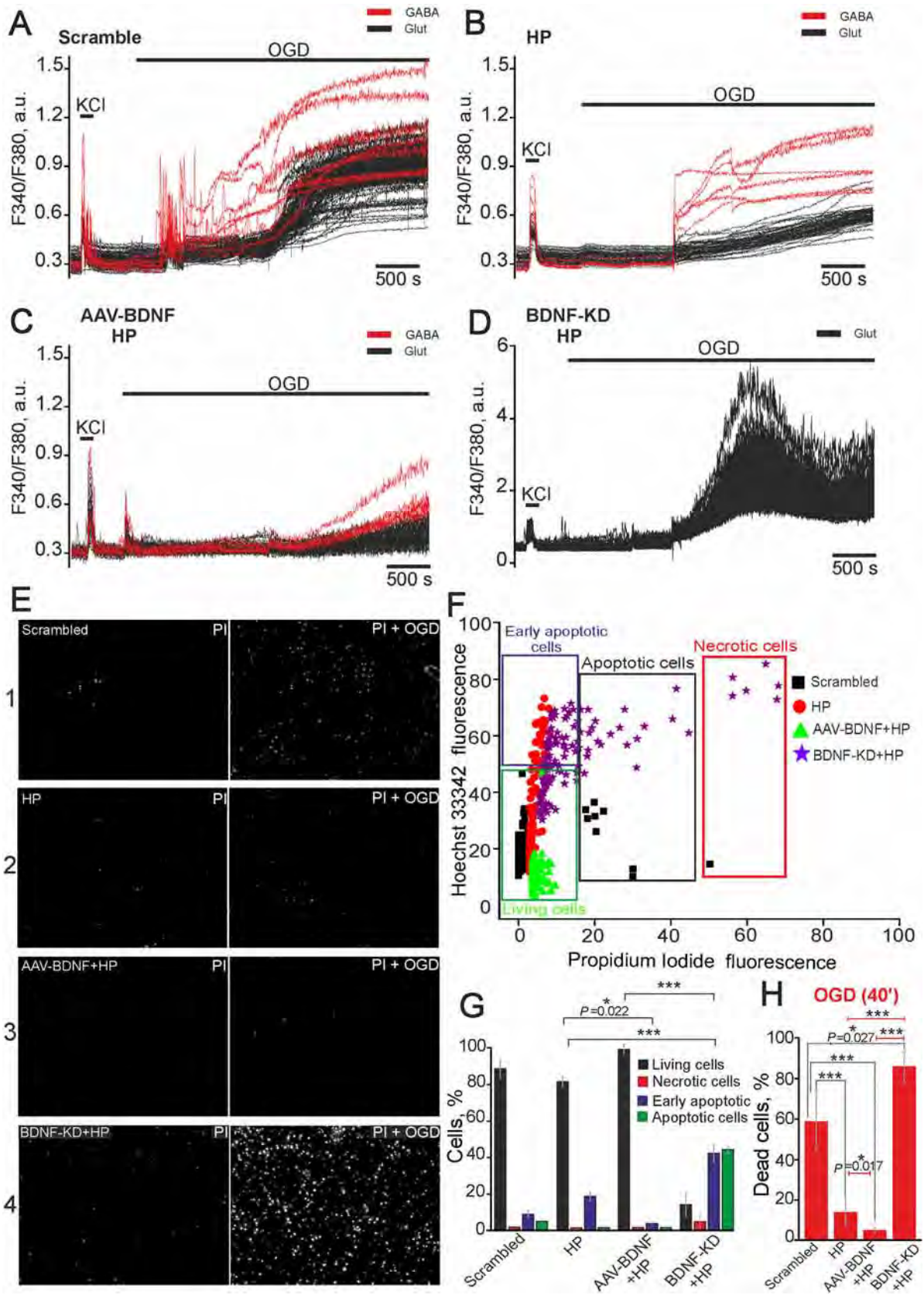
Fig. S2A). In contrast, fluorescence of anti-BDNF antibodies was not observed in any cells from the siRNA-transfected cultures (Fig. S2B, C). RT-PCR assays revealed that expression of the gene encoding BDNF was almost completely suppressed in cultures with BDNF knockdown (Fig. S2D), while the expression in the scrambled group was similar to controls (without exposure). Thus, all subsequent experiments were performed using cultures with confirmed BDNF knockdown.

Preconditioning of the transfected cultures with episodes of hypoxia led to an increase of necrotic cells to $8\% \pm 3\%$ (Fig. 3G, E), while the proportion of apoptotic cells was 85%, including $40\% \pm 12\%$ early and $43\% \pm 7\%$ late apoptotic cells (Fig. 3F, G). Two phases of the OGD-induced Ca^{2+} response occurred in glutamatergic neurons (Fig. 3D) in cultures with BDNF knockdown, and the amplitude of the Ca^{2+} signal during the second phase was 4 times that of the other experimental groups. Immunostaining of the transfected cultures with anti-GAD65/67 antibodies revealed the absence of GABAergic neurons, indicating their death during preconditioning. The percentage of dead cells after OGD reached $87\% \pm 13\%$ (Fig. 3H). The transfection procedure did not cause these effects of BDNF knockdown on GABAergic neurons because these neurons were detected after OGD in the scrambled group and the basal percentage of dead cells was similar to controls (Lipofectamine RNAiMAX and siRNA without additional exposure) (Fig. 7).

To investigate the delayed effects of BDNF overexpression and HP under OGD, the preconditioned cultures were exposed to 40-min OGD and returned to a CO_2 incubator for 24 h. Next, the cells were stained with PI and Hoechst 33342 (HO342). This model can be considered as more toxic because replacement of the ischemic medium leads to reoxygenation that promotes apoptosis and necrosis after OGD [30]. The increased fluorescence intensity of HO342 and PI in the scrambled group (without preconditioning) indicated the activation of apoptosis and necrosis 24 h after OGD (Fig. 4A). The percentage of late-apoptotic cells was $32\% \pm 7\%$ and of necrotic cells $57\% \pm 9\%$ (Fig. 4B, C), while early-apoptotic cells were virtually absent in this group. The cells preconditioned with HP mainly survived 24 h after OGD ($82\% \pm 6\%$, Fig. 4A). The percentage of necrotic cells was $17\% \pm 8\%$, and only individual apoptotic cells were detected (Fig. 4B, C).

Necrotic cells were not detected in the preconditioned cell cultures with BDNF overexpression (Fig. 4A), while the percentage of apoptotic cells was similar to that in preconditioned cultures (Fig. 4B, C). Thus, BDNF overexpression enhanced the protective effect of HP, suppressing necrosis and increasing the percentage of living cells to $90\% \pm 10\%$ (Fig. 4C).

We found massive cell death after OGD in the preconditioned cultures with BDNF knockdown (Fig. 4A). According to the fluorescence intensity of HO342 and PI, the percentage of late apoptotic cells was $62\% \pm 18\%$, while that of necrotic cells was $41\% \pm 7\%$ (Fig. 4C).

Thus, preconditioning of hippocampal cell cultures with brief episodes of hypoxia promoted the decrease of OGD-induced Ca^{2+} responses in glutamatergic neurons, and the percentages of necrotic cells immediately after OGD, as well as 24 h later, decreased in this case. The OGD-induced responses of glutamatergic as well as GABAergic neurons were significantly reduced in the transduced cultures after HP. BDNF enhanced the neuroprotective effect of HP, promoting cell survival after OGD and completely suppressing cell death. Experiments with BDNF knockdown confirmed this conclusion. Massive apoptotic and necrotic cell death occurred in the cultures with suppressed BDNF expression and the OGD-induced Ca^{2+} influx was more intense. Interestingly, GABAergic neurons were not detected by immunostaining in cultures with BDNF knockdown. Most of the cells were identified as late apoptotic or necrotic 24 h after 40-min OGD in the cultures with knockdown. Thus, BDNF can be considered as a pivotal neurotrophic factor protecting hippocampal cells, especially GABAergic neurons, against OGD-induced damage. HP had no neuroprotective effect in cultures with BDNF knockdown, and the loss of GABAergic neurons possibly occurred during preconditioning.

BDNF Overexpression Alters the Basal and Hypoxia-induced Expression of Genes Involved in the Development of Hypoxic Preconditioning

Real-time PCR analysis showed that BDNF overexpression in hippocampal neurons led to a decrease in Grik1 expression by 42% ($P = 0.014$) and in Grik2 by 46% ($P = 0.013$) compared to controls (Fig. 5). These genes encode the GluK1 and GluK2 subunits of kainate receptors. Grik1 expression was reduced by 67% ($P \leq 0.001$) 24 h after HP in non-transduced cultures, while Grik2 expression increased by 43% ($P = 0.0016$). Grik1 expression was reduced by 65% ($P \leq 0.001$) and Grik2 expression by 30% ($P = 0.021$) in transduced cultures after HP.

Interestingly, expression of the Gabra1 and Gabbr1 genes, which encode the α1 subunit of $GABA_A$ and the β1 subunit of $GABA_B$ receptors, decreased by 86% ($P \leq 0.001$) and 81% ($P \leq 0.001$), respectively, 24 h after hypoxia/reoxygenation in non-transduced cultures (Fig. 5A). It can be concluded that the decreased expression of subunits of critical inhibitory receptors leads to attenuation of the inhibition of neuronal networks. However, the expression of these genes dramatically increased 24 h after hypoxia/reoxygenation in the cultures with
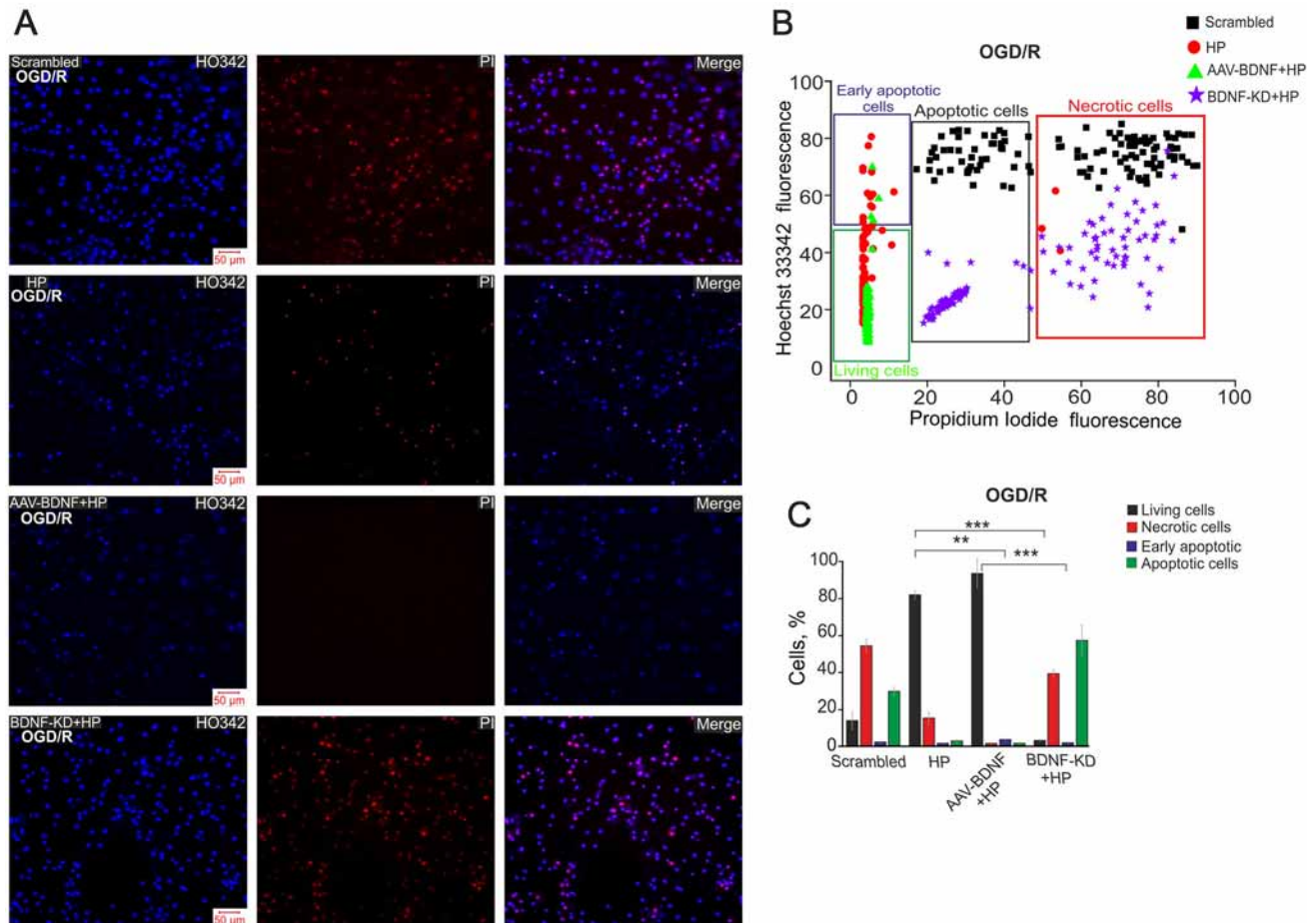
Fig. 4 Protective effect of hypoxic preconditioning and BDNF overexpression 24 h after OGD. **A** Double staining of cells with Hoechst 33342 (HO342) and propidium iodide (PI) and merged images (Merge) 24 h after 40-min OGD. **B** Cytogram of the viability of hippocampal cells (X-axis, intensity of PI fluorescence; Y-axis, intensity of Hoechst 33342 fluorescence; cells were stained with probes 24 h after HP). **C** Effects of HP, BDNF, and its knockdown on the induction of necrosis and apoptosis 24 h after OGD. Percentages of living cells (black) and cells in which early apoptosis (violet), apoptosis (green), and necrosis (red) were detected. Cultures were returned to a CO_2 incubator for 24 h after HP, then used in OGD experiments (40-min OGD) and returned to the CO_2 incubator for 24 h, after which, they were stained with HO342 and PI. (***$P \leq 0.001$, HP *vs* Scrambled, AAV-BDNF + HP *vs* Scrambled, and BDNF-KD + HP *vs* Scrambled; **$P = 0.008$, HP *vs* AAV-BDNF + HP; ***$P \leq 0.001$, HP *vs* BDNF-KD + HP and AAV-BDNF + HP *vs* BDNF-KD + HP).

BDNF overexpression; Gabra1 expression increased by 146% ($P \leq 0.001$) and Gabbr1 expression by 194% ($P \leq 0.001$). The basal Gabra1 expression did not change in the transduced cell cultures, but Gabbr1 expression increased by 147% ($P \leq 0.001$). BDNF overexpression in neurons also changed the expression of the Vglut1 and Vglut2 genes that encode vesicular glutamate transporter 1 and 2. Their expression increased slightly ($P = 0.27$) in transduced cultures without exposure to HP (Fig. 5A). However, the expression levels of these genes decreased by 65% (Vglut1, ***$P \leq 0.001$) and 87% (Vglut2, ***$P \leq 0.001$) 24 h after HP in cultures without overexpression. Vglut1 expression increased by 76% ($P \leq 0.001$) in transduced cells after HP. The expression of this gene was higher than the basal expression in transduced cultures without hypoxia. In contrast, Vglut2 expression after hypoxia was 50% lower than control ($P = 0.011$). We also compared the expression of all these genes after HP in transduced and non-transduced cultures (Fig. 5A) and found a significant decrease of Grik2 expression in the transduced cultures ($P \leq 0.001$). In turn, the expression of Gabra1 ($P \leq 0.001$), Gabbr1 ($P \leq 0.001$), Vglut1 ($P \leq 0.001$), and Vglut2 ($P \leq 0.001$) increased, which may be considered a protective effect.

BDNF overexpression led to decreases in the basal expression of the Pik3ca gene by 53% ($P = 0.014$) and the Pik3cb gene by 34% ($P = 0.026$), while Pik3cg expression increased by 428% ($P \leq 0.001$) (Fig. 5B). The expression of these genes in controls increased by 129% for Pik3ca ($P \leq 0.001$), 143% for Pik3cb ($P \leq 0.001$), and 166% for

Fig. 5 Effects of BDNF over-expression in neurons on the expression of genes in controls and after brief episodes of hypoxia/reoxygenation. **A–C** Expression levels of: (**A**) genes encoding subunits of kainate receptors (Grik1 and Grik2), GABA receptors (Gabra1 and Gabbr1), and genes encoding vesicular glutamate transporters (Vglut1 and Vglut2); (**B**) genes encoding subunits of PI3-kinase (Pik3ca, Pik3cb, and Pik3cg), genes of the target of rapamycin (Mtorc1 and Mtorc2), and the gene of fibroblast growth factor receptor substrate 2 (Frs2); (**C**) genes encoding BDNF and its precursor, pro-BDNF, along with those encoding the receptors of pro-BDNF and BDNF (Ntrk1, Ntrk2, and p75). **D** Expression levels of genes that regulate inflammation and apoptosis [dashed line level of gene expression in controls (non-transduced cell cultures without hypoxia) was set at 1]. ***$P \leq 0.001$ (green asterisks: significance of differences between non-transduced groups with and without BDNF).
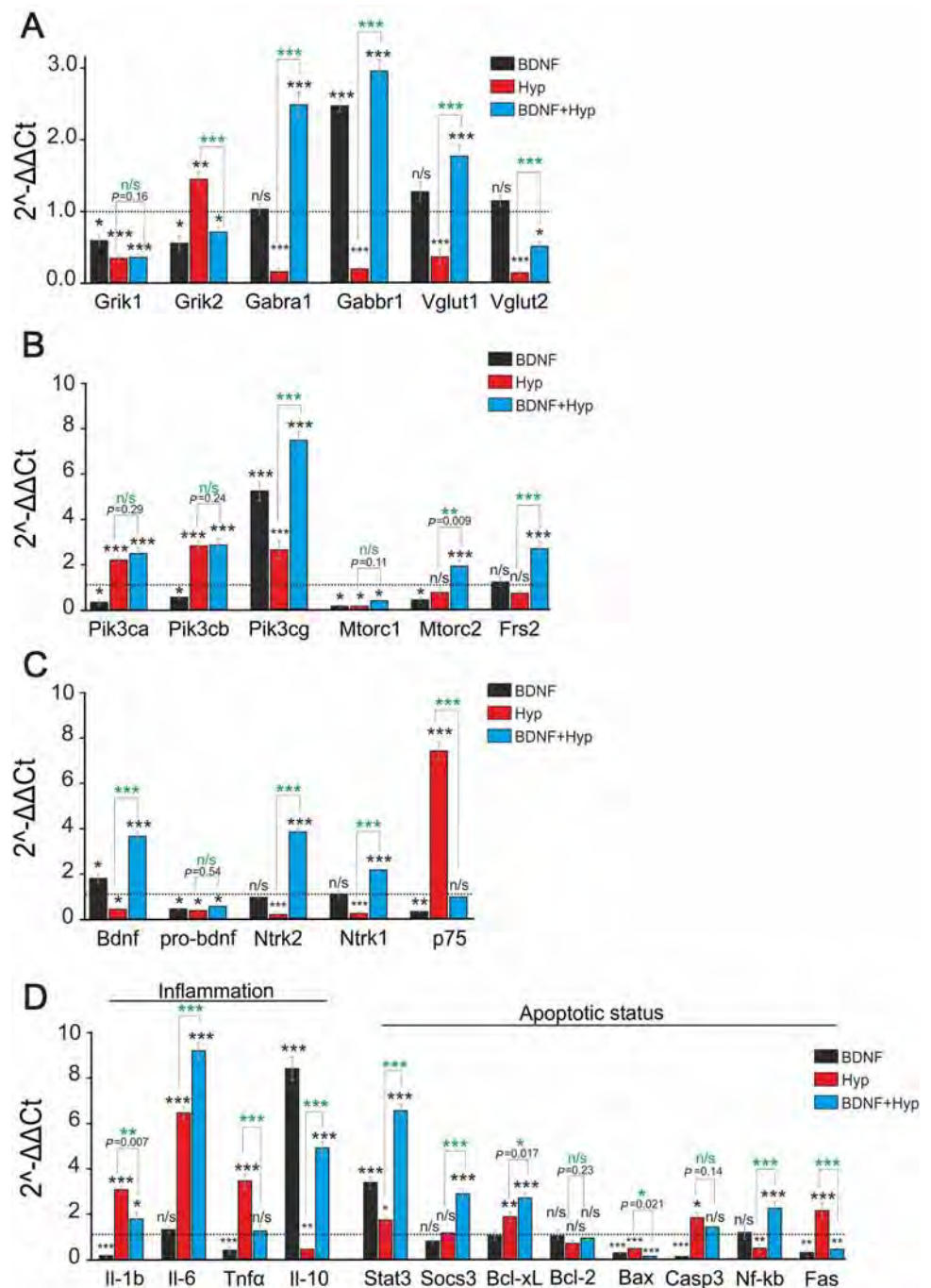
Pik3cg ($P \leq 0.001$) after hypoxic episodes. Pik3ca and Pik3cb expression in the transduced cultures did not change after hypoxia compared to non-transduced cultures (Fig. 5), while the increases were significant compared with controls ($P \leq 0.001$). However, Pik3cg expression increased by 648% ($P \leq 0.001$), substantially exceeding the basal expression in the transduced cultures and the post-hypoxic level in the non-transduced cultures.

Mtorc1 expression decreased by 88% ($P = 0.012$) in non-transduced cultures after HP and in transduced cultures without hypoxia. A lower decrease in Mtorc1 expression by 74% ($P = 0.022$) was found 24 h after HP in cultures with BDNF overexpression. Mtorc2 expression increased by 197% ($P \leq 0.001$) in transduced cell cultures 24 h after hypoxia. In turn, Mtorc2 expression decreased by 55% ($P = 0.021$) in the BDNF group. A decrease was also found in the non-transduced group (24%), but this was not significant ($P = 0.086$). A significant increase of Frs2 expression was found in the BDNF-transduced cell cultures after hypoxia (197%, $P \leq 0.001$; Fig. 5B). However, the

changes in Frs2 expression were not significant in the BDNF ($P = 0.044$) and non-transduced ($P = 0.049$) groups. We found significant increases in the expression of Pik3cg (250%, ***$P \leq 0.001$), Mtorc2 (121%, **$P = 0.009$), and Frs (254%, ***$P \leq 0.001$) after HP in transduced compared to non-transduced cultures (Fig. 5B).

It is known that BDNF and pro-BDNF activate different cascades with opposite physiological effects [31]. BDNF overexpression in neurons increased basal Bdnf expression by 90% ($P = 0.021$). Nevertheless, pro-BDNF expression decreased by 56% ($P = 0.006$) and that of p75 by 68% ($P = 0.008$) (Fig. 5C). Basal expression of the genes encoding TrkA (Ntrk1) and TrkB (Ntrk2) receptors changed in the range of 10%–12% ($P = 0.77$) in the transduced cultures without hypoxia compared to controls. The expression of Bdnf, pro-BDNF, Ntrk1, and Ntrk2 decreased by 50% ($P = 0.015$), 67% ($P = 0.015$), 75% ($P \leq 0.001$), and 89% ($P \leq 0.001$), respectively, in the non-transduced cultures 24 h after HP. In contrast, p75 expression increased by 646% ($P \leq 0.001$) (Fig. 5C). In turn, Bdnf, Ntrk1, and Ntrk2 expression increased by 270% ($P \leq 0.001$), 115% ($P \leq 0.001$), and 273% ($P \leq 0.001$), respectively, after hypoxia in cultures with BDNF overexpression in neurons. Pro-BDNF expression fell by 50% ($P = 0.014$) in this group, but p75 expression did not differ from its expression in control cultures without hypoxia ($P = 0.79$). In the transduced cultures (Fig. 5C), hypoxic episodes enhanced the expression of the genes encoding BDNF ($P \leq 0.001$) and its receptors (Ntrk1, $P \leq 0.001$; Ntrk2, $P \leq 0.001$) compared to non-transduced cultures. However, expression of the p75 gene was substantially reduced in transduced compared to non-transduced cultures ($P \leq 0.001$).

The basal expression of IL-1β decreased by 85% ($P \leq 0.001$) and TNFα by 47% ($P = 0.003$) in transduced cultures (Fig. 5D), while the difference in IL-6 expression was not significant ($P = 0.28$). IL-10 expression increased by 799% ($P \leq 0.001$) at the same time. IL-1β increased by 218% ($P \leq 0.001$), IL-6 by 596% ($P \leq 0.001$), and TNFα by 265% ($P \leq 0.001$) in non-transduced cultures 24 h after hypoxia, whereas IL-10 expression fell by 54% ($P = 0.008$). IL-1β expression increased by 98% ($P = 0.022$) after hypoxic episodes in cultures with BDNF overexpression. In addition, IL-6 expression increased by 885% ($P \leq 0.001$) and IL-10 by 415% ($P \leq 0.001$). The level of TNFα expression was the same as that in control cultures without hypoxia ($P = 0.69$). Comparing (AAV)-Syn-BDNF-EGFP-transduced and non-transduced cultures, we found that the expression of genes encoding anti-inflammatory cytokines increased after HP (IL-10 by 1043%, $P \leq 0.001$; IL-6 by 53%, $P = 0.007$) in transduced compared to non-transduced cultures (Fig. 5D). In contrast, the expression of genes encoding pro-inflammatory cytokines was reduced (IL-1β by 55%, $P \leq 0.001$; TNFα by 124%, $P \leq 0.001$) in cultures with BDNF overexpression compared to non-transduced cultures.

Stat3 expression was 254% higher than controls ($P \leq 0.001$) in cultures with BDNF overexpression in neurons. Furthermore, expression of the pro-apoptotic genes Bax, Casp3, and Fas was lower by 74% ($P \leq 0.001$), 98% ($P \leq 0.001$), and 77% ($P = 0.004$) than controls. Stat3 and Bcl-xL expression increased by 85% ($P = 0.019$) and 100% ($P = 0.005$) after hypoxic episodes in non-transduced cell cultures, while the expression of the pro-apoptotic genes Bax and NF-κB decreased by 63% ($P \leq 0.001$) and 58% ($P = 0.004$), thus suppressing apoptosis. However, the expression of the pro-apoptotic genes Casp3 and Fas in the non-transduced group increased by 87% ($P = 0.018$) and 123% ($P \leq 0.001$), contributing to apoptosis activation (Fig. 5D). Enhanced expression of anti-apoptotic genes was found 24 h after HP in cultures with BDNF overexpression. Stat3, Socs3, and Bcl-xL expression increased by 589% ($P \leq 0.001$), 203% ($P \leq 0.001$), and 187% ($P \leq 0.001$), respectively. In contrast, the expression of most pro-apoptotic genes was reduced, but the expression of NF-κB increased by 174% ($P \leq 0.001$). Bax expression fell by 93% ($P \leq 0.001$) and Fas by 56% ($P = 0.006$), while the increase of Casp3 expression was not significant ($P = 0.24$) (Fig. 5D). Interestingly, although the expression of many pro- and anti-apoptotic genes significantly changed with hypoxia or BDNF expression and hypoxia, the changes of Bcl-2 and NF-κB expression in the BDNF group without hypoxia were not significant. We also compared the expression of these genes in (AAV)-Syn-BDNF-EGFP-transduced and non-transduced cultures after HP. In the transduced cultures, hypoxia increased the expression of Stat3 by 277% ($P \leq 0.001$), Socs3 by 210% ($P \leq 0.001$), Bcl-xL by 36% ($P = 0.017$), and NF-κB by 287% ($P \leq 0.001$) compared to non-transduced cultures, while the expression of Bax and Fas decreased by 67% ($P = 0.021$) and 312% ($P \leq 0.001$). The expression of the other genes regulating apoptosis did not significantly differ between the non-transduced groups with and without BDNF.

Thus, the expression of most genes was decreased 24 h after HP in non-transduced cultures compared to control cultures without episodes of hypoxia. However, only the decreased Grik1, Bax, and NF-κB expression can be considered neuroprotective. The expression of 8 of the 41 studied genes was increased. Only the increased expression of PI3K, Bcl-xL, and IL-6 can be considered a positive effect, while that of p75, IL-1β, TNFα, and Fas can promote apoptosis and inflammation. The expression of 20 out of the 33 studied genes was increased 24 h after hypoxia in (AAV)-Syn-BDNF-EGFP-transduced cultures compared to the basal expression in these cultures. It
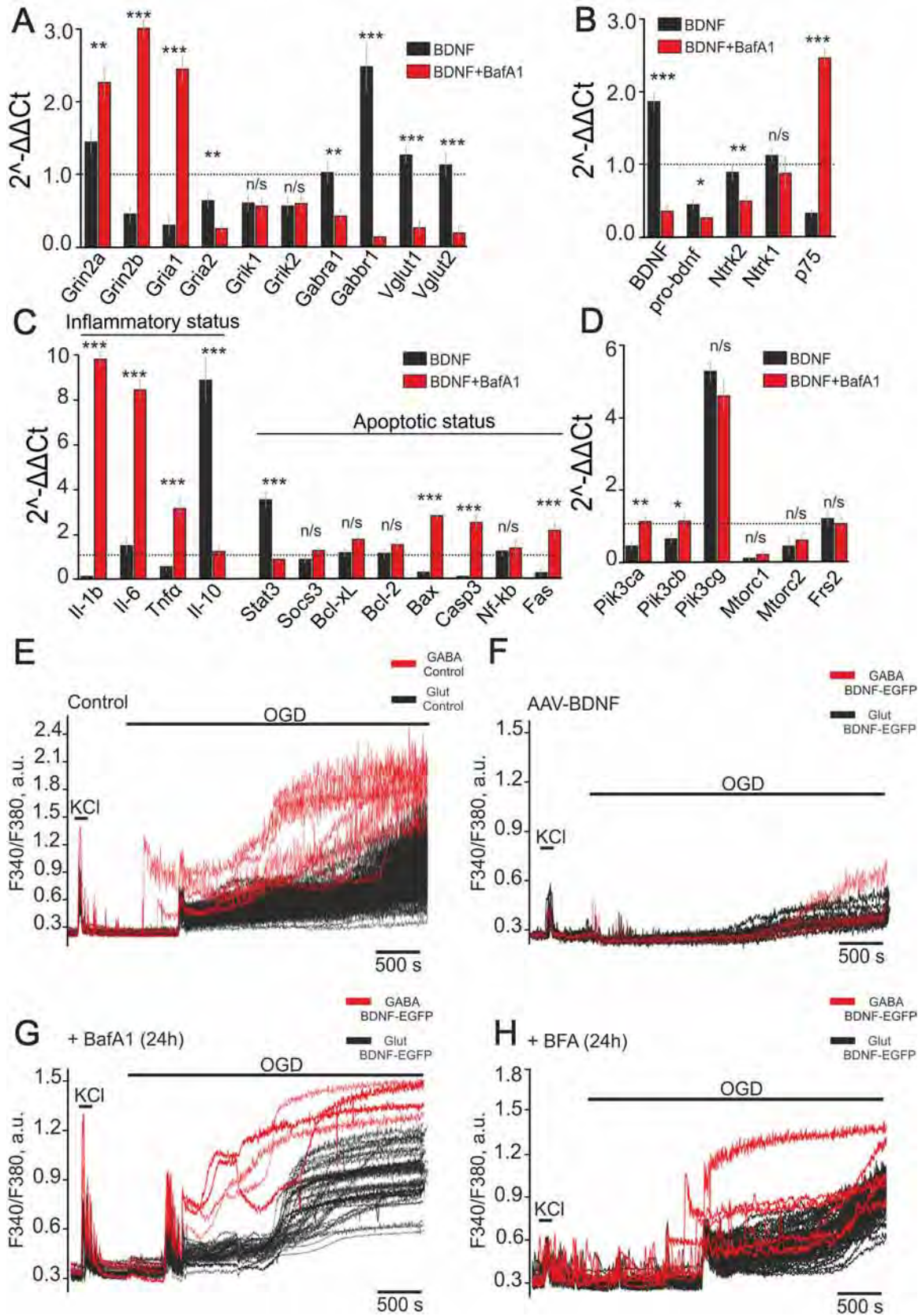
◄**Fig. 6** Effects of bafilomycin A1 on gene expression, changes of intracellular Ca^{2+} concentration under OGD, and OGD-induced cell death in (AAV)-Syn-BDNF-EGFP-transduced hippocampal cultures. **A–D** Effects of BafA1 on the expression of genes encoding glutamate transporters and subunits of the receptors (**A**); genes encoding BDNF and its precursor, pro-BDNF, and their receptors (**B**); genes regulating apoptosis and inflammation (**C**); genes encoding subunits of PI3K (Pik3ca, Pik3cb, and Pik3cg), mammalian target of rapamycin (Mtorc1 and Mtorc2) and fibroblast growth factor receptor substrate 2 (Frs2) (**D**) [expression of the selected genes in non-transduced cultures (control) set at 1 (dashed line); differences are relative to the BDNF group without BafA1 pre-incubation; *P*-values in text]. **E–H** OGD-induced Ca^{2+} responses of glutamatergic (black traces) and GABAergic (red traces) neurons from non-transduced cultures (Control, **E**), (AAV)-Syn-BDNF-EGFP-transduced hippocampal cultures (**F**, AAV-BDNF), (AAV)-Syn-BDNF-EGFP-transduced hippocampal cultures after 24-h pre-incubation with 1 μmol/L bafilomycin A1 (+BafA1) (**G**), and with the vesicular trafficking inhibitor, 50 μmol/L brefeldin A (**H**, +BFA).

should be noted that 16 of these genes encode proteins involved in neuroprotection. Vglut2 expression decreased, while Vglut1 expression increased, indicating a possible compensatory effect. The suppressed Fas expression can be considered a protective effect of BDNF overexpression. So, BDNF overexpression in neurons not only enhances the basal expression of the protective genes and suppresses the expression of pro-apoptotic or pro-inflammatory genes, but also strengthens the protective effects of HP. Moreover, hypoxia leads to a decrease in the expression of a smaller number of protective genes.

Vesicular Release of BDNF Mediates Its Neuroprotective Action Under OGD

We have previously shown that BDNF is released by hippocampal cells under OGD and glutamate toxicity [22], and others have reported the same results [32]. We showed that the release of BDNF is a Ca^{2+}-dependent process that is suppressed by BafA1, a vacuolar ATPase inhibitor [22]. Incubation of (AAV)-Syn-BDNF-EGFP-transduced hippocampal cultures with BafA1 (1 μmol/L) for 24 h evoked a dramatic change in the basal expression of the genes encoding the vesicular glutamate transporters and subunits of GABA and glutamate receptors (Fig. 6A). Grin2a expression increased by 64% (*P* = 0.008), Grin2b by 731% (*P* ≤ 0.001), and Gria1 by 737% (*P* ≤ 0.001) compared to transduced cultures without BafA1 pre-incubation (Fig. 6A). It has been noted that the GluA2 subunit regulates the Ca^{2+} conductivity of AMPARs. Increased Gria1 expression was found along with suppressed Gria2 expression that probably contributes to the formation of Ca^{2+}-permeable AMPARs. Gabra1 and Gabbr1 expression decreased by 60% (*P* = 0.003) and 94% (*P* ≤ 0.001) after 24-h pre-incubation with BafA1.

Interestingly, the levels of Grik1 and Grik2 expression were not affected by BafA1 (*P* = 0.1 and *P* = 0.11). Furthermore, Vglut1 and Vglut2 expression also decreased by 80% and 84% (*P* ≤ 0.001 for both). However, the expression of the genes encoding kainate receptor subunits did not change in transduced cultures after pre-incubation with BafA1.

The expression of the genes encoding BDNF and pro-BDNF decreased by 81% (*P* ≤ 0.001) and 47% (*P* = 0.017) after pre-incubation with BafA1, compared to the transduced cultures without BafA1 (Fig. 6B). The basal expression of Ntrk2 was significantly lower (44%, *P* = 0.005) while p75 expression was elevated by 668% (*P* ≤ 0.001), which may stimulate the induction of apoptosis and necrosis.

Indeed, the expression of genes encoding pro-inflammatory cytokines was substantially higher [650% (*P* ≤ 0.001) for IL-1β, 463% (*P* ≤ 0.001) for IL-6, and 494% (*P* ≤ 0.001) for TNFα] (Fig. 6C), while the expression of the IL-10 gene fell by 613% (*P* ≤ 0.001). Basal expression of the anti-apoptotic gene Stat3 decreased by 317% (*P* ≤ 0.001) after 24-h pre-incubation with BafA1, whereas expression of the pro-apoptotic genes Bax, Casp-3, and Fas increased by 190% (*P* ≤ 0.001), 200% (*P* ≤ 0.001), and 834% (*P* ≤ 0.001), respectively. The elevated expression of pro-apoptotic genes points to the abolition of the anti-apoptotic effect of BDNF in the presence of BafA1. BafA1 did not significantly change the expression of the anti-apoptotic genes Socs3 (*P* = 0.47), Bcl-xL (*P* = 0.4), and Bcl-2 (*P* = 0.38).

Pik3ca and Pik3cb expression increased by 144% (*P* = 0.004) and 74% (*P* = 0.019) after 24-h pre-incubation with BafA1 (Fig. 6D). However, the expression levels of these genes in the transduced cultures were similar to those in the non-transduced cultures (Fig. 6D). BafA1 did not significantly change the expression of Pik3cg (*P* = 0.16), Mtorc1 (*P* = 0.21), Mtorc2 (*P* = 0.24), and Frs2 (*P* = 0.13).

OGD evoked biphasic Ca^{2+} responses in glutamatergic and GABAergic neurons (Fig. 6E). The first phase occurred synchronously in glutamatergic and in most GABAergic neurons after a lag period, whose duration varied from culture to culture. It should be noted that some GABAergic neurons responded to OGD earlier than other GABAergic and glutamatergic neurons. The amplitudes of the $[Ca^{2+}]_i$ increase during the second phase of the OGD-induced Ca^{2+} response were higher for GABAergic than for glutamatergic neurons. Staining with PI showed 80% ± 16% dead cells after OGD, while PI fluorescence was detected only in individual cells before the experiments (Fig. 7A).

The first phase of the OGD-induced Ca^{2+} responses was significantly suppressed in glutamatergic and GABAergic
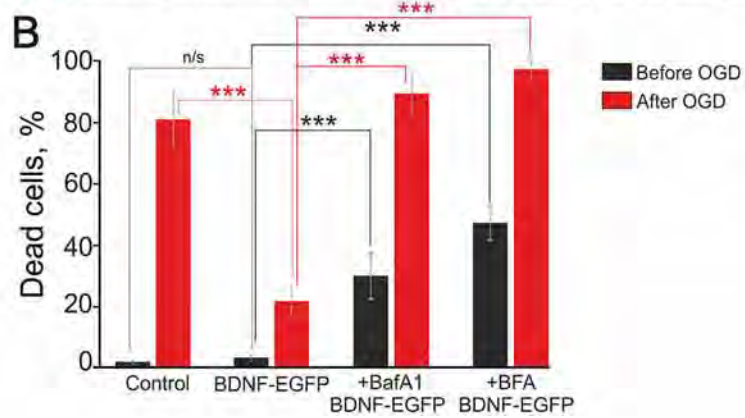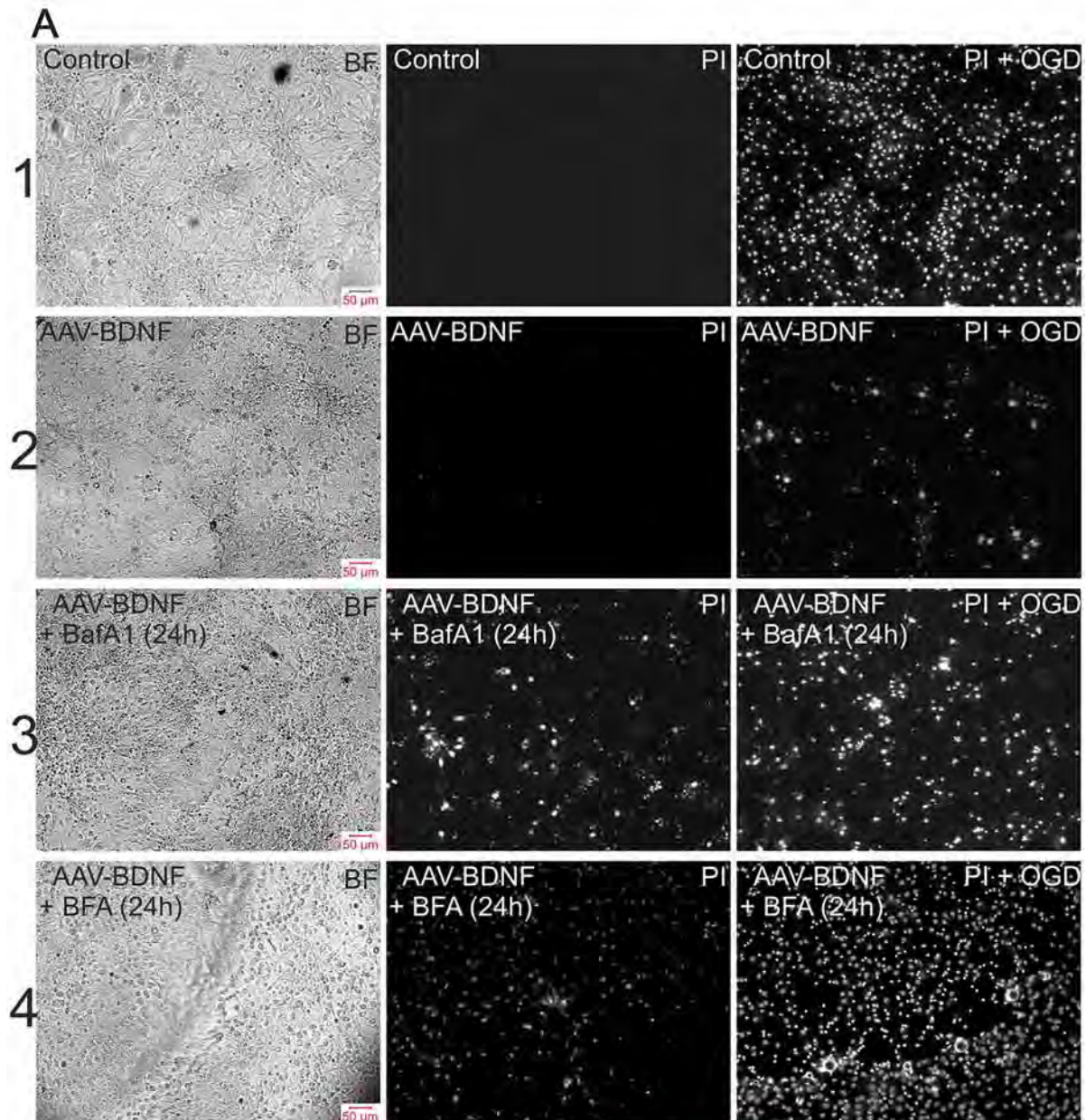
◄ **Fig. 7** Viability of hippocampal cells after 40-min OGD in control and (AAV)-Syn-BDNF-EGFP-transduced cultures incubated with inhibitors of vesicular release. **A** Representative microphotographs of hippocampal cell cultures: bright-field images (left panels) and PI fluorescence (white dots) before (PI, central panels) and after OGD (PI + OGD, right panels). 1: Control, non-transduced cultures; 2: cultures transduced with (AAV)-Syn-BDNF-EGFP; 3: transduced cultures pre-incubated for 24 h with 1 μmol/L bafilomycin A1; 4: transduced cultures pre-incubated for 24 h with 50 μmol/L brefeldin A. **B** Average percentages of dead cells before (black) and after (red) 40-min OGD in control, (AAV)-Syn-BDNF-EGFP-transduced cultures, and (AAV)-Syn-BDNF-EGFP-transduced cultures with 24-h pre-incubation with 1 μmol/L bafilomycin A1 and 50 μmol/L brefeldin A (***$P \leq 0.001$, n/s $P = 0.28$; vitality tests were made before and after OGD, see Fig. 6).

neurons in the (AAV)-Syn-BDNF-EGFP-transduced cultures (Fig. 6F). The second phase (a global $[Ca^{2+}]_i$ increase) was also suppressed. The number of dead cells decreased dramatically due to this protective effect of BDNF overexpression in neurons. However, the number of dead cells after 40-min OGD in (AAV)-Syn-BDNF-EGFP-transduced cultures was 20% ± 6% (Fig. 7A, B). It should be noted that the protective effect of BDNF overexpression in neurons was abolished after 24-h pre-incubation of the transduced cells with BafA1. And a biphasic $[Ca^{2+}]_i$ elevation occurred in glutamatergic and GABAergic neurons (Fig. 6G). Furthermore, the proportion of dead cells after 40-min OGD rose to 91% ± 5% after pre-incubation with BafA1 (Fig. 7A, B). PI staining revealed that the percentage of dead cells in cultures with BDNF overexpression in neurons was 6% ± 4% before the experiments (Fig. 7A, B). Nevertheless, 33% ± 11% of dead cells were found before the experiments after 24-h pre-incubation with BafA1 (Fig. 7B).

Similar to BafA1, incubation of the (AAV)-Syn-BDNF-EGFP-transduced cultures for 24 h with BFA (50 μmol/L), an inhibitor of protein transport, abolished the protective effect of BDNF overexpression (Fig. 6H). Two phases of OGD-induced Ca^{2+} response were detected in glutamatergic and GABAergic neurons. The amplitude of the response during the first phase was lower compared to the incubation with BafA1. GABAergic neurons demonstrated increased OGD-induced Ca^{2+} activity (Fig. 6H) that can be a sign of hyperexcitation. BFA induced the death of 25% ± 12% of cells before the experiments, and this increased to 94% ± 6% (Fig. 7A, B) after 40-min OGD.

HP activated protective mechanisms predominantly in glutamatergic neurons (Fig. 3), thus promoting their survival under OGD. The experiments were performed using cell cultures preconditioned with repetitive hypoxia/reoxygenation episodes (Fig. 8). Cultures were divided into two groups after preconditioning. The first group was used as a

control, while BafA1 (1 μmol/L) or TeNT (50 ng/mL) was added to the second group. The cultures were used in experiments 24 h after the preconditioning.

We found that the first and especially the second phase of OGD-induced Ca^{2+} responses were suppressed in glutamatergic neurons relative to control cultures (Fig. 8A) and the percentage of necrotic cells was reduced to 17% ± 6% (Fig. 8D, E). However, the amplitudes of the first phase of OGD-induced responses of GABAergic neurons (Fig. 8A) were higher than those in glutamatergic neurons and the responses of GABAergic neurons were characterized by high-amplitude irreversible elevation of $[Ca^{2+}]_i$ during the second phase.

In cultures pre-incubated with BafA1, high-amplitude Ca^{2+} responses in glutamatergic and GABAergic neurons appeared immediately after (without a lag-period) the application of OGD-medium (Fig. 8B), and high-amplitude Ca^{2+} oscillations occurred. The percentage of necrotic cells was 83% ± 8% (Fig. 8D, E). TeNT, an inhibitor of Ca^{2+}-dependent vesicular fusion, also abolished the protective effects of HP. A high-amplitude, reversible $[Ca^{2+}]_i$ elevation appeared in glutamatergic neurons after a lag (Fig. 8C) and was followed by an irreversible global $[Ca^{2+}]_i$ increase 3–6 min later. Both phases of OGD-induced Ca^{2+} responses were also detected in GABAergic neurons after pre-incubation with TeNT (Fig. 8C). However, the amplitudes of signals during the second phase were higher in GABAergic than in glutamatergic neurons, and the second phase occurred earlier. The percentage of dead cells in the HP + TeNT group after OGD was 79% ± 7% (Fig. 8D, E), not significantly different from the HP + BafA1 group. It should be noted that the differences between the percentages of dead cells before OGD in the HP (8% ± 5%), HP + BafA1 (12% ± 6%), and HP + TeNT (10% ± 5%) groups were not significant (Fig. 8D, E).

Using confocal microscopy, we established that the overexpressed BDNF was distributed in cells as individual vesicles demonstrating EGFP fluorescence (Fig. 9A). Addition of the O_2 scavenger sodium dithionite to the glucose-free medium led to a rapid decrease in EGFP fluorescence intensity (Fig. 9B) and the disappearance of most BDNF-containing vesicles (Fig. 9D), indicating BDNF release under OGD. Incubation of (AAV)-Syn-BDNF-EGFP-transduced cultures for 24 h with 1 μmol/L BafA1 and 50 ng/mL TeNT (Fig. 9A) changed the number and size of vesicles. Basal EGFP fluorescence was significantly lower in these experimental groups than in controls (Fig. 9C). This finding indirectly indicated a decrease of the BDNF level in cells after pre-incubation with BafA1 and TeNT. The addition of dithionite to neurons pre-incubated with BafA1 induced the release of individual BDNF-containing vesicles (Fig. 9B, D), while
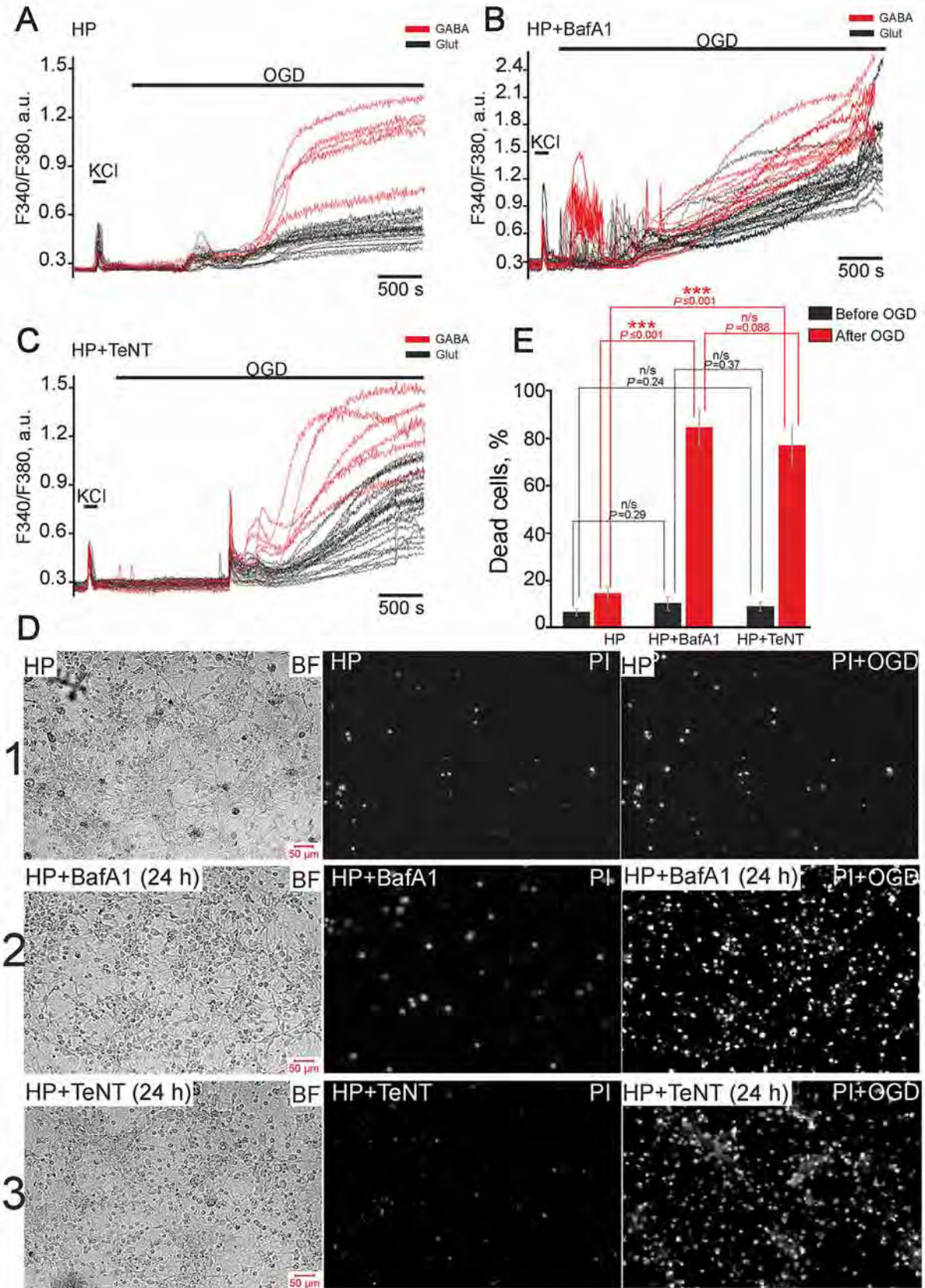
◀**Fig. 8** Suppression of vesicular release abolishes the protective effects of hypoxic preconditioning and promotes the death of hippocampal cells under OGD. **A–C** OGD-induced Ca^{2+} responses of glutamatergic (black traces) and GABAergic (red traces) neurons from cultures preconditioned with brief episodes of hypoxia/reoxygenation. (**A**) Controls (HP); cultures pre-incubated for 24 h with 1 μmol/L bafilomycin A1 (HP + BafA1) (**B**) and 50 ng/mL tetanus toxin (HP + TeNT) (**C**). **D** Representative microphotographs of hippocampal cultures: bright-field (left panels); PI fluorescence (white dots) before (central panels) and after OGD (right panels). 1: cultures preconditioned with HP; 2: preconditioned cultures pre-incubated for 24 h with 1 μmol/L BafA1; 3: preconditioned cultures pre-incubated for 24 h with 50 ng/mL TeNT. **E** Average percentage of dead cells before (black) and after (red) 40-min OGD in preconditioned cultures: control; pre-incubated for 24 h with 1 μmol/L BafA1 or 50 ng/mL TeNT. Vitality tests were performed before and after the OGD experiments in **A**, **B**, and **C**.

the intensity of EGFP fluorescence decreased dramatically after application of the detergent digitonin. More pronounced suppression of dithionite-induced BDNF release was found in neurons from (AAV)-Syn-BDNF-EGFP-transduced cultures incubated with TeNT, an inhibitor of Ca^{2+}-dependent vesicular fusion (Fig. 9B), and BDNF release was almost completely suppressed (Fig. 9E).

Thus, BafA1 and TeNT inhibited BDNF release from neurons transduced with (AAV)-Syn-BDNF-EGFP and affected the number and size of BDNF-containing vesicles. Suppression of vesicular secretion of BDNF abolished its protective action, and this was realized *via* the regulation of gene expression. The basal expression of genes encoding subunits of glutamate receptors increased substantially against the backdrop of reduced expression of the vesicular glutamate transporters and subunits of the GABA receptors. Furthermore, the expression of pro-inflammatory and pro-apoptotic genes also increased, indicating the induction of cell death by BafA1. The results of vitality tests, which were performed before the experiments, confirmed this conclusion (Fig. 7). These changes of gene expression may promote dysregulation of Ca^{2+} homeostasis in GABAergic neurons, leading to an irreversible global increase in $[Ca^{2+}]_i$ followed by death under OGD.

Thus, suppression of vesicular BDNF release abolished the protective effects of BDNF on hippocampal glutamatergic and GABAergic neurons under OGD, while the profile of gene expression turned towards apoptosis and excitotoxicity. Preconditioning of non-transduced cultures (without BDNF overexpression) with hypoxia/reoxygenation episodes promoted the development of resistance to OGD-induced damage. This effect of HP was expressed as decreases in the amplitudes of OGD-induced Ca^{2+} responses. However, we did not find this effect in GABAergic neurons. Moreover, the inhibitors of vesicular release abolished the protective action of HP in glutamatergic neurons. This finding indicated a pivotal role of vesicular release in the development of the protective effects of HP and the survival of glutamatergic neurons even in cultures without BDNF overexpression.

Discussion

We demonstrated in the present study the mechanisms underlying the neuroprotective action of vesicular BDNF release by neurons transduced with an adeno-associated virus construct. These mechanisms involved changes of expression of genes that promote the activation of HP in GABAergic neurons and enhancement of this phenomenon in glutamatergic neurons. We showed that BDNF overexpression in neurons affected the conductivity of ion channels of glutamate receptors, the intensity of inhibitory neurotransmission, and the expression of pro- and anti-apoptotic genes, probably promoting cell survival under further prolonged episodes of O_2 or O_2-glucose deprivation.

It has been reported that the effects of hypoxia are dual or even in opposition. It has been demonstrated that rats exposed to hypoxia while sleeping have memory impairments caused by damage to specific populations of neurons in the hippocampus and cortex [33] due to hypoxia-induced apoptosis, oxidative stress, and endoplasmic reticulum stress [34]. Some of the effects of hypoxia on the gene expression in our experiments can be considered negative. We demonstrated in previous work that episodes of hypoxia-reoxygenation promote apoptosis in GABAergic neurons, while on the contrary, such episodes activate protective mechanisms in glutamatergic neurons [11]. Nevertheless, these effects were virtually suppressed in transduced cultures with BDNF overexpression in neurons. So, these negative effects can be explained by the suppression of BDNF synthesis in control cultures after hypoxia. It has been shown that BDNF is necessary for the consolidation of long-term synaptic plasticity [35, 36]. The expression of BDNF during chronic intermittent hypoxia decreases along with the expression of plasmin, which transforms pro-BDNF to BDNF; that is, BDNF synthesis is also attenuated. The application of BDNF restores the amplitude of long-term potentiation (LTP) in mouse hippocampal slices under hypoxia. Moreover, microinjection of BDNF into mice prevents the impairment of LTP [34].

It should be noted that the RNA used for PCR assay was extracted from all cells, including neurons and astroglia. However, the results of imaging experiments and vitality tests demonstrated that the protective effects of BDNF and HP, which promote the survival of GABAergic neurons, may be caused by the demonstrated changes in expression
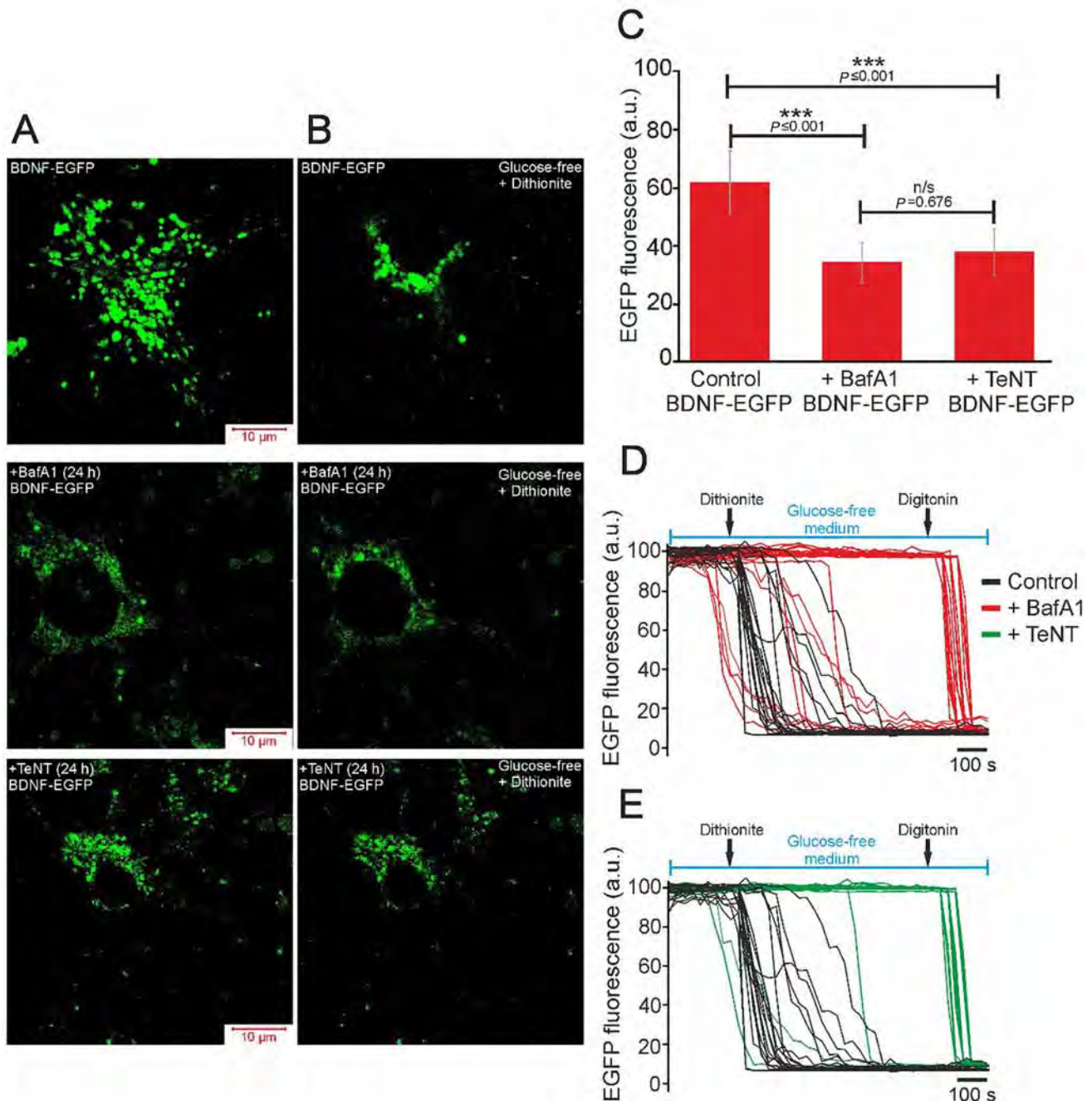
Fig. 9 Effects of bafilomycin A1 (BafA1) and tetanus toxin (TeNT) on vesicular BDNF release under chemical OGD. **A**, **B** Images of individual representative neurons from a control cell culture transduced with the (AAV)-Syn-BDNF-EGFP construct (BDNF-EGFP) and a transduced cell culture pre-incubated for 24 h with BafA1 (1 µmol/L) or TeNT (50 ng/mL). The images were captured before (**A**) and after (**B**) 10-min chemical OGD (glucose-free medium + dithionite). All images were captured using the same settings of gain, laser power, and pinhole. **C** Average intensity of EGFP fluorescence in controls and 24 h after incubation with BafA1 or TeNT. **D**, **E** Plots showing a dithionite-induced decrease of BDNF–EGFP fluorescence intensity recorded by time-lapse confocal microscopy in individual neurons in control (black traces), and after 24-h pre-incubation with BafA1 (**D**, red traces) or TeNT (**E**, green traces). Decreased EGFP fluorescence was only found in cultures pre-incubated with BafA1 and TeNT after application of 3 µmol/L digitonin.

of the genes. Abolition of the protective effects of BDNF occurred upon the suppression of vesicular release and was accompanied by feedback changes of gene expression.

Clearly, neuronal and neuroglial interactions can contribute to these effects and deserve investigation in further work. It is generally accepted that the damage and death of the most

vulnerable populations of neurons under ischemia leads to excessive glutamate release and the intensification of brain injury. Activation of the preconditioning mechanisms can eliminate this secondary effect, which is caused by the death of cells. Glutamate excitotoxicity is mediated by the activation of glutamate receptors, primarily NMDARs and AMPARs. The expression of genes encoding subunits of NMDARs decreased significantly after episodes of hypoxia, whereas basal Grin2a expression was substantially higher. It has been reported that BDNF potentiates excitatory synaptic transmission in postsynaptic terminals by regulating the expression and trafficking of GluA1 subunits [37] as well as *via* the enhancement of GluN1, GluN2a, and GluN2B expression [38]. It has been shown that BDNF downregulates NMDAR function and decreases the NMDAR-mediated increase in $[Ca^{2+}]_i$ [39]. These findings agree with our results demonstrating decreased amplitudes of NMDA-induced Ca^{2+} responses in cultures with BDNF overexpression. Reduction of the number of GluA2-containing AMPARs under ischemia increases the vulnerability of neurons to glutamate excitotoxicity and Ca^{2+} overload [40]. A shift in the GluA1/GluA2 ratio is caused by a decrease of GluA2 expression [41]. In our experiments, the expression of both subunits was decreased in cultures with BDNF overexpression in neurons, indicating a reduction of the number of AMPARs in general. Increased Gria2 expression after hypoxia can be considered to be a neuroprotective effect.

It is known that the incubation of cells with BDNF does not alter the level of GAD65/67, the molecular marker of GABAergic neurons [42]. However, exogenous BDNF promotes the formation of inhibitory synapses in *in vitro* and *in vivo* models, while BDNF scavenging decreases the number of inhibitory synapses [43, 44]. In our experiments, increased expression of genes encoding GABA$_A$ and GABA$_B$ receptor subunits indicated the strengthening of inhibition in networks with BDNF overexpression and after episodes of hypoxia.

Interestingly, the expression of genes encoding the vesicular glutamate transporters Vglut1 and Vglut2 was elevated in the transduced cultures. Vglut1 expression increased further after episodes of hypoxia. Then, the expression of both genes decreased 24 h after episodes of hypoxia in non-transduced cultures. Vesicular glutamate transporters play a pivotal role in neurotransmission. The intensity of their expression correlates with synaptic strength [45], synapse formation, and the recycling of synaptic vesicles [46]. VGLUT1-deficient mice show decreased spontaneous glutamate release and suppressed quantal synaptic transmission in the hippocampus [44]. VGLUT1 overexpression enhances AMPAR-induced EPSCs *via* increasing the amount of glutamate in vesicles [47]. Decreased VGLUT1 and VGLUT2 expression

changes the shape of secretory vesicles and their quantity in a synapse [46]. A deficit in VLUT2 suppresses glutamate secretion and attenuates long-term depression in synapses of the CA3–CA1 fields of the hippocampus in postnatal mice [48]. Decreased VGLUT1 expression causes memory impairment and depressive behavior [49], while VGLUT2-deficient heterozygous mice are characterized by neuropathic pain and defense responses [50]. The effects of BDNF on vesicular transporters have also been reported. It has been shown that BDNF enhances the expression of VGLUT1 and VGLUT2 *via* activation of Ntrk2 and PLCγ during the development of the hippocampus [42]. BDNF overexpression prevents the decrease of VGLUT1 expression and loss of glutamatergic synapses in a mouse model of Huntington's disease [51].

Brief episodes of hypoxia promoted the increase of expression of PI3K subunits in both control and (AAV)-Syn-BDNF-EGFP-transduced cultures, and the activation of PI3K mediates many neuroprotective mechanisms. The PI3K/Akt signaling pathway plays a pivotal role in cell survival [52], the trafficking of synaptic proteins, and the regulation of protein synthesis [53]. The mTOR complex is one of the key proteins that mediate these effects [54]. BDNF/mTOR is involved in the modulation of autophagy and the maintenance of synaptic plasticity. Inhibition of mTOR causes autophagy-mediated degradation of AMPARs in spines [55]. Interestingly, the effects of hypoxia on the translation of proteins are mediated by the inhibition of mTORC1 [56], which is considered to be the main regulator of cell growth, proliferation, and protein synthesis [57]. Hypoxia-induced disturbances of mTORC1 regulation are coupled with cancerous growth [58]. It has been demonstrated that mTOR activation is necessary for angiogenesis under hypoxia and the proliferation of cells forming blood vessels [59]. On the one hand, hypoxia activates mTOR and stimulates angiogenesis [60], as well as the proliferation of lung fibroblasts and cells of the aortic wall [59], and increases the activity and concentration of hypoxia-inducible factor 1α [61]. On the other hand, hypoxia inhibits mTOR activity in the fibroblasts of mouse embryos and suppresses protein synthesis [62]. It has been shown that both mTORC1 and mTORC2 mediate the response of cells to hypoxia [63]. We showed that the expression of genes encoding mTOR and growth factor receptor substrate 2 (FRS-2) was suppressed after episodes of hypoxia. FRS-2 interacts with Trk proteins and activates the protective PI3K/Akt and MAPK cascades [64]. This finding can explain the decreased expression of many mTOR-regulated genes in control cultures after hypoxia. On the other hand, mTOR and Frs-2 expression increased in (AAV)-Syn-BDNF-EGFP-transduced cultures after hypoxia, thus promoting the development of HP and cell survival. It is known that the pro-inflammatory cytokine

IL-1β suppresses the neuroprotective effects of BDNF and inhibits Akt [65]. Therefore, IL-1β can act as an endogenous inhibitor of the signaling pathway involving mTOR. In our experiments, Il-1β expression increased in control cultures after hypoxia, suggesting inhibition of mTOR by IL-1β. It has been demonstrated that the simultaneous application of IL-1β and BDNF or rapamycin (an inhibitor of mTOR) and BDNF causes cell death in a caspase-3-independent manner [66]. Therefore, mTOR activation is necessary for the realization of the neuroprotective effects of BDNF.

It is well-known that BDNF stimulates the expression of a range of anti-apoptotic genes and suppresses the expression of some pro-apoptotic genes. Overexpression of BDNF in hippocampal neurons treated with β-amyloid suppresses apoptosis *via* the activation of Bcl-2 expression and the prevention of cytosolic Ca^{2+} overload [67]. Activation of PI3K after preconditioning prevents cell death under ischemia *via* the suppression of Bax expression and the enhancement of Bcl-2 expression [68]. We demonstrated that the expression of anti-apoptotic genes such as Stat3, Socs3, and Bcl-xL increased in (AAV)-Syn-BDNF-EGFP-transduced cultures after hypoxia. In addition, the expression of genes encoding the anti-inflammatory cytokines IL-6 and IL-10 also increased in the transduced cultures 24 h after hypoxia. The same effect on the IL-10 level has been demonstrated after intranasal BDNF administration after ischemia [69].

Transcription of the BDNF gene is regulated by NF-κB and Ca^{2+} ions entering through ion channels and glutamate receptors [70–72]. Decreased levels of NF-κB and CREB have been demonstrated in models of post-traumatic stress disorder and "learned helplessness" [23]. We found decreased NF-κB expression in control cultures 24 h after hypoxia, while the expression of this gene was increased in transduced cultures with BDNF overexpression in neurons. Therefore, decreased NF-kB expression in controls can decrease the BDNF level.

Uncleaved pro-BDNF activates the high-affinity p75 receptor, which in turn induces pro-apoptotic signaling pathways [73]. Expression of the gene encoding pro-BDNF decreased in non-transduced cultures after hypoxia. Expression of Ntrk1 and Ntrk2 also decreased against the backdrop of elevated p75 expression. Mature BDNF activates tropomyosin-related kinase receptor type B (TrkB) [74] and the low-affinity neurotrophin receptor p75. The balance between the activity of these receptors determines the activation of signaling pathways promoting cell survival or cell death. Morphological changes and caspase-3 activation have been demonstrated in neurons with p75 overexpression three days after ischemia in the penumbra [75]. BDNF overexpression in neurons increased the Ntrk2 expression in our experiments. At the same time,

p75 expression decreased substantially in the transduced cultures before as well as 24 h after hypoxia, thus preventing activation of the pro-apoptotic signaling cascades. Receptors for BDNF are expressed in glutamatergic and GABAergic neurons. BDNF is mainly localized in the presynaptic terminals of glutamatergic neurons during *in vitro* neurogenesis and maturation, while TrkB receptors are localized on both GABAergic and glutamatergic terminals. Interestingly, TrkB receptors are extrasynaptic and often co-localize with NMDARs and GABA_A receptors [76]. Selective knockout of TrkB receptors in corticolimbic GABAergic interneurons promotes the development of social dominance in male mice, while optogenetic inhibition of the excitatory activity of neurons normalizes social behavior [77]. TrkA and TrkB receptors are often localized in GABAergic and glutamatergic neurons [78], and their activation by nerve growth factor or BDNF has anti-apoptotic effects [79, 80]. It is known that the expression of BDNF and TrkA receptors in hippocampal neurons decreases after cerebral ischemia [81, 82], but the expression of TrkB receptors increases [82]. The expression of BDNF and its TrkB receptor recovers better in preconditioned hippocampal neurons [83]. The expression of genes encoding TrkA and TrkB receptors decreased after episodes of hypoxia-reoxygenation in our experiments. This decrease coincided with the decrease of BDNF expression that can be considered a negative effect. On the contrary, the expression of BDNF and its receptors increased in cultures with BDNF overexpression, thus promoting the activation of HP in GABAergic neurons and enhancing this phenomenon in glutamatergic neurons. Taking into account that BDNF modulates both excitatory and inhibitory neurotransmission, it can be concluded that the changes of TrkA and TrkB expression affect glutamatergic and GABAergic neurons.

The effects of BDNF are realized *via* vesicular secretion and further binding with its receptors [84]. All the protective effects of BDNF overexpression in our experiments were abolished after inhibition of vesicular transmission with BafA1 and BFA. Clearly, the increased expression of some genes after incubation of cultures with BafA1 cannot be explained only by suppressed vesicular BDNF release. It is evident that BafA1 affects other aspects of cell function. The best known and well-described effects of BafA1 are the induction of apoptosis in a caspase-independent manner and downregulation of Bcl-2 and Bcl-xL [85]. Nevertheless, we found that caspase-3, Bcl-2, and Bcl-xL expression was increased after 24-h pre-incubation with BafA1, indicating that the contribution of BafA1-induced apoptosis can be considered insignificant.

It is known that GABAergic neurons are sensitive to hypoxia. We showed in recent reports that elevation of

$[Ca^{2+}]_i$ during brief episodes of hypoxia/reoxygenation occurs exclusively in GABAergic neurons. In addition, the percentage of necrotic cells 24 h after preconditioning is similar to that of GABAergic neurons in cell cultures [6, 11, 20]. It should be noted that mixed hippocampal cultures contain different cell types, including glutamatergic neurons, GABAergic neurons, and glial cells. In the present study, some conclusions were drawn based on data obtained as a result of non-selective analysis of large numbers of cells of the neuroglial complex (RT-PCR and vitality tests). The levels of expression of protective genes were higher in cultures with BDNF overexpression than in controls or preconditioned non-transduced cultures. In addition, OGD-induced necrosis and apoptosis were suppressed in transduced cultures, while pre-incubation of neuroglial cell cultures with inhibitors of vesicular release always enhanced the expression of pro-apoptotic and pro-inflammatory genes and increased the number of dead cells after OGD. Thus, most likely, BDNF overexpression also promotes the activation of neuroprotective signaling cascades in GABAergic neurons, because the percentage of living cells 24 h after 40-min OGD was $\sim 100\%$ (Fig. 4). All these data agree with the recordings of $[Ca^{2+}]_i$ dynamics in GABAergic neurons under OGD when BDNF overexpression promoted the development of the protective effects of HP and the suppression of global $[Ca^{2+}]_i$ elevation. Notably, preconditioning of non-transduced cultures with episodes of hypoxia induced the activation of protective signaling cascades and suppression of the OGD-induced Ca^{2+} responses only in glutamatergic neurons, thus indicating the protective effect of BDNF overexpression on GABAergic neurons.

Thus, we have demonstrated the critical role of BDNF in the development of cell tolerance to hypoxic conditions. Understanding the mechanisms of HP will help to determine pharmacological targets whose activation with endogenous or exogenous agonists may arrest the negative effects of global hypoxia or ischemia.

Conflict of interest The authors declare no conflict of interest.

References

1. Giaccia AJ, Simon MC, Johnson R. The biology of hypoxia: the role of oxygen sensing in development, normal function, and disease. Genes Dev 2004, 18: 2183–2194.
2. Erecińska M, Silver IA. Tissue oxygen tension and brain sensitivity to hypoxia. Respiration Physiology 2001, 128: 263–276.
3. Mukandala G, Tynan R, Lanigan S, O'Connor J. The effects of hypoxia and inflammation on synaptic signaling in the CNS. Brain Sciences 2016, 6: 6.
4. Hiraide T, Katsura K, Muramatsu H, Asano G, Katayama Y. Adenosine receptor antagonists cancelled the ischemic tolerance phenomenon in gerbil. Brain Res 2001, 910: 94–98.
5. Turovskaya MV, Gaidin SG, Mal'tseva VN, Zinchenko VP, Turovsky EA. Taxifolin protects neurons against ischemic injury *in vitro* via the activation of antioxidant systems and signal transduction pathways of GABAergic neurons. Mol Cell Neurosci 2019, 96: 10–24.
6. Turovsky EA, Zinchenko VP, Gaidin SG, Turovskaya MV. Calcium-binding proteins protect GABAergic neurons of the hippocampus from hypoxia and ischemia *in vitro*. Biochem Moscow Suppl A 2018, 12: 74–84.
7. Tretyakov AV, Farber HW. Endothelial cell tolerance to hypoxia. Potential role of purine nucleotide phosphates. J Clin Invest 1995, 95: 738–744.
8. Pugh CW, Ratcliffe PJ. Regulation of angiogenesis by hypoxia: role of the HIF system. Nat Med 2003, 9: 677–684.
9. Xi L, Tekin D, Gursoy EL, Tekin D, Gursoy EL, Salloum F, Levasseur JE, Kukreja RC. Evidence that NOS2 acts as a trigger and mediator of late preconditioning induced by acute systemic hypoxia. Am J Physiol Heart Circ Physiol 2002, 283: 5–12.
10. Park AM, Nagase H, Vinod Kumar S, Suzuki YJ. Acute intermittent hypoxia activates myocardial cell survival signaling. Am J Physiol Heart Circ Physiol 2007, 292: 751–757.
11. Turovskaya MV, Turovsky EA, Kononov AV, Zinchenko VP. Short-term hypoxia induces a selective death of GABAergic neurons. Biochem Moscow Suppl Ser A 2014, 8: 14–135.
12. Schurr A, Reid KH, Tseng MT, West C, Rigor BM. Adaptation of adult brain tissue to anoxia and hypoxia *in vitro*. Brain Res 1986, 374: 244–248.
13. Stagliano NE, Perez-Pinzon MA, Moskowitz MA, Huang PL. Focal ischemic preconditioning induces rapid tolerance to middle cerebral artery occlusion in mice. J Cereb Blood Flow Metab 1999, 19: 757–761.
14. Lu GW, Yu S, Li RH, Cui XY, Gao CY. Hypoxic preconditioning: a novel intrinsic cytoprotective strategy. Mol Neurobiol 2005, 31: 255–271.
15. Turovskaya MV, Zinchenko VP, Babaev AA, Epifanova EA, Tarabykin VS, Turovsky EA, *et al*. Mutation in the Sip1 transcription factor leads to a disturbance of the preconditioning

of AMPA receptors by episodes of hypoxia in neurons of the cerebral cortex due to changes in their activity and subunit composition. The protective effects of interleukin-10. Arch Biochem Biophys 2018, 654: 126–135.

16. Gidday JM. Cerebral preconditioning and ischaemic tolerance. Nat Rev 2006, 7: 437–448.

17. Bickler PE, Fahlman CS. Expression of signal transduction genes differs after hypoxic or isoflurane preconditioning of rat hippocampal slice cultures. Anesthesiology 2009, 111: 258–266.

18. Arthur PG, Lim SC, Meloni BP, Munns SE, Chan A, Knuckey NW. The protective effect of hypoxic preconditioning on cortical neuronal cultures is associated with increases in the activity of several antioxidant enzymes. Brain Res 2004, 1017: 146–154.

19. Pérez-Pinzón MA, Born JG, Centeno JM. Calcium and increase excitability promote tolerance against anoxia in hippocampal slices. Brain Res 1999, 833: 20–26.

20. Turovsky EA, Turovskaya MV, Kononov AV, Zinchenko VP. Short-term episodes of hypoxia induce posthypoxic hyperexcitability and selective death of GABAergic hippocampal neurons. Exp Neurol 2013, 250: 1–7.

21. Kim J, Yang JH, Ryu IS, Sohn S, Kim S, Choe ES. Interactions of glutamatergic neurotransmission and brain-derived neurotrophic factor in the regulation of behaviors after nicotine administration. Int J Mol Sci 2019, 20: 2943.

22. Gaidin SG, Turovskaya MV, Gavrish MS, Babaev AA, Mal'tseva VN, Blinova EV, et al. The selective BDNF overexpression in neurons protects neuroglial networks against OGD and glutamate-induced excitotoxicity. Int J Neurosci 2019. https://doi.org/10.1080/00207454.2019.1691205.

23. Baranova KA, Rybnikova EA, Samoilov MO. The neurotrophin BDNF is involved in the development and prevention of stress-induced psychopathologies. Neurochem J 2015, 9: 108–115.

24. Mitroshina EV, Mishchenko TA, Usenko AV, Epifanova EA, Yarkov RS, GavrishMS, et al. AAV-Syn-BDNF-EGFP virus construct exerts neuroprotective action on the hippocampal neural network during hypoxia in vitro. Int J Mol Sci 2018, 19: E2295.

25. Zinchenko VP, Turovsky EA, Turovskaya MV, Berezhnov AV, Sergeev AI, Dynnik VV. NAD causes dissociation of neural networks into subpopulations of neurons by inhibiting the network synchronous hyperactivity evoked by ammonium ions. Biochem Moscow Suppl Ser A 2016, 10: 118–125.

26. Zinchenko VP, Turovskaya MV, Teplov IYu, Berezhnov AV, Turovsky EA. The role of parvalbumin-containing interneurons in the regulation of spontaneous synchronous activity of brain neurons in culture. Biophysics 2016, 61: 85–93.

27. Schmid I, Uittenbogaart C, Jamieson BD. Live-cell assay for detection of apoptosis by dual-laser flow cytometry using Hoechst 33342 and 7-amino-actino-mycin D Nat Protoc 2007, 2: 187–190.

28. Livak KJ, Thomas D Schmittgen. Analysis of relative gene expression data using real-time quantitative PCR and the $2^{-\Delta\Delta Ct}$ method. Methods 2001, 25: 402–408.

29. Kosenkov AM, Teplov IY, Sergeev AI, Maiorov S., Zinchenko VP, Gaidin SG. Domoic acid suppresses hyperexcitation in the network due to activation of kainate receptors of GABAergic neurons. Arch Biochem Biophys 2019, 671: 52–61.

30. Gaidin SG, Turovskaya MV, Mal'tseva VN, Zinchenko VP, Blinova EV, Turovsky EA. A complex neuroprotective effect of alpha-2-adrenergic receptor agonists in a model of cerebral ischemia–reoxygenation in vitro. Biochem (Moscow) Suppl Ser A 2019, 13: 319–333.

31. Kowiański P, Lietzau G, Czuba E, Waśkow M, Steliga A, Moryś J. BDNF: A key factor with multipotent impact on brain signaling and synaptic plasticity. Cell Mol Neurobiol 2018, 38: 579–593.

32. Goodman LJ, Valverde J, Lim F, Geschwind MD, Federoff HJ, Gellar AI, et al. Regulated release and polarized localization of brain-derived neurotrophic factor in hippocampal neurons. Mol Cell Neurosci 1996, 7: 222–238.

33. Gozal D, Daniel JM, Dohanich GP. Behavioral and anatomical correlates of chronic episodic hypoxia during sleep in the rat. J Neurosci 2001, 21: 2442–2450.

34. Xie H, Yung WH. Chronic intermittent hypoxia-induced deficits in synaptic plasticity and neurocognitive functions: a role for brain-derived neurotrophic factor. Acta Pharmacol Sin 2012, 33: 5–10.

35. Pang PT, Teng HK, Zaitsev E, Woo NT, Sakata K, Zhen S, et al. Cleavage of proBDNF by tPA/plasmin is essential for long-term hippocampal plasticity. Science 2004, 306: 487–491.

36. Mishchenko TA, Mitroshina EV, Usenko AV, Voronova NV, Astrakhanova TA, Shirokova OM, et al., Vedunova MV Features of neural network formation and their functions in primary hippocampal cultures on the background of chronic TrkB receptor system influence. Front. Physiol 2019, 9:1925.

37. Caldeira MV, Melo CV, Pereira DB, Carvalho R, Correia SS, Backos DS, et al. Brain-derived neurotrophic factor regulates the expression and synaptic delivery of alpha-amino-3-hydroxy-5-methyl-4-isoxazole propionic acid receptor subunits in hippocampal neurons. J Biol Chem 2007, 282: 12619–12628.

38. Crozier RA, Black IB, Plummer MR. Blockade of NR2B-containing NMDA receptors prevents BDNF enhancement of glutamatergic transmission in hippocampal neurons. Learn Mem 1999, 6: 257–266.

39. Brandoli C, Sanna A, De Bernardi MA, Follesa P, Brooker G, Mocchetti I, et al. Brain-derived neurotrophic factor and basic fibroblast growth factor downregulate NMDA receptor function in cerebellar granule cells. J Neurosci 1998, 18: 7953–7961.

40. Liu S, Lau L, Wei J, Zhu D, Zou S, Sun HS, et al. Expression of Ca2 + -permeable AMPA receptor channels primes cell death in transient forebrain ischemia. Neuron 2004, 43: 43–55.

41. Han X.-J, Shi ZS, Xia LX, Zhu LH, Zeng L, Nie JH, et al. Changes in synaptic plasticity and expression of glutamate receptor subunits in the CA1 and CA3 areas of the hippocampus after transient global ischemia. Neuroscience 2016, 327: 64–78.

42. Melo CV, Mele M, Curcio M, Comprido D, Silva CG, Duarte CB. BDNF regulates the expression and distribution of vesicular glutamate transporters in cultured hippocampal neurons. PLoS One 2013, 8: e53793.

43. Bao S, Chen L, Qiao X, Thompson RF. Transgenic brain-derived neurotrophic factor modulates a developing cerebellar inhibitory synapse. Learn Mem 1999, 6: 276–283.

44. Gonzalez MI. Brain-derived neurotrophic factor promotes gephyrin protein expression and GABAA receptor clustering in immature cultured hippocampal cells. Neurochem Int 2014, 72: 14–21.

45. Wojcik SM, Rhee JS, Herzog E, Sigler A, Jahn R, Takamori S, et al. An essential role for vesicular glutamate transporter 1 (VGLUT1) in postnatal development andcontrol of quantal size. Proc Natl Acad Sci USA 2004, 101: 7158–7163.

46. Fremeau RT, Jr., Kam K, Qureshi T, Johnson J, Copenhagen DR, Storm-Mathisen J, et al. Vesicular glutamate transporters 1 and 2 target to functionally distinct synaptic release sites. Science 2004, 304: 1815–1819.

47. Wilson NR, Kang J, Hueske EV, Leung T, Varoqui H, Murnick JG, et al. Presynaptic regulation of quantal size by the vesicular glutamate transporter VGLUT1. J Neurosci 2005, 25: 6221–6234.

48. He H, Mahnke AH, Doyle S, Fan N, Wang C-C, Hall BJ, et al. Neurodevelopmental role for VGLUT2 in pyramidal neuron plasticity, dendritic refinement, and in spatial learning. J Neurosci 2012, 32: 15886–15901.

49. Tordera RM, Totterdell S, Wojcik SM, Brose N, Elizalde N, Lasheras B, et al. Enhanced anxiety, depressive-like behaviour and impaired recognition memory in mice with reduced expression of the vesicular glutamate transporter 1 (VGLUT1). Eur J Neurosci 2007, 25: 281–290.

50. Moechars D, Weston MC, Leo S, Callaerts-Vegh Z, Goris I, Daneels G, et al. Vesicular glutamate transporter VGLUT2 expression levels control quantal size and neuropathic pain. J Neurosci 2006, 26: 12055–12066.

51. Giralt A, Carreton O, Lao-Peregrin C, Martin ED, Alberch J. Conditional BDNF release under pathological conditions improves Hunting-ton's disease pathology by delaying neuronal dysfunction. Mol Neurodegener 2011, 6: 71.

52. Brunet A, Datta SR, Greenberg ME. Transcription-dependent and independent control of neuronal survival by the PI3K-Akt signaling pathway. Curr Opin Neurobiol 2001, 11: 297–305.

53. Yoshii A, Constantine-Paton M. BDNF induces transport of PSD-95 to dendrites through PI3K-AKT signaling after NMDA receptor activation. Nat Neurosci 2007, 10: 702–711.

54. Takei N, Inamura N, Kawamura M, Namba H, Hara K, Yonezawa K, et al. Brain-derived neurotrophic factor induces mammalian target of rapamycin-dependent local activation of translation machinery and protein synthesis in neuronal dendrites. J Neurosci 2004, 24: 9760–9769.

55. Shehata M, Matsumura H, Okubo-Suzuki R, Ohkawa N, Inokuchi K. Neuronal stimulation induces autophagy in hippocampal neurons that is involved in AMPA receptor degradation after chemical long-term depression. J Neurosci 2012, 32: 10413–10422.

56. Koritzinsky M, Magagnin MG, van den Beucken T, Seigneuric R, Savelkouls K, Dostie J, et al. Gene expression during acute and prolonged hypoxia is regulated by distinct mechanisms of translational control. EMBO J 2006, 25: 1114–1125.

57. Ma XM, Blenis J. Molecular mechanisms of mTOR-mediated translational control. Nat Rev Mol Cell Biol 2009, 10: 307–318.

58. Schneider A, Younis RH, Gutkind JS. Hypoxia-induced energy stress inhibits the mTOR pathway by activating an AMPK/REDD1 signaling axis in head and neck squamous cell carcinoma. Neoplasia 2008, 10: 1295–1302.

59. Humar R, Kiefer FN, Berns H, Resink TJ, Battegay EJ. Hypoxia enhances vascular cell proliferation and angiogenesis *in vitro* via rapamycin (mTOR)-dependent signaling. FASEB J 2002, 16: 771–780.

60. Bernardi R, Guernah I, Jin D, Grisendi S, Alimonti A, Teruya-Feldstein J, et al. PML inhibits HIF-1alpha translation and neoangiogenesis through repression of mTOR. Nature 2006, 442:779–785.

61. Hudson CC, Liu M, Chiang GG, Otterness DM, Loomis DC, Kaper F, et al. Regulation of hypoxia-inducible factor 1alpha expression and function by the mammalian target of rapamycin. Mol Cell Biol 2002, 22: 7004–7014.

62. Brugarolas J, Lei K, Hurley RL, Manning BD, Reiling JH, Hafen E, et al. Regulation of mTOR function in response to hypoxia by REDD1 and the TSC1/TSC2 tumor suppressor complex. Genes Dev 2004, 18: 2893–2904.

63. Li W, Petrimpol M, Molle KD, Hall MN, Battegay EJ, Humar R. Hypoxia-induced endothelial proliferation requires both mTORC1 and mTORC2. Circ Res 2007, 100: 79–87.

64. Lessmann V, Gottmann K, Malcangio M. Neurotrophin secretion: current facts and future prospects. Prog Neurobiol 2003, 69: 341–374.

65. Tong L, Balazs R, Soiampornkul R, Thangnipon W, Cotman CW. Interleukin-1 beta impairs brain derived neurotrophic factor-induced signal transduction. Neurobiol Aging 2008, 29: 1380–1393.

66. Smith ED, Prieto GA, Tong L, Sears-Kraxberger I, Rice JD, Steward O, et al. Rapamycin and interleukin-1β impair brain-derived neurotrophic factor-dependent neuron survival by modulating autophagy. J Biol Chem 2014, 289: 20615–20629.

67. Liu Z, Ma D, Feng G, Ma Y, Hu H: Recombinant AAV-mediated expression of human BDNF protects neurons against cell apoptosis in Abeta-induced neuronal damage model. J Huazhong Univ Sci Technolog Med Sci 2007, 27: 233–236.

68. Zhang YB, Guo ZD, Li MY, Li SJ, Niu JZ, Yanf MF, et al. Cerebrospinal fluid from rats given hypoxic preconditioning protects neurons from oxygen-glucose deprivation-induced injury. Neural Regener Res 2015, 10: 1471–1476.

69. Jiang Y, Wei N, Lu T, Zhu J, Xu G, Liu X. Intranasal brain-derived neurotrophic factor protects brain from ischemic insult via modulating local inflammation in rats. Neuroscience 2011. 172: 398–405.

70. West AE, Chen WG, Dalva MB, Dolmetsch RE, Kornhauser JM, Shaywitz AJ, et al. Calcium regulation of neuronal gene expression. Proc Natl Acad Sci USA 2001, 98: 11024–11131.

71. Shieh PB, Hu SC, Bobb K, Timmusk T, Ghosh A. Identification of a signaling pathway involved in calcium regulation of BDNF expression. Neuron 1998, 20: 727–740.

72. Lipsky RH, Xu K, Zhu D, Kelly C, Terhakopian A, Novelli A, et al. Nuclear factor kappaB is a critical determinant in N-methyl-D-aspartate receptor-mediated neuroprotection. J Neurochem 2001, 78: 254–264.

73. Teng HK, Teng KK, Lee R, Wright S, Tevar S, Almeida RD, et al. ProBDNF induces neuronal apoptosis via activation of a receptor complex of p75NTRand sortilin. J Neurosci 2005, 25: 5455–5463.

74. Massa SM, Yang T, Xie Y, Shi J, Bilgen M, Joyce JN, et al. Small molecule BDNF mimetics activate TrkB signaling and prevent neuronal degeneration in rodents. J Clin Invest 2010, 120: 1774–1785.

75. Angelo MF, Aviles-Reyes RX, Villarreal A, Barker P, Reines AG, Ramos AJ, et al. p75 NTR expression is induced in isolated neurons of the penumbra after ischemia by cortical devascularization. J Neurosci Res 2009, 87: 1892–1903.

76. Swanwick CC, Harrison MB, Kapur J. Synaptic and extrasynaptic localization of brain-derived neurotrophic factor and the tyrosine kinase B receptor in cultured hippocampal neurons. J Comp Neurol 2004, 478: 405–417.

77. Tan S, Xiao Y, Yin HH, Chen AI, Soong TW, JE HS, Postnatal TrkB ablation in corticolimbic interneurons induces social dominance in male mice. Proc Natl Acad Sci USA 2018, 115: E9909–E9915.

78. Bibel M, Barde YA. Neurotrophins: key regulators of cell fate and cell shape in the vertebrate nervous system. Genes Dev 2000, 14: 2919–2937.

79. Nguyen TL, Kim CK, Cho JH, Lee KH, Ahn JY. Neuroprotection signaling pathway of nerve growth factor and brain-derived neurotrophic factor against staurosporine induced apoptosis in hippocampal H19-7/IGF-IR [corrected]. Exp Mol Med 2010, 42: 583–595.

80. Vedunova MV, Mishchenko TA, Mitroshina EV, Mukhina IV. TrkB-mediated neuroprotective and antihypoxic properties of Brain-derived neurotrophic factor. Oxid Med Cell Longev 2015, 453901. https://doi.org/10.1155/2015/453901.

81. Lindvall O, Ernfors P, Bengzon J, Kokaia Z, Smith ML, Siesjo BK, et al. Differential regulation of mRNAs for nerve growth factor, brain-derived neurotrophic factor, and neurotrophin 3 in the adult rat brain following cerebral ischemia and hypoglycemic coma. Proc Natl Acad Sci U S A 1992, 89: 648–652.

82. Merlio JP, Ernfors P, Kokaia Z, Middlemas DS, Bengzon J, Kokaia M, et al. Increased production of the TrkB protein

tyrosine kinase receptor after brain insults. Neuron 1993, 10: 151–164.

83. Lee TH, Yang JT, Ko YS, Kato H, Itoyama Y, Kogure K. Influence of ischemic preconditioning on levels of nerve growth factor, brain-derived neurotrophic factor and their high-affinity receptors in hippocampus following forebrain ischemia. Brain Res 2008, 1187: 1–11.

84. Matsuda N, Lu H, Fukata Y, Noritake J, Gao H, Mukherjee S, *et al.* Differential activity-dependent secretion of brain-derived neurotrophic factor from axon and dendrite. J Neurosci 2009, 29: 14185–1498.

85. Yan Y, Jiang K, Liu P, Zhang X, Dong X, Gao J, *et al.* Bafilomycin A1 induces caspase-independent cell death in hepatocellular carcinoma cells via targeting of autophagy and MAPK pathways. Sci Rep 2016, 6: 37052.

ORIGINAL ARTICLE

Altered Energy Metabolism During Early Optic Nerve Crush Injury: Implications of Warburg-Like Aerobic Glycolysis in Facilitating Retinal Ganglion Cell Survival

Jingyi Zhu[1] · Ping Li[2] · Yuan-Guo Zhou[2] · Jian Ye[1]

Abstract Neurons, especially axons, are metabolically demanding and energetically vulnerable during injury. However, the exact energy budget alterations that occur early after axon injury and the effects of these changes on neuronal survival remain unknown. Using a classic mouse model of optic nerve-crush injury, we found that traumatized optic nerves and retinas harbor the potential to mobilize two primary energetic machineries, glycolysis and oxidative phosphorylation, to satisfy the robustly increased adenosine triphosphate (ATP) demand. Further exploration of metabolic activation showed that mitochondrial oxidative phosphorylation was amplified over other pathways, which may lead to decreased retinal ganglion cell (RGC) survival despite its supplement to ATP production. Gene set enrichment analysis of a microarray (GSE32309) identified significant activation of oxidative phosphorylation in injured retinas from wild-type mice compared to those from mice with deletion of phosphatase and tensin homolog (PTEN), while PTEN-/- mice had more robust RGC survival. Therefore, we speculated that the oxidation-favoring metabolic pattern after optic nerve-crush injury could be adverse for RGC survival. After redirecting metabolic flux toward glycolysis (magnifying the Warburg effect) using the drug meclizine, we successfully increased RGC survival. Thus, we provide novel insights into a potential bioenergetics-based strategy for neuroprotection.

Keywords Optic nerve crush · ATP · Glycolysis · Oxidative phosphorylation · RGC survival

Introduction

Neuronal death is a major factor that causes permanent neurological disability after traumatic axonal injury, and the prevention of neuron loss has long been the focus of research on multiple fronts [1, 2]. In these research efforts, energy metabolism is a key factor, since central nervous system (CNS) tissues, particularly axons, are among the most metabolically demanding tissues [3, 4].

Early after CNS trauma, injured axons require extra energy to maintain subsequent energy-intensive processes, such as cytoskeletal structural rearrangements [5, 6]. Energy deficits in axons have been reported to decrease neuronal function and survival [7]. Few attempts have been made to investigate the metabolic patterns of traumatized neurons and their translational significance for neuroprotection [8]. However, our understanding of energetics-based pathological mechanisms in injured neurons is rather limited, hindering the development of bioenergetics-based treatments to address neuronal death [9]. Energy in the form of adenosine triphosphate (ATP) is generated by glucose metabolism in the CNS, predominantly through two main routes, glycolysis and oxidative phosphorylation.

✉ Yuan-Guo Zhou
yuanguo.zhou@gmail.com

✉ Jian Ye
yejian1979@163.com

1 Department of Ophthalmology, Army Medical Center of the People's Liberation Army (PLA), Army Medical University, Chongqing 400042, China

2 Molecular Biology Center, State Key Laboratory of Trauma, Burn, and Combined Injury, Research Institute of Surgery, Army Medical Center of the PLA, Army Medical University, Chongqing 400042, China

Each route has its own merits [10]; therefore, these routes are favored by cells in different states and serve diverse cellular processes. For instance, cancer cells and embryonic retinal cells prefer glycolysis and lactate metabolism even with abundant oxygen – this is also termed aerobic glycolysis or the Warburg effect [11–14]. However, the dependence of traumatized neurons on glycolysis and oxidative phosphorylation remains unclear [9]. A better understanding of the precise adaptation of energetic pathways to CNS trauma may be critical for providing novel insights into neuroprotection.

We therefore set out to investigate altered energy metabolism in injured neurons and determine its potential significance for neuronal survival early after trauma using the mouse optic nerve crush (ONC) model [15, 16].

Materials and Methods

Animals

All protocols were approved by the Administration of Affairs Concerning Experimental Animals Guidelines of the Third Military Medical University. Eight- to ten-week-old adult C57BL/6 male mice weighing ∼22 g–26 g were purchased from the Jackson Laboratory and housed in the Animal Care Center of the Research Institute of Surgery and Daping Hospital (Third Military Medical University, Chongqing, China). The mice were housed in groups of three under a 12-h light/dark cycle at room temperature (RT) of 22°C and given access to food and water *ad libitum*. All efforts were made to minimize animal suffering.

Experimental Design and Statistical Analysis

Physiological and biochemical indexes were measured on day 1 after surgery, unless otherwise noted, to evaluate the early-stage response.

Surgical Procedures

Mice were anesthetized *via* an intraperitoneal (i.p.) injection of pentobarbital sodium (50 mg/kg). The conjunctiva of the left eye was incised, and the orbital muscles were carefully moved aside to avoid damage to blood vessels. The exposed optic nerve was crushed 2 mm distal to the eyeball for 20 s using extra-fine self-closing forceps following previously published methods [16–18]. Proparacaine hydrochloride was applied during surgery and postoperatively as a local anesthetic. A sham operation was performed on the right eye as a self-control. All surgery was performed at 08:00, and tissue was harvested at the same time the next day, unless otherwise noted.

Energy Metabolism Measurements

ATP, ADP, and ADP/ATP Ratio Assays

The mice were sacrificed by cervical dislocation and the retinas and optic nerves were removed immediately. Approximately 6 mm of the optic nerve from the optic head containing the lesion was removed immediately and placed in lysis buffer (Cat. S0026, Beyotime, Chengdu, China) to halt metabolism. The tissue was dissected into small pieces and sonicated as described in a previous study [19]. The supernatant was collected after centrifugation at 12,000 rpm for 10 min at 4°C. The protein concentration was measured using a bicinchoninic acid protein assay kit (Cat. P0012, Beyotime). The supernatant was mixed with the prepared reagent and measured using a firefly luciferase-based ATP assay kit (Cat. S0026, Beyotime), an EnzyLight adenosine diphosphate (ADP) assay kit (Cat. EADP-100, BioAssay Systems, USA), and an Enzy-Light^{TM} ADP/ATP Ratio assay kit (Cat. ELDT-100, BioAssay Systems) according to the manufacturers' instructions using a monochromator microplate reader (SafireII, Tecan, Switzerland). ATP concentrations were calculated from a log–log plot of the standard curve and normalized to the protein concentration.

Lactate Assay

Retinas were harvested and homogenized as described above. The lactate level in the supernatant was determined using a commercial colorimetric kit (Cat. AMEKO2677, Lianshuo Biological, China) according to the manufacturer's protocol.

Lactate Dehydrogenase (LDH) Activity

Supernatants of freshly dissected, homogenized optic nerves were obtained as described above. LDH activity in the samples was measured using an LDH assay kit (Cat. A020, Jiancheng, Nanjing, China) following the manufacturer's protocol.

Staining Protocol

Retinal Whole-Mount Immunofluorescence Assay

Retinal ganglion cell (RGC) survival was determined by counting the number of β-III-tubulin (Tuj1)-positive RGCs in retinal whole-mounts. Tuj1 specifically recognizes neuronal tubulin and is used as an RGC marker [20, 21]. The mice were anesthetized and transcardially perfused with 0.9% saline and 4% paraformaldehyde (PFA), after which the retinas were carefully harvested. Four

symmetrical radial cuts were made on each retina. After postfixation in 4% PFA for 1 h at 4°C, the retinas were rinsed three times with phosphate-buffered saline (PBS) and simultaneously permeabilized and blocked in a solution of 3% Triton X-100 in 10% normal goat serum (Cat. ab7481, Abcam, Cambridge, UK) in PBS at room temperature. The samples were incubated with the primary antibody (1:600, Cat. ab78078, Abcam) for 2 days at 4°C. The retinas were washed three times with PBS for 15 min each and then incubated overnight with secondary antibodies [1:400, anti-mouse antibody conjugated with Alexa Fluor 488 (Cat. A-11001, Thermo Fisher Scientific, Waltham, MA, USA)] at 4°C.

Frozen Retinal and Optic Nerve Sections

Eyeballs embedded in optimal cutting temperature compound were cut into 10-μm sections along the sagittal axis on a freezing microtome. The middle portions of the optic nerves were cut into serial sections 8 μm thick.

Diaminobenzidine Cytochrome Oxidase Histochemistry

Mitochondrial activity was investigated using diaminobenzidine cytochrome oxidase (DAB COX) histochemistry. COX is the terminal enzyme in oxidative phosphorylation and a reliable, well-established marker for measuring mitochondrial ATP generation. Frozen optic nerve sections were placed onto microscope slides and immersed. The DAB COX histochemistry procedure was conducted according to the manufacturer's protocol (Cat. Lt, R20440, Yuanye Biotechnology Co., Shanghai, China).

Five randomly-selected visual fields from each section proximal to the crush site were subsequently photographed. Brown or tan staining of the cytoplasm and/or membrane indicated positive labeling, and the mean optical density of brown or tan staining was analyzed.

LDH Histochemistry

A fresh slide of optic nerve was obtained as described above, and LDH was stained following the manufacturer's protocol (Cat. G2362, Solarbio, Beijing, China). Blue/purple staining indicated positive labeling. Histochemical staining was automatically categorized as strongly positive, positive, weakly positive, or negative; then the number of positive cells was counted, and the samples were rated by ImageJ IHC Profiler (https://sourceforge.net/projects/ihc profiler/) as listed in Tables S1 and S2 in the Supplementary materials.

Image Acquisition and Analysis

All immunofluorescence images were acquired on an SP8 confocal microscope (Leica, Germany), and immunohistochemistry images were captured using a camera (Dfc290, Leica) attached to an upright microscope (Dm1000, Leica Microsystems, Germany).

To obtain RGC counts in retinal whole-mounts, eight fields from each retinal explant were randomly sampled at central and peripheral locations with progressive eccentricity from the optic nerve head through the midline of the four retinal quadrants at distances of 1.0 and 1.5 mm from the margin of the optic disc. Tuj1-positive RGCs in all fields were counted with ImageJ software (developed by Wayne Rasband, National Institutes of Health, Bethesda, MD; available at http://rsb.info.nih.gov/ij/index.html). The counts were averaged for each explant.

Calculation of Changes in Glycolysis and Respiration Rates

Three types of unilateral optic nerve crush (ONC) models were adopted; saline, carbonyl cyanide 3-chlorophenylhydrazone (CCCP), or 2-deoxyglucose (2DG) was injected 1 h prior to retinal extraction in each group. Then, ATP levels were measured in the following: the contralateral intact optic nerve (CON), the injured optic nerve (ONC), the contralateral intact optic nerve after 2DG treatment (CON_{2DG}), and the injured optic nerve after 2DG treatment (ONC_{2DG}). The difference between CON and CON_{2DG} is the energy produced by glycolysis in the intact optic nerve ($E_{2DG/C}$), and the difference between ONC and ONC_{2DG} is the energy produced by glycolysis in the injured optic nerve ($E_{2DG/O}$). The ONC/CON ratio was a fixed cutoff point and the ONC_{2DG}/CON_{2DG} and ONC_{CCCP}/CON_{CCCP} ratios were compared to determine if the glycolysis and respiration rates increased or decreased. The specific calculations are shown in Fig. 5A.

Reverse Transcription qPCR (RT-qPCR)

TRIzol reagent was used for RNA extraction according to the manufacturer's instructions. The total RNA concentrations in the samples were measured using a NanoDrop system (Thermo Scientific). Then, the RNA was reverse-transcribed using a reverse transcription kit (Cat. RR037A, TaKaRa Bio Inc.). Gene expression was quantified using a real-time fluorescence-based quantitative PCR kit (Cat. RR039B, TaKaRa Bio Inc.). Beta-actin was used as an internal control to normalize the RT-qPCR readout.

764

Neurosci. Bull. July, 2020, 36(7):761–777

Flow Cytometry

Thy-1-Positive RGC Counting

A previously reported flow cytometry-based Thy-1-labeling RGC counting method was also applied to assess RGC survival rates. RGCs were isolated using the method described by Chintalapudi [22, 23], with some modifications. Suspensions of retinal cells were generated using enzymatic digestion and subsequently filtered through a sterile 70-µm nylon strainer to obtain single-cell suspensions. Each suspension was centrifuged for 10 min at 200 × g, and the supernatant was discarded. The pellet was resuspended in PBS/1% FBS, and the cell density was determined. Two microliters of rat anti-mouse Thy-1.2 phycoerythrin (PE) (BD Biosciences, Cat. 553014) antibody were used to stain $\sim 5.0 \times 10^6$ cells in a 1000 µL volume for 6 min at RT. The samples were analyzed using an ACEA NovoCyte instrument.

Mitochondrial Labeling

Mitochondrial function was evaluated with mitochondrial membrane potential-dependent ($\Delta\psi$m) MitoTracker Deep Red FM staining. The cells were incubated with 100 nmol/L MitoTracker Deep Red FM for 8 min at RT. Deep red fluorescence (excitation at 644 nm, emission at 665 nm) was detected through the allophycocyanin channel.

Derivation and Analysis of Microarray Data

We used the gene set enrichment analysis (GSEA) computational method to analyze results in the form of pathway rankings that indicated which pathways play important roles in injured wild-type mice compared to PTEN-deficient mice [24, 25]. The GSE32309 gene microarray data were downloaded from the Gene Expression Omnibus database [26] (http://www.ncbi.nlm.nih.gov/geo/), which included three normal mice (GSM800486, GSM800487, and GSM800488) and three mice with PTEN deletion (GSM800489, GSM8004870, and GSM8004871) based on the Mouse Gene 1.0 ST Array from Affymetrix, Inc. (Santa Clara, CA, USA) [27]. The original CEL files were converted into expression measures and normalized using the affy package in the R language (http://www.bioconductor.org/packages/3.0/bioc/) [28]. Then, the data were analyzed with GSEA-3.0 software with the default parameters, except for the permutation parameter selection, which was set to "geneset" instead of "phenotype" [25]. The enrichment score, normalized enrichment score, P value, and false discovery rate Q value were obtained from the GSEA output reports, and these were then used to rank the gene sets.

Drug Administration and Effectiveness

Doses of 500 mg/kg 2DG (D8375, Sigma-Aldrich), 4 mg/kg CCCP (C2759, Sigma-Aldrich), 100 mg/kg meclizine (B1786, Apexbio), and 50 mg/kg or 5 µmol/kg ATP (PV3227, Thermo Fisher) were injected intraperitoneally.

We injected 500 mg/kg 2DG or 4 mg/kg CCCP immediately after surgery to investigate the numbers of surviving RGCs after inhibition of glycolysis and oxidative phosphorylation. For the analysis of glucose metabolism (Fig. 5), mice were injected with the same dose of 2DG (500 mg/kg)/iodoacetic acid (60 mg/kg)/oligomycin (0.5 mg/kg)/CCCP (4 mg/kg) 1 h prior to euthanasia.

Statistical Methods

The experimenter was blinded to the treatment of the mice when collecting and analyzing the data. The data are presented as the mean ± SD, and the error bars indicate the 95% confidence intervals. Paired t-tests were applied to compare eyes from the same animal or the optic nerve and retina from the same eye, and independent-samples t-tests were used for unrelated samples. Multiple comparisons were performed using one-way analysis of variance (ANOVA) followed by Tukey's or Dunnett's *post hoc* test, or two-way ANOVA followed by Sidak's *post hoc* test. Correlations were analyzed using the Pearson correlation test as appropriate. A P value <0.05 indicated statistical significance.

Statistical analyses were performed using Sigma Plot version 13.0 and PRISM version 6.0 (GraphPad Software). Graphics were plotted in PRISM version 6.0 and Adobe Illustrator [29, 30].

Results

ONC Triggers Metabolic Activation in Injured Optic Nerves and Retinas

In this study, we used the ONC model to investigate the role of the energy budget in the pathology of acute traumatic axon injury (Fig. 1A). ONC is a classic animal model of neurodegeneration, with early axon loss and cell death 1 day after injury [31, 32]. The visual system ranks among the most energy-demanding systems in the brain [33]. Consistently, our results showed that the retina had a much higher ATP content than the cortex and hippocampus in mature C57BL/6 mice at baseline (Fig. 1B).

We first measured the energy levels of retinas and corresponding optic nerves and found that the ATP levels were moderately increased after ONC (Fig. 1C). Their ADP levels also increased (Fig. 1D), supporting the
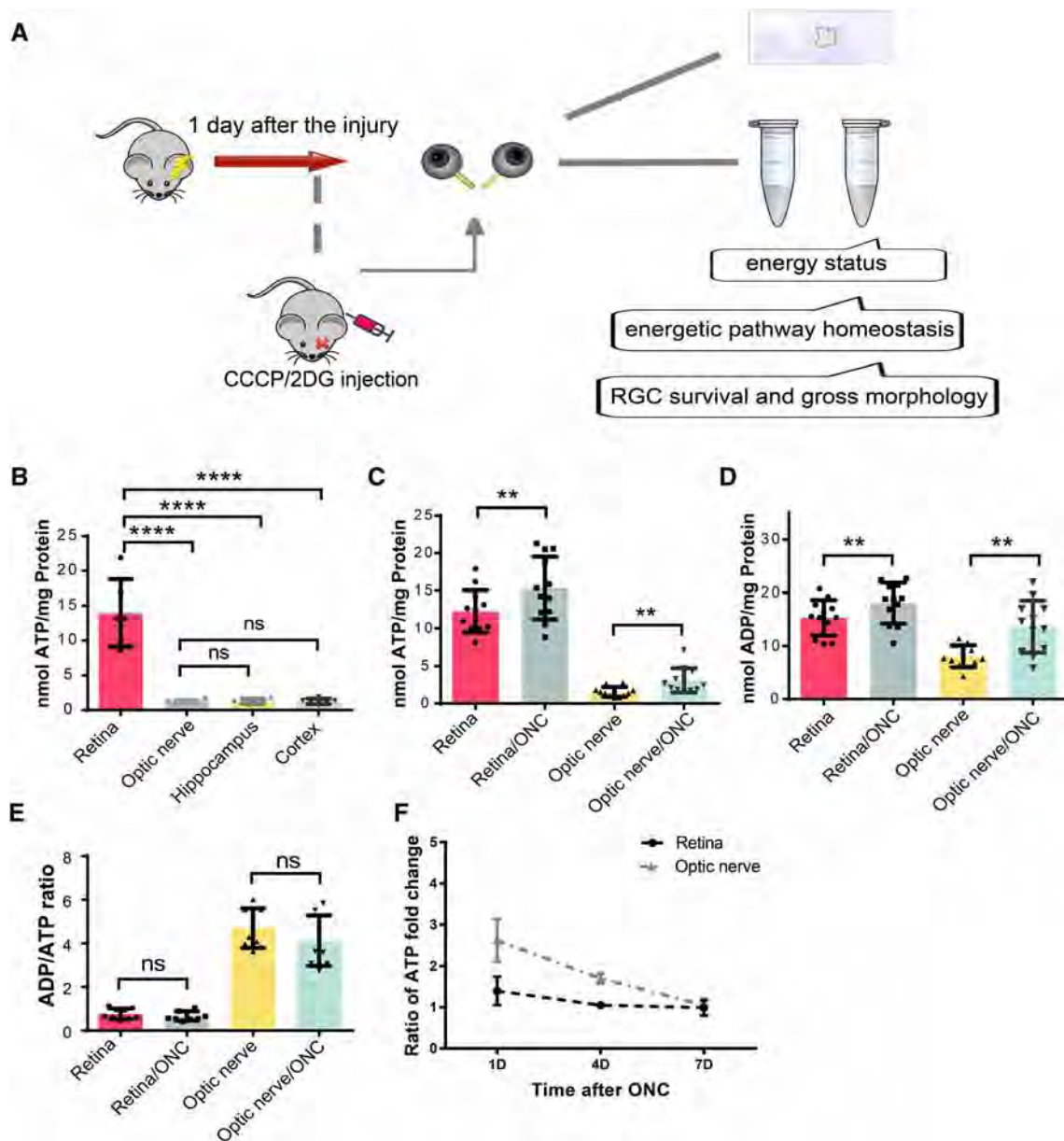
Fig. 1 Optic nerve crush (ONC)-stimulated energy metabolism in the retina and optic nerve. **A** Schematic of the experimental design. The main outcome measurements included the energy status (ATP levels, ADP levels, and the ADP/ATP ratio), energetic pathway homeostasis (glycolysis and oxidative phosphorylation activity and relative proportions), and retinal ganglion cell (RGC) status (numbers of surviving cells and gross morphology). **B** Basal ATP levels in the retina, optic nerve, hippocampus, and cortex. **C, D** ATP and ADP levels in retina and optic nerve 1 day after ONC. **E** The dynamic balance of energy metabolism presented as the ADP/ATP ratio. **F** ATP concentration-time curves for retinas and optic nerves 1, 4, and 7 days after ONC. $**P < 0.01$, $****P < 0.0001$; ns, not significant.

hypothesis that neurons rapidly undergo a series of energy-expensive processes in response to injury [5]. The ATP and ADP increases were smaller in retinas than in optic nerves, probably because the nerves were directly traumatized, while only a small portion of the retinal cells (RGCs) was affected. However, the ADP/ATP ratio, a critical parameter of energy consumption and balance [34], showed no decrease, indicating that the relative energy equilibrium was maintained through robust energy consumption and generation (Fig. 1E).

We confirmed the stimulation of energy metabolism in the ONC model. Notably, when monitoring ATP concentrations for a longer period (3 and 7 days after injury) (Fig. 1F), this increase was not apparent in the retina but still occurred in the optic nerve after 3 days. Subsequently, this trend disappeared in both locations 7 days after injury.

766

Neurosci. Bull. July, 2020, 36(7):761–777

We further evaluated the activity of the two main glucose metabolism pathways in the visual system, glycolysis and mitochondrial oxidative phosphorylation. To assess mitochondrial activity in RGCs, we used a previously-reported flow cytometry-based assay. Isolated retinal cells were co-stained with MitoTracker Deep Red, a $\Delta\psi$m-dependent dye that binds to metabolically active mitochondria, and Thy-1.2, an RGC-specific marker. The mean fluorescence intensity of MitoTracker Deep Red staining in Thy-1.2-positive cells indicated that the number of active mitochondria in RGCs increased after ONC (Fig. 2A). We then evaluated mitochondrial COX activity in the optic nerve using DAB staining. A substantial increase in mitochondrial staining was observed in the injured nerve (Fig. 2B). Moreover, the mRNA levels of tricarboxylic acid cycle enzymes (citrate synthase, α-ketoglutarate dehydrogenase, fumarate hydratase, and isocitrate dehydrogenase 1) were increased in the nerve (Fig. 2C). Based on these results, mitochondrial oxidative phosphorylation is enhanced in the ONC model.

The level of glycolysis is indicated by the expression and activity of the glycolytic enzyme LDH, a key enzyme in anaerobic respiration that catalyzes the final step of glycolysis by converting pyruvate to lactate. Quantitative analyses of LDH activity in tissue homogenates revealed a slight increase in injured optic nerve, but this activity remained basically unchanged in the whole retina (Fig. 2D). Qualitative analyses of LDH histochemistry also showed a higher level of staining in injured optic nerve (Fig. 2E and Table S1). The ganglion cell layer of the retina also displayed intense LDH staining in the ONC group, but no significant changes were evident in the rest of the retina (Fig. 2E). Thus, the LDH increase in RGCs may be masked by the remaining part of the retina, as shown in Fig. 2D. qRT-PCR revealed increased expression of the glycolysis enzymes hexokinase 1 and 2, phosphofructokinase-1, glyceraldehyde 3-phosphate dehydrogenase, pyruvate kinase, and lactate dehydrogenase A in optic nerve following ONC (Fig. 2F). Together, these findings indicate a trend of increased glycolysis in injured optic nerve.

Neither Systemic Increases in Internal Energy Levels nor Supplementation with Exogenous ATP Improves RGC Survival

What is the biological significance of this energetic activation? Since neurons are metabolically demanding and energy-dependent, we suspected that this post-trauma metabolic response was essential for RGCs to avoid energy deficits and survive. To test this hypothesis, we intraperitoneally injected mice with 2DG, an inhibitor of the glycolytic enzyme hexokinase, and CCCP, a protonophore (H$^+$ ionophore) and uncoupler of mitochondrial oxidative phosphorylation, immediately after surgery to restrict glycolysis or oxidative phosphorylation, respectively. The numbers of surviving RGCs were counted in Tuj1-labeled retina whole-mount preparations and using the flow cytometry-based Thy-1.2-labeling RGC sorting method. CCCP and 2DG significantly reduced RGC survival in the ONC model at 1 day; however, there were no significant effects on the intact retina (Fig. 3A, B).

Since blocking intense energy production is detrimental to RGC survival, does a larger energy reserve help protect against RGC loss? In other words, does a mouse with greater internal energy levels after injury have an advantage in terms of RGC survival? To determine the inherent energy potential of each mouse after injury, the ADP/ATP ratios of the injured and intact optic nerves from the same mouse were calculated. Pearson correlation analyses and regression analyses were used to examine the relationship between RGC survival and the fold change in the ADP/ATP ratio (Fig. 4A). Surprisingly, no significant correlation was found ($n = 25$; $r = -0.2507$; $P = 0.2268$). Therefore, mice with a more energetically active optic nerve after injury have no advantage in terms of reduced RGC death.

Energy supply tends to promote neuronal survival following CNS injury [35, 36]. Given that more internal energy failed to produce more surviving RGCs, we questioned whether supplying extrinsic ATP would confer any benefit for RGC survival. ATP was injected at a relatively high dose (50 mg/kg) [37, 38] and a low dose (5 μmol/kg; ~2.865 mg/kg) [39]. Intraperitoneal injections did not have a significant effect on RGC survival in either injured or intact eyes (Fig. 4B, C).

Energetic Reliance Shifts to Mitochondrial Respiration in Injured Optic Nerve

Following our observation that both glycolysis and mitochondrial oxidative phosphorylation are upregulated after ONC, we questioned how strongly each pathway became elevated and contributed to ATP production. We established three groups of unilateral ONC models and measured the ATP content in the corresponding optic nerves (the meaning of each value is explained in the Methods). CCCP and 2DG were injected to inhibit respiration and glycolysis, respectively, into ONC mice, while saline was injected into control mice. Both crushed and sham-operated optic nerves were extracted 1 h after the injection, and the ATP levels were measured. According to the formula shown in Fig. 5A, the ATP ONC/CON ratios were set as fixed cutoff points to differentiate changes in the proportions of the different pathways after injury, and the ONC$_{2DG}$/CON$_{2DG}$ and ONC$_{CCCP}$/CON$_{CCCP}$ ratios were compared to the ONC/CON value to determine if the rates
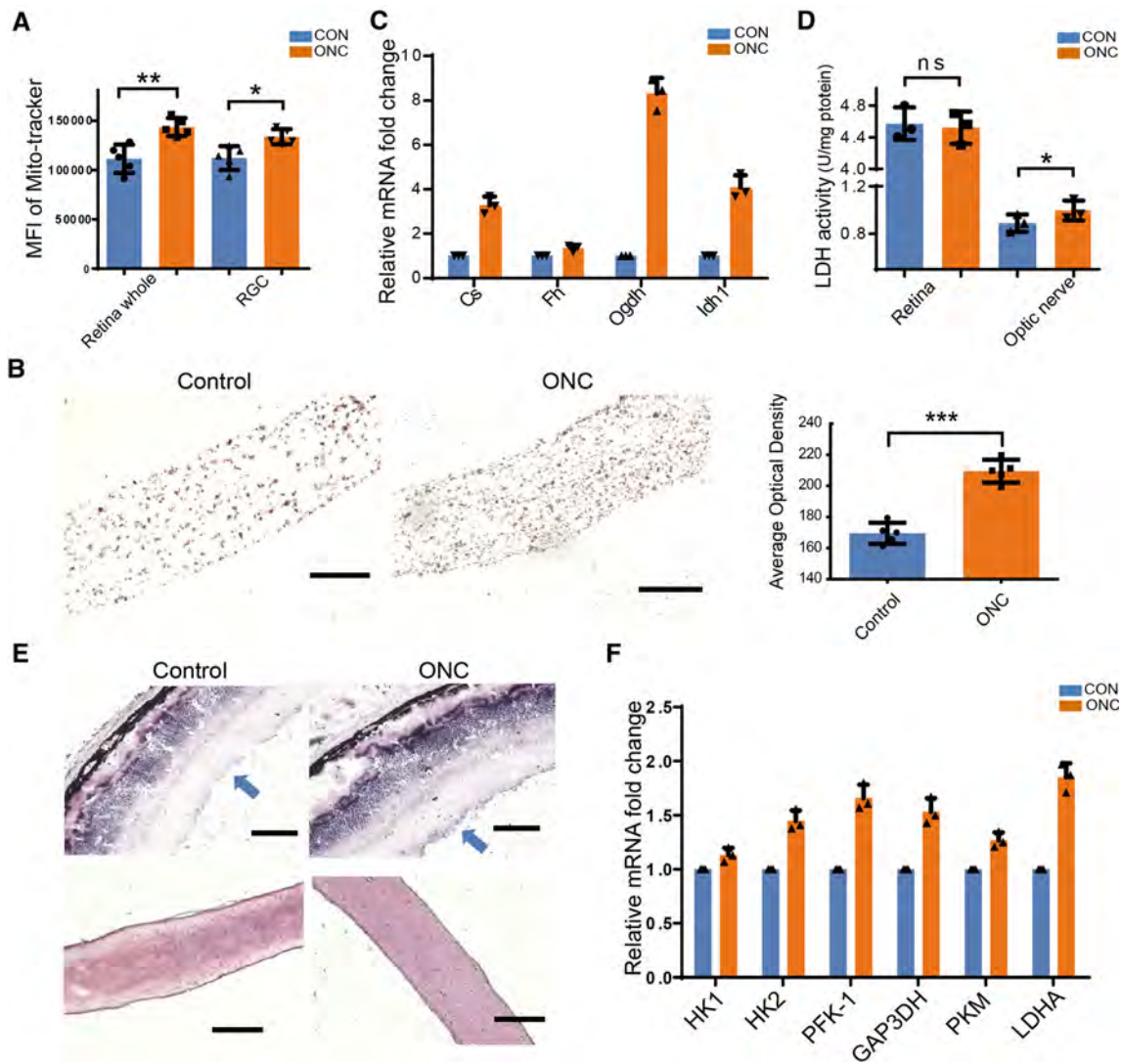
Fig. 2 Changes in glycolysis and mitochondrial oxidative phosphorylation after ONC. **A** Statistical analysis of the mean fluorescence intensity of MitoTracker staining in retinal cells and RGCs. **B** Representative images and quantitative analysis of diaminobenzidine staining of cytochrome oxidase in injured and sham-operated optic nerves. **C** mRNA levels of tricarboxylic acid cycle enzymes in crushed optic nerves after ONC. **D** Quantitative analysis of lactate dehydrogenase (LDH) activity in the optic nerve and whole retina after ONC. **E** Representative images of LDH activity (blue/purple staining) in the retina (upper) and the optic nerve (lower) after injury [note intense and disseminated staining in the RGC layer (blue arrows); qualitative analysis in Table S1]. **F** mRNA levels of glycolytic enzymes in optic nerves after ONC. Scale bars in B and E, 100 μm.

of glycolysis and respiration increased or decreased. The data showed that the ONC/CON value after the CCCP injection (ONC_{CCCP}/CON_{CCCP}) was greater than the control ONC/CON value, while no significant difference was found between ONC/CON and ONC_{2DG}/CON_{2DG} (Fig. 5B). These calculations suggested a greater proportion of oxidative phosphorylation in the injured optic nerve than in the intact nerve. For further validation, additional glycolysis and oxidative phosphorylation inhibitors were applied – iodoacetic acid was used to inactivate glyceraldehyde-3-P dehydrogenase, and oligomycin was used to block membrane-bound mitochondrial ATP synthase and

proton channels – and they produced similar results (Fig. 5C). Thus, metabolic activation along with a metabolic shift toward respiration occurs in traumatized optic nerves.

The disproportionate increase in respiration caught our attention, raising the question of its biological significance. Is it beneficial or deleterious for RGC preservation? Experiments with PTEN deletion mice helped to provide answers to these questions. PTEN deletion is well established as a general factor controlling neuronal growth, and it has frequently been shown to preserve neurons in the context of CNS injury [40]. Downregulation of PTEN has
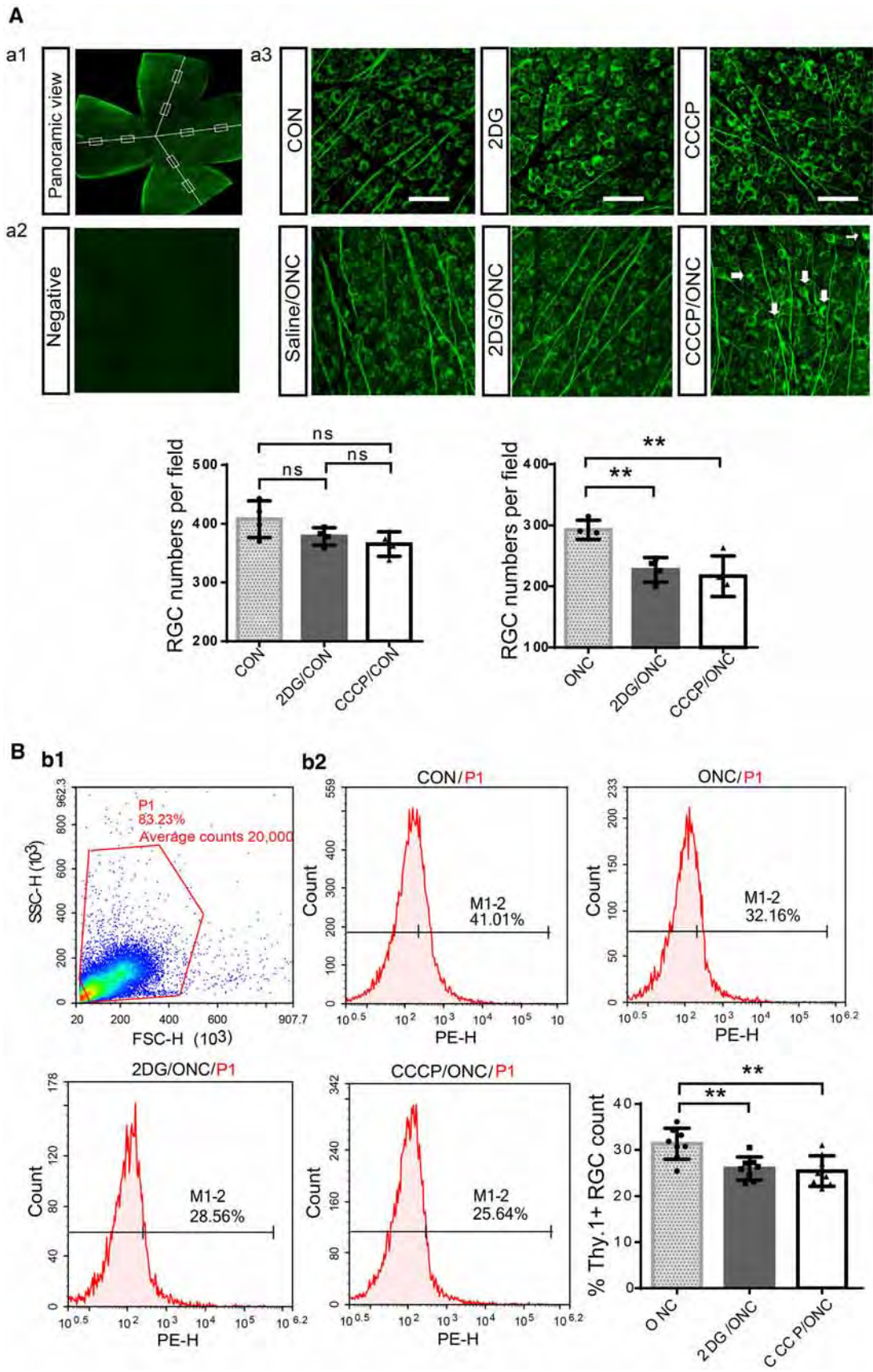
◀ **Fig. 3** Blocking the ATP supply by inhibiting glycolysis or oxidative phosphorylation increases the retinal damage. **A** Images of flat-mounted retinas stained with Tuj1; eight fields from each retinal explant (boxes) were analyzed. **a1** Representative example of RGC layers in a whole-mount retina stained for Tuj1 (green). **a2** Representative image of the negative control, from which the primary antibody (Tuj1) was omitted. **a3** Representative confocal images from the central regions of retinas in each group. The ONC group with carbonyl cyanide 3-chlorophenylhydrazone (CCCP) injection displayed swollen somata with tubulin accumulation (arrows). Scale bars, 200 μm. **B** Flow cytometry-based sorting strategy for Thy-1.2-positive cells. **b1** An initial gated population (P1) was plotted to discard clumped cells or aggregates and obtain a single-cell population. **b2** Post-sorting analysis of the percentage of Thy-1.2-positive RGCs (M1-2) in each group (note greater RGC death in the 2DG and CCCP groups 1 day after ONC).

been shown to increase RGC survival in an ONC model [20, 41]. PTEN is also a metabolic regulator that can suppress glycolysis and cause an energetic shift toward mitochondrial respiration when activated [42, 43]. Based on this evidence, we investigated whether respiration-biased metabolism contributes to the limited neuron survival we found and whether PTEN deletion restricts respiration, thus protecting RGCs.

The GSEA results from a microarray (GSE32309) of PTEN-deficient and wild-type mice subjected to ONC supported our hypothesis. The data revealed that the top five pathways enriched in wild-type mice were KEGG_OXIDATIVE_PHOSPHORYLATION, KEGG_RIBOSOME, KEGG_ETHER_LIPID_METABOLISM, KEGG_RNA_POLYMERASE, and KEGG_RETINOL_METABOLISM (Fig. 6A). Although oxidative phosphorylation was ranked first in the wild-type group, it was not enriched in the PTEN-deficient group (Fig. 6B). Thus, a high level of oxidative phosphorylation is a prominent and potentially adverse process occurring in retinal neurons after optic nerve injury.

Redirecting Metabolism toward Glycolysis (Warburg Effect) Protects against RGC Loss

If the above hypothesis is correct, then restricting oxidative phosphorylation should benefit RGC survival in the ONC model. We tried to increase the activity of another primary energy source, i.e., glycolysis over respiration, similar to the "Warburg effect" in tumors and PTEN-deficient mice, to avoid oxidative phosphorylation overload and simultaneously maintain ATP production. We performed a literature search and identified a drug that shifts energy dependence to glycolysis. Paul S Brookes and Vamsi K Mootha examined > 3,500 small molecules and discovered that the clinically-used drug meclizine attenuates mitochondrial respiration without reducing mitochondrial

biogenesis or viability and augments glycolysis in various models [44, 45]. We intraperitoneally injected 100 mg/kg meclizine 17 h and 3 h before ONC, as suggested in previous reports [44, 45], and measured the metabolic effects. Although total ATP levels and the ADP/ATP ratio were not significantly altered in injured optic nerves (Fig. 7A, B), LDH staining and activity were markedly increased in meclizine-treated optic nerves (Fig. 7C, D). The contribution of glycolysis to the energy output increased, while the contribution of mitochondrial respiration decreased (Fig. 7E). Thus, meclizine was able to shift the metabolic dependence toward glycolysis rather than mitochondrial respiration.

As the preference for mitochondria-derived ATP production is reduced by activating glycolysis, meclizine achieved a favorable reduction in RGC death (Fig. 8A, B). To confirm that activation of glycolysis is indispensable for this neuroprotective effect, we injected 2DG into the meclizine-protected ONC model and found a mitigation of the positive effect manifested as further RGC loss (Fig. 8A). Therefore, the disproportionate activation of respiration following acute axon injury is a major contributor to RGC damage, and the redirection of energy metabolism toward glycolysis may enhance neuronal survival (Fig. 8B).

Discussion

To help injured neurons better survive an injury energetically, we must determine their reactions to intense post-injury energy demands [5]. Metabolic plasticity enables cells to adapt to acute energy demands, with which neurons are not typically associated. However, in the present study, the optic nerve and retina displayed metabolic activation 1 day after injury, with signs of increased ATP and ADP levels and enhanced glycolysis and oxidative phosphorylation (Figs 1 and 2). These results differ from the findings of several *in vitro* studies in which neurons tend to display energy deficits after trauma originating from mitochondrial degeneration [7, 46], but they are consistent with an *in vivo* study showing that injury increases the number of motile mitochondria during the early phase of motor nerve regeneration [47]. This discrepancy may be explained by differences between *in vitro* and *in vivo* conditions. *In vivo*, neurons are supported by the surrounding environment, particularly relying on astrocytes to provide lactate and pyruvate for oxidative phosphorylation [48–50]. Energetic support from activated astrocytes to neurons is important during early neurodegeneration and periods of increased energy demand [51–53], while isolated cultured neurons are typically cultured in 25 mmol/L glucose, a hyperglycemic environment that may disturb glucose
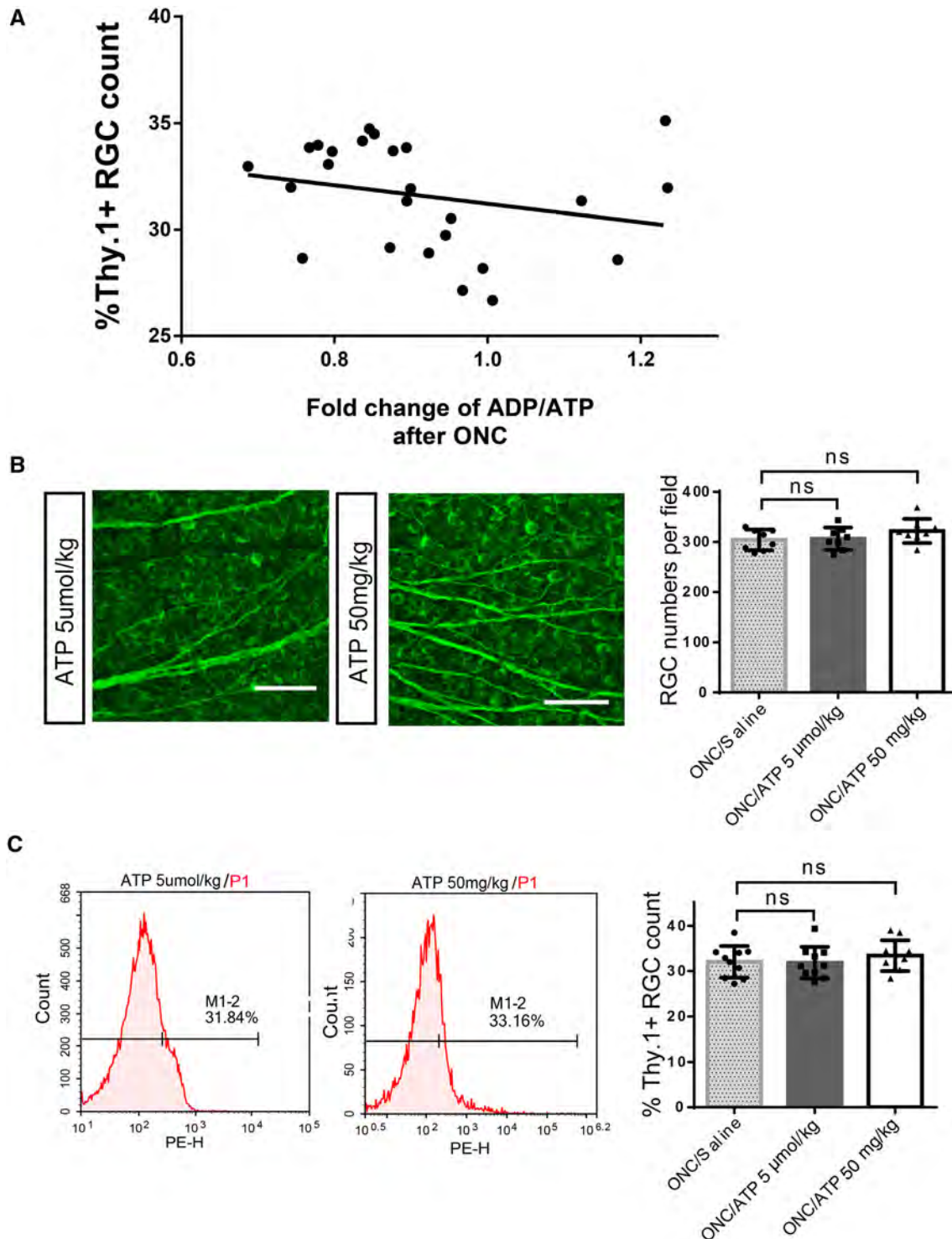
Fig. 4 Neither greater endogenous energy reserves nor exogenous ATP supplementation results in reduced RGC loss. **A** Pearson's correlation analysis revealed no significant correlation between the numbers of Thy-1.2-positive RGCs and ATP reserves ($n = 25$; $r = -0.2507$; $P = 0.2268$). The line represents the linear regression equation of the data ($Y = -4.337 \cdot X + 35.55$, $R^2 = 0.06283$, not significant), r, correlation coefficient. R^2 is calculated from the multivariate linear regression. **B** Neither 5 µmol/kg nor 50 mg/kg ATP injection had an effect on RGC survival after ONC (scale bars, 200 µm). **C** Percentages of Thy-1.2-positive RGCs with and without ATP injection.

metabolism, and these neurons rarely survive on their own. The mitochondrial degeneration *in vitro* may reflect

ongoing neuronal death with inactive neuron repair and recovery after damage. Notably, we monitored the energy
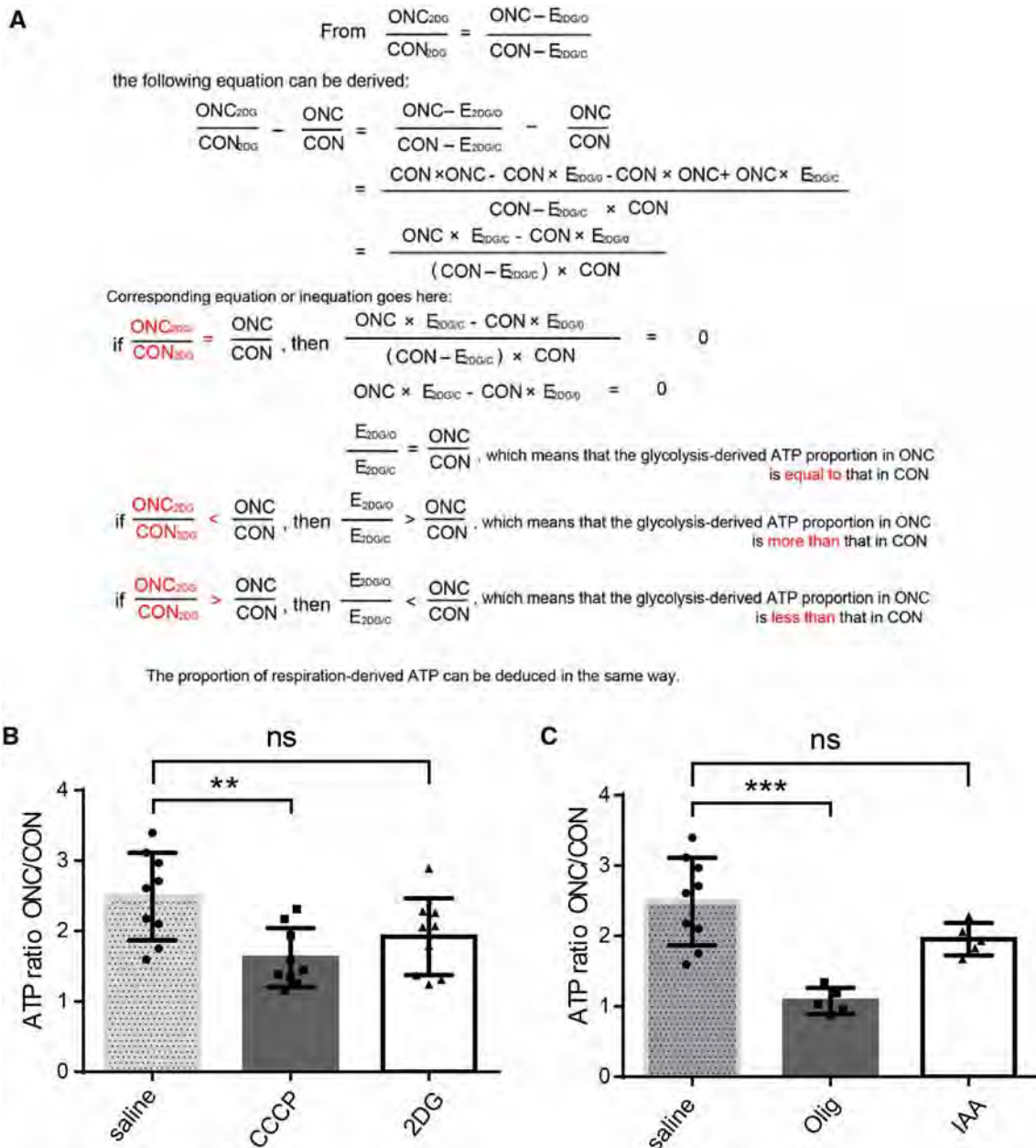
Fig. 5 Energy metabolism shifts to oxidative phosphorylation in injured optic nerve. **A** Derivation of the formula for measuring the changes in each pathway and their contributions to energy production. The algorithm establishes ONC_{2DG}/CON_{2DG} as an index for evaluating an altered ratio of glycolysis and respiration. **B**, **C** Calculated ATP ratios from injured/intact optic nerves. ONC_{CCCP}/CON_{CCCP} and $ONC_{oligomycin}/CON_{oligomycin}$ were decreased in traumatized optic nerves (note that the relative contribution of oxidative phosphorylation to the energy supply increased following ONC and the proportion of glycolysis showed no significant change)

status at the tissue level (whole retina with a mixture of cells and optic nerve with predominantly RGC axons), because it is technically difficult to separate the metabolism of neurons and glia. Thus, the potential neuronal origin of these metabolic changes remains unclear. Measurements at the cellular level are needed to address this problem in future studies.

Although intense energy production is vital for RGC survival after ONC (Fig. 3), increasing the energy level largely failed to promote RGC survival. Our results suggested that inherently high energy levels in the injured optic nerve have no significant effect on RGC survival (Fig. 4A), probably because the spontaneous metabolic activation in the optic nerve and retina is sufficient to satisfy most urgent energy demands during early trauma. Energy-boosting neuroprotection has exhibited great potential in several chronic neurodegenerative conditions, such as Huntington's disease and Parkinson's disease [54–56].

Fig. 6 Gene set enrichment analysis demonstrating enriched pathways in injured wild-type *versus* PTEN-deleted retinas. **A** The top five pathways enriched in injured wild-type mice compared to PTEN-deleted mice, with oxidative phosphorylation ranked first. Bar plot, SIZE of the top 5 enriched gene sets; red, enrichment score; green, normalized enrichment score. (ES, the degree to which a gene set is overrepresented at the top or bottom of a ranked list of genes; NES, differences in gene set size and correlations between gene sets and the expression dataset; SIZE, number of genes in the gene set after filtering out those not in the expression dataset). **B** Enrichment plot of the KEGG_OXIDATIVE_ PHOSPHORYLATION pathway (note that significant enrichment of "oxidative phosphorylation" genes was found in injured retinal cells from wild-type mice compared with those from PTEN deletion mice).
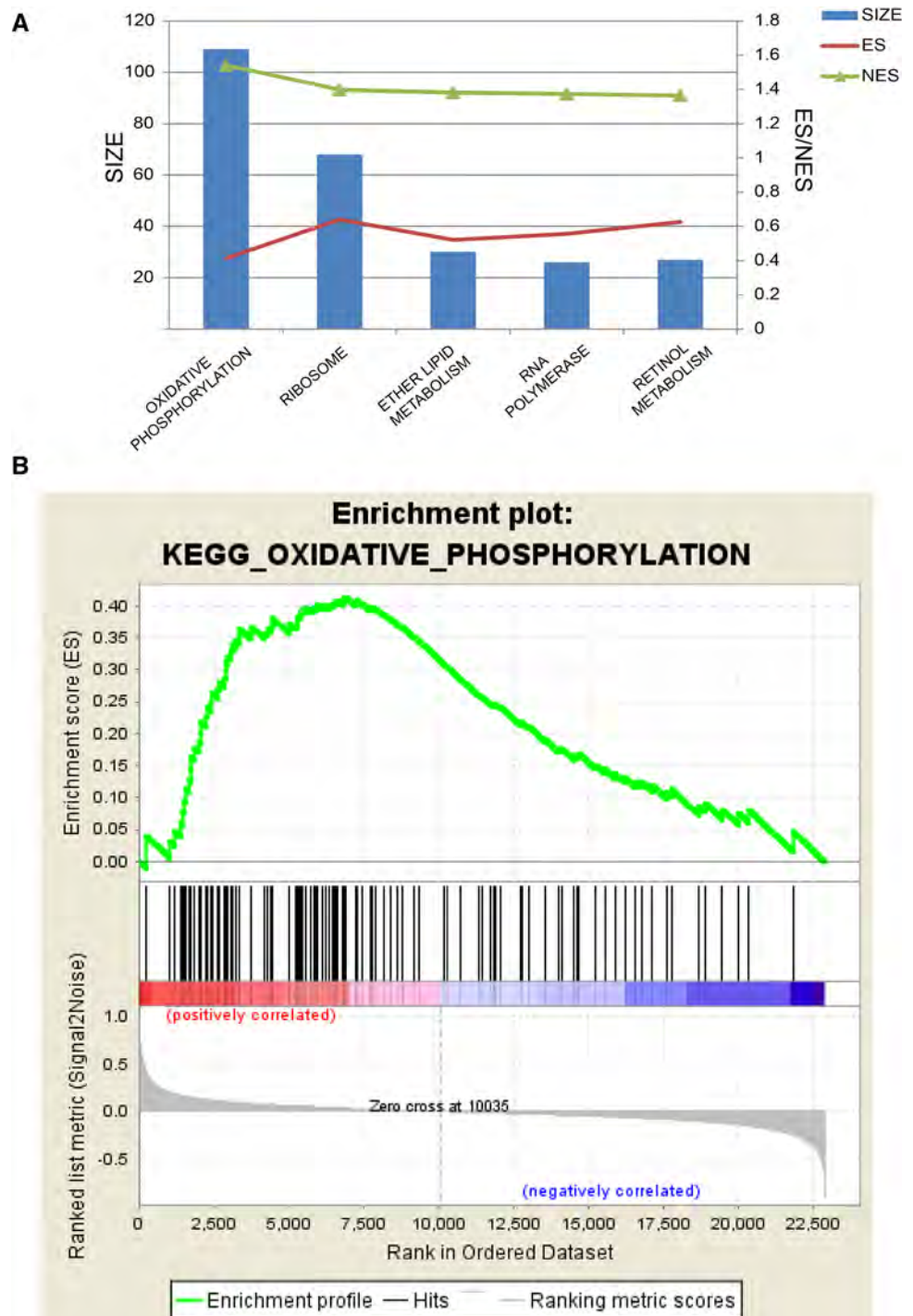
However, during acute clinical neuronal injury, such as stroke, this approach is ineffective or even detrimental [57], similar to our acute ONC model. The timing of treatment during the progression of neuronal demise may be a factor. Our results revealed that the increased ATP levels gradually declined over time (1, 3, and 7 days) in the ONC model (Fig. 1F), indicating that the activated energetic response may be an acute adaptation during the early stage of trauma and that energy exhaustion may occur in the later stage of acute neuronal trauma, thus mimicking a chronic neurodegenerative state. Evidence related to glaucoma, a chronic optic nerve injury, also supports our suspicion. RGCs from DBA/2J mice with early-stage glaucoma show higher expression of oxidative phosphorylation genes than those from healthy mice [58]; however, mice with later-stage chronic glaucoma display
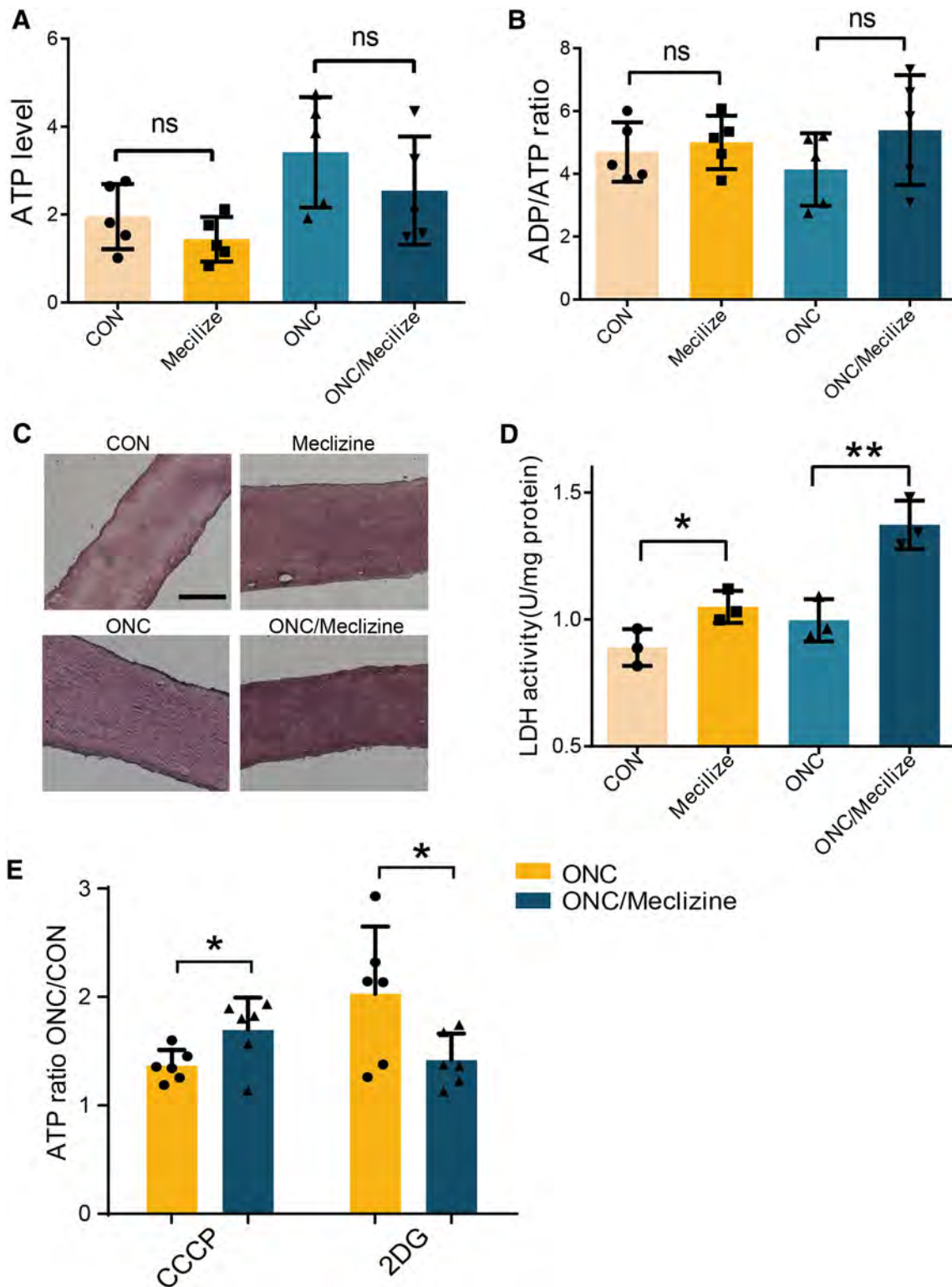
Fig. 7 Meclizine redirects metabolic flux toward glycolysis. **A**, **B** Pretreatment with meclizine did not significantly change ATP levels (**A**) or ADP/ATP ratios (**B**). **C** Representative images of LDH staining (note the stronger staining in the meclizine group than in the control group, and in the meclizine pretreatment ONC group than in the ONC group; histochemical ratings in Table S2). Scale bar, 100 μm. **D** LDH activity in the meclizine treatment and the ONC/meclizine groups. **E** Effects of pretreatment with meclizine on ONC_{CCCP}/CON_{CCCP} and ONC_{2DG}/CON_{2DG} in injured optic nerves.
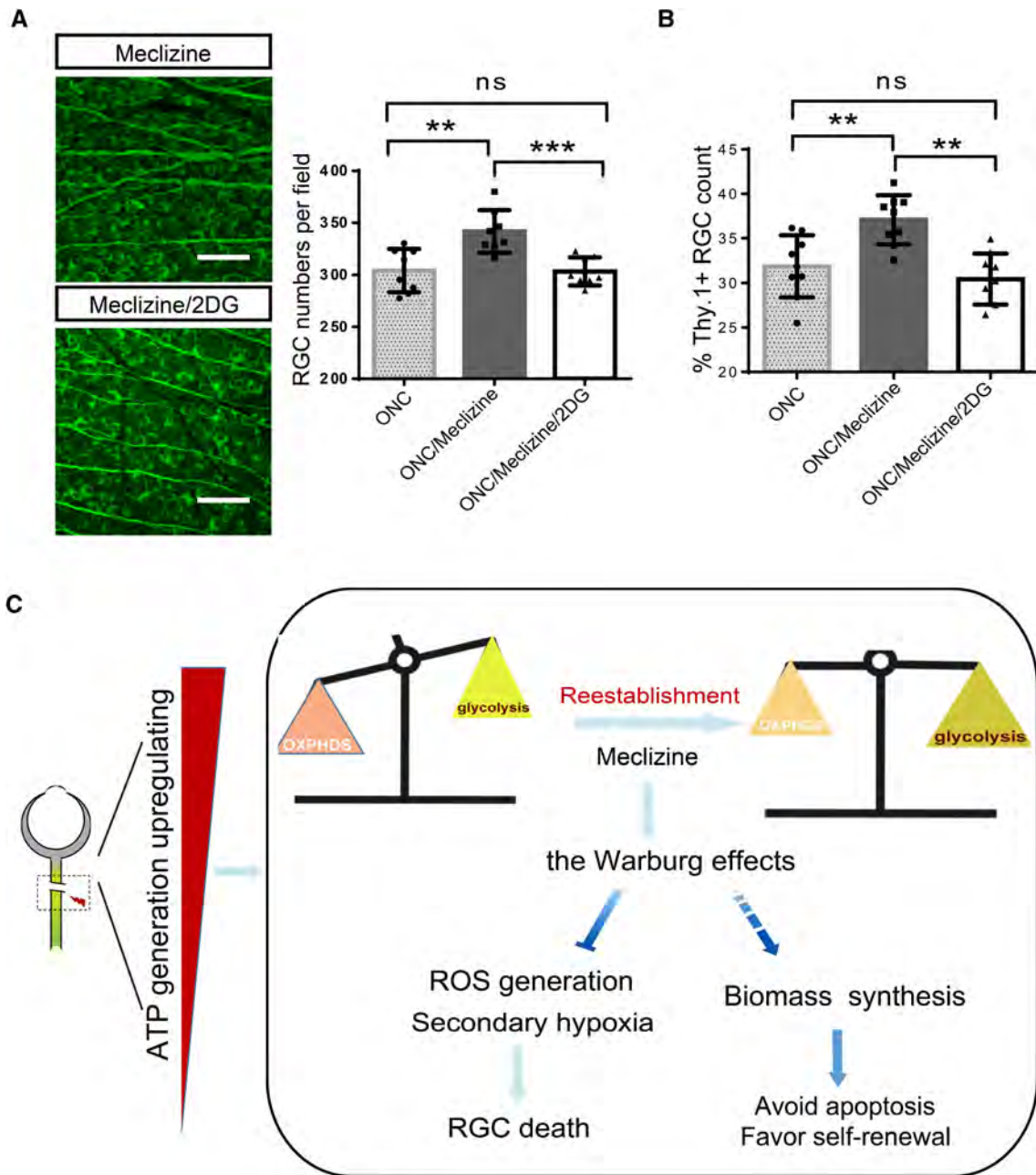
Fig. 8 Meclizine pretreatment protects RGCs from death, and this is reversed by 2DG. **A** Meclizine pretreatment prevents RGC death, and 2DG supplementation diminishes this effect. Scale bars, 200 μm. Representative images of whole-mount retina stained for Tuj1 in Meclizine-treated group and Meclizine/2DG-treated group. **B** RGC numbers based on flow cytometry (note that they are consistent with the findings from retinal whole mounts). **C** A working model of metabolic redirection toward glycolysis (Warburg effect) to benefit RGC survival. Disproportionate upregulation of oxidative phosphorylation over glycolysis after ONC may confer several vulnerabilities for RGC survival, including reactive oxygen species (ROS) accumulation and secondary hypoxia. However, re-establishing energy homeostasis by restoring the preference for glycolysis is hypothesized to provide survival advantages to the cells, such as favoring macromolecule biosynthesis and promoting self-renewal.

mitochondrial dysfunction and energy compromise [59], and patients with advanced primary open-angle glaucoma suffer from oxidative phosphorylation complex-I damage and impaired ATP synthesis [60, 61].

We found increased glycolysis and oxidative phosphorylation and that oxidative phosphorylation temporarily outperforms other pathways, providing a stronger response to the increased demand (Fig. 5). The relative contributions of glycolytic flux and oxidative phosphorylation under normal conditions or in response to changing energy requirements in the CNS have not been previously described, potentially because of the lack of available

measurement tools and sensitive assays. Our conclusion was first drawn according to calculations using formulas. However, statistical analysis cannot provide an accurate value for the percentage increase or decrease. As more advanced techniques emerge, these proportions should be precisely measured.

Our data showed that prominent activation of oxidative phosphorylation was associated with a poor prognosis for RGC survival (Fig. 6), as suggested by comparisons between PTEN conditional knockout mice and wild-type mice. Meclizine is an 'older' FDA-approved compound that has been shown in a drug screen and multiple animal models to be capable of reprogramming energy metabolism [44]. Our study found that, by redirecting metabolism toward glycolysis using meclizine, RGC survival was promoted (Fig. 8A, B). Why is the pharmacological augmentation of glycolysis protective? The underlying causes may be similar in our model and in the "Warburg effect" in tumors (Fig. 8) [62–64]. Overactive oxidative phosphorylation can cause extensive ROS production, and the resultant oxidative stress has been confirmed to be a major cause of RGC apoptosis after axon injury [65–67]. In addition, respiratory substrate influx into mitochondria may cause sensitivity to mitochondria-mediated apoptosis [68–70], which may also lead to excessive respiration-induced RGC loss in the ONC model. Furthermore, a metabolic preference for glycolysis is an inherent trait of neural progenitor cells [71, 72], which may indicate neural stem cell activation in our model, potentially representing an additional step toward neuronal protection and regeneration. In conclusion, we provided clues that pathologically augmented mitochondrial respiration may be a double-edged sword in the injured optic nerve. That is, excessive activation of mitochondrial respiration causes massive secondary damage to RGCs despite producing energy (Fig. 8C). This model can also explain why increased internal energy generation is not significantly correlated with RGC survival, as illustrated in Fig. 3. Exactly how these imbalances in the reallocation of energy production pathways lead to neuropathology warrants further investigation. Overall, as a first step toward elucidating how neuronal energy metabolism adapts to axonal insults *in vivo*, our study puts forward a potential bioenergetic strategy to facilitate neuronal survival in the traumatized CNS that involves shifting energy metabolism toward glycolysis (the Warburg effect).

References

1. Volpicelli-Daley L, Luk K, Patel T, Tanik S, Riddle D, Stieber A, *et al.* Exogenous α-synuclein fibrils induce Lewy body pathology leading to synaptic dysfunction and neuron death. Neuron 2011, 72: 57–71.
2. Frakes A, Ferraiuolo L, Haidet-Phillips A, Schmelzer L, Braun L, Miranda C*, et al.* Microglia induce motor neuron death via the classical NF-κB pathway in amyotrophic lateral sclerosis. Neuron 2014, 81: 1009–1023.
3. Belanger M, Allaman I, Magistretti PJ. Brain energy metabolism: focus on astrocyte-neuron metabolic cooperation. Cell Metab 2011, 14: 724–738.
4. Mink JW, Blumenschine RJ, Adams DB. Ratio of central nervous system to body metabolism in vertebrates: its constancy and functional basis. Am J Physiol 1981, 241: R203–212.
5. Bradke F, Fawcett JW, Spira ME. Assembly of a new growth cone after axotomy: the precursor to axon regeneration. Nat Rev Neurosci 2012, 13: 183–193.
6. Kiryu-Seo S, Ohno N, Kidd G, Komuro H, Trapp B. Demyelination increases axonal stationary mitochondrial size and the speed of axonal mitochondrial transport. J Neurosci 2010, 30: 6658–6666.
7. Yokota S, Takihara Y, Arimura S, Miyake S, Takamura Y, Yoshimura N, *et al.* Altered transport velocity of axonal mitochondria in retinal ganglion cells after laser-induced axonal injury *in vitro*. Invest Ophthalmol Vis Sci 2015, 56: 8019–8025.
8. White H, Venkatesh B. Clinical review: Ketones and brain injury. Critical Care 2011, 15: 219–219.
9. Yellen G. Fueling thought: Management of glycolysis and oxidative phosphorylation in neuronal metabolism. J Cell Biol 2018, 217: 2235–2246.
10. Pfeiffer T, Schuster S, Bonhoeffer S. Cooperation and competition in the evolution of ATP-producing pathways. Science 2001, 292: 504–507.
11. Warburg O, Wind F, Negelein E. The metabolism of tumors in the body. J Gen Physiol 1927, 8: 519–530.
12. Winkler BS. Glycolytic and oxidative metabolism in relation to retinal function. J Gen Physiol 1981, 77: 667–692.
13. Winkler BS, Starnes CA, Twardy BS, Brault D, Taylor RC. Nuclear magnetic resonance and biochemical measurements of glucose utilization in the cone-dominant ground squirrel retina. Invest Ophthalmol Vis Sci 2008, 49: 4613–4619.
14. House SW, Burk D, Schade AL. On respiratory impairment in cancer cells. Science 1956, 124: 267–272.

776

Neurosci. Bull. July, 2020, 36(7):761–777

15. Magharious MM, D'Onofrio PM, Koeberle PD. Optic nerve transection: a model of adult neuron apoptosis in the central nervous system. J Vis Exp 2011, 51: e2241.

16. Huntwork-Rodriguez S, Wang B, Watkins T, Ghosh A, Pozniak C, Bustos D, et al. JNK-mediated phosphorylation of DLK suppresses its ubiquitination to promote neuronal apoptosis. J Cell Biol 2013, 202: 747–763.

17. Watkins T, Wang B, Huntwork-Rodriguez S, Yang J, Jiang Z, Eastham-Anderson J, et al. DLK initiates a transcriptional program that couples apoptotic and regenerative responses to axonal injury. Proc Natl Acad Sci U S A 2013, 110: 4039–4044.

18. Mac Nair CE, Schlamp CL, Montgomery AD, Shestopalov VI, Nickells RW. Retinal glial responses to optic nerve crush are attenuated in Bax-deficient mice and modulated by purinergic signaling pathways. J Neuroinflammation 2016, 13: 93.

19. Gkotsi D, Begum R, Salt T, Lascaratos G, Hogg C, Chau K, et al. Recharging mitochondrial batteries in old eyes. Near infra-red increases ATP. Exp Eye Res 2014, 122: 50–53.

20. Park KK, Liu K, Hu Y, Smith PD, Wang C, Cai B, et al. Promoting axon regeneration in the adult CNS by modulation of the PTEN/mTOR pathway. Science 2008, 322: 963–966.

21. Smith PD, Sun F, Park KK, Cai B, Wang C, Kuwako K, et al. SOCS3 deletion promotes optic nerve regeneration in vivo. Neuron 2009, 64: 617–623.

22. Chintalapudi SR, Djenderedjian L, Stiemke AB, Steinle JJ, Jablonski MM, Morales-Tirado VM. Isolation and molecular profiling of primary mouse retinal ganglion cells: Comparison of phenotypes from healthy and glaucomatous retinas. Front Aging Neurosci 2016, 8, 93. https://doi.org/10.3389/fnagi.2016.00093.

23. Chintalapudi SR, Patel NN, Goldsmith ZK, Djenderedjian L, Wang XD, Marion TN, et al. Isolation of primary murine retinal ganglion cells (RGCs) by flow cytometry. J Vis Exp 2017, 125. https://doi.org/10.3791/55785.

24. Mootha VK, Lindgren CM, Eriksson KF, Subramanian A, Sihag S, Lehar J, et al. PGC-1α-responsive genes involved in oxidative phosphorylation are coordinately downregulated in human diabetes. Nat Genetics 2003, 34: 267.

25. Subramanian A, Tamayo P, Mootha VK, Mukherjee S, Ebert BL, Gillette MA, et al. Gene set enrichment analysis: A knowledge-based approach for interpreting genome-wide expression profiles. Proc Natl Acad Sci U S A 2005, 102: 15545–15550.

26. Edgar R, Domrachev M, Lash AE. Gene Expression Omnibus: NCBI gene expression and hybridization array data repository. Nucleic Acids Res 2002, 30: 207–210.

27. Sun F, Park KK, Belin S, Wang D, Lu T, Chen G, et al. Sustained axon regeneration induced by co-deletion of PTEN and SOCS3. Nature 2011, 480: 372–375.

28. Bolstad BM, Gautier L, Cope L, Irizarry RA. Affy—analysis of Affymetrix GeneChip data at the probe level. Bioinformatics 2004, 20: 307–315.

29. Maldonado EN, Lemasters JJ. ATP/ADP ratio, the missed connection between mitochondria and the Warburg effect. Mitochondrion 2014, 19 Pt A: 78–84.

30. Mor I, Cheung E, Vousden K. Control of glycolysis through regulation of PFK1: old friends and recent additions. Cold Spring Harb Symp Quant Biol 2011, 76: 211–216.

31. Giedrius K, Oglesby EN, Zack DJ, Cone FE, Steinhart MR, Jing T, et al. Retinal ganglion cell morphology after optic nerve crush and experimental glaucoma. Invest Ophthalmol Vis Sci 2012, 90: 3847–3857.

32. Kayama M, Omura K, Murakami Y, Reshef E, Thanos A, Morizane Y, et al. Combined inhibition of apoptosis and necrosis promotes transient neuroprotection of retinal ganglion cells and partial axon regeneration after optic nerve damage. bioRxiv 357566. https://doi.org/10.1101/357566.

33. Niven J, Laughlin S. Energy limitation as a selective pressure on the evolution of sensory systems. J Exp Biol 2008, 211: 1792–1804.

34. Metallo CM, Vander Heiden MG. Understanding metabolic regulation and its influence on cell physiology. Mol Cell 2013, 49: 388–398.

35. Cartoni R, Norsworthy MW, Bei F, Wang C, Li S, Zhang Y, et al. The mammalian-specific protein Armcx1 regulates mitochondrial transport during axon regeneration. Neuron 2016, 92: 1294–1307.

36. Wu D, Lee S, Luo J, Xia H, Gushchina S, Richardson PM, et al. Intraneural injection of ATP stimulates regeneration of primary sensory axons in the spinal cord. J Neurosci 2018, 38: 1351–1365.

37. Ren H, Teng Y, Tan B, Zhang X, Jiang W, Liu M, et al. Toll-like receptor-triggered calcium mobilization protects mice against bacterial infection through extracellular ATP release. Infect Immun 2014, 82: 5076–5085.

38. Xiang Y, Wang X, Yan C, Gao Q, Li SA, Liu J, et al. Adenosine-5'-triphosphate (ATP) protects mice against bacterial infection by activation of the NLRP3 inflammasome. PLoS One 2013, 8: e63759.

39. Stachon P, Geis S, Peikert A, Heidenreich A, Michel NA, Unal F, et al. Extracellular ATP induces vascular inflammation and atherosclerosis via purinergic receptor Y2 in mice. Arterioscler Thromb Vasc Biol 2016, 36: 1577–1586.

40. Knafo S, Esteban JA. PTEN: Local and global modulation of neuronal function in health and disease. Trends Neurosci 2017, 40: 83–91.

41. Shabanzadeh AP, D'Onofrio PM, Magharious M, Choi KAB, Monnier PP, Koeberle PD. Modifying PTEN recruitment promotes neuron survival, regeneration, and functional recovery after CNS injury. Cell Death Dis 2019, 10: 567.

42. Qian X, Li X, Shi Z, Xia Y, Cai Q, Xu D, et al. PTEN suppresses glycolysis by dephosphorylating and inhibiting autophosphorylated PGK1. Mol Cell 2019, 76: 516–527.E7.

43. Garcia-Cao I, Song MS, Hobbs RM, Laurent G, Giorgi C, de Boer VC, et al. Systemic elevation of PTEN induces a tumor-suppressive metabolic state. Cell 2012, 149: 49–62.

44. Gohil VM, Sheth SA, Nilsson R, Wojtovich AP, Lee JH, Perocchi F, et al. Nutrient-sensitized screening for drugs that shift energy metabolism from mitochondrial respiration to glycolysis. Nat Biotechnol 2010, 28: 249–255.

45. Hong CT, Chau KY, Schapira AHV. Meclizine-induced enhanced glycolysis is neuroprotective in Parkinson disease cell models. Sci Rep 2016, 6: 25344.

46. Zhou B, Yu P, Lin MY, Sun T, Chen Y, Sheng ZH. Facilitation of axon regeneration by enhancing mitochondrial transport and rescuing energy deficits. J Cell Biol 2016, 214: 103–119.

47. Han SM, Baig HS, Hammarlund M. Mitochondria localize to injured axons to support regeneration. Neuron 2016, 92: 1308–1323.

48. Philips T, Rothstein J. Oligodendroglia: metabolic supporters of neurons. J Clin Invest 2017, 127: 3271–3280.

49. Bélanger M, Allaman I, Magistretti P. Brain energy metabolism: focus on astrocyte-neuron metabolic cooperation. Cell Metab 2011, 14: 724–738.

50. Zhang Z, Chen W, Zhao Y, Yang Y. Spatiotemporal imaging of cellular energy metabolism with genetically-encoded fluorescent sensors in brain. Neurosci Bull 2018, 34: 875–886.

51. Kuter K, Olech L, Glowacka U, Paleczna M. Astrocyte support is important for the compensatory potential of the nigrostriatal system neurons during early neurodegeneration. J Neurochem 2018, 148: 63–79.

52. Coggan J, Keller D, Calì C, Lehväslaiho H, Markram H, Schürmann F, et al. Norepinephrine stimulates glycogenolysis in

astrocytes to fuel neurons with lactate. PLoS Comput Biol 2018, 14: e1006392.

53. Sun D, Moore S, Jakobs TC. Optic nerve astrocyte reactivity protects function in experimental glaucoma and other nerve injuries. J Exp Med 2017, 214: 1411–1430.

54. Weinrich TW, Coyne A, Salt TE, Hogg C, Jeffery G. Improving mitochondrial function significantly reduces metabolic, visual, motor and cognitive decline in aged Drosophila melanogaster. Neurobiol Aging 2017, 60: 34–43.

55. Nakano M, Imamura H, Sasaoka N, Yamamoto M, Uemura N, Shudo T, et al. ATP maintenance via two types of ATP regulators mitigates pathological phenotypes in mouse models of Parkinson's disease. EBioMedicine 2017, 22: 225–241.

56. Lee J, Kosaras B, Del Signore S, Cormier K, McKee A, Ratan R, et al. Modulation of lipid peroxidation and mitochondrial function improves neuropathology in Huntington's disease mice. Acta Neuropathol 2011, 121: 487–498.

57. Zhang M, Li W, Niu G, Leak R, Chen J, Zhang F. ATP induces mild hypothermia in rats but has a strikingly detrimental impact on focal cerebral ischemia. J Cereb Blood Flow Metab 2013, 33: e1–e10.

58. Williams PA, Harder JM, Foxworth NE, Cochran KE, Philip VM, Porciatti V, et al. Vitamin B3 modulates mitochondrial vulnerability and prevents glaucoma in aged mice. Science 2017, 355: 756–760.

59. Harun-Or-Rashid M, Pappenhagen N, Palmer PG, Smith MA, Gevorgyan V, Wilson GN, et al. Structural and functional rescue of chronic metabolically stressed optic nerves through respiration. J Neurosci 2018, 38: 5122–5139.

60. Van Bergen NJ, Crowston JG, Craig JE, Burdon KP, Kearns LS, Sharma S, et al. Measurement of systemic mitochondrial function in advanced primary open-angle glaucoma and leber hereditary optic neuropathy. PLoS One 2015, 10: e0140919.

61. Lee S, Leo S, Crowston JG, Van Bergen NJ, Van, O'Neill EC, O'Hare F, et al. Impaired complex-I-linked respiration and ATP synthesis in primary open-angle glaucoma patient lymphoblasts. Invest Ophthalmol Vis Sci 2012, 53: 2431–2437.

62. Chen X, Qian Y, Wu S. The Warburg effect: evolving interpretations of an established concept. Free Radic Biol Med 2015, 79: 253–263.

63. Liberti MV, Locasale JW. The Warburg effect: how does it benefit cancer cells? Trends Biochem Sci 2016, 41: 211–218.

64. Dasgupta S, Rajapakshe K, Zhu B, Nikolai BC, Yi P, Putluri N, et al. Metabolic enzyme PFKFB4 activates transcriptional coactivator SRC-3 to drive breast cancer. Nature 2018, 556: 249–254.

65. Ott M, Gogvadze V, Orrenius S, Zhivotovsky B. Mitochondria, oxidative stress and cell death. Apoptosis 2007, 12: 913–922.

66. Akiyama G, Azuchi Y, Guo X, Noro T, Kimura A, Harada C, et al. Edaravone prevents retinal degeneration in adult mice following optic nerve injury. Invest Ophthalmol Vis Sci 2017, 58: 4908–4914.

67. Wang DY, Arjun R, Kathryn R, Ceren E, Hyman BT, Wei H, et al. Global gene expression changes in rat retinal ganglion cells in experimental glaucoma. Invest Ophthalmol Vis Sci 2010, 51: 4084–4095.

68. Jeong D, Kim T, Cho I, Kim I. Modification of glycolysis affects cell sensitivity to apoptosis induced by oxidative stress and mediated by mitochondria. Biochem Biophys Res Commun 2004, 313: 984–991.

69. Borutaite V, Budriunaite A, Morkuniene R, Brown GC. Release of mitochondrial cytochrome c and activation of cytosolic caspases induced by myocardial ischaemia. Biochim Biophys Acta 2001, 1537: 101–109.

70. Shawgo ME, Shelton SN, Robertson JD. Caspase-mediated Bak activation and cytochrome c release during intrinsic apoptotic cell death in Jurkat cells. J Biol Chem 2008, 283: 35532–35538.

71. Agathocleous M, Love NK, Randlett O, Harris JJ, Liu J, Murray AJ, et al. Metabolic differentiation in the embryonic retina. Nat Cell Biol 2012, 14: 859–864.

72. Tokuda K, Kuramitsu Y, Baron B, Kitagawa T, Tokuda N, Kobayashi M, et al. Changes in metabolic proteins in ex vivo rat retina during glutamate-induced neural progenitor cell induction. Mol Cell Biochem 2016, 419: 177–184.

www.neurosci.cn
www.springer.com/12264

ORIGINAL ARTICLE

SOCS3 Attenuates GM-CSF/IFN-γ-Mediated Inflammation During Spontaneous Spinal Cord Regeneration

Xuejie Zhang[1,2] · Bingqiang He[1,2] · Hui Li[1,2] · Yingjie Wang[1,2] · Yue Zhou[3] ·
Wenjuan Wang[1,2] · Tiancheng Song[1,2] · Nan Du[1,2] · Xingxing Gu[1,2] ·
Yi Luo[1,2] · Yongjun Wang[1,2]

Abstract SOCS3, a feedback inhibitor of the JAK/STAT signal pathway, negatively regulates axonal regrowth and inflammation in the central nervous system (CNS). Here, we demonstrated a distinct role of SOCS3 in the injured spinal cord of the gecko following tail amputation. Severing the gecko spinal cord did not evoke an inflammatory cascade except for an injury-stimulated elevation of the granulocyte/macrophage colony-stimulating factor (GM-CSF) and interferon gamma (IFN-γ) cytokines. Simultaneously, the expression of SOCS3 was upregulated in microglia, and unexpectedly not in neurons. Enforced expression of SOCS3 was sufficient to suppress the GM-CSF/IFN-γ-driven inflammatory responses through its KIR domain by attenuating the activities of JAK1 and JAK2. SOCS3 was also linked to GM-CSF/IFN-γ-induced cross-tolerance. Transfection of adenovirus overexpressing SOCS3 in the injured cord resulted in a significant decrease of inflammatory cytokines. These results reveal a distinct role of SOCS3 in the regenerating spinal cord, and provide new hints for CNS repair in mammals.

✉ Yongjun Wang
wyjbs@ntu.edu.cn

1   Key laboratory of Neuroregeneration of Jiangsu and The Ministry of Education, Nantong University, Nantong 226001, China

2   Co-innovation Center of Neuroregeneration, Nantong University, Nantong 226001, China

3   Department of Rehabilitation Medicine, Affiliated Hospital of Nantong University, Nantong 226001, China

Introduction

Traumatic spinal cord injury (SCI) always results in an excessive inflammatory response, which contributes to secondary tissue damage that is characterized by the formation of an ellipsoidal, loculated cystic cavity [1–4]. Inflammation is initiated by infiltrating leukocytes or resident microglia that bind with endogenous damage-associated molecular pattern (DAMP) molecules through their pattern recognition receptors on the cell surface [5]. The subsequent release of cytokines and chemokines from these cells in turn recruits and activates more immune cells, forming a progressive inflammatory cascade at the site of tissue damage. The deteriorating milieu is neurotoxic, with tumor necrosis factor alpha (TNF-α), interleukin (IL)-1β, glutamate, nitric oxide synthase (iNOS), and free radicals [6, 7]. Inflammation starts soon after SCI and is sustained for days and weeks. Pharmaceutical treatment, such as methylprednisone, has been shown to delay post-traumatic inflammation and retard neuronal degeneration in the central nervous system (CNS) [8, 9].

Granulocyte/macrophage colony-stimulating factor (GM-CSF) was first characterized as a soluble factor with the ability to differentiate bone marrow precursor cells into granulocytes and macrophages [10, 11]. Later, it was proposed to support myeloid cell survival and proliferation in a dose-dependent manner [10, 12], and its pathophysiological significance has been emphasized in its association with inflammation and autoimmune diseases. Evidence indicates that the aberrant expression of GM-CSF exacerbates autoimmune diseases such as rheumatoid arthritis,

which is a chronic inflammatory disorder characterized by joint pain and deterioration [13], and experimental autoimmune encephalomyelitis, which is an autoimmune disorder of the CNS [14, 15]. Macrophages are one of the GM-CSF-sensitive cell types that release inflammatory cytokines, including IL-1, TNF-α, and IL-6 [16, 17]. In the CNS, GM-CSF-driven inflammation by macrophages/microglia seems more relevant to tissue damage and pathogenicity than that of T-cells, as the latter do not express the GM-CSF receptor α-chain [11, 18, 19]. The receptor for GM-CSF is abundant on macrophages and other myeloid cells. Ligation of GM-CSF to the receptor activates intracellular signaling by the trans-phosphorylation of Janus kinase 2 (JAK2), which triggers the activation of downstream STAT5 and associated kinases [20–22]. IFN-γ, the priming stimulus for macrophages, can act synergistically with GM-CSF to promote the production of cytokines [17, 23]. The signaling displays a crosslink with GM-CSF, as the α and β chains of the IFN-γ receptor are constitutively associated with JAK1 and JAK2, respectively [23].

Suppressor of cytokine signaling-3 (SOCS3) is a feedback inhibitor of the JAK/STAT signaling pathway [24, 25]. Several cytokines activate the JAK/STAT pathway by binding to their associated cell-surface receptors, leading to the recruitment and phosphorylation of receptor-associated JAK1 and JAK2, which phosphorylate and cause dimerization of the STAT proteins. These proteins promote the expression of target genes including SOCS3, which in turn negatively regulates JAK/STAT signaling by binding to the receptors or JAKs *via* a 12-amino-acid kinase-inhibitory region (KIR) [24, 26]. SOCS3 has been found to suppress inflammation in response to multiple stimuli in the contexts of pathophysiology and tissue damage [24, 25, 27, 28]. In addition, SOCS3 is rapidly induced in neurons with trauma of the peripheral and central nervous systems, and it plays inhibitory roles in neuronal regrowth. Its deficiency in primary sensory neurons or adult retinal ganglion cells results in a significant promotion of axonal elongation [26, 29]. The negative regulation of SOCS3 in both inflammatory responses and axonal growth leads to a somewhat difficult tradeoff in promoting CNS repair without evoking inflammation.

Unlike mammals, regenerating organisms such as fish, amphibians, and reptiles are capable of spinal cord regeneration after injury [30–35]. Clearly, axonal regrowth in these non-mammals occurs in a permissive milieu without inhibitory extracellular matrix components, glial scarring, or excessive activation of inflammation [30, 32]. Some DAMPs and cytokines are released but do not evoke uncontrolled inflammatory cascades [31]. A real possibility

is that some negative regulators of inflammation play active roles in the regenerative process, but the details of such regulatory mechanisms remain unclear. Since the signal transduction of SOCS3, GM-CSF, and IFN-γ converge on JAK/STAT signaling, we used *Gekko japonicus* as an experimental SCI model to investigate the regulatory mechanism of SOCS3 in suppressing inflammation that was boosted by GM-CSF and IFN-γ without affecting axonal regrowth during natural spinal cord regeneration.

Materials and Methods

Animals

Adult *G. japonicus* were used as described by Dong *et al.* [31]. Briefly, adult geckos were fed *ad libitum* with mealworms and housed in an air-conditioned room with a controlled temperature (22 °C–25 °C) and saturated humidity. Anesthesia was induced by cooling the geckos on ice prior to tail amputation. Amputation was performed at the sixth caudal vertebra, which was identified based on the special tissue structure that is present at that position [36], by placing a slipknot of nylon thread and pulling gently until the tail was detached, thus mimicking the natural defense mechanism.

All of the experiments were conducted in accordance with the guidelines of the NIH (*Guide for the Care and Use of Laboratory Animals*, 1985) and the Society for Neuroscience (*Guidelines for the Use of Animals in Neuroscience Research*). The experiments were approved by the Animal Care and Use Committee of Nantong University and the Jiangsu Province Animal Care Ethics Committee. All geckos were anesthetized on ice prior to sacrifice.

Cloning and Analysis of Gecko SOCS3

To obtain the full length of gecko SOCS3, the anti-sense primer 5′–TAG AAG AGG CGG TGG TGG CA–3′ and the sense primer 5′–ACA CCT TTC CTC CCC TGC CG–3′ were designed according to their genome sequences [33]. Both 5′–rapid amplification of cDNA ends (RACE) and 3′–RACE were performed using the BD SMART RACE cDNA amplification kit (Clontech, USA) according to the manufacturer's instructions. Comparison against the GenBank protein database was performed using the PSI-BLAST network server at the National Center for Biotechnology Information [37]. Multiple protein sequences were aligned by the MegAlign program using the Clustal method in the DNASTAR software package [38].

780

Neurosci. Bull. July, 2020, 36(7):778–792

Production of Adenovirus Overexpressing SOCS3

Adenoviruses (GV314-SOCS3 or GV314-mSOCS3) over-expressing SOCS3 or mutated SOCS3 (F4A) were produced by Genechem Co. Ltd. (Shanghai) according to the manufacturer's procedures. The open reading frame of SOCS3 family members was cloned into a GV314 vector *via* the Bam HI and AgeI sites. SOCS3 expression was driven by the EF-1α promoter, and the expression of the reporter-enhanced green fluorescent protein (eGFP) was driven by a CMV promoter. Both SOCS3 and the eGFP sequence were incorporated into an adenovirus. The adenovirus was produced using 293T cells, and the viral titers reached 2×10^{10} plaque-forming units/mL for further studies.

Cell Culture and Treatment

Mouse macrophage RAW 264.7 cells (Chinese Academy of Sciences, Shanghai Institutes for Biological Sciences Cell Resource Center) were cultured in Dulbecco's modified Eagle's medium (Gibco BRL) supplemented with 10% (*v/v*) fetal bovine serum in a 37 °C humidified incubator with 5% CO_2. The cells were treated with 10 ng/mL IFN-γ and/or 50 ng/mL GM-CSF for 0.5 h–2 h (R&D Systems) or transfected with a GV314-vector, GV314-SOCS3 or a GV314-mSOCS3 adenovirus for 48 h before stimulation with the cytokines, and then collected for subsequent assays.

Quantitative Real-Time Polymerase Chain Reaction (Q-PCR)

Total RNA was prepared with TRIzol (Gibco) from mouse macrophage RAW 264.7 cells after the designated treatment. For the Q-PCR examination of cytokine transcriptional expression, first-strand cDNA was synthesized using the Omniscript reverse transcription kit (Qiagen) in a 20-μL reaction system containing 2 μg total RNA, 0.2 U/μL M-MLV reverse transcriptase, 0.5 mmol/L dNTP mix, and 1 μmol/L Oligo-dT primer. The cDNA was diluted 1:4 before use in Q-PCR assays. The sequence-specific primers were designed and synthesized by Invitrogen (Shanghai, China). The primer pair and probe for IL-6 were: forward primer 5′–GCG AGA GTC CTT CAG AGA GA–3′, reverse primer 5′–GGT CTT GGT CCT TAG CCA CT–3′; and for iNOS were: forward primer 5′–TGT GCT CCA TAG TTT CCA GAA G–3′, reverse primer 5′–GGA CAT AGT TCA ACA TCT CCT GG–3′. The Q-PCR reactions were performed in a final volume of 20 μL (1 μL cDNA template and 19 μL Q-PCR reaction buffer containing 2.5 mmol/L $MgCl_2$, 0.2 mmol/L dNTPs, 0.5 μmol/L antisense and sense primers, 0.4 μmol/L TaqMan probe,

0.2 μL DNA polymerase, and 1×DNA polymerase buffer). Rotor-Gene 5 software (Rotor-Gene, Corbett Research, Sydney, Australia) was used for the real-time PCR analysis. The reactions were processed using one initial denaturation cycle at 94 °C for 5 min followed by 45 cycles of 94 °C for 30 s, 60 °C for 30 s, and 72 °C for 30 s. Fluorescence was recorded during each annealing step. At the end of each PCR run, the data were automatically analyzed by the system, and the amplification plots were obtained. The full-length SOCS3 plasmid was used to prepare the standard curves and was used as a specificity control for real-time PCR. The expression levels of the cytokines were normalized to an endogenous GAPDH cDNA using the forward primer 5′–TGA AGT CGC AGG AGA CAA CC–3′ and the reverse primer 5′–GGT GGA GCC AAA AGG GTC A–3′. In addition, a negative control without the first-strand cDNA was included.

ELISA Assays

A two-site sandwich ELISA was used to quantify TNF-α and IL-1β in the extracts of 0.5-cm spinal cord segments following GV314-SOCS3 adenovirus transfection, or in the extracts of RAW 264.7 cells cultured with 10 ng/mL IFN-γ and/or 50 ng/mL GM-CSF recombinant proteins for 2 h following adenovirus transfection for 48 h. The cell supernatants were harvested and the cells were lysed in buffer containing 1% SDS, 100 mmol/L Tris-HCl, 1 mmol/L PMSF, and 0.1 mmol/L β-mercaptoethanol. The lysates were centrifuged at 12,000 g for 15 min. The levels of TNF-α and IL-1β were assessed using the appropriate ELISA kits (BD Biosciences) according to the manufacturer's directions. The plates were read using a 96-well plate reader (Biotek Synergy2) at a wavelength of 450 nm.

Western Blot

Proteins were extracted from 0.5-cm spinal cord segments or cultured cells with a buffer containing 1% SDS, 100 mmol/L Tris–HCl, 1 mmol/L PMSF, and 0.1 mmol/L β-mercaptoethanol. The protein concentration of each specimen was assessed by the Bradford method to maintain the same loads. The protein extracts were heat-denatured at 95 °C for 5 min, electrophoretically separated on 10% SDS–PAGE, and transferred to PVDF membranes. The membranes were reacted with a 1:1000 dilution of primary antibodies in TBS buffer at 4 °C overnight, followed by reaction with a secondary antibody conjugated with goat anti-rabbit or goat anti-mouse HRP (Proteintech), diluted 1:1000, at room temperature for 2 h. After the membrane was washed, the HRP activity was detected using an ECL kit. The image was scanned with a GS800 densitometer

scanner (Bio-Rad), and the data were analyzed using ImageJ 1.41o (National Institutes of Health). β-actin (1:5000) was used as an internal control. The antibodies used in the Western blots were: SOCS1 or SOCS3 (polyclonal rabbit anti-gecko antibody commercially prepared using peptides synthesized by GenScript Biotech Corp., or purchased from Abcam), STAT1 (Cell Signaling Technology), pSTAT1 Tyr701 (Abcam), STAT3 (Cell Signaling Technology), pSTAT3 Tyr705 (Cell Signaling Technology), STAT5 (Cell Signaling Technology), pSTAT5 Tyr694 (Cell Signaling Technology), JAK1 (Merck), JAK2 (Cell Signaling Technology), and β-actin (Proteintech).

Immunoprecipitation

The macrophage RAW 264.7 cells were washed twice with cold phosphate-buffered saline and then extracted with lysis buffer (20 mmol/L Tris-HCl, pH 7.5, 150 mmol/L NaCl, 1 mmol/L EDTA, 1 mmol/L EGTA, 1% Triton X-100, 2.5 mmol/L sodium pyrophosphate, 1 mmol/L β-glycerophosphate, 1 mmol/L Na_3VO_4, 1 mmol/L phenylmethylsulphonyl fluoride, and Roche Applied Science's complete protease inhibitors). Whole cell extracts were centrifuged at 14,000 rpm for 20 min to remove the debris. The proteins in the supernatant were measured using Protein Assay Kit II (Bio-Rad). For the immunoprecipitation analysis, 500 μg of total cell lysates were precleared with protein A plus G-Sepharose before incubation with specific antibodies, followed by the addition of protein A plus G-Sepharose. The precipitated proteins were resolved in 2× SDS-PAGE sample buffer and separated by electrophoresis on 10%–12% SDS-PAGE. After transfer onto a polyvinylidene difluoride membrane (Millipore Corp.), they were incubated with anti-JAK1 or JAK2 or an anti-Flag antibody and further incubated with a horseradish peroxidase-conjugated secondary antibody (Santa Cruz).

Cytokine Detection

The cytokine protein analysis experiments were performed by homogenization of relevant tissues in PBS + 1% (*v/v*) Triton X cytokines were assayed using the mouse cytokine array panel kit (ary006; R&D Systems) according to the manufacturer's instructions.

Tissue Immunohistochemistry

The spinal cord segments were harvested, post-fixed, and sectioned. The sections were incubated with polyclonal rabbit anti-gecko SOCS3 or mouse anti-SOCS3 antibodies (1:500 dilution, Abcam), monoclonal mouse anti-CD68 antibody (1:200, Abcam), monoclonal mouse anti-OX42

antibody (1:200, Abcam), or mouse anti-NeuN antibody (1:200, Abcam) at 4 °C for 36 h. The sections were further reacted with the Cy3-labeled goat anti-mouse IgG secondary antibody (1:400, Gibco) or the FITC-labelled goat anti-rabbit IgG secondary antibody (1:400, Gibco) at 4 °C overnight, followed by observation under a confocal laser scanning microscope (Leica, Heidelberg, Germany).

Statistical Analysis

The statistical significance of differences between groups was analyzed by one-way analysis of variance (ANOVA) followed by Bonferroni's *post-hoc* comparison tests with SPSS 15.0 (SPSS, Chicago, IL). The normality and homoscedasticity of the data were verified before any statistical analysis using Levene's test. Statistical significance was set at the $P < 0.05$ level.

Results

GM-CSF and IFN-γ are Strongly Induced After SCI Without Evoking an Excessive Inflammatory Reaction

Mammalian SCI always elicits a robust inflammatory response through the activation of microglia/macrophages by DAMPs or inflammatory cytokines [39, 40]. To understand whether SCI is able to induce equivalent inflammatory profiles in a regenerating model, we screened 0.5-cm cord segments at the lesion sites following gecko tail amputation with a mouse cytokine protein detection array that has been shown to be effective even in amphibians [39]. Tests of several typical cytokines in the amniotic gecko also show consistent results [31]. A total of 40 cytokines, chemokines, and inflammatory markers have been examined (data partially shown). Unexpectedly, we detected low levels of pro-inflammatory cytokine profiles that are normally induced in the mammalian counterparts. TNF-α expression was moderately elevated at 1 day but decreased with the progression of regeneration. The expression of IFN-γ, together with IL-1α, was induced from 3 days after cord amputation. In contrast, the production of other detected cytokines was suppressed in the regenerative process (Fig. 1A).

The myeloid colony-stimulating factors that are relevant to proliferation, differentiation, polarity, and secretion of the cytokines of myeloid cells were also simultaneously determined. M-CSF and G-CSF are important for steady-state myelopoiesis, while GM-CSF is becoming increasingly known as a major mediator of tissue inflammation [41]. Both GM-CSF and G-CSF were significantly induced from 3 days after cord amputation, whereas M-CSF

expression showed a slight elevation (Fig. 1B). Dissimilar to SCI in mammals, SCI in the gecko does not evoke excessive inflammation, even though the expression of GM-CSF and IFN-γ is aberrantly induced.

To evaluate the effects of both GM-CSF and IFN-γ on the activation of inflammatory responses, macrophage RAW 264.7 cells were stimulated with recombinant GM-CSF (50 ng/mL) and/or IFN-γ (10 ng/mL) proteins for 2 h. These two cytokines were highly efficient in inducing TNF-α and IL-1β production in the macrophages, although there were no effects on the secretion of IL-1β. IFN-γ showed a synergistic effect on the activation of inflammation (Fig. 1C).

Expression of gSOCS3 was Dynamically Induced in the Microglia/Macrophages of the Regenerating Spinal Cord Following SCI

Since GM-CSF and/or IFN-γ are insufficient to activate the inflammatory response in the injured spinal cord of the regenerative model, contrary to reports *in vitro*, gecko SOCS3 (gSOCS3) was thought to function in the negative regulation of the GM-CSF- and IFN-γ-mediated signaling pathways. To test this possibility, the protein levels of gSOCS3 were first examined in the 0.5-cm cord segments proximal to the amputation plane. Western blot analysis demonstrated that the expression of gSOCS3 in the injured spinal cord specimens collected at 0, 1, and 3 days, and 1 and 2 weeks increased from 1 day onwards and was sustained to 2 weeks (Fig. 1D, E). Accordingly, its upstream regulators STAT1, STAT3, and STAT5 were also dynamically activated through phosphorylation (Fig. 1D, E). These data indicate that the expression of gSOCS3 is dynamically induced by SCI following tail amputation in the gecko.

In mammals, SOCS3 has been shown to negatively regulate axonal growth and inflammatory activation [24, 29, 42–44]. To better understand the roles of gSOCS3 in the regenerating spinal cord, we observed its localization in the microglia/macrophages and neurons of the amputated spinal cord in the gecko. Immunostaining showed that gSOCS3 was absent from NeuN-positive neurons but was co-localized with CD68-positive macrophages at 3 days following amputation (Fig. 2A–D). The gSOCS3 protein was undetectable in the resident microglia when they were immunostained with OX42 but was expressed by the infiltrating macrophages in both vessels and lesioned cord on days 1–3 after tail amputation (Fig. 2D–H). The data indicate that injury-induced gSOCS3 uniquely performs inflammation-related functions in the regenerating spinal cord.

SOCS3 Orthologs Show High Degrees of Identity in Amniotes

To shed light on the structural characteristics of gSOCS3, we cloned *gSOCS3* (GenBank accession number XP_015272482) and aligned the deduced amino-acid sequence with those of other vertebrates. Results showed that gSOCS3 consists of a KIR domain, SOCS (suppressor of cytokine signaling) box, and SH2 (Src-homology 2) domain [45, 46], sharing 88.8%, 89.8%, 90.2%, and 96.1% identity with human, mouse, chicken and lizard SOCS3, respectively, while it shares only 64.2% identity with zebrafish and 74.9% with frog (Fig. 3A–C). The phylogenetic tree showed that gSOCS3 clusters with those of amniotes rather than with regenerative model organisms (Fig. 3D), suggesting a conserved physiological function of SOCS3 during the evolution of amniotes.

Enforced Expression of gSOCS3 Attenuates the Production of Inflammatory Cytokines Mediated by GM-CSF/IFN-γ

To investigate the negative regulatory action of gSOCS3 in the GM-CSF/IFN-γ-mediated inflammatory response, macrophage RAW 264.7 cells were transfected with GV314-SOCS3 or GV314-vector adenovirus for 48 h, followed by treatment with recombinant GM-CSF (50 ng/mL) or/and IFN-γ (10 ng/mL) protein for 2 h. ELISA assays revealed that the enforced expression of gSOCS3 was able to significantly decrease the levels of TNF-α and IL-1β in the supernatant and/or lysate (Fig. 4A). Furthermore, it suppressed the expression of other inflammatory cytokines, such as IL-6 and iNOS (Fig. 4B). These data indicate that gSOCS3 overexpression efficiently attenuates the production of inflammatory cytokines that is mediated by GM-CSF/IFN-γ.

gSOCS3 Inhibits the JAK/STAT Pathway that is Triggered by GM-CSF/IFN-γ

The cytokines GM-CSF and IFN-γ are able to activate the JAK/STAT signaling, which appears to govern the inflammatory signature [47–49]. To demonstrate that the suppression of inflammation by gSOCS3 is involved in inhibiting the activation of the STATs, the protein levels of phosphorylated STAT1, STAT3, and STAT5 were determined following macrophage transfection with control, GV314-SOCS3, or GV314-mSOCS3 (F4A in KIR) for 48 h. The cells were additionally incubated with recombinant GM-CSF (50 ng/mL) or/and IFN-γ (10 ng/mL) for 2 h. The results revealed that the enforced expression of gSOCS3 significantly reduced the phosphorylation of STAT1 and STAT5 in comparison with the control
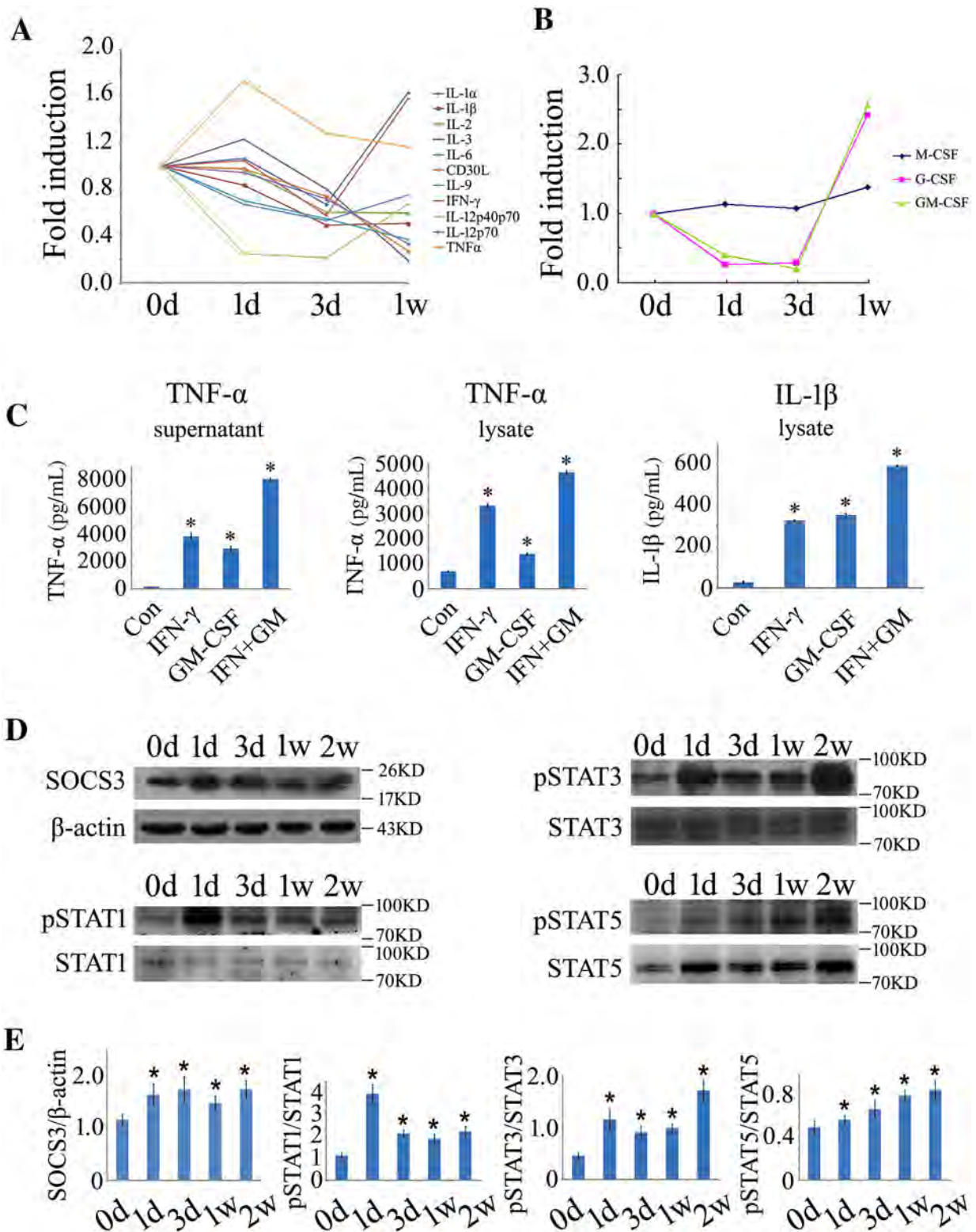
Fig. 1 Determination of inflammatory cytokines and gSOCS3 protein levels in the injured spinal cord of gecko and cell cultures. **A**, **B** Inflammatory cytokine profiles of 0.5-cm cord segments at the lesion sites following gecko tail amputation at 0, 1, and 3 days (d) and 1 week (w). Each data point shows the mean of two separate experiments with 10 animals/sample. **C** Production of TNF-α and IL-1β assessed by ELISA after RAW 264.7 cells were stimulated with recombinant GM-CSF (50 ng/mL) and/or IFN-γ (10 ng/mL) for 2 h. **D** Western blots of gSOCS3 and STAT1/3/5 phosphorylation in 0.5-cm segments of injured spinal cord at different times following gecko tail amputation ($n = 6$). **E** Statistical analysis of data as in (**D**). Data are expressed as the mean $\pm$ SEM; $*P < 0.05$.

following the stimulation of cells with IFN-γ (Fig. 5A, B). By contrast, it decreased the levels of pSTAT1, pSTAT3, and pSTAT5 after the stimulation of cells with GM-CSF or a combination of GM-CSF and IFN-γ (Fig. 5C, D). Notably, gSOCS3 was also efficient in limiting the phosphorylation of STAT1 and STAT3 when cells were treated with TNF-α/IFN-γ (Fig. S1). SOCS3 with a KIR mutation (GV314-mSOCS3) failed to inhibit the JAK/STAT pathway (Fig. 5A–D), suggesting that the KIR domain is indispensable for the inhibitory function of SOCS3.

gSOCS3 Suppresses GM-CSF/IFN-γ-Mediated Inflammation *via* Negative Regulation of JAK1 and JAK2

SOCS3 has been shown to bind to the gp130 receptor or to JAK1 and JAK2 proteins to inhibit the signal transduction induced by IL-6 [27]. Thus, in the context of GM-CSF/IFN-γ stimulation, JAK1 and/or JAK2 are potential target(s) of SOCS3 action. To clarify the kinase(s) that interact with gSOCS3, co-immunoprecipitation was applied to assay the JAKs/gSOCS3 interaction.
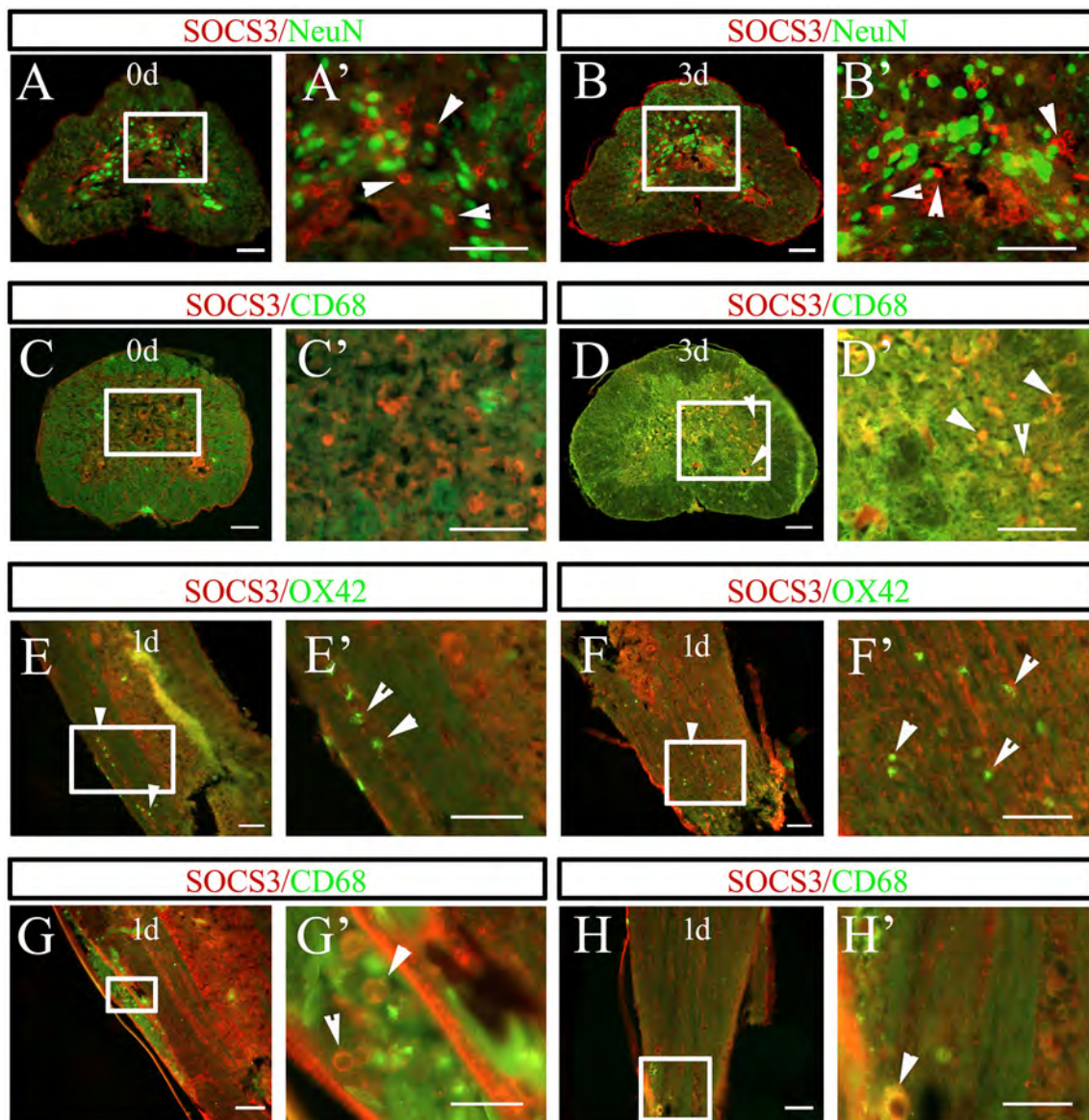
Fig. 2 Tissue distribution of gSOCS3 in the injured spinal cord following tail amputation (*n* = 5). **A–D** Representative images showing the absence of gSOCS3 in NeuN-positive neurons, but co-localization with CD68-positive microglia/macrophages at 0 and 3 days (rectangles, regions magnified in **A'–D'**). **E–H** Representative images showing co-localization of gSOCS3 with CD68- but not with OX42-positive cells in the injured spinal cord 1 day after tail amputation (rectangles, regions magnified in **E'–H'**). Arrowheads indicate positive staining. Scale bars, 100 μm in **A–D** and **A'–D'**; 50 μm in **E–H**; 25 μm in **E'–H'**.
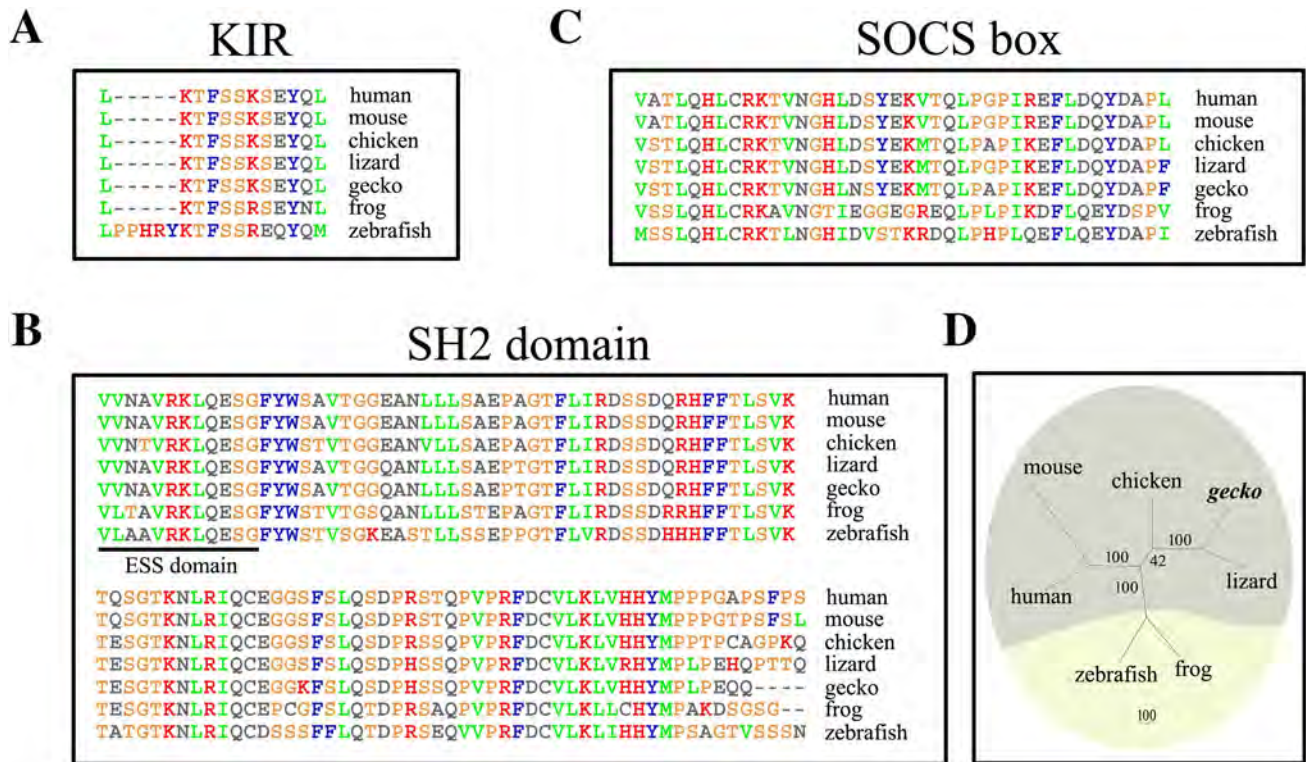
Fig. 3 Sequence analysis of gSOCS3. **A–C** Sequence alignment of SOCS3 proteins of vertebrates. Gaps introduced into sequences to optimize alignment are represented by dashes. The kinase inhibitory region (KIR) domain (**A**), a central Src-homology 2 (SH2) domain (**B**), and a C-terminal SOCS box (**C**). The 12-amino-acid extended SH2 subdomain (ESS) is underlined. **D** Unrooted phylogenetic tree of SOCS3 proteins from the representative species constructed by the neighbor-joining method in the PHYLIP 3.5c package. Bootstrap majority consensus values on 1000 replicates are indicated at each branch point as percentages. The sequences from GenBank are gecko *Gekko japonicus* SOCS3 (XP_015272482); human *Homo sapiens* SOCS3 (NP_003946); mouse *Mus musculus* SOCS3 (NP_031733); chicken *Gallus gallus* SOCS3 (NP_989931); green anole *Anolis carolinensis* SOCS3 (XP_008102404); frog *Xenopus tropicalis* SOCS3 (NP_001005696); and zebrafish *Danio rerio* SOCS3 (NP_998469).

Macrophage RAW 264.7 cells were transfected with GV314-SOCS3 or GV314-vector for 72 h, followed by protein extraction. As shown in Fig. 6, both JAK1 and JAK2 were present in the Flag-associated complexes when they were immunoprecipitated with the anti-Flag antibody (Fig. 6A). These results indicate that gSOCS3 negatively regulates JAK1/2 following stimulation with GM-CSF/IFN-γ.

To further validate that the activity of JAK1/2 is critical for GM-CSF/IFN-γ-related signal transduction, the JAK1/2-specific inhibitor AG490 was added at a concentration of 100 μmol/L to the culture medium of the macrophages that also contained different concentrations of recombinant GM-CSF or IFN-γ. The results showed that the addition of AG490 inhibited the downstream activation of STAT1, STAT3, and STAT5, as well as downstream SOCS3, which were significantly induced by recombinant GM-CSF at 0 ng/mL–100 ng/mL or IFN-γ at 0 ng/mL–40 ng/mL (Fig. 6B, C).

SOCS3 is Linked to GM-CSF/IFN-γ-Induced Inflammatory Tolerance

Different concentrations of GM-CSF induced the expression of endogenous SOCS3 in macrophages, while IFN-γ induced both SOCS1 and SOCS3 after cell incubation for 0.5 h (Fig. 7A, B). An elevation of intracellular SOCS3 that was induced by pre-stimulation with one cytokine likely desensitized the activation of the JAK/STAT pathway by the other cytokines. To address the correlations, macrophages were pretreated with recombinant IFN-γ (10 ng/mL) or GM-CSF (50 ng/mL) protein for 0.5 h, followed by a secondary stimulation with recombinant GM-CSF (50 ng/mL) or IFN-γ (10 ng/mL) for 1.5 h with or without changes of the culture medium. Combinations of IFN-γ/GM-CSF, GM-CSF/TNF-α (10 ng/mL), or TNF-α (10 ng/mL)/IFN-γ were simultaneously performed as controls. The results demonstrated that the pretreatment of macrophages with GM-CSF or IFN-γ decreased the levels of pSTAT1, pSTAT3, and pSTAT5 in response to a secondary challenge with the other (Fig. 7C–H). Accordingly,

Fig. 4 Enforced expression of gSOCS3 reduces the production of inflammatory cytokines mediated by GM-CSF/IFN-γ. **A** TNF-α and IL-1β protein levels determined by ELISA in supernatants and lysates of cell cultures. RAW 264.7 cells were transfected with GV314-SOCS3 or GV314-vector adenovirus for 48 h following treatment with recombinant GM-CSF (50 ng/mL) or/and IFN-γ (10 ng/mL) protein for 2 h. **B** Expression of IL-6 and iNOS assessed by RT-PCR after cell treatment with the same approach as in **A**. Data are expressed as the mean ± SEM; *$P < 0.05$.
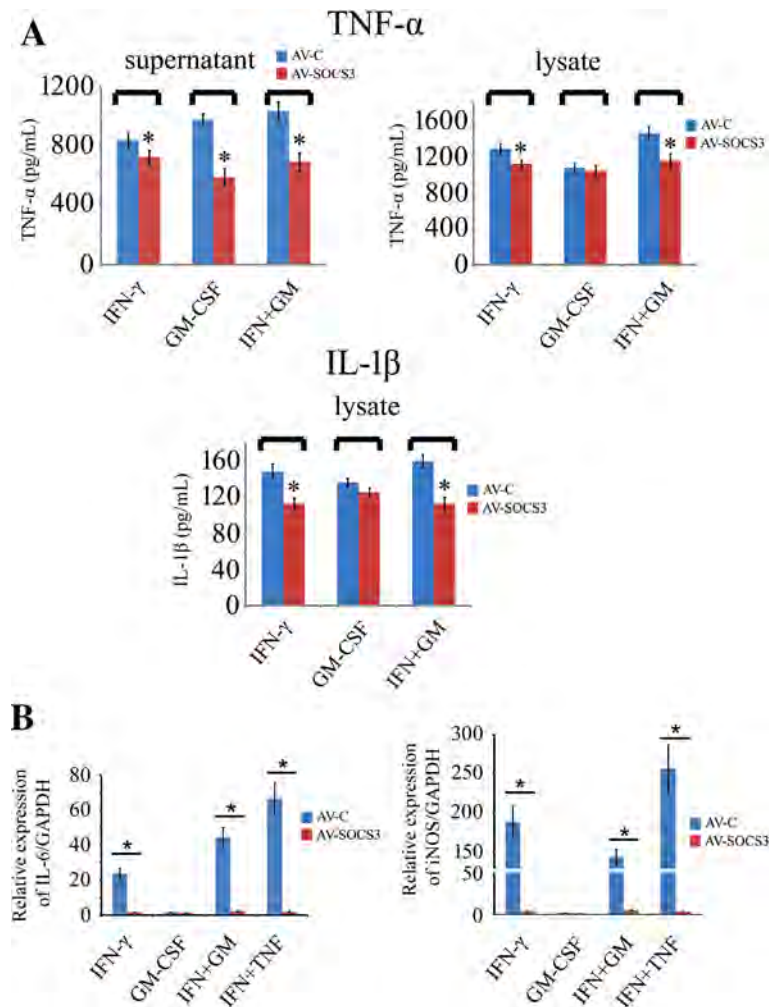
the subsequent production of TNF-α and IL-1β was also suppressed by such pretreatment (Fig. 7I–K). These data indicate that SOCS3 is involved in GM-CSF/IFN-γ-induced inflammatory tolerance.

Overexpression of gSOCS3 in the Severed Spinal Cord Decreases the Levels of Inflammatory Cytokines

To elucidate the physiological function of gSOCS3 in the injured spinal cord, a total of 9 μL of GV314-SOCS3 or GV314-vector adenovirus in three aliquots were immediately injected into the intervertebral space 2 mm–3 mm anterior to the amputation plane of the gecko tail. The transfection efficiency was evaluated by the intensity of GFP fluorescence in cross-sections of the spinal cord at 1, 2, and 3 days following adenovirus injection (Fig. 8A). Western blot analysis also showed a significant elevation of gSOCS3 expression in the cord, indicating efficient transfection in this non-mammalian species (Fig. 8B). Notably, the adenovirus was found to infect not only the

macrophages/microglia but other cell types in the cord (data not shown). The ELISA data demonstrated that the production of TNF-α and IL-1β was significantly reduced following GV314-SOCS3 transfection at 1, 3, and 7 days (Fig. 8C, D), emphasizing the important roles of gSOCS3 in blocking the inflammatory response in the injured spinal cord.

Discussion

SOCS3 is intracellularly induced by multiple cytokines in a variety of cell types, such as myeloid-derived cells and nerve cells, in response to stimulation with TNF-α, IL-1, lipopolysaccharide (LPS), ciliary neurotrophic factor, oncostatin M, insulin-like growth factor-1, and IL-6 [24, 27]. In the mammalian central and peripheral nervous systems, SOCS3 is upregulated in neuronal and glial cells, inhibiting neuronal protection and axonal regeneration, as well as decreasing astrocytic reactivity through negative regulation by STAT3 phosphorylation
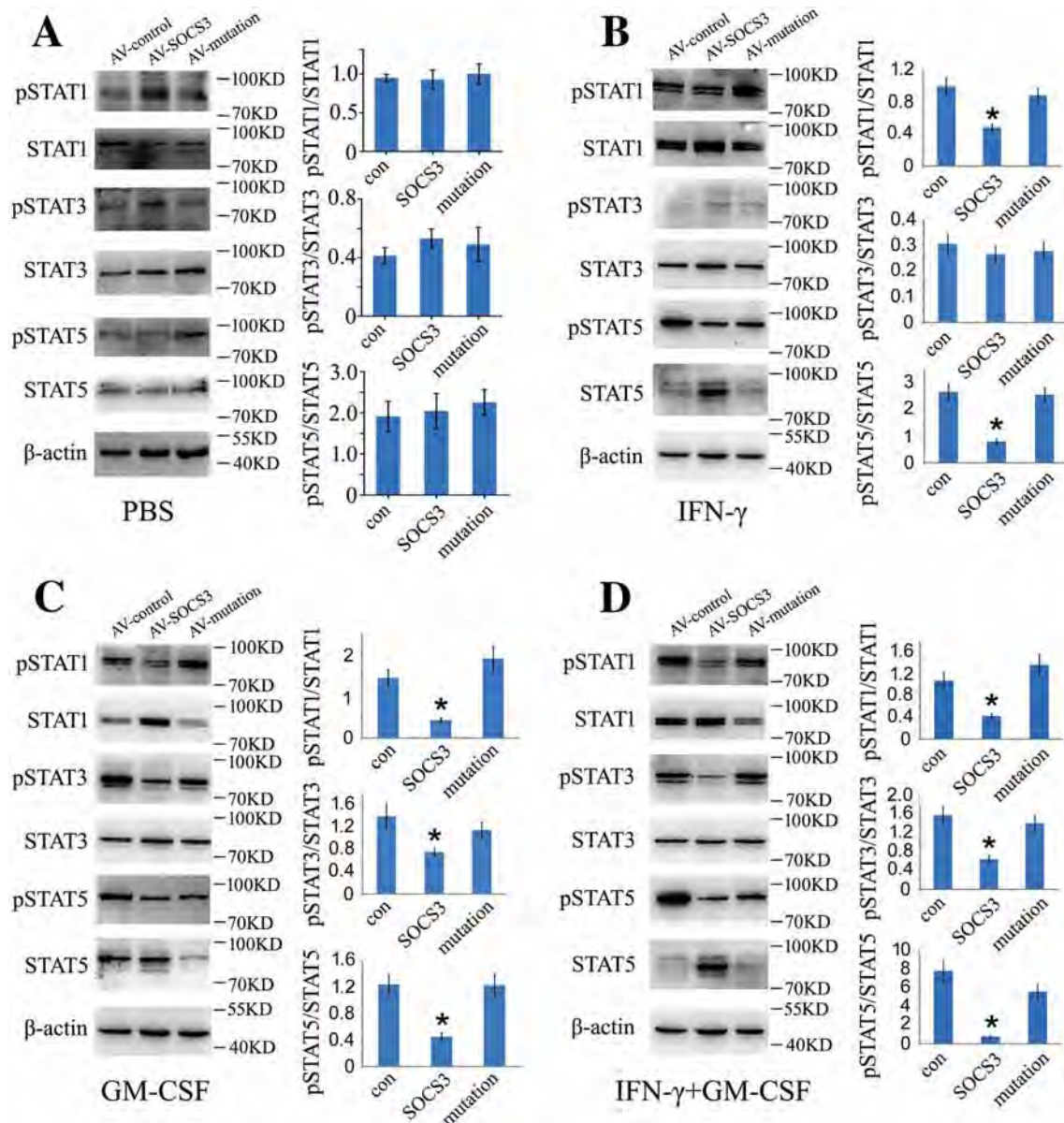
Fig. 5 gSOCS3 negatively regulates the phosphorylation of STAT1/3/5 through the KIR domain. **A–D** Macrophages were transfected with GV314-SOCS3 or GV314-mSOCS3 (F4A in KIR domain) adenovirus for 48 h before treatment with 0.1 mol/L PBS (pH 7.4) (**A**), 10 ng/mL IFN-γ (**B**), 50 ng/mL GM-CSF (**C**), or combinations of 50 ng/mL GM-CSF and 10 ng/mL IFN-γ (**D**) for 2 h. Phosphorylation of STAT1/3/5 was determined by Western blot. Data are expressed as the mean ± SEM; *$P < 0.05$.

[26, 29, 43, 44, 50–52]. SOCS3 is also inducibly expressed in dendritic cells, T cells, and macrophages, which are recruited to the CNS under inflammatory conditions [24]. Interestingly, SOCS3 is absent from the neurons of the gecko spinal cord, suggesting its important roles in suppressing inflammation, rather than in affecting axonal regrowth. Whether such a strategy is used by other models of regeneration remains unclear. By screening the gecko genome, we found two paralogs of SOCS3, designated SOCS3a and SOCS3b (Fig. S2A). In the present study, gSOCS3 clustered with and was thus named SOCS3b.

SOCS3a, which lacks a KIR domain in the N-terminus, co-localized with neurons (Fig. S2B, C). Further investigation will be helpful in elucidating the distinct functions of the two paralogs in animal models of regeneration.

GM-CSF, together with other CSFs, was first regarded as a pro-inflammatory cytokine due to its ability to stimulate the formation of the neutral protease plasminogen activator in macrophages [53]. This pleiotropic cytokine is secreted by a wide variety of cells, including endothelial cells, monocytes, astrocytes, and T cells [54]. Aberrant expression of GM-CSF is associated with multiple
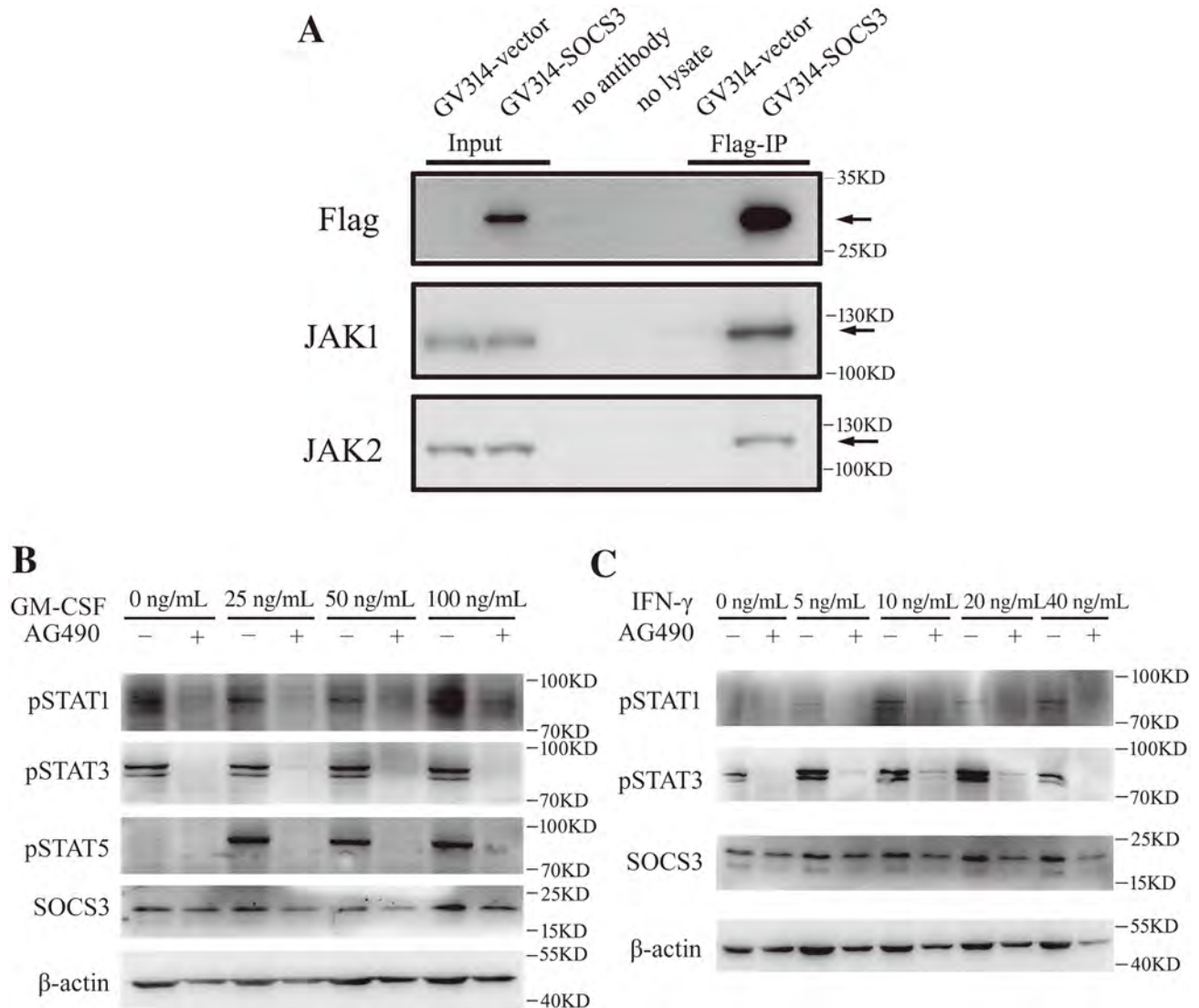
Fig. 6 gSOCS3 binds with JAK1 and JAK2 to negatively regulate the activation of STAT1/3/5. **A** Binding assays of gSOCS3 with JAK1/2 in macrophages transfected with GV314-SOCS3 adenovirus for 72 h. Immunoprecipitation using anti-Flag antibody and detection of the components of the Flag(SOCS3)-associated complexes with anti-JAK1 or -JAK2 antibody. **B, C** Addition of 100 μmol/L JAK1/2 inhibitor AG490 decreases the levels of pSTAT1/3/5 in the context of stimulation with the cytokine GM-CSF or IFN-γ.

neurological disorders such as Alzheimer's disease (AD), vascular dementia, and multiple sclerosis [55, 56]. Neutralization of GM-CSF by antibodies is capable of suppressing microglial activation in the cerebral cortex of a mouse AD model [57]. Therefore, GM-CSF promotes CNS inflammation *via* microglial activation. Studies on GM-CSF-induced pro-inflammatory mediators have shown different outcomes. For example, GM-CSF fails to induce TNF-α and NO in the activation of microglia [54], while a low dose of recombinant GM-CSF is sufficient to facilitate the production of TNF-α in human mononuclear cells [17]. LPS has been shown to significantly increase the GM-CSF-induced production of cytokines, indicating that GM-CSF might directly or indirectly activate inflammation, depending on the different cell types. In this study, we demonstrated that GM-CSF induced the production of TNF-α and IL-1β by macrophages, with IFN-γ acting in a synergistic manner. GM-CSF-mediated CNS inflammation is re-emphasized following SCI.

GM-CSF activates intracellular JAK2/STAT5 signaling through the GM-CSF receptors of the plasma membrane and is required for the proliferation, differentiation, and inflammatory activation of myeloid cells [10]. Although enforced gSOCS3 inhibited the phosphorylation of STAT1 and STAT3 in macrophages (Fig. 5C), the GM-CSF-mediated inflammatory response appeared to be exclusively regulated *via* STAT5, as the addition of recombinant GM-CSF to macrophage cultures resulted in insignificant

Fig. 7 Determination of GM-CSF/IFN-γ-induced inflammatory tolerance mediated by SOCS3. **A**, **B** Western blots showing that treatment with IFN-γ or GM-CSF recombinant protein induces the expression of endogenous SOCS1 and/or SOCS3 in macrophages following treatment at different concentrations for 0.5 h. **C**, **E**, **G** Western blots of pSTAT1/3/5 following different treatments. pi indicates GM-CSF or IFN-γ pretreatment for 0.5 h without a change of culture medium, followed by the addition of the other cytokine for 1.5 h; p indicates pretreatment with GM-CSF or IFN-γ for 0.5 h with a change of medium, followed by the other cytokine for 1.5 h. **D**, **F**, **H** Statistical analysis of data as in **C**, **E**, and **G**, respectively. **I–K** ELISA assays of TNF-α and IL-1β in the supernatant and lysate of cell cultures after various treatments. Data are expressed as the mean ± SEM; *P < 0.05.
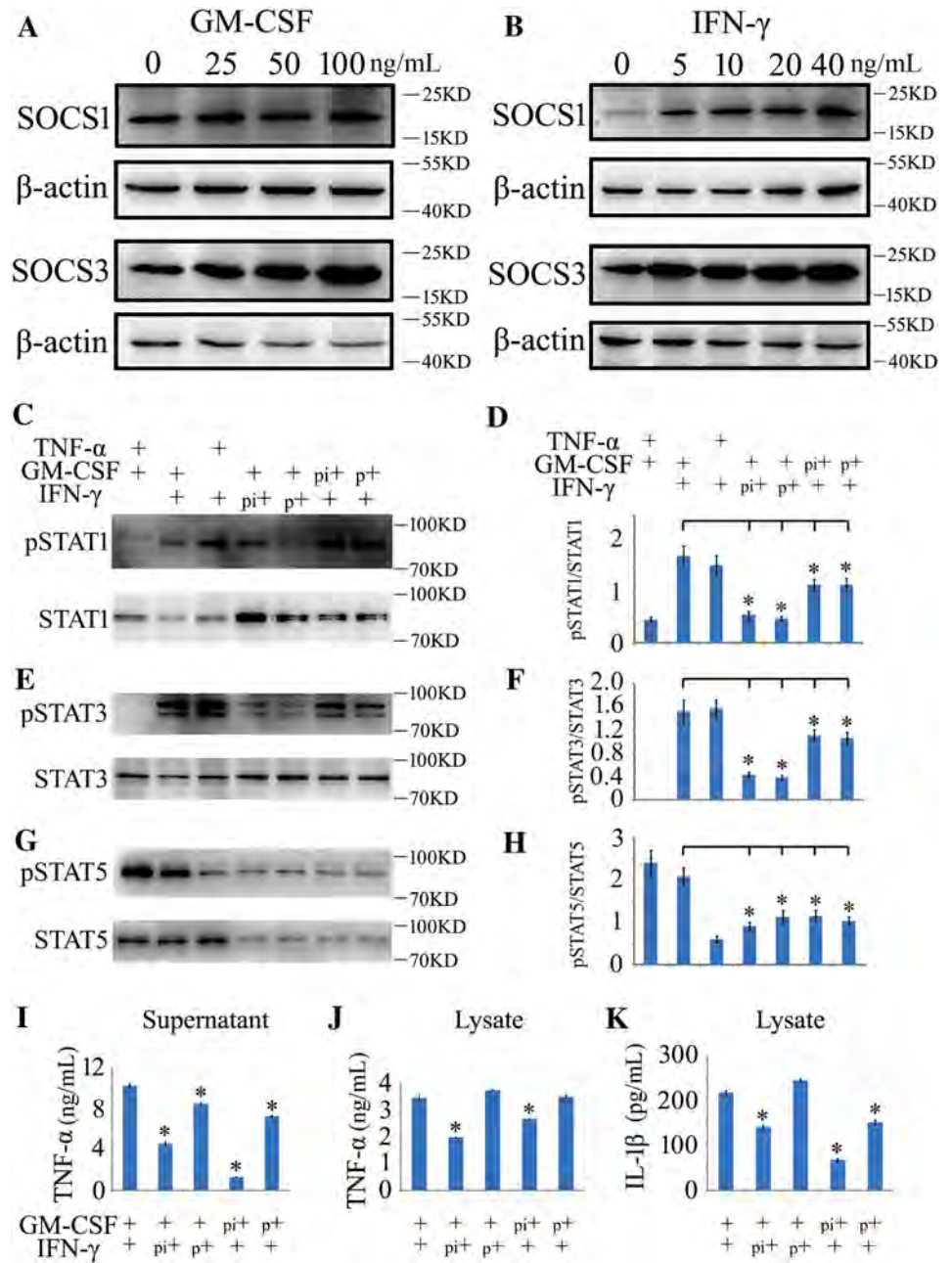
increases of pSTAT1 and pSTAT3 (Fig. 6B). In contrast, IFN-γ activated STAT1 and STAT3 through JAK2 signaling (Fig. 6C), consistent with the findings of other investigations [49, 58]. However, gSOCS3 overexpression only reduced the levels of pSTAT1 and pSTAT5 (Fig. 5B), suggesting an unknown mechanism of dephosphorylation in STAT3 resembling that of STAT1 by protein tyrosine phosphatases [59].

Pretreatment of the macrophages with GM-CSF or IFN-γ resulted in desensitization of the JAK/STAT pathway in a secondary cytokine challenge through reductions in pSTAT1, pSTAT3, and pSTAT5. A low concentration of

IFN-γ (5 ng/mL) activates SOCS1 and SOCS3 within 20 min [58], and this is sufficient to negatively regulate the activities of JAK1 and JAK2, leading to suppressed phosphorylation of downstream STAT1, STAT3, and STAT5. GM-CSF has also been shown to induce intracellular SOCS3, which might be effective in the desensitization of the JAK/STAT pathway that is mediated by other cytokines.

In conclusion, SOCS3 is specifically induced in the microglia rather than in the neurons of the regenerating spinal cord. This protein acts to limit excessive inflammatory responses in the macrophages/microglia that are

Fig. 8 gSOCS3 overexpression in the injured spinal cord decreases the levels of inflammatory cytokines. **A** Representative images of GFP fluorescence in the injured cord at 1, 2, and 3 days (scale bars, 100 μm). **B** Western blots of gSOCS3 in the injured spinal cord following transfection with GV314-SOCS3 adenovirus. **C, D** ELISA assays of TNF-α and IL-1β production in the injured spinal cord transfected with GV314-SOCS3 adenovirus on days 0, 1, 3 and 7. Data are expressed as the mean ± SEM; *$P < 0.05$.
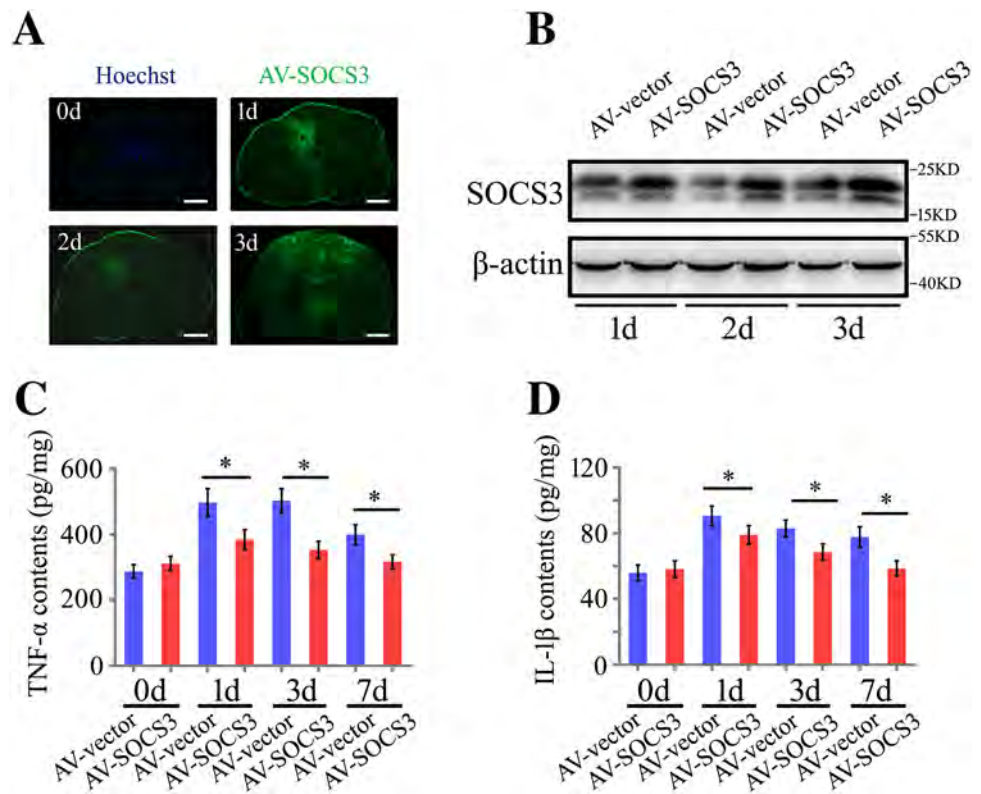
mediated by GM-CSF/IFN-γ through the negative regulation of JAK1/2 activity. Our results reveal a distinct regulatory phenomenon of SOCS3 in the injured spinal cord of non-mammalian amniotes.

Conflict of interest The authors declared that there were no competing interests.

References

1. Ransohoff RM, Brown MA. Innate immunity in the central nervous system. J Clin Invest 2012, 122: 1164–1171.
2. Popovich PG, Longbrake EE. Can the immune system be harnessed to repair the CNS? Nat Rev Neurosci 2008, 9: 481–493.
3. Niu Z, Yang L, Wu X, Zhu Y, Chen J, Fang Y. The relationship between neuroimmunity and bipolar disorder: mechanism and translational application. Neurosci Bull 2019, 35: 595–607.
4. Qin C, Zhou LQ, Ma XT, Hu ZW, Yang S, Chen M, et al. Dual functions of microglia in ischemic stroke. Neurosci Bull 2019, 35: 921–933.
5. Gadani SP, Walsh JT, Lukens JR, Kipnis J. Dealing with danger in the CNS: The response of the immune system to injury. Neuron 2015, 87: 47–62.
6. Olmos G, Llado J. Tumor necrosis factor alpha: a link between neuroinflammation and excitotoxicity. Mediat Inflamm 2014, 2014: 861231.
7. Roth TL, Nayak D, Atanasijevic T, Koretsky AP, Latour LL, McGavern DB. Transcranial amelioration of inflammation and cell death after brain injury. Nature 2014, 505: 223–228.
8. Kosmac K, Bantug GR, Pugel EP, Cekinovic D, Jonjic S, Britt WJ. Glucocorticoid treatment of MCMV infected newborn mice attenuates CNS inflammation and limits deficits in cerebellar development. PLoS Pathog 2013, 9: e1003200.
9. Zhang Z, Zhang Z, Artelt M, Burnet M, Schluesener HJ. Dexamethasone attenuates early expression of three molecules associated with microglia/macrophages activation following rat traumatic brain injury. Acta Neuropathol 2007, 113: 675–682.
10. Bhattacharya P, Budnick I, Singh M, Thiruppathi M, Alharshawi K, Elshabrawy H, et al. Dual role of GM-CSF as a pro-inflammatory and a regulatory cytokine: implications for immune therapy. J Interferon Cytokine Res 2015, 35: 585–599.

11. Hamilton JA. Colony-stimulating factors in inflammation and autoimmunity. Nat Rev Immunol 2008, 8: 533–544.

12. Guthridge MA, Barry EF, Felquer FA, McClure BJ, Stomski FC, Ramshaw H, *et al.* The phosphoserine-585-dependent pathway of the GM-CSF/IL-3/IL-5 receptors mediates hematopoietic cell survival through activation of NF-kappaB and induction of bcl-2. Blood 2004, 103: 820–827.

13. Burmester GR, Feist E, Sleeman MA, Wang B, White B, Magrini F. Mavrilimumab, a human monoclonal antibody targeting GM-CSF receptor-alpha, in subjects with rheumatoid arthritis: a randomised, double-blind, placebo-controlled, phase I, first-in-human study. Ann Rheum Dis 2011, 70: 1542–1549.

14. Ponomarev ED, Shriver LP, Maresz K, Pedras-Vasconcelos J, Verthelyi D, Dittel BN. GM-CSF production by autoreactive T cells is required for the activation of microglial cells and the onset of experimental autoimmune encephalomyelitis. J Immunol 2007, 178: 39–48.

15. Codarri L, Gyulveszi G, Tosevski V, Hesske L, Fontana A, Magnenat L, *et al.* RORgammat drives production of the cytokine GM-CSF in helper T cells, which is essential for the effector phase of autoimmune neuroinflammation. Nat Immunol 2011, 12: 560–567.

16. Bischof RJ, Zafiropoulos D, Hamilton JA, Campbell IK. Exacerbation of acute inflammatory arthritis by the colony-stimulating factors CSF-1 and granulocyte macrophage (GM)-CSF: evidence of macrophage infiltration and local proliferation. Clin Exp Immunol 2000, 119: 361–367.

17. Sisson SD, Dinarello CA. Production of interleukin-1 alpha, interleukin-1 beta and tumor necrosis factor by human mononuclear cells stimulated with granulocyte-macrophage colony-stimulating factor. Blood 1988, 72: 1368–1374.

18. Rosas M, Gordon S, Taylor PR. Characterisation of the expression and function of the GM-CSF receptor alpha-chain in mice. Eur J Immunol 2007, 37: 2518–2528.

19. Croxford AL, Spath S, Becher B. GM-CSF in neuroinflammation: Licensing myeloid cells for tissue damage. Trends Immunol 2015, 36: 651–662.

20. Askenase MH, Han SJ, Byrd AL, Morais da Fonseca D, Bouladoux N, Wilhelm C, *et al.* Bone-marrow-resident NK cells prime monocytes for regulatory function during infection. Immunity 2015, 42: 1130–1142.

21. Hercus TR, Thomas D, Guthridge MA, Ekert PG, King-Scott J, Parker MW, *et al.* The granulocyte-macrophage colony-stimulating factor receptor: linking its structure to cell signaling and its role in disease. Blood 2009, 114: 1289–1298.

22. Shiomi A, Usui T. Pivotal roles of GM-CSF in autoimmunity and inflammation. Mediat Inflamm 2015, 2015: 568543.

23. Ma J, Chen T, Mandelin J, Ceponis A, Miller NE, Hukkanen M, *et al.* Regulation of macrophage activation. Cell Mol Life Sci 2003, 60: 2334–2346.

24. Baker BJ, Akhtar LN, Benveniste EN. SOCS1 and SOCS3 in the control of CNS immunity. Trends Immunol 2009, 30: 392–400.

25. Carow B, Rottenberg ME. SOCS3, a Major Regulator of Infection and Inflammation. Front Immunol 2014, 5: 58.

26. Miao T, Wu D, Zhang Y, Bo X, Subang MC, Wang P, *et al.* Suppressor of cytokine signaling-3 suppresses the ability of activated signal transducer and activator of transcription-3 to stimulate neurite growth in rat primary sensory neurons. J Neurosci 2006, 26: 9512–9519.

27. Alexander WS. Suppressors of cytokine signalling (SOCS) in the immune system. Nat Rev Immunol 2002, 2: 410–416.

28. Qin H, Holdbrooks AT, Liu Y, Reynolds SL, Yanagisawa LL, Benveniste EN. SOCS3 deficiency promotes M1 macrophage polarization and inflammation. J Immunol 2012, 189: 3439–3448.

29. Smith PD, Sun F, Park KK, Cai B, Wang C, Kuwako K, *et al.* SOCS3 deletion promotes optic nerve regeneration *in vivo*. Neuron 2009, 64: 617–623.

30. Diaz Quiroz JF, Echeverri K. Spinal cord regeneration: where fish, frogs and salamanders lead the way, can we follow? Biochem J 2013, 451: 353–364.

31. Dong Y, Gu Y, Huan Y, Wang Y, Liu Y, Liu M, *et al.* HMGB1 protein does not mediate the inflammatory response in spontaneous spinal cord regeneration: a hint for CNS regeneration. J Biol Chem 2013, 288: 18204–18218.

32. Lee-Liu D, Edwards-Faret G, Tapia VS, Larrain J. Spinal cord regeneration: lessons for mammals from non-mammalian vertebrates. Genesis 2013, 51: 529–544.

33. Liu Y, Zhou Q, Wang Y, Luo L, Yang J, Yang L, *et al.* Gekko japonicus genome reveals evolution of adhesive toe pads and tail regeneration. Nat Commun 2015, 6: 10033.

34. Shen T, Wang Y, Zhang Q, Bai X, Wei S, Zhang X, *et al.* Potential involvement of snail members in neuronal survival and astrocytic migration during the gecko spinal cord regeneration. Front Cell Neurosci 2017, 11: 113.

35. Wang Y, Dong Y, Song H, Liu Y, Liu M, Yuan Y, *et al.* Involvement of gecko SNAP25b in spinal cord regeneration by promoting outgrowth and elongation of neurites. Int J Biochem Cell Biol 2012, 44: 2288–2298.

36. McLean KE, Vickaryous MK. A novel amniote model of epimorphic regeneration: the leopard gecko, Eublepharis macularius. BMC Dev Biol 2011, 11: 50.

37. Altschul SF, Madden TL, Schaffer AA, Zhang J, Zhang Z, Miller W, *et al.* Gapped BLAST and PSI-BLAST: a new generation of protein database search programs. Nucleic Acids Res 1997, 25: 3389–3402.

38. Burland TG. DNASTAR's Lasergene sequence analysis software. Methods Mol Biol 2000, 132: 71–91.

39. Godwin JW, Pinto AR, Rosenthal NA. Macrophages are required for adult salamander limb regeneration. Proc Natl Acad Sci U S A 2013, 110: 9415–9420.

40. Zhang B, Gensel JC. Is neuroinflammation in the injured spinal cord different than in the brain? Examining intrinsic differences between the brain and spinal cord. Exp Neurol 2014, 258: 112–120.

41. Becher B, Tugues S, Greter M. GM-CSF: From growth factor to central mediator of tissue inflammation. Immunity 2016, 45: 963–973.

42. Yin Y, Liu W, Dai Y. SOCS3 and its role in associated diseases. Hum Immunol 2015, 76: 775–780.

43. Li S, He Q, Wang H, Tang X, Ho KW, Gao X, *et al.* Injured adult retinal axons with Pten and Socs3 co-deletion reform active synapses with suprachiasmatic neurons. Neurobiol Dis 2015, 73: 366–376.

44. Sun F, Park KK, Belin S, Wang D, Lu T, Chen G, *et al.* Sustained axon regeneration induced by co-deletion of PTEN and SOCS3. Nature 2011, 480: 372–375.

45. Kershaw NJ, Murphy JM, Lucet IS, Nicola NA, Babon JJ. Regulation of Janus kinases by SOCS proteins. Biochem Soc Trans 2013, 41: 1042–1047.

46. Starr R, Willson TA, Viney EM, Murray LJ, Rayner JR, Jenkins BJ, *et al.* A family of cytokine-inducible inhibitors of signalling. Nature 1997, 387: 917–921.

47. Croxford AL, Lanzinger M, Hartmann FJ, Schreiner B, Mair F, Pelczar P, *et al.* The cytokine GM-CSF drives the inflammatory signature of CCR2+ monocytes and licenses autoimmunity. Immunity 2015, 43: 502–514.

48. Hu X, Ivashkiv LB. Cross-regulation of signaling pathways by interferon-gamma: implications for immune responses and autoimmune diseases. Immunity 2009, 31: 539–550.

49. Schroder K, Hertzog PJ, Ravasi T, Hume DA. Interferon-gamma: an overview of signals, mechanisms and functions. J Leukoc Biol 2004, 75: 163–189.

50. Park KW, Lin CY, Lee YS. Expression of suppressor of cytokine signaling-3 (SOCS3) and its role in neuronal death after complete spinal cord injury. Exp Neurol 2014, 261: 65–75.

51. Ben Haim L, Ceyzeriat K, Carrillo-de Sauvage MA, Aubry F, Auregan G, Guillermier M, et al. The JAK/STAT3 pathway is a common inducer of astrocyte reactivity in Alzheimer's and Huntington's diseases. J Neurosci 2015, 35: 2817–2829.

52. Jin D, Liu Y, Sun F, Wang X, Liu X, He Z. Restoration of skilled locomotion by sprouting corticospinal axons induced by co-deletion of PTEN and SOCS3. Nat Commun 2015, 6: 8074.

53. Hamilton JA, Stanley ER, Burgess AW, Shadduck RK. Stimulation of macrophage plasminogen activator activity by colony-stimulating factors. J Cell Physiol 1980, 103: 435–445.

54. Parajuli B, Sonobe Y, Kawanokuchi J, Doi Y, Noda M, Takeuchi H, et al. GM-CSF increases LPS-induced production of proin-flammatory mediators via upregulation of TLR4 and CD14 in murine microglia. J Neuroinflamm 2012, 9: 268.

55. Mellergard J, Edstrom M, Vrethem M, Ernerudh J, Dahle C. Natalizumab treatment in multiple sclerosis: marked decline of chemokines and cytokines in cerebrospinal fluid. Mult Scler 2010, 16: 208–217.

56. Tarkowski E, Wallin A, Regland B, Blennow K, Tarkowski A. Local and systemic GM-CSF increase in Alzheimer's disease and vascular dementia. Acta Neurol Scand 2001, 103: 166–174.

57. Manczak M, Mao P, Nakamura K, Bebbington C, Park B, Reddy PH. Neutralization of granulocyte macrophage colony-stimulating factor decreases amyloid beta 1–42 and suppresses microglial activity in a transgenic mouse model of Alzheimer's disease. Hum Mol Genet 2009, 18: 3876–3893.

58. Song MM, Shuai K. The suppressor of cytokine signaling (SOCS) 1 and SOCS3 but not SOCS2 proteins inhibit interferon-mediated antiviral and antiproliferative activities. J Biol Chem 1998, 273: 35056–35062.

59. Haspel RL, Darnell JE, Jr. A nuclear protein tyrosine phosphatase is required for the inactivation of Stat1. Proc Natl Acad Sci U S A 1999, 96: 10188–10193.

ORIGINAL ARTICLE

Increased EZH2 Levels in Anterior Cingulate Cortex Microglia Aggravate Neuropathic Pain by Inhibiting Autophagy Following Brachial Plexus Avulsion in Rats

Xiang-Lei Meng[1,2,3] · Pengfei Fu[4] · Lin Wang[5] · Xun Yang[1,2,3] · Guanghui Hong[1,2,3] · Xin Zhao[1,2,3] · Jie Lao[1,2,3]

Abstract After brachial plexus avulsion (BPA), microglia induce inflammation, initiating and maintaining neuropathic pain. EZH2 (enhancer of zeste homolog 2) has been implicated in inflammation and neuropathic pain, but the mechanisms by which it regulates neuropathic pain remain unclear. Here, we found that EZH2 levels were markedly upregulated during BPA-induced neuropathic pain *in vivo* and *in vitro*, stimulating pro-inflammatory cytokines (IL-1β, TNF-α, and IL-6) secretion *in vivo*. In rats with BPA-induced neuropathic pain, mechanical and cold hypersensitivities were induced by EZH2 upregulation and inhibited by EZH2 downregulation in the anterior cingulate cortex. Microglial autophagy was also significantly inhibited, with EZH2 inhibition activating autophagy and reducing neuroinflammation *in vivo*. However, this effect was impaired by inhibiting autophagy with 3-methyladenine, suggesting that the MTOR signaling pathway is a functional target of EZH2. These data suggest that EZH2 regulates neuroinflammation and neuropathic pain *via* a novel MTOR-mediated autophagy signaling pathway, providing a promising approach for managing neuropathic pain.

Introduction

Neuropathic pain, defined as pain caused by a lesion or disease of the somatosensory system [1], reduces the quality of life and causes psychological diseases. Brachial plexus avulsion (BPA) is common in patients with high-energy trauma. Neuropathic pain is a common complication with a prevalence of 67%–71% in BPA patients [2]. The anterior cingulate cortex (ACC) is an important region of the brain [3] that has been found, in animal studies, to activate ACC–spinal dorsal horn projections, directly potentiate spinal sensory transmission, and generate neuropathic pain [4]. Yang *et al.* [5] reported that nerve injury-induced neuropathic pain elevates the intrinsic excitation of pyramidal neurons in the ACC of mice, suggesting that the ACC plays an important role in neuropathic pain. Microglia are the main type of immune cell in the central nervous system (CNS). Studies [6–8] have shown that microglia are activated to release pro-inflammatory cytokines, which are critical for initiating and maintaining neuropathic pain.

Enhancer of zeste homolog 2 (EZH2) is a crucial catalytic subunit of polycomb repressive complex 2 (PRC2), a methyltransferase that acts on histone H3 lysine27 (H3K27) to produce trimethylated H3K27 (H3K27TM), resulting in gene silencing. It has been suggested that EZH2 might be involved in the development

✉ Jie Lao
laojiefd@sina.com

1 Department of Hand Surgery, Huashan Hospital, Fudan University, Shanghai 200040, China

2 Key Laboratory of Hand Reconstruction, Ministry of Health, Shanghai 200032, China

3 Shanghai Key Laboratory of Peripheral Nerve and Microsurgery, Shanghai 200032, China

4 Department of Neurosurgery, Huashan Hospital, Fudan University, Shanghai 200040, China

5 Health Management Center, The First Affiliated Hospital of Zhengzhou University, Zhengzhou 450001, China

and maintenance of neuropathic pain by positively modulating pro-inflammatory cytokines *in vivo* [9]. Moreover, another study revealed that EZH2 might control inflammatory target genes by modulating the interferon regulatory factor (IRF) and signal transducer and activator of transcription (STAT) signaling pathways, which are well-established mechanisms that regulate inflammatory disorders *in vivo* and *in vitro* [10]. Recent evidence has suggested that microRNAs can negatively regulate neuroinflammation and neuropathic pain by binding to the 3′-untranslated region sequence of EZH2 [11]. Collectively, these studies indicate that EZH2-mediated signaling pathways are involved in the pathophysiology of neuropathic pain, and may help identify promising therapeutic strategies for treating neuropathic pain.

Autophagy is a crucial aspect of human health that has been shown to affect physiology, homeostasis, development, and lifespan [12]. It is an evolutionarily-conserved cellular process that delivers damaged organelles and long-lived proteins to the lysosome for degradation [13]. Evidence indicates that autophagy is involved in the modulation of neuropathic pain. One study reported that autophagy in GABAergic interneurons affects neuropathic pain [14], while another indicated that autophagy regulates neuropathic pain *via* the rapamycin-mediated mammalian target of rapamycin (MTOR) signaling pathway [15]. Moreover, microRNA has also been shown to contribute to neuropathic pain by modulating neuroinflammation *via* a novel mechanism in which it targets the *ATG14* gene [6]. Based on the findings of these studies, we hypothesized that autophagy plays an important role in the initiation and maintenance of neuropathic pain.

Although EZH2, autophagy, microglia, neuroinflammation, and the ACC may all be involved in neuropathic pain, the underlying molecular mechanisms remain elusive. In this study, we used the rat model of BPA-induced neuropathic pain to examine EZH2 expression, autophagy, and neuroinflammation in the ACC and to investigate the mechanism underlying neuropathic pain.

Materials and Methods

Animals and Neuropathic Pain Model

Adult male Sprague–Dawley rats weighing 200 ± 10 g were purchased from the Shanghai Laboratory Animal Research Center (Shanghai, China) and 3–4 rats per cage were maintained under specific pathogen-free conditions (23–24 °C, 12/12-h light/dark cycle, 40%–60% relative humidity). The rats were provided with food and water ad libitum and acclimated for one week prior to experiments. This study was approved by the Animal Ethics

Committee of Fudan University, and all experimental procedures were carried out in accordance with the guidelines of the International Association for the Study of Pain. A total of 232 rats were used in this study and efforts were made to minimize the number of rats used.

Neuropathic pain was induced surgically in each rat following the procedure of Wang *et al.* [16]. Briefly, each rat was anesthetized with 1% sodium pentobarbital (40 mg/kg) and placed in a supine position with the head oriented close to the surgeon and the left forepaw abducted and extended. Using a scalpel, a 2-cm horizontal incision was made 2 mm above the clavicle, the superficial fascia was separated, and the sternocleidomastoid exposed. The sternocleidomastoid was then transected to expose the left brachial plexus, the C5-T1 spinal nerve roots were avulsed using mosquito forceps, and finally the incision was closed using 4-0 silk suture. The same procedure was performed on the sham-operated rats but the brachial plexus was left intact.

Isolation of ACC Microglia

Microglia were isolated from the ACC using the Percoll density gradient centrifugation method described by Willemen *et al.* [17]. Briefly, each rat was deeply anesthetized as above, then the ACC was dissected from the brain and transferred immediately into 4 mL of ice-cold Hanks' balanced salt solution. Next, the ACC suspension was passed through a 70-µm cell strainer (BD Biosciences, Alphen aan de Rijn, The Netherlands) and centrifuged at $400 \times g$ for 7 min. The cells (4 mL) were then centrifuged in a density gradient consisting of 75% Percoll, 3 mL 50% Percoll, 3 mL 35% Percoll, and 2 mL PBS at $1000 \times g$ and 10 °C for 20 min. Cells at the 50%/75% interface were collected, washed in ice-cold phosphate-buffered saline (PBS), and re-suspended in PBS containing 1% bovine serum albumin (BSA).

Pain Behavior Assessment

Measurement of Mechanical Allodynia

To assess mechanical allodynia, we measured the 50% mechanical withdrawal threshold (50% MWT) of the left hind paw according to the method described by Rubens *et al.* [18]. Briefly, each rat was placed on a metal mesh platform 30 cm above the floor and covered with a transparent plastic box. The rats were acclimatized for 30 min to reduce the effect of exploratory behavior on the measurements, which were carried out using Von Frey filaments (Stoelting, Wood Dale, IL) with bending forces of 0.4 g, 0.6 g, 1.0 g, 2.0 g, 4.0 g, 6.0 g, 8.0 g, and 15.0 g using Dixon's up-and-down method [19]. The 50% MWT

was assessed the day before surgery (day -1) and then on days 3, 7, and 14 post-surgery. Rats without evidence of pain after surgery were eliminated from the study.

Measurement of Cold Allodynia

To assess cold allodynia, we used the acetone spray test [20] with the same conditions and time points used to measure mechanical allodynia. Briefly, 250 μL of ice-cold acetone (0°C) was sprayed onto the center of the left hind paw. Then the cold withdrawal score (CWS) was determined according to the following criteria: 0, the paw did not respond to the cold acetone; 1, the paw responded mildly (withdrawal with little or no weight on paw); 2, the paw.

Intraperitoneal Drug Administration

GSK126, 3-methyladenine (3-MA), and rapamycin (Rapa) from APExBIO Technology (Houston, TX, USA) were dissolved in PBS with 5% dimethyl sulfoxide (DMSO). GSK126 (7 mg/kg), 3-MA (10 mg/kg), and Rapa (1 mg/kg) were intraperitoneally injected into the neuropathic pain or sham-operated rats once per day from day 1 to days 3, 7, or 14 after surgery.

Western Blot Analysis and Antibodies

To evaluate protein levels of EZH2, H3K27TM, p62, LC3 II (microtubule-associated protein 1A/1B-light chain 3), MTOR, phosphorylated MTOR (pMTOR), P70S6K, and phosphorylated P70S6K (pP70S6K), we carried out western blot analysis as described previously [9, 21]. Briefly, tissues or cells were collected and lysed with NP-40 lysis buffer (25 mmol/L Tris–HCl, 150 mmol/L NaCl, 1 mmol/L EDTA, 1% NP-40; pH 7.6) supplemented with a protease inhibitor cocktail, and protein concentration was quantified using BCA reagent. Protein samples (20 μg) were separated by sodium dodecyl sulfate–polyacrylamide gel electrophoresis, transferred onto nitrocellulose membranes, and incubated with primary antibodies (Table 1). Blots were developed with horseradish peroxidase-conjugated secondary antibodies and a chemiluminescent substrate on Kodak X-ray films (Rochester, NY, USA).

Quantitative Real-Time PCR (q-RT PCR)

Total RNA was extracted using TRIzol reagent (Invitrogen, Carlsbad, CA, USA) and reverse-transcribed using an M-MLV Reverse Transcriptase kit (Invitrogen, Carlsbad, CA, USA). Samples were then analyzed in triplicate by q-RT PCR using a standard SYBR Green PCR kit (Toyobo, Osaka, Japan) and a Rotor-Gene RG-3000A (Corbett Life Science, Sydney, New South Wales, Australia) according to each manufacturer's instructions. The primers used for q-RT PCR are listed in Table 2. Values were normalized to those of the housekeeping gene GAPDH and relative gene expression levels were quantified using the $2^{-\Delta\Delta Ct}$ method.

Enzyme-Linked Immunosorbent Assay (ELISA)

Protein samples were prepared for ELISA as for western blot analysis. The interleukin (IL)-1β, tumor necrosis factor (TNF)-α and IL-6 levels were determined using ELISA kits (R&D Systems, Minneapolis, MN, USA) according to the manufacturer's instructions.

Table 1 Information for primary antibodies

Name	Cat. number	Supplier	Application: dilution
Rabbit anti-EZH2	#5246	Cell Signaling Technology	WB: 1:1000 IF: 1:100
Mouse anti-NeuN	#94403	Cell Signaling Technology	IF: 1:100
Mouse anti-Iba-1	#MABN92	Millipore	IF: 1:100
Mouse anti-GFAP	#3670	Cell Signaling Technology	IF: 1:200
Rabbit anti-H3K27TM	#9733	Cell Signaling Technology	WB: 1:1000
Rabbit anti-p62	#39786	Cell Signaling Technology	WB: 1:1000 IF: 1:200
Rabbit anti-LC3	#3868	Cell Signaling Technology	WB: 1:1000
Rabbit anti-MTOR	#2983	Cell Signaling Technology	WB: 1:1000
Rabbit anti-pMTOR	#5536	Cell Signaling Technology	WB: 1:1000
Rabbit anti-P70S6K	#9202	Cell Signaling Technology	WB: 1:1000
Rabbit anti-pP70S6K	#9205	Cell Signaling Technology	WB: 1:1000
Mouse anti-β-actin	A5441	Sigma	WB: 1:5000

WB western blot, *IF* immunofluorescence

Table 2 Primers used for q-RT PCR

Gene	Forward ($5' \rightarrow 3'$)	Reverse ($5' \rightarrow 3'$)
GAPDH	CTGGGCTACACTGAGCACC	AAGTGGTCGTTGAGGGCAATG
EZH2	ACATCCTTTTCATGCAACACC	GTATCCACATCCTCAGCGGG
p62	AGCGTCAGGAAGGTGCCATT	CCTGTAGACGGGTCCACTTC

Immunofluorescence Analysis

To obtain tissue samples for immunofluorescence analysis, each rat was anesthetized and perfused through the ascending aorta with 200 mL heparinized PBS (0.01 mol/L, pH 7.35) followed by 4% paraformaldehyde. The brain was removed, fixed in 4% paraformaldehyde overnight, and dehydrated in 20% and 30% sucrose at 4 °C. Next, the brain was cut into 10-μm sections on a cryostat and those containing the ACC were collected. Immunofluorescence staining was performed according to the methods described by Yadav and Weng [9]. Briefly, the sections were blocked with 5% BSA containing 0.1% Triton X-100 for 1 h, incubated with primary rabbit polyclonal antibodies overnight at 4 °C, and then incubated with fluorescein isothiocyanate-conjugated secondary antibodies for 2 h at room temperature in the dark. The nuclei were stained and the sections mounted with Vectashield mounting medium [22]. Then the sections were examined using a fluorescence laser scanning confocal microscope (Leica, Wetzlar, Hessen, Germany).

Statistical Analysis

All data are presented as the mean ± SEM and GraphPad Prism 5.0 (GraphPad, San Diego, CA, USA) was used for statistical analysis. Between-group comparisons were performed using two-tailed unpaired t-tests with a 95% confidence interval set. Multiple comparisons were performed by one-way analysis of variance (ANOVA) followed by Tukey's or Dunnett's test to assess pairwise between-group differences. Behavioral data for each group were analyzed by repeated-measures ANOVA followed by Bonferroni's *post hoc* test. P values of < 0.05 were considered statistically significant.

Results

BPA Causes Mechanical and Cold Allodynia in Rats

Following BPA surgery, we performed behavioral assessments to establish that mechanical and cold allodynia had been induced in the rats before they were used for any biochemical assays. Rats with no observable neuropathic pain following BPA surgery were excluded from the study.

Of the rats included in the study, the 50% MWT baseline (measured on the day before surgery) was 7.78 ± 0.26 g in the neuropathic pain (NeuP) group and 9.22 ± 1.34 g in the sham-operated (Sham) group, with no significant difference between them ($P > 0.05$). At all other time points studied (days 3, 7, and 14 post-surgery), the 50% MWT of the left hind paw in the NeuP group was significantly lower than their own baseline and the Sham group (Fig. S1A). The CWS baselines (measured the day before surgery) were 0.22 ± 0.11 in the NeuP group and 0.44 ± 0.11 in the Sham group ($P > 0.05$). At all other time points studied (days 3, 7, and 14 post-surgery), the CWS of the left hind paw in the NeuP group was significantly higher than their own baseline and the Sham group (Fig. S1B). Thus, these data showed that BPA causes neuropathic pain in rats.

EZH2 and H3K27TM Expression is Upregulated in Microglia *In Vivo* and *In Vitro*

Previously, Yadav and Weng [9] showed that spinal EZH2 expression is upregulated in rats with neuropathic pain following partial sciatic nerve ligation. They identified EZH2 as a crucial mediator of neuroinflammation and neuropathic pain treatment. However, it remains unclear whether EZH2 is upregulated in the ACC of rats with BPA-induced neuropathic pain. Here, we found that EZH2 was promptly upregulated in the ACC on day 3 post-surgery in the NeuP group and was sustained at higher levels than in the Sham group for 14 days (Fig. 1A). Consistent with these western blot findings, q-RT PCR analysis revealed that EZH2 mRNA expression was strongly induced on days 3, 7, and 14 post-surgery in the ACC of the NeuP group compared with the Sham group (Fig. 1B). To determine whether EZH2 overexpression enhanced its catalytic activity, we measured H3K27TM expression by western blot analysis. The ACC of rats in the NeuP group displayed higher H3K27TM expression on days 3, 7, and 14 post-surgery than the Sham group (Fig. 1C). Taken together, these data suggest that EZH2 activity is enhanced in the ACC of rats with BPA-induced neuropathic pain, but it remained unclear in which cell type EZH2 was expressed. To determine this, we examined the localization of EZH2 within the ACC sections from the NeuP group on day 3 post-surgery, and found that EZH2 overexpression was co-localized with Iba1 (ionized Ca^{2+}-binding adaptor
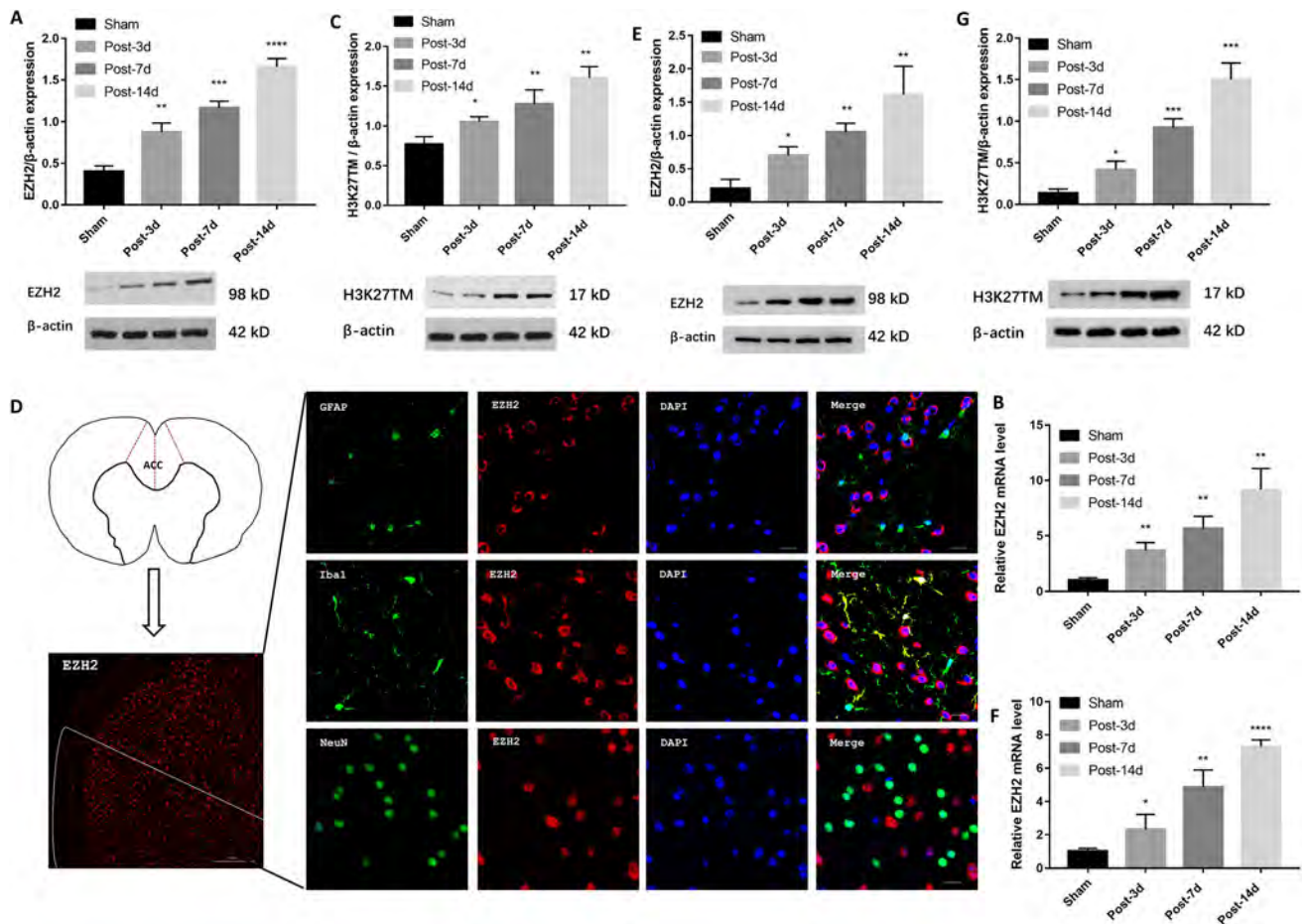
Fig. 1 Expression of EZH2 and H3K27TM is increased in microglia *in vivo* and *in vitro*. **A–C** The relative expression of EZH2 (**A**), EZH2 mRNA (**B**), and H3K27TM (**C**) in the ACC of the Sham and NeuP groups on days 3, 7, and 14 post-surgery (mean ± SD; *n* = 8; *$P < 0.05$, **$P < 0.01$, ***$P < 0.001$, ****$P < 0.0001$ *vs* Sham group). **D** Right panels, representative images of co-localization of EZH2 (red) with different cellular markers (green): GFAP for astrocytes, Iba1 for microglia, and NeuN for neurons (scale bar,

20 μm). Left panels, diagram of brain cross-section through the ACC, and low-magnification image of EZH2 in the ACC of the right hemisphere (scale bar, 100 μm). **E–G** Relative expression of EZH2 (**E**), EZH2 mRNA (**F**), and H3K27TM (**G**) in primary microglia from Sham and NeuP groups on days 3, 7, and 14 post-surgery (mean ± SD; *n* = 3; *$P < 0.05$, **$P < 0.01$, ***$P < 0.001$, ****$P < 0.0001$ *vs* Sham group).

molecule 1), a microglia-specific marker (Fig. 1D). To confirm that EZH2 was overexpressed in the ACC microglia, we isolated primary microglia from the ACC of Sham and NeuP rats on days 3, 7, and 14 post-surgery. We found that the EZH2 protein and mRNA levels and the H3K27TM levels were significantly upregulated in primary microglia from the ACC of the NeuP rats on each day post-surgery compared to those in the Sham rats (Fig. 1E–G).

Neuroinflammation is Increased in the ACC of Rats with BPA-Induced Neuropathic Pain

Microglia are the predominant type of immune cell in the CNS and express pro-inflammatory cytokines when activated by nerve injury. Therefore, we investigated the levels of pro-inflammatory cytokines secretion in the ACC of

NeuP rats and found that the IL-1β, TNF-α, and IL-6 levels were markedly higher on days 3, 7, and 14 post-surgery than in Sham rats (Fig. 2A–C). These findings strongly suggest that increased neuroinflammation is positively correlated with EZH2 upregulation in the ACC of rats with BPA-induced neuropathic pain.

Autophagy is Suppressed in Microglia *In Vivo* and *In Vitro*

Previously, Shi *et al.* [6] showed that autophagy participates in neuropathic pain modulation and pro-inflammatory cytokines secretion. Here, we found that the expression of the autophagy-associated proteins LC3II and p62 changed in the ACC of NeuP rats on days 3, 7, and 14 post-surgery. Moreover, LC3II levels were markedly lower in the ACC
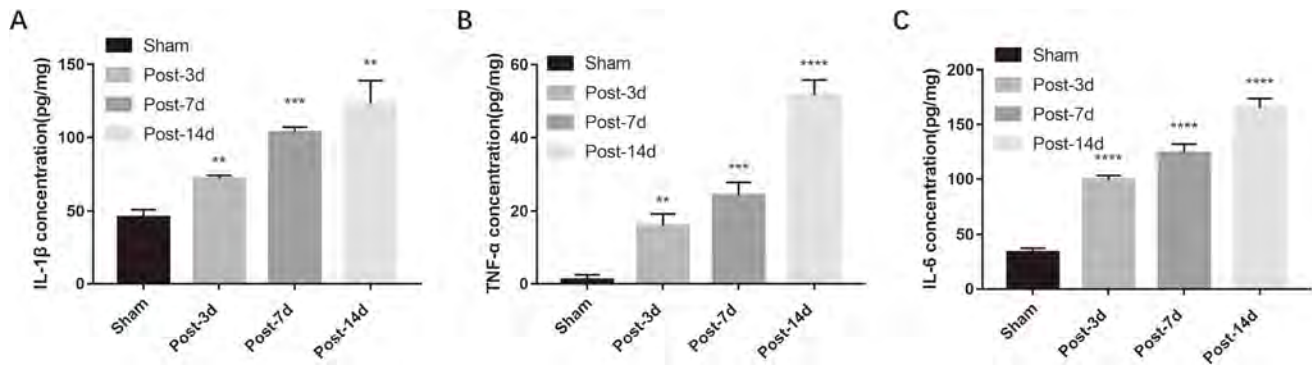
Fig. 2 Expression of pro-inflammatory cytokines is increased in the ACC of rats with BPA-induced neuropathic pain. **A–C** ELISA analysis showing the IL-1β (**A**), TNF-α (**B**), and IL-6 (**C**) expression levels in the ACC of Sham and NeuP rats on days 3, 7, and 14 post-surgery compared with Sham rats (mean ± SD; n = 8; **$P < 0.01$, ***$P < 0.001$, ****$P < 0.0001$ vs Sham group).
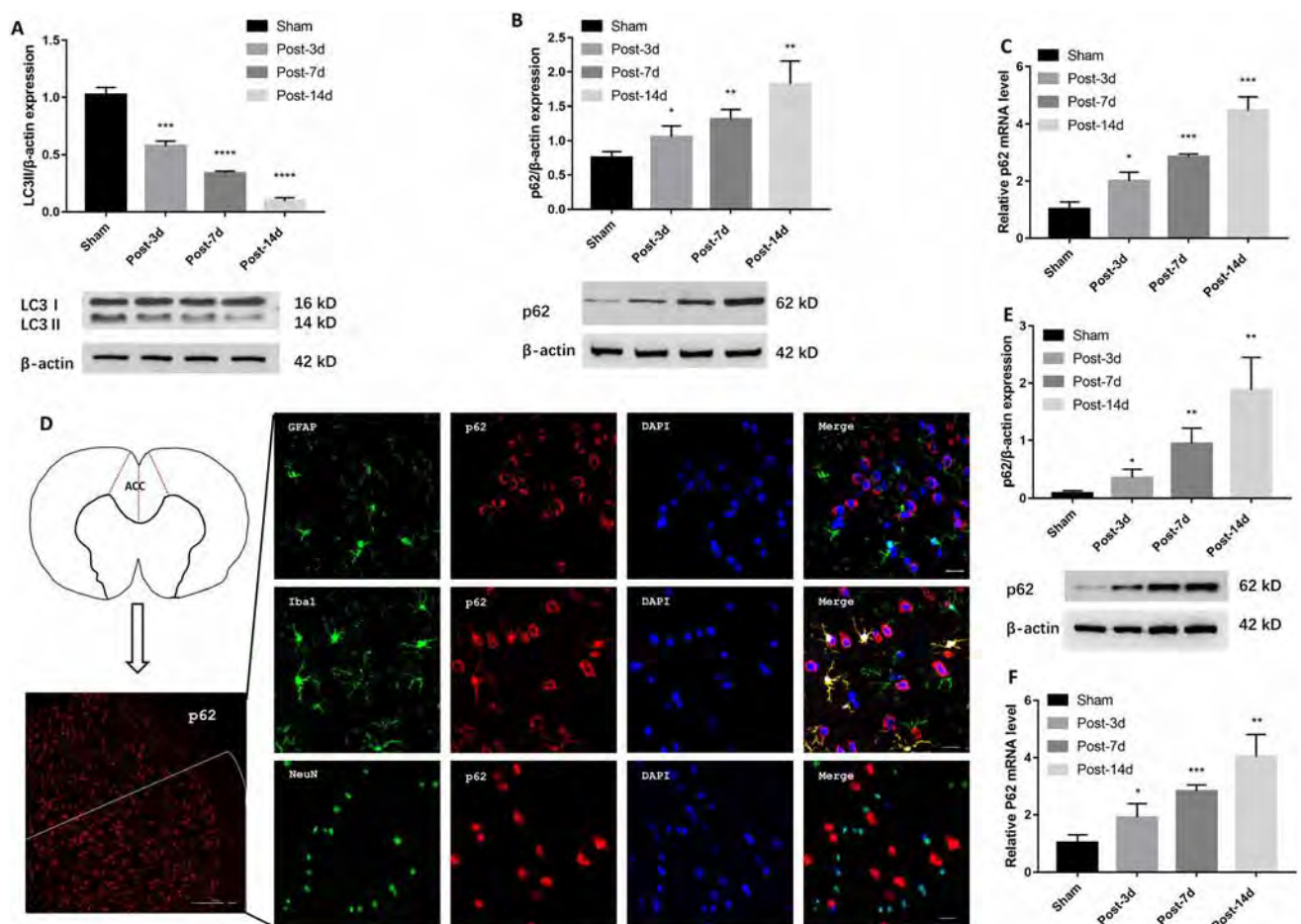
Fig. 3 Autophagy is inhibited in microglia *in vivo* and *in vitro*. **A–C** Relative expression of LC3II (**A**), p62 protein (**B**), and p62 mRNA (**C**) in the ACC of Sham and NeuP groups (n = 8 for each). **D** Right panels, representative images of co-localization of p62 (red) with different cellular markers (green): GFAP for astrocytes, Iba1 for microglia, and NeuN for neurons (scale bar, 20 μm). Left panels, diagram of brain cross-section with the ACC, and low-magnification image of p62 in the ACC of the left hemisphere (scale bar, 100 μm). **E, F** Relative expression of p62 (**E**) and p62 mRNA (**F**) in primary microglia (n = 3). Mean ± SD; *$P < 0.05$, **$P < 0.01$, ***$P < 0.001$, ****$P < 0.0001$ vs Sham group.

of NeuP rats on each of the days post-surgery than in Sham rats (Fig. 3A). Conversely, p62 levels progressively accumulated in the ACC of NeuP rats compared to Sham rats on

each of the days post-surgery (Fig. 3B). Consistent with the western blot findings, p62 mRNA expression was strongly induced in the ACC of NeuP rats on each of the days post-

surgery (Fig. 3C), suggesting that the progress of autophagy is impaired in rats with BPA-induced neuropathic pain.

Consequently, we evaluated whether autophagy was impaired in the ACC microglia of NeuP rats. Fluorescence microscopic analysis of the ACC sections revealed that p62 accumulation was co-localized with Iba1, indicating that autophagy was mainly suppressed in the microglia (Fig. 3D). To confirm this finding, we isolated primary microglia from the ACC of NeuP and Sham rats on days 3, 7, and 14 after surgery. Consistent with the results from the ACC sections, the p62 protein and mRNA levels were significantly higher in the primary microglia from the NeuP rats on each of the days after surgery than those from the Sham rats (Fig. 3E, F). Taken together, these data suggest that autophagy is suppressed in the ACC microglia of rats with BPA-induced neuropathic pain.

EZH2 Inhibition Suppresses Neuroinflammation and Induces Autophagy

To further elucidate the function of EZH2 in the regulation of autophagy and whether inhibiting EZH2 has an analgesic effect, we examined autophagy activation after treating NeuP rats with GSK126, a selective EZH2 inhibitor. The inhibition of EZH2 by GSK126 attenuated the mechanical and cold allodynia in the NeuP rats compared to those without GSK126 treatment on days 3, 7, and 14 post-surgery (Fig. 4A, B). Meanwhile, GSK126 markedly inhibited the EZH2 and H3K27TM expression levels in the ACC of the Sham group compared with DMSO treatment on each of the days after surgery (Fig. 4C, D). Therefore, we investigated the relationship between EZH2, neuroinflammation, and autophagy activation. GSK126 downregulated the IL-1β, TNF-α, and IL-6 secretion levels in the ACC of NeuP rats on each of the days post-surgery compared to those treated with DMSO (Fig. 4E–G), whereas the LC3II levels were upregulated and p62 levels were downregulated in the ACC compared with DMSO treatment in the Sham group on each of the days post-surgery (Fig. 4H, I).

Autophagy Upregulation Suppresses Neuroinflammation and Neuropathic Pain

To better understand the exact role of autophagy activation in the ACC with respect to neuropathic pain, we treated NeuP rats with Rapa to validate the function of autophagy. Rapa reduced the mechanical and cold allodynia in these rats on days 3, 7, and 14 post-surgery (Fig. 5A, B) and upregulated LC3II expression in the ACC on each day compared to DMSO treatment (Fig. 5C). Consistent with this, the p62 protein levels were markedly downregulated

in the ACC of NeuP rats following Rapa treatment on each of the days post-surgery (Fig. 5D). To further explore the relationship between autophagy and neuroinflammation, we measured the IL-1β, TNF-α and IL-6 secretion levels in the ACC of NeuP rats, and found that Rapa repressed neuroinflammation (Fig. 5E–G). Taken together, these data suggest that upregulation of autophagy can attenuate neuroinflammation and neuropathic pain.

EZH2 Negatively Regulates Autophagy in Rats with BPA-Induced Neuropathic Pain

To elucidate the relationship between EZH2 and autophagy, NeuP rats were intraperitoneally injected with both GSK126 and 3-MA once per day from day 1 to day 3 post-surgery. We found that the alleviation of mechanical (Fig. 6A) and cold allodynia (Fig. 6B) was reversed after treatment with both GSK126 and 3-MA compared with GSK126 treatment only, and there was no significant difference in the degree of mechanical and cold allodynia between the NeuP and 3-MA + GSK126 groups. These findings indicate that inhibiting autophagy with 3-MA impairs the pain relief induced by the EZH2 inhibitor. To determine the mechanism by which 3-MA impaired the pain relief induced by GSK126, we measured the EZH2 and H3K27TM expression levels using western blot analysis. EZH2 (Fig. 6C) and H3K27TM (Fig. 6D) expression was lower in the 3-MA + GSK126 group than in the NeuP group, but there was no significant difference between the 3-MA + GSK126 and GSK126 groups, indicating that 3-MA does not influence the GSK126-induced downregulation of EZH2 and H3K27TM. We also analyzed the expression of the autophagy-associated proteins LC3II and p62, and found that the LC3II levels (Fig. 6E) were downregulated in the 3-MA + GSK126 group compared to the GSK126 group and the p62 protein levels (Fig. 6F) were upregulated in the 3-MA + GSK126 group compared to the GSK126 group, indicating that 3-MA reversed the enhanced autophagy induced by GSK126. In addition, the IL-1β (Fig. 6G), TNF-α (Fig. 6H), and IL-6 (Fig. 6I) levels were higher in the 3-MA + GSK126 group than in the GSK126 group, but there was no significant difference between the 3-MA + GSK126 and NeuP groups, indicating that 3-MA also impaired the remission of inflammation induced by GSK126. In conclusion, these data indicate that inhibiting autophagy using 3-MA impairs EZH2-induced pain relief and neuroinflammation remission, suggesting that autophagy is a downstream target of EZH2, which aggravates neuroinflammation and neuropathic pain in rats with BPA-induced neuropathic pain.
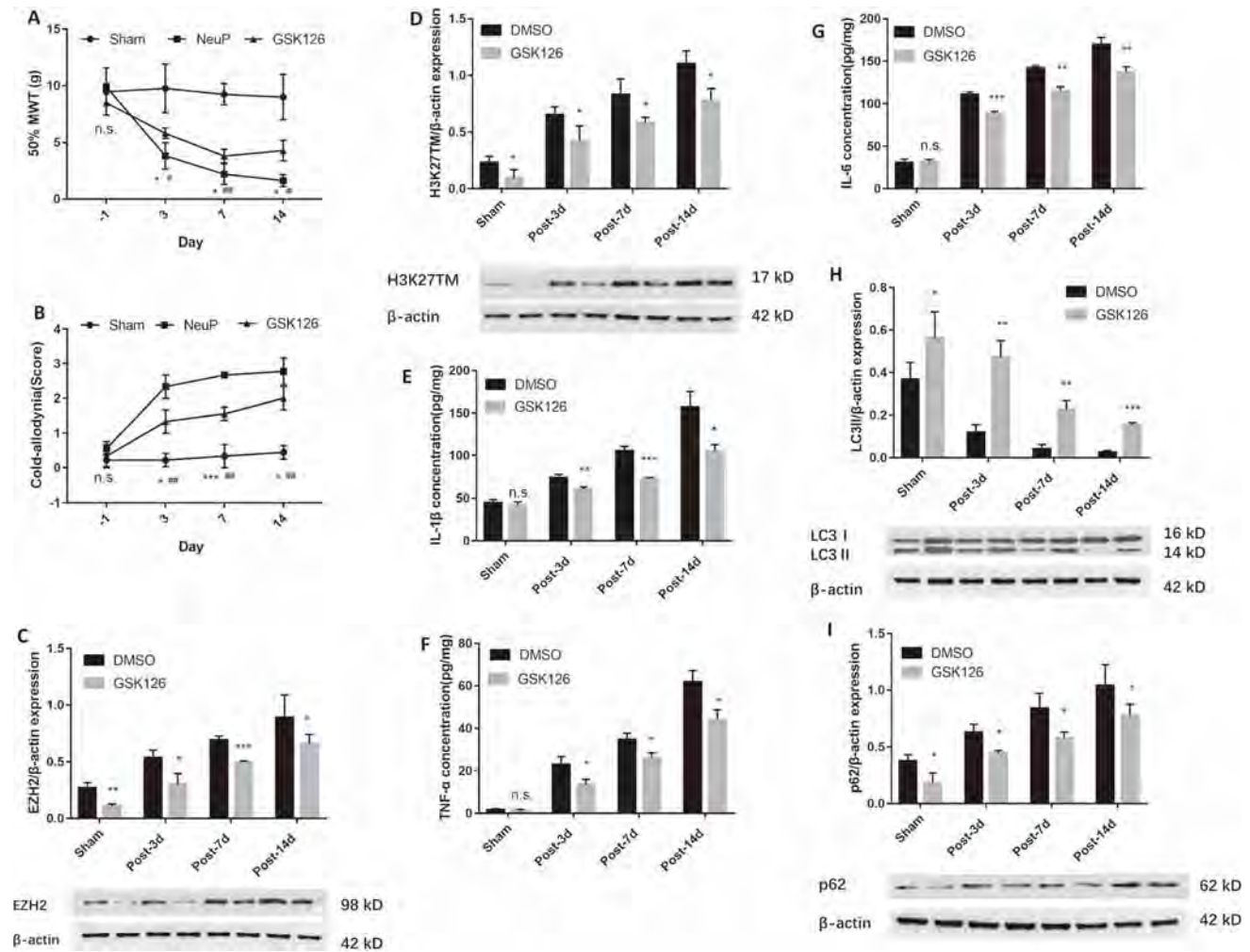
Fig. 4 Inhibition of EZH2 by GSK126 suppresses neuroinflammation and induces autophagy. **A**, **B** The 50%MWT (**A**) and CWS (**B**) in the Sham and NeuP groups after GSK126 treatment from day 3 to day 14 post-surgery (mean ± SD; *n* = 8; n.s., no significant difference among Sham, NeuP and GSK126 groups; *P < 0.05, **P < 0.01, ***P < 0.001 vs NeuP group; #P < 0.05, ##P < 0.01 vs Sham group). **C**, **D** Relative expression of EZH2 (**C**) and H3K27TM (**D**) in the ACC of the Sham and NeuP groups after GSK126 treatment. **E**–

G ELISA analysis of IL-1β (**E**), TNF-α (**F**), and IL-6 (**G**) expression levels in the ACC of the Sham and NeuP groups after GSK126 treatment from day 3 to day 14 post-surgery. **H**, **I** Relative expression of LC3II (**H**) and p62 protein (**I**) in the ACC of the Sham and NeuP groups after GSK126 treatment from day 3 to day 14 post-surgery. For **C**–**I**: mean ± SD; *n* = 8; n.s., no significant difference; *P < 0.05, **P < 0.01, ***P < 0.001 vs DMSO group.

EZH2 Regulates Autophagy *Via* an MTOR-Dependent Signaling Pathway

Previously, Wei *et al.* [21] showed that EZH2 epigenetically regulates autophagy in colorectal carcinoma cells *via* the MTOR signaling pathway, whose activation is known to suppress autophagy while its inhibition enhances autophagy. Therefore, we determined whether EZH2 upregulation inhibits autophagy *via* the MTOR pathway in the ACC microglia of rats with BPA-induced neuropathic pain. To do so, we measured pMTOR and pP70S6K expression levels, which are main markers of MTOR activity. The expression of both pMTOR and pP70S6K was upregulated in NeuP rats on days 3, 7, and 14 post-surgery

compared with Sham rats (Fig. 7A, B). To confirm that EZH2 acts *via* the MTOR pathway, we intraperitoneally injected GSK126 into NeuP rats from day 1 to day 3 post-surgery, and found that MTOR activity was induced and the pMTOR and pP70S6K levels were reduced (Fig. 7C, D). These results indicate that EZH2 regulates autophagy *via* an MTOR-dependent signaling pathway.

Discussion

Neuropathic pain is unbearable and highly refractory, so treatments to attenuate it are important for improving the quality of life of patients following BPA. An increasing
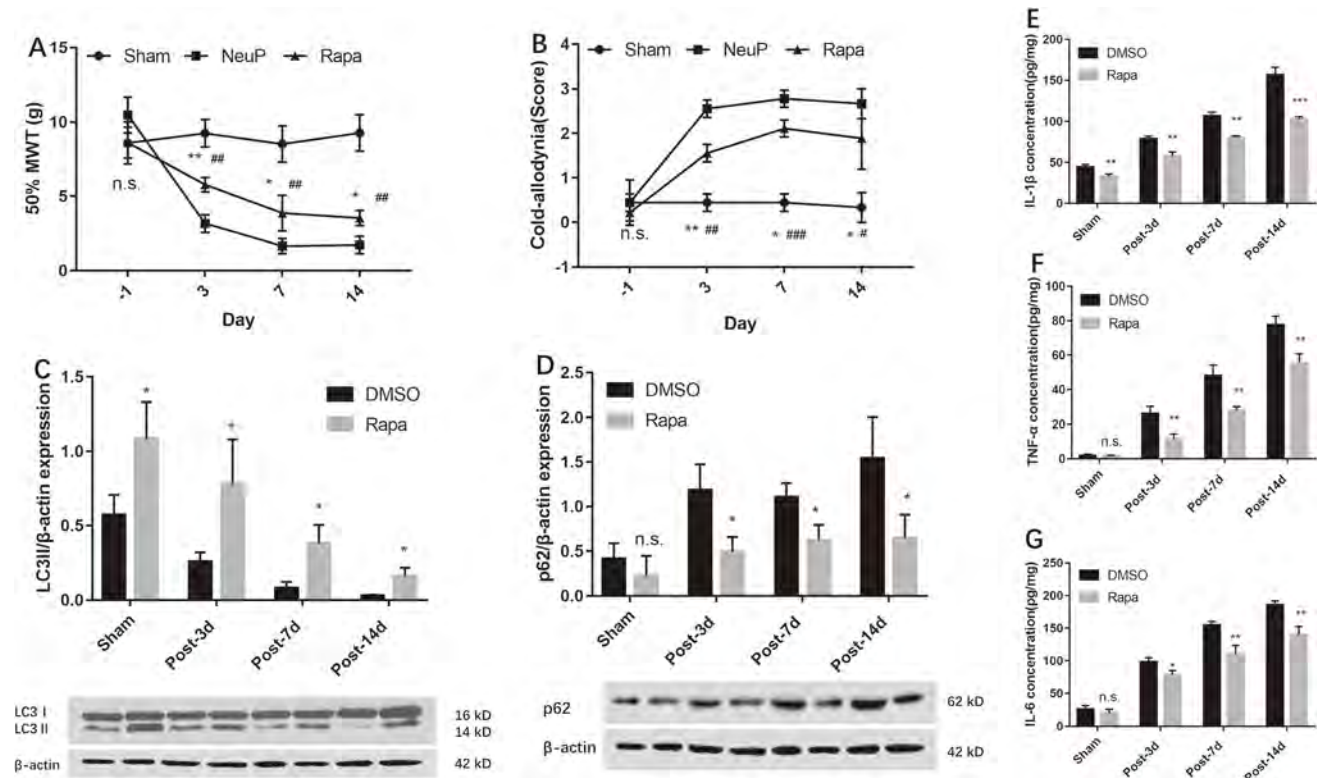
Fig. 5 Upregulation of autophagy suppresses neuroinflammation and attenuates neuropathic pain. **A**, **B** The 50%MWT (**A**) and CWS (**B**) in the sham and neuropathic pain groups after rapamycin treatment from day 3 to day 14 post-surgery (mean ± SD; $n = 8$; n.s., no significant difference among Sham, NeuP and GSK126 groups; $*P < 0.05$, $**P < 0.01$ vs NeuP group; $^{\#}P < 0.05$, $^{\#\#}P < 0.01$, $^{\#\#\#}P < 0.001$ vs Sham group). **C**, **D** Relative expression of LC3II (**C**) and p62 protein (**D**) in the ACC of the Sham and NeuP groups after rapamycin treatment compared with DMSO treatment from day 3 to day 14 post-surgery. **E**–**G** ELISA analysis of the IL-1β (**E**), TNF-α (**F**), and IL-6 (**G**) expression levels in the ACC of the Sham and NeuP groups after rapamycin treatment from day 3 to day 14 post-surgery. For **C**–**G**: mean ± SD; $n = 8$; n.s., no significant difference; $*P < 0.05$, $**P < 0.01$, $***P < 0.001$, vs DMSO group.

number of studies have shown that neuropathic pain might be caused by comprehensive alterations in neurons and glial cells, particularly microglia [23]. Microglia constitute the major population of glial cells in the CNS, supporting the hypothesis that they play a leading role in regulating neuroinflammation [24]. Signaling molecules released following peripheral nerve injury may activate microglia in the CNS, causing them to release pro-inflammatory cytokines and chemokines such as IL-1β, TNF-α, IL-6, and brain-derived neurotrophic factor, which play primary key roles in initiating and maintaining neuropathic pain [25, 26]. Recent studies regarding the role of microglia in neuropathic pain have mainly focused on the dorsal horn of the spinal cord [7]; however, the underlying mechanisms by which microglia modulate neuropathic pain in the ACC remain poorly understood.

Evidence has shown that epigenetic alterations may initiate and maintain neuropathic pain [27, 28], while the EZH2-mediated histone modification of gene expression has been shown to correlate with human cancers, including prostate cancer, colorectal cancer, and lymphoma [29–32]. Moreover, abnormal EZH2 has been associated with the

inflammatory response and neurodegeneration. For instance, Zhang *et al.* [33] reported that EZH2 induces pro-inflammatory gene expression by mediating toll-like receptors, and EZH2 depletion attenuates autoimmune inflammation in colitis and autoimmune encephalomyelitis. In addition, EZH2 expression is upregulated in rats with chronic sciatic nerve injury-induced neuropathic pain, and its overexpression reverses the decreased pro-inflammatory cytokines expression [11].

In this study, we investigated whether abnormal EZH2 expression affects the secretion of pro-inflammatory cytokines and the pathophysiology of neuropathic pain in rats with BPA-induced neuropathic pain. We showed that EZH2 expression was strongly upregulated in NeuP rats, while inhibiting EZH2 decreased the IL-1β, TNF-α, and IL-6 secretion. More importantly, inhibiting EZH2 decreased the mechanical and cold allodynia. Therefore, our results suggest that EZH2 plays a role in the molecular mechanisms of neuropathic pain.

Consequently, we also investigated the molecular mechanisms by which EZH2 regulates neuropathic pain. Autophagy is a key process that regulates immunity and
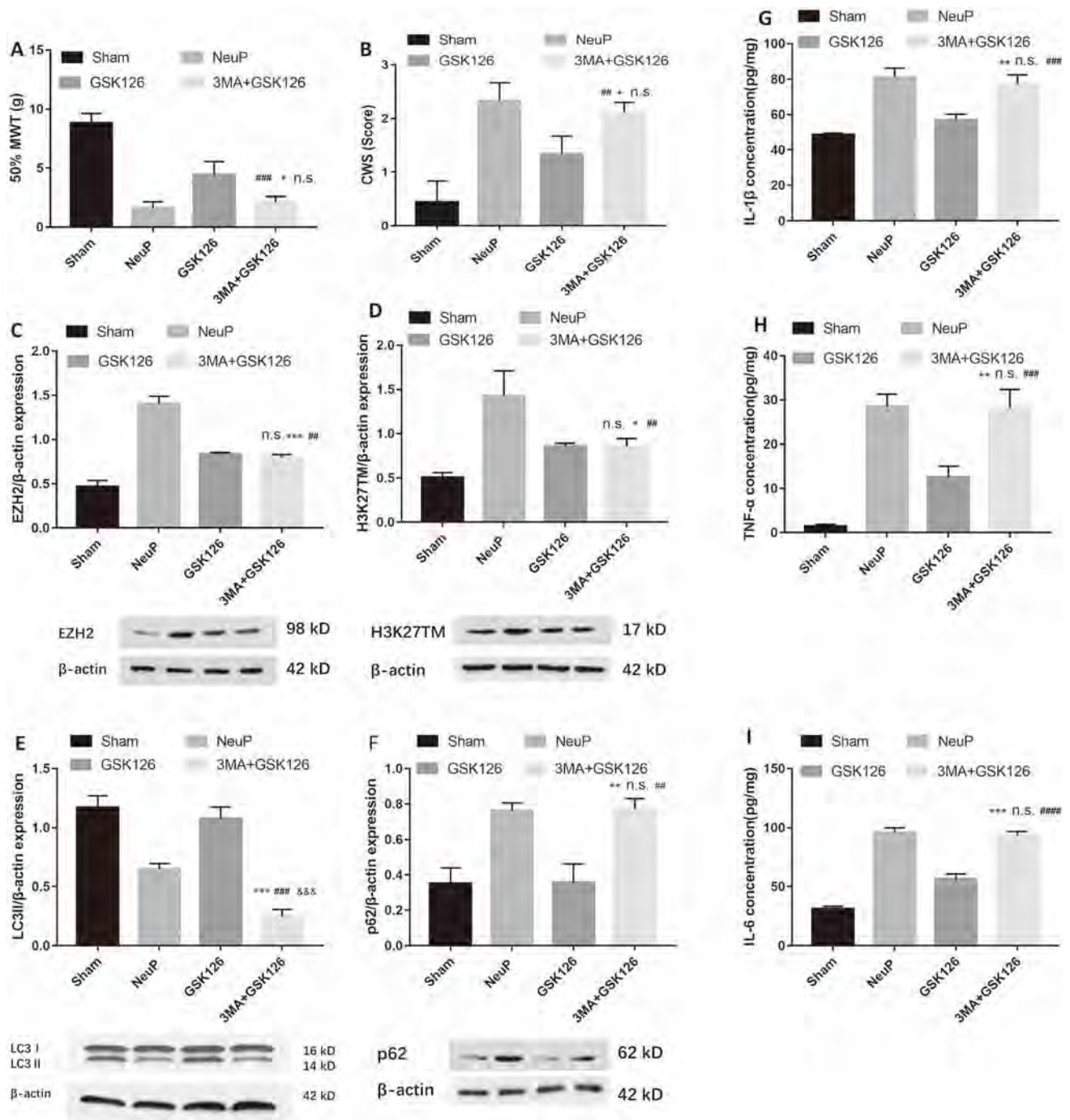
Fig. 6 Inhibition of autophagy by 3-MA impairs EZH2 inhibitor-induced pain relief and neuroinflammation remission. **A, B** Mechanical allodynia (**A**) and cold allodynia (**B**) in sham-operated and neuropathic pain groups after 3-MA combined with GSK126 treatment from day 1 to day 3 post-surgery (mean ± SD; $n = 8$; n.s., no significant difference vs NeuP group; *$P < 0.05$ vs GSK126 group; $^{\#\#}P < 0.01$, $^{\#\#\#}P < 0.001$ vs Sham group). **C–F** Relative expression of EZH2 (**C**) and H3K27TM (**D**) (mean ± SD; $n = 8$; n.s., no significant difference vs GSK126 group; *$P < 0.05$, ***$P < 0.001$ vs NeuP group; $^{\#\#}P < 0.01$ vs Sham group), LC3II (**E**) (mean ± SD; $n = 8$; ***$P < 0.001$ vs NeuP group; $^{\#\#\#}P < 0.001$ vs GSK126 group; $^{\&\&\&}P < 0.001$ vs Sham group), and p62 protein (**F**) (mean ± SD; $n = 8$; **$P < 0.01$ vs GSK126 group; n.s., no significant difference vs NeuP group; $^{\#\#}P < 0.01$ vs Sham group) in the ACC of rats after 3-MA combined with GSK126 treatment from day 1 to day 3 post-surgery. **G–I** ELISA analysis of IL-1β (**G**), TNF-α (**H**), and IL-6 (**I**) expression levels in the ACC of the Sham and NeuP groups after 3-MA combined with GSK126 treatment from day 1 to day 3 post-surgery (mean ± SD; $n = 8$; n.s., no significant difference vs NeuP group; **$P < 0.01$, ***$P < 0.001$ vs GSK126 group; $^{\#\#\#}P < 0.001$, $^{\#\#\#\#}P < 0.0001$ vs Sham group).
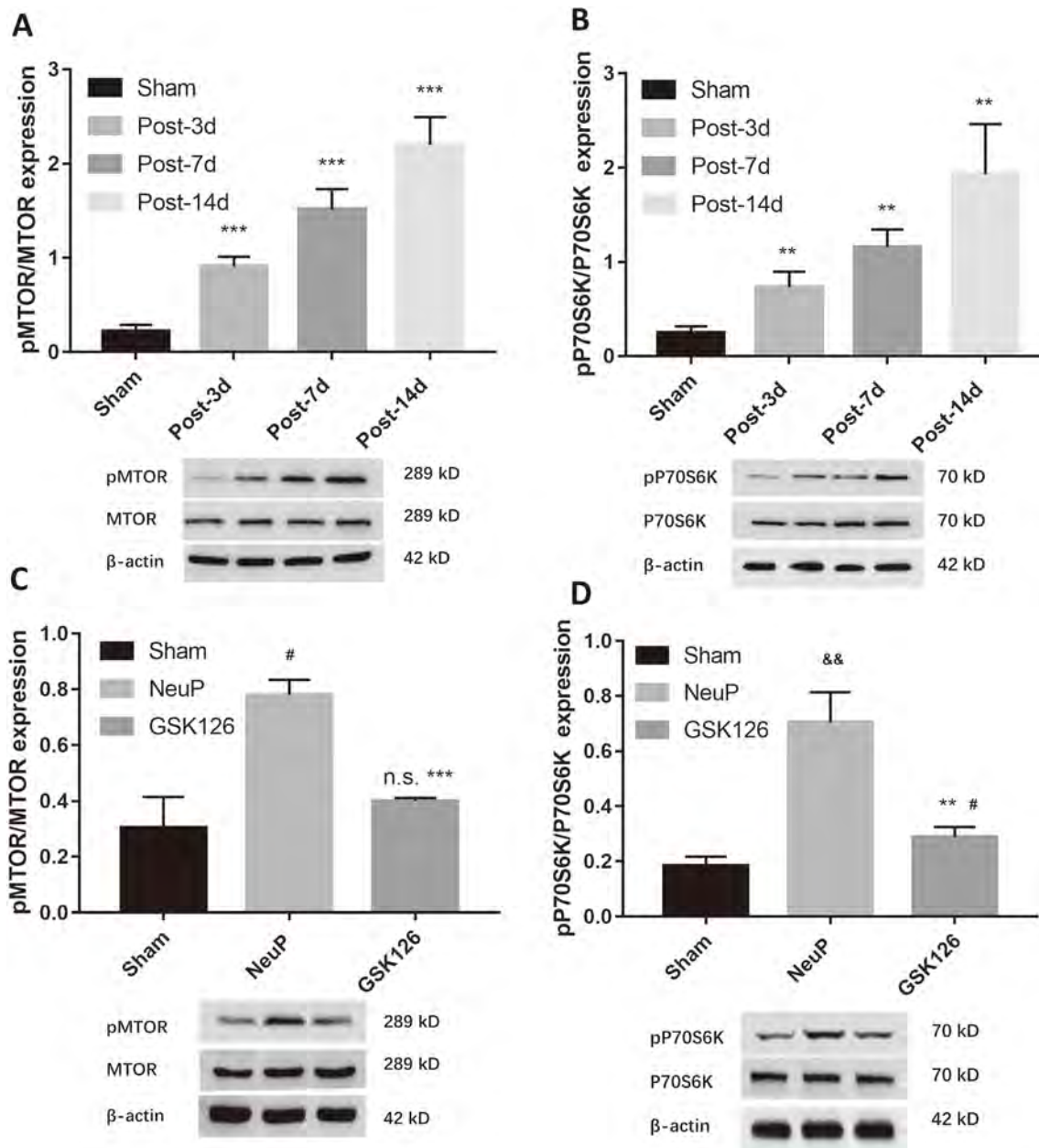
Fig. 7 EZH2 regulates autophagy *via* an MTOR-dependent signaling pathway. **A–D** Relative expression of pMTOR (**A**) and pP70S6K (**B**) (mean ± SD; $n = 8$; $**P < 0.01$, $***P < 0.001$ *vs* Sham group), pMTOR (**C**) (mean ± SD; $n = 8$; $***P < 0.001$ *vs* NeuP group; n.s., no significant difference *vs* Sham group; $^{#}P < 0.05$ *vs* Sham group), and pP70S6K (**D**) (mean ± SD; $n = 8$; $**P < 0.01$ *vs* NeuP group; $^{#}P < 0.05$ *vs* Sham group; $^{\&\&}P < 0.01$ *vs* Sham group) in the ACC of rats after GSK126 treatment from day 1 to day 3 post-surgery.

inflammation; several studies have demonstrated a relationship between EZH2 and autophagy in the etiology of diseases such as colorectal cancer and laryngeal squamous cell carcinoma. However, their regulatory mechanisms have not yet been elucidated [34, 35]. It has also been suggested that EZH2 may affect autophagy *via* microRNA, STAT, or fuse-binding protein 1-c-Myc in osteoarthritis, breast cancer, endometrial carcinoma, cholangiocarcinoma, and osteosarcoma, while the signaling pathway by which

EZH2 regulates autophagy has not yet been confirmed [36–40]. In this study, we found that pharmacologically inhibiting EZH2 promoted the suppression of autophagy induced by BPA, while inhibiting autophagy activation impaired the GSK126-induced reduction of neuroinflammation and neuropathic pain. Therefore, these findings indicate that autophagy activity acts downstream of EZH2 and is involved in neuropathic pain.

To improve our understanding of the effect of autophagy on neuropathic pain, we used Rapa to reveal the pathophysiology of BPA-induced neuropathic pain. We found that increasing autophagy with Rapa suppressed neuropathic pain and the release of pro-inflammatory cytokines while reducing MTOR phosphorylation. These data suggested that autophagy negatively regulates neuroinflammation via the MTOR signaling pathway, and this could be the direct cause of neuropathic pain. Although our results revealed that EZH2 regulated autophagy via the MTOR pathway, we were unable to determine how EZH2 phosphorylates MTOR in nerve injury-induced neuropathic pain. However, it has been shown that EZH2 regulates TSC2 (tuberous sclerosis complex 2) expression by interacting with MTA2 (metastasis-associated 1 family member 2), and subsequently phosphorylates MTOR [21]. To our knowledge, this is the first study to identify a specific autophagy regulatory molecule that is regulated by EZH2. Recently, another study found that inhibiting EZH2 reduces phosphorylated AKT expression and thus represses pMTOR production in pancreatic cancer [41], suggesting that EZH2 regulates MTOR phosphorylation via the AKT signaling pathway. These studies provide possible directions for future research to elucidate how EZH2 regulates autophagy via the MTOR pathway.

In conclusion, we found that targeting the EZH2/autophagy signaling pathway is a promising option for regulating neuroinflammation and managing neuropathic pain. Thus, our findings suggest a novel approach for treating BPA-induced neuropathic pain.

References

1. Jensen TS, Baron R, Haanpää M, Kalso E, Loeser JD, Rice AS, et al. A new definition of neuropathic pain. Pain 2011, 152: 2204–2205.
2. Teixeira MJ, da Paz MG, Bina MT, Santos SN, Raicher I, Galhardoni R, et al. Neuropathic pain after brachial plexus avulsion-central and peripheral mechanisms. BMC Neurol 2015, 15: 73.
3. Iannetti GD, Mouraux A. From the neuromatrix to the pain matrix (and back). Exp Brain Res 2010, 205: 1–12.
4. Chen T, Taniguchi W, Chen QY, Tozaki-Saitoh H, Song Q, Liu RH, et al. Top–down descending facilitation of spinal sensory excitatory transmission from the anterior cingulate cortex. Nat Commun 2018, 9: 1886–1902.
5. Yang Z, Tan Q, Cheng D, Zhang L, Zhang J, Gu EW, et al. The changes of intrinsic excitability of pyramidal neurons in anterior cingulate cortex in neuropathic pain. Front Cell Neurosci 2018, 12: 436.
6. Shi G, Shi J, Liu K, Liu N, Wang Y, Fu Z, et al. Increased miR-195 aggravates neuropathic pain by inhibiting autophagy following peripheral nerve injury. Glia 2013, 61: 504–512.
7. Tsuda M. Microglia of pain and itch by spinal glia. Neurosci Bull 2018, 34: 178–185.
8. Wang B, Fan B, Dai Q, Xu X, Jiang P, Zhu L, et al. Fascin-1 contributes to neuropathic pain by promoting inflammation in rat spinal cord. Neurochem Res 2018, 43: 287–296.
9. Yadav R, Weng HR. EZH2 regulates spinal neuroinflammation in rats with neuropathic pain. Neuroscience 2017, 349: 106–117.
10. Arifuzzaman S, Das A, Kim SH, Yoon T, Lee YS, Jung KH, et al. Selective inhibition of EZH2 by a small molecule inhibitor regulates microglial gene expression essential for inflammation. Biochem Pharmacol 2017, 137: 61–80.
11. Zhang Y, Liu HL, An LJ, Li L, Wei M, Ge DJ, et al. miR-124-3p attenuates neuropathic pain induced by chronic sciatic nerve injury in rats via targeting EZH2. J Cell Biochem 2019, 120: 5747–5755.
12. Menzies FM, Fleming A, Caricasole A, Bento CF, Andrews SP, Ashkenazi A, et al. Autophagy and neurodegeneration: pathogenic mechanisms and therapeutic opportunities. Neuron 2017, 93: 1015–1034.
13. Yang Z, Klionsky DJ. Eaten alive: a history of macroautophagy. Nat Cell Biol 2010, 12: 814–822.
14. Zhang E, Yi MH, Ko Y, Kim HW, Seo JH, Lee YH, et al. Expression of LC3 and Beclin 1 in the spinal dorsal horn following spinal nerve ligation-induced neuropathic pain. Brain Res 2013, 1519: 31–39.
15. Guo JS, Jing PB, Wang JA, Zhang R, Jiang BC, Gao YJ, et al. Increased autophagic activity in dorsal root ganglion attenuates neuropathic pain following peripheral nerve injury. Neurosci Lett 2015, 599: 158–163.
16. Wang L, Yuzhou L, Yingjie Z, Jie L, Xin Z. A new rat model of neuropathic pain: complete brachial plexus avulsion. Neurosci Lett 2015, 589: 52–56.
17. Willemen HL, Eijkelkamp N, Wang H, Dantzer R, Dorn GW 2nd, Kelley KW, et al. Microglial/macrophage GRK2 determines duration of peripheral IL-1beta-induced hyperalgesia: contribution of spinal cord CX3CR1, p38 and IL-1 signaling. Pain 2010, 150: 550–560.
18. Rubens RF, Adair RS, Jayme AB, João BC. Avulsion injury of the rat brachial plexus triggers hyperalgesia and allodynia in the hindpaws. Brain Res 2003, 982: 186–194.
19. Dixon WJ. Efficient analysis of experimental observations. Annu Rev Pharmacol Toxicol 1980, 20: 441–462.
20. Choi Y, Yoon YW, Na HS, Kim SH, Chung JM. Behavioral signs of ongoing pain and cold allodynia in a rat model of neuropathic pain. Pain 1994, 59: 369–376.
21. Wei FZ, Cao Z, Wang X, Wang H, Cai MY, Li T, et al. Epigenetic regulation of autophagy by the methyltransferase EZH2 through an MTOR-dependent pathway. Autophagy 2015, 11: 2309–2322.
22. Fujita N, Itoh T, Omori H, Fukuda M, Noda T, Yoshimori T. The Atg16L complex specifies the site of LC3 lipidation for membrane biogenesis in autophagy. Mol Biol Cell 2008, 19: 2092–2100.
23. Ji RR, Chamessian A, Zhang YQ. Pain regulation by non-neuronal cells and inflammation. Science 2016, 354: 572–577.
24. Brifault C, Kwon H, Campana WM, Gonias SL. LRP1 deficiency in microglia blocks neuro-inflammation in the spinal dorsal horn and neuropathic pain processing. Glia 2019, 67: 1210–01224.

25. Kiguchi N, Kobayashi D, Saika F, Matsuzaki S, Kishika S. Pharmacological Regulation of Neuropathic Pain Driven by Inflammatory Macrophages. Int J Mol Sci 2017, 18: 2296–2311.

26. Gong X, Chen Y, Chang J, Huang Y, Cai M, Zhang M. Environmental enrichment reduces adolescent anxiety- and depression-like behaviors of rats subjected to infant nerve injury. J Neuroinflammation 2018, 15: 262.

27. Penas C, Navarro X. Epigenetic modifications associated to neuroinflammation and neuropathic pain after neural trauma. Front Cell Neurosci 2018, 12: 158.

28. Feng XL, Deng HB, Wang ZG, Wu Y, Ke JJ, Feng XB. Suberoylanilide hydroxamic acid triggers autophagy by influencing the mTOR pathway in the spinal dorsal horn in a rat neuropathic pain model. Neurochem Res 2019, 44: 450–0464.

29. Wang D, Ding L, Wang L, Zhao Y, Sun Z, Karnes RJ, *et al.* LncRNA MALAT1 enhances oncogenic activities of EZH2 in castration-resistant prostate cancer. Oncotarget 2015, 6: 41045–041055.

30. Wang X, Sehgal L, Jain N, Khashab T, Mathur R, Samaniego F. LncRNA MALAT1 promotes development of mantle cell lymphoma by associating with EZH2. J Transl Med 2016, 14: 346.

31. Li P, Zhang X, Wang H, Wang L, Liu T, Du L, *et al.* MALAT1 is associated with poor response to oxaliplatin-based chemotherapy in colorectal cancer patients and promotes chemoresistance through EZH2. Mol Cancer Ther 2017, 16: 739–0751.

32. Yamagishi M, Uchimaru K. Targeting EZH2 in cancer therapy. Curr Opin Oncol 2017, 29: 375–0381.

33. Zhang X, Wang Y, Yuan J, Li N, Pei S, Xu J, *et al.* Macrophage/microglial Ezh2 facilitates autoimmune inflammation through inhibition of Socs3. J Exp Med 2018, 215: 1365–01382.

34. Yao Y, Hu H, Yang Y, Zhou G, Shang Z, Yang X, *et al.* Downregulation of enhancer of zeste homolog 2 (EZH2) is essential for the induction of autophagy and apoptosis in colorectal cancer cells. Genes (Basel) 2016, 7: E83.

35. Chen L, Jia J, Zang Y, Li J, Wang B. MicroRNA-101 regulates autophagy, proliferation and apoptosis via targeting EZH2 in laryngeal squamous cell carcinoma. Neoplasma 2019, 66: 507–0515.

36. Lian WS, Ko JY, Wu RW, Sun YC, Chen YS, Wu SL, *et al.* MicroRNA-128a represses chondrocyte autophagy and exacerbates knee osteoarthritis by disrupting Atg12. Cell Death Dis 2018, 9: 919.

37. Liu F, Sang M, Meng L, Gu L, Liu S, Li J, *et al.* miR-92b promotes autophagy and suppresses viability and invasion in breast cancer by targeting EZH2. Int J Oncol 2018, 53: 1505–1515.

38. Wang C, Liu B. miR-101-3p induces autophagy in endometrial carcinoma cells by targeting EZH2. Arch Gynecol Obstet 2019, 297: 1539–1548.

39. Ma J, Weng L, Wang Z, Jia Y, Liu B, Wu S, *et al.* MiR-124 induces autophagy-related cell death in cholangiocarcinoma cells through direct targeting of the EZH2-STAT3 signaling axis. Exp Cell Res 2018, 366: 103–113.

40. Xiong X, Zhang J, Liang W, Cao W, Qin S, Dai L, *et al.* Fuse-binding protein 1 is a target of the EZH2 inhibitor GSK343, in osteosarcoma cells. Int J Oncol 2016, 49: 623–628.

41. Xu H, Zhang L, Qian X, Zhou X, Yan Y, Zhou J, *et al.* GSK343 induces autophagy and downregulates the AKT/mTOR signaling pathway in pancreatic cancer cells. Exp Ther Med 2019, 18: 2608–2616.

LETTER TO THE EDITOR

Enhancement of Neuronal Activity in the Auditory Thalamus After Simulated Slow-Wave Oscillation

Lixia Gao[1,2,3] · Yuanqing Zhang[1,2] · Xinjian Li[1,3] · Jufang He[3,4]

Dear Editor,

Sleep is essential for survival in mammals, and there are many examples of how the brain fails to function properly without sleep. These include the importance of sleep for plasticity during development [1], memory formation and consolidation [2], and the erasure of undesired memories [3] as well as the improvement of memory [4], perceptual skills [5], and learning abilities after sleep [6]. These studies suggest that sleep not only benefits individual memories formed before sleep but also enhances individual performance on sensory discrimination tasks and learning ability after sleep. However, whether and how sleep contributes to sensory signal processing remains largely unknown.

Sleep has different phases, one of which is slow-wave sleep (SWS), characterized by low-frequency (<1 Hz), high-amplitude slow-wave oscillation (SWO) in the thalamocortical circuity [7], which is prevalent in both anesthetized and naturally sleeping animals. Accumulating evidence indicates that the SWO originates from thalamocortical circuitry [7]. During SWO, intracellular recordings have revealed that both cortical and thalamic neurons exhibit spontaneous membrane potential (MP) fluctuations—an alternation between a depolarized UP state and a hyperpolarized DOWN state [8, 9]. In the DOWN state, the MP of thalamic neurons is as low as −75 to −90 mV and the duration is in the range of 1 to 10 s (3.9 ± 2.2 s, mean ± SD) [9]. It has been reported that SWO plays a critical role in the induction of long-term synaptic plasticity [8], triggering the reactivation of associated memories and memory retention [10] as well as homeostatic regulation [11]. Moreover, previous studies have shown that visual and barrel cortical neurons exhibit distinct reponses to visual or tactile stimuli during the UP and DOWN states [12, 13], suggesting that the SWO plays a critical role in visual and tactile processing during sleep. The question we address is whether the long-lasting, hyperpolarized DOWN state in auditory thalamic neurons affects sound processing during and after SWO. We performed sharp electrode recordings in the medial geniculate body (MGB) of anesthetized guinea pigs and injected hyperpolarizing current into the recorded neurons to simulate SWO, and thus investigated the function of SWO in sound processing in the MGB.

To monitor the depth of anesthesia, local field potentials (LFPs) were recorded simultaneously in the auditory cortex of the animals during intracellular recordings in MGB neurons. Consistent with the thalamocortical basis of SWO, we found 22 out of 42 (52.4%) MGB neurons exhibited spontaneous UP and DOWN MP fluctuations with a slow rhythm (<1 Hz) during periods in which the cortical LFP exhibited SWO (Fig. 1A). Similar to a previous report [9],

✉ Lixia Gao
lxgao10@zju.edu.cn

✉ Jufang He
jufanghe@cityu.edu.hk

1 Department of Neurology of the Second Affiliated Hospital, Interdisciplinary Institute of Neuroscience and Technology, Zhejiang University School of Medicine, Hangzhou 310029, China

2 Key Laboratory of Biomedical Engineering of the Ministry of Education, College of Biomedical Engineering and Instrument Science, Zhejiang University, Hangzhou 310027, China

3 Department of Rehabilitation Sciences, The Hong Kong Polytechnic University, Hung Hom, Kowloon, Hong Kong, China

4 Department of Biomedical Sciences, City University of Hong Kong, Kowloon Tong, Hong Kong, China

Spontaneous UP and DOWN membrane potential fluctuations

Evoked response (ER) at UP and DOWN states
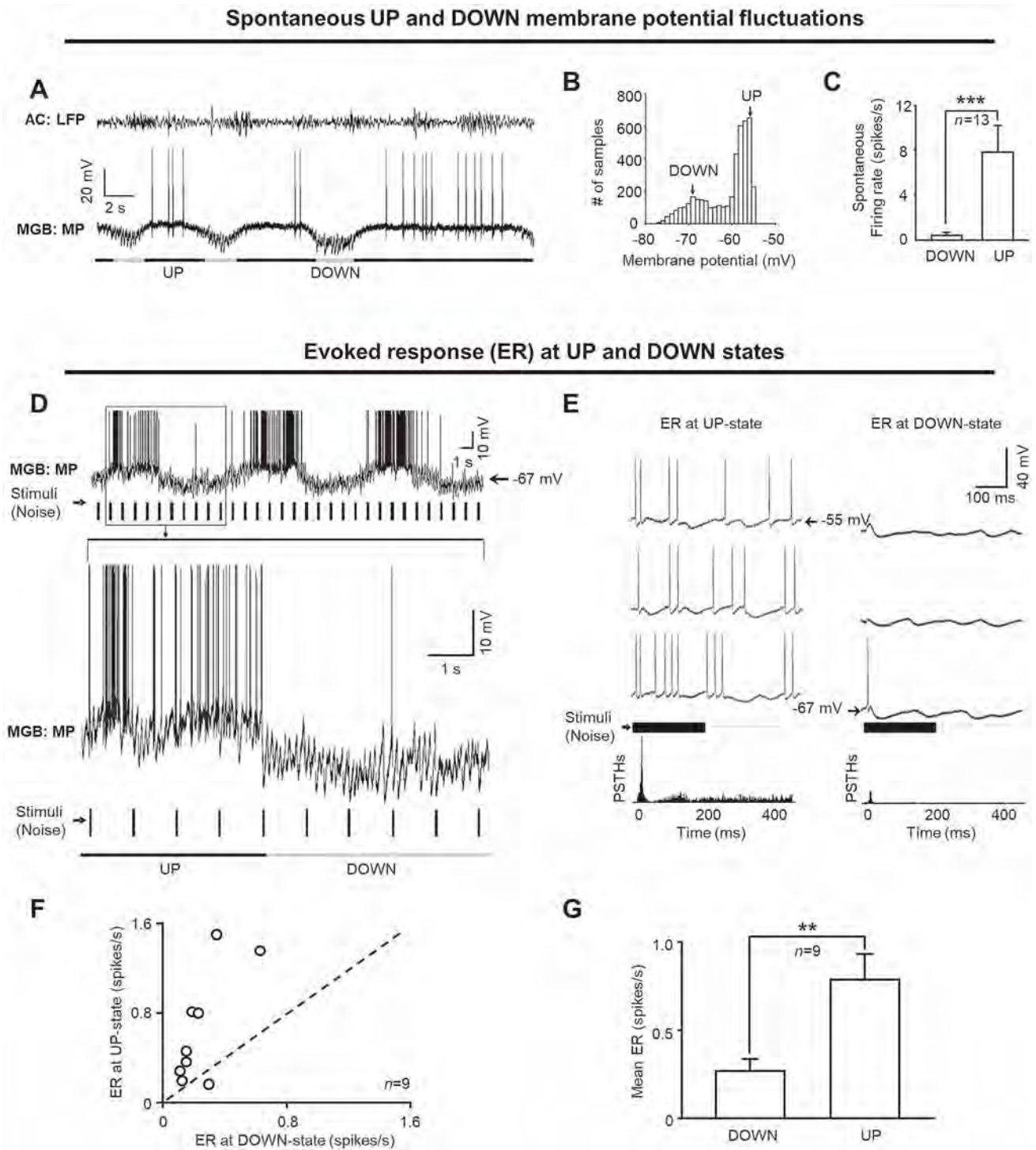
Fig. 1 MGB neurons exhibit stronger spontaneous and sound-evoked responses in the UP than in the DOWN state. **A** An example showing simultaneous local field potential (LFP) recordings in the auditory cortex (AC) and intracellular recording in an auditory thalamic neuron (MGB) of an anesthetized guinea pig. Line below indicates UP (black) and DOWN (grey) states. **B** Distribution of MPs during SWO over a 25-s recording period for the MGB neuron shown in **A**, binned at 1 ms. Arrows, average MP in the UP (−56 mV) and DOWN state (−69 mV). **C** Mean spontaneous firing rate of 13 MGB neurons in the UP and DOWN states (***$P < 0.001$, paired t test). **D** A representative MGB neuron with sound-evoked responses in the UP and DOWN states. Black rectangle, expanded below; lines below, UP (black) and DOWN (grey) states. **E** Example of sound-evoked responses in the UP (left) and DOWN (right) states aligned by the onset of the noise stimuli for the neuron in **D**. The post-stimulus time histograms below show the corresponding auditory responses of this neuron to 20 noise stimuli in the UP and DOWN states. **F** Evoked responses of 9 MGB neurons in the UP state plotted against those in the DOWN state. **G** Mean sound-evoked responses of these MGB neurons in the UP and DOWN states (**$P < 0.01$, paired t test).

the MP of an MGB neuron with SWO showed a bimodal distribution (Fig. 1B), and we used the two peaks as the mean MPs for the UP and DOWN states. The transitions between the UP and DOWN states were detected using a method described previously [9, 14]. For MGB neurons with spontaneous UP and DOWN MP fluctuations, spontaneous firing occurred primarily in the UP but not in the DOWN state. The mean firing rate in the UP state was 7.82 ± 2.38 (SD) spikes/s whereas that in the DOWN state was 0.41 ± 0.28 spikes/s (Fig. 1C, $n = 13$, $P < 0.001$), suggesting a differential neuronal signaling in the MGB UP *versus* DOWN states.

Since the spontaneous firing rate of MGB neurons in the UP state was distinct from that in the DOWN state, we speculated that the sound processing of MGB neurons may differ in the UP and the DOWN states. To investigate this possibility, we delivered repeated auditory stimuli (white broadband noise, duration: 200 ms, sound level: 70 dB SPL, inter-stimulus interval: 1 s) while performing *in vivo* intracellular recordings in MGB neurons with spontaneous UP and DOWN MP fluctuations (Fig. 1D). Consistent with the higher spontaneous activity in the UP than the DOWN state, we found that MGB neurons responded robustly to acoustic stimuli delivered in the UP state (Fig. 1E, left), but rarely exhibited a spiking response to the noise stimuli in the DOWN state (Fig. 1E, right). For most MGB neurons (8/9), the sound-evoked firing rate in the UP state was higher than that in the DOWN state (Fig. 1F). The mean sound-evoked responses were 0.66 ± 0.17 spikes/s in the UP state and 0.25 ± 0.05 spikes/s in the DOWN state (Fig. 1G, $n = 9$, $P = 0.008$, paired t test). Our results are consistent with previous studies in the visual cortex, which showed stronger responses to visual stimuli in the UP state than in the DOWN state [12]. The visual response of a cell is enhanced during the UP state due to an effective increase of the coherent neural activity in the local network. In contrast, in the primary somatosensory cortex, whisker deflections evoke fewer spikes and a smaller subthreshold response during the UP state, which may be due to driving force changes of excitation and inhibition and decreased input resistance as well as short-term depression of excitatory synapses [13]. UP and DOWN fluctuations in MGB neurons with MP separated by up to 20 mV play a crucial role in regulating the auditory spiking response to acoustic stimuli. However, we cannot exclude the possible contributions of driving force, input resistance, and other factors.

Our previous study showed that approximately two-thirds of auditory thalamic neurons exhibited a spontaneous SWO (<1 Hz) [9], which was higher than the proportion of MGB neurons with SWO in the current study. This discrepancy may be due to the bias of recording sites. MGB neurons with SWO are more prominent in non-

lemniscal (MGBd and MGBm) than lemniscal neurons (MGBv). We preferred to record from the ventral (MGBv) rather than the dorsal and medial divisions (MGBd and MGBm) first of all because the MGBv, which is the primary region for auditory processing, exhibits few spontaneous episodes of SWO. This made it a more suitable area for comparing the sound processing ability before and after induction of SWO.

We hypothesized that UP and DOWN MP fluctuations in SWO may change the neuronal responses to sensory inputs after SWS because an important function of sleep is to maintain synaptic balance [11]. The long-lasting hyperpolarized DOWN state in SWO may re-normalize synaptic strength that may be sustainable and beneficial for subsequent sensory processing during the awake state. To test this hypothesis, we selected MGB neurons without spontaneous UP and DOWN MP fluctuations ($n = 20$) and artificially mimicked the slow rhythm of SWO by hyperpolarizing their MP to the DOWN state by injecting negative current (Fig. 2A). Both the slow rhythm and hyperpolarized DOWN state were comparable to the SWO during natural slow-wave sleep. We found that, after tens of hyperpolarizing current injections (HCI; duration = 1–3 s, interval = 3–6 s, 12–30 pulses/session), spontaneous firing of the manipulated neurons increased (Fig. 2A). The mean spontaneous firing rate increased from 1.53 ± 0.40 spikes/s to 2.75 ± 0.66 spikes/s after induction of SWO (Fig. 2B–C, $n = 13$, $P = 0.004$, paired t-test).

Next, we determined whether the induction of simulated SWO influenced the auditory response of MGB neurons without intrinsic SWO. We found that the evoked responses of MGB neurons to acoustic stimuli increased after the induction of SWO (Fig. 2D). Using an induction index (ID) defined as the ratio of firing rate after HCI to that before HCI, 11 out of 14 neurons showed increased responses to sound stimuli after HCI (ID > 1.2), 1 neuron showed a decreased firing rate (ID < 0.8), and 2 neurons showed no rate change (Fig. 2E; 0.8 < ID < 1.2). On average, the sound-evoked response increased from 0.78 ± 0.25 spikes/s to 1.73 ± 0.70 spikes/s after induction of SWO (Fig. 2F, $n = 14$, $P = 0.040$). This increased firing rate was accompanied by a decrease in the first spike latency from 14.5 ± 1.5 ms to 13.7 ± 1.4 ms (Fig. 2G–I, $n = 14$, $P = 0.002$, paired t-test). Thus, as both increased firing rate and decreased latency indicate an enhanced sensory response, these data suggest that simulation of SWO facilitates sensory processing in auditory thalamic neurons *in vivo*.

Multiple lines of evidence suggest that sleep is associated with memory consolidation [1, 2, 6, 15] and homeostatic regulation [11] as well as enhancement of perceptual skill [5] and learning ability [6]. However, sleep is not a uniform state, and it is composed of both

Spontaneous activity change after HCl

Evoked response (ER) change after HCl

810

Neurosci. Bull. July, 2020, 36(7):806–810
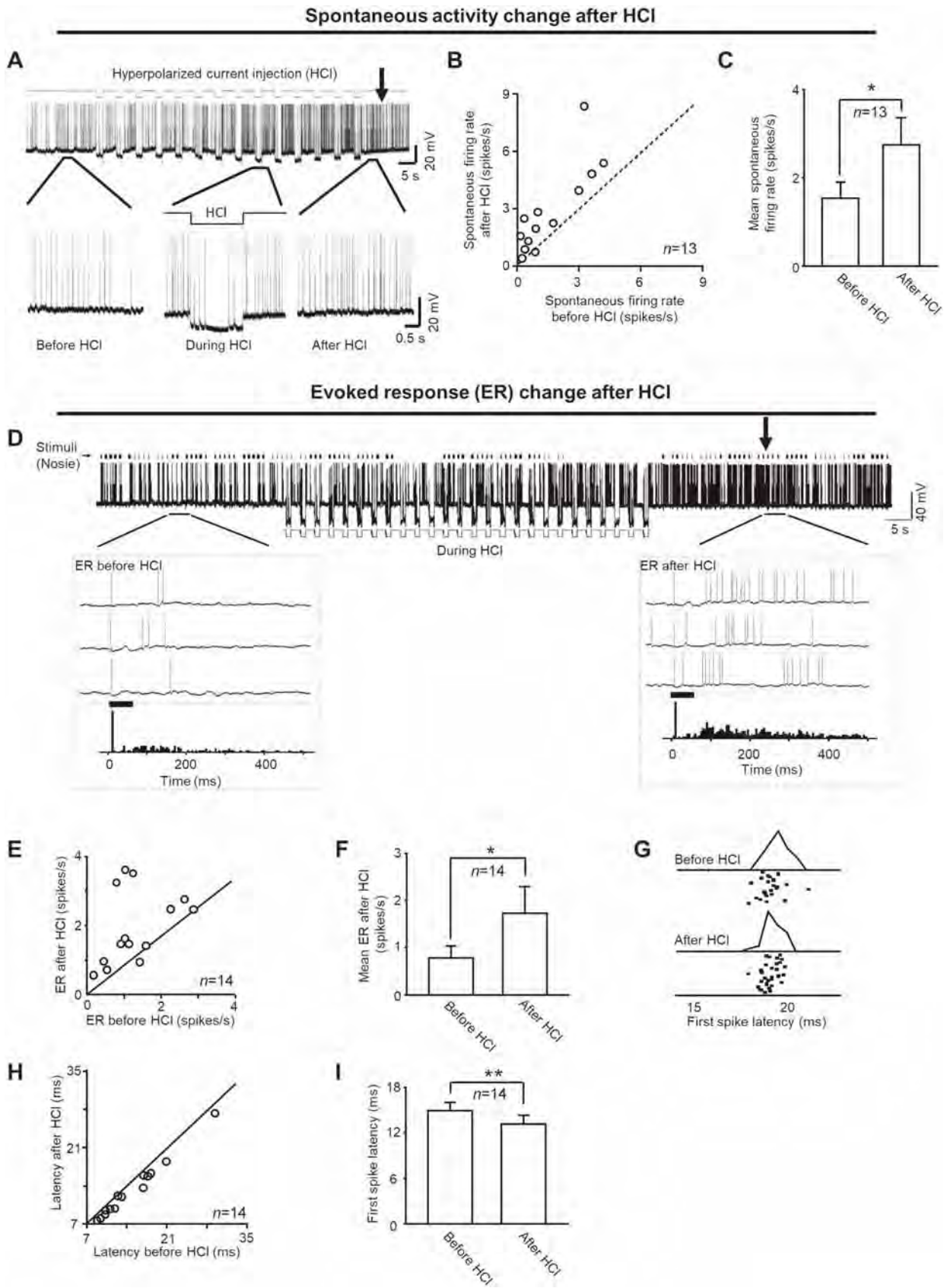
◄**Fig. 2** Spontaneous and sound-evoked responses of MGB neurons increase after simulated SWO. **A** A representative MGB neuron exhibiting increased spontaneous firing (arrow) after sequential hyperpolarized current injection (HCI) applied to the neuron. Lower panel: three episodes expanded from the periods before, during, and after HCI. **B** Spontaneous firing rates of 13 MGB neurons plotted against that of the same neurons after HCI. **C** Mean spontaneous firing rates of the same MGB neurons before and after HCI ($*P <$ 0.05, paired t-test). **D** Responses of an MGB neuron to noise stimuli (white broadband noise, duration: 200 ms, sound level: 70 dB SPL, inter-stimulus interval: 1 s) before and after induction of simulated SWO. Sound-evoked responses before (left) and after HCI (right); aligned to the onset of the noise stimuli and the corresponding PSTHs (dashed grey boxes). **E–F** Scatter plot (E) and bar chart (F) of sound-evoked responses of 14 MGB neurons before and after induction of SWO ($*P < 0.05$, paired t-test). **G** Raster plot of the sound-evoked responses of the neuron in **D** to noise stimuli before and after induction of SWO. **H** Latency to the first spike of 14 MGB neurons in response to acoustic stimuli before induction of SWO plotted against that of the same neurons after induction of SWO. **I** Average of the first spike latency of these14 MGB neurons before and after induction of SWO ($**P < 0.01$, paired t-test).

SWS and rapid eye movement sleep. Neuronal activity and neuromodulation are very different in these two sleep states. It is still hard to determine which phase of sleep plays a specific role as it is difficult to manipulate only one phase *in vivo*. In the present study, we applied HCI to induce a hyperpolarized DOWN state in MGB neurons without intrinsic SWO and simulated the slow rhythm of SWO in individual neurons. We found (1) simulation of SWO significantly changed the responsiveness of individual thalamic neurons, leading to increased spontaneous and sound-evoked responses to stimuli, and (2) a shortened latency, which indicated that SWO enhances neural activity in the auditory thalamus immediately after short-term simulation of SWO. These findings provide new insight into the function of SWO in auditory processing and provide a new framework for further research.

References

1. Frank MG, Issa NP, Stryker MP. Sleep enhances plasticity in the developing visual cortex. Neuron 2001, 30: 275–287.
2. Diekelmann S, Born J. The memory function of sleep. Nat Rev Neurosci 2010, 11: 114–126.
3. Rolls A, Makam M, Kroeger D, Colas D, de Lecea L, Heller HC. Sleep to forget: interference of fear memories during sleep. Mol Psychiatry 2013, 18: 1166–1170.
4. Benedict C, Scheller J, Rose-John S, Born J, Marshall L. Enhancing influence of intranasal interleukin-6 on slow-wave activity and memory consolidation during sleep. FASEB J 2009, 23: 3629–3636.
5. Karni A, Tanne D, Rubenstein BS, Askenasy JJ, Sagi D. Dependence on REM sleep of overnight improvement of a perceptual skill. Science 1994, 265: 679–682.
6. Stickgold R, James L, Hobson JA. Visual discrimination learning requires sleep after training. Nat Neurosci 2000, 3: 1237–1238.
7. Steriade M, Contreras D, Curro Dossi R, Nunez A. The slow (< 1 Hz) oscillation in reticular thalamic and thalamocortical neurons: scenario of sleep rhythm generation in interacting thalamic and neocortical networks. J Neurosci 1993, 13: 3284–3299.
8. Chauvette S, Seigneur J, Timofeev I. Sleep oscillations in the thalamocortical system induce long-term neuronal plasticity. Neuron 2012, 75: 1105–1113.
9. Gao L, Meng X, Ye C, Zhang H, Liu C, Dan Y, *et al.* Entrainment of slow oscillations of auditory thalamic neurons by repetitive sound stimuli. J Neurosci 2009, 29: 6013–6021.
10. Lu Y, Zhu ZG, Ma QQ, Su YT, Han Y, Wang X, *et al.* A critical time-window for the selective induction of hippocampal memory consolidation by a brief episode of slow-wave sleep. Neurosci Bull 2018, 34: 1091–1099.
11. Vyazovskiy VV, Olcese U, Hanlon EC, Nir Y, Cirelli C, Tononi G. Local sleep in awake rats. Nature 2011, 472: 443–447.
12. Azouz R, Gray CM. Cellular mechanisms contributing to response variability of cortical neurons *in vivo*. J Neurosci 1999, 19: 2209–2223.
13. Petersen CC, Hahn TT, Mehta M, Grinvald A, Sakmann B. Interaction of sensory responses with spontaneous depolarization in layer 2/3 barrel cortex. Proc Natl Acad Sci U S A 2003, 100: 13638–13643.
14. Loewenstein Y, Mahon S, Chadderton P, Kitamura K, Sompolinsky H, Yarom Y, *et al.* Bistability of cerebellar Purkinje cells modulated by sensory stimulation. Nat Neurosci 2005, 8: 202–211.
15. Stickgold R. Sleep-dependent memory consolidation. Nature 2005, 437: 1272–1278.

www.neurosci.cn
www.springer.com/12264

LETTER TO THE EDITOR

Correlation Between CCG Polymorphisms and CAG Repeats During Germline Transmission in Chinese Patients with Huntington's Disease

Hong-Rong Cheng[1] · Xiao-Yan Li[1] · Hui-Li Yu[1] · Miao Xu[2] · Yan-Bin Zhang[3] ·
Shi-Rui Gan[3] · Hong-Lei Li[1] · Zhi-Ying Wu[1,4]

Dear Editor,

Huntington's disease (HD) is an autosomal dominant neurodegenerative disease characterized by movement disorder, progressive dementia, and psychiatric and behavioral changes. It is caused by unstable expanded CAG trinucleotide repeats in exon 1 of the huntingtin (*HTT*) gene, located on chromosome 4p16.3 [1]. The number of CAG repeats is inversely correlated with the onset age of HD, with more expanded CAG repeats correlated with an earlier onset [2]. In previous studies, we have confirmed the inverse correlation between the onset age and the CAG repeat size in Chinese HD patients [3, 4].

Hong-Rong Cheng and Xiao-Yan Li have contributed equally to this work.

✉ Hong-Lei Li
   lihonglei@zju.edu.cn

✉ Zhi-Ying Wu
   zhiyingwu@zju.edu.cn

1 Department of Neurology and Research Center of Neurology in the Second Affiliated Hospital, and Key Laboratory of Medical Neurobiology of Zhejiang Province, Zhejiang University School of Medicine, Hangzhou 310009, China

2 Department of Neurology and Institute of Neurology, Huashan Hospital, Shanghai Medical College, Fudan University, Shanghai 200040, China

3 Department of Neurology, First Affiliated Hospital, Fujian Medical University, Fuzhou 350005, China

4 Joint Institute for Genetics and Genome Medicine between Zhejiang University and the University of Toronto, Zhejiang University, Hangzhou 310058, China

It has been reported that the expanded CAG trinucleotides are unstable during germline transmission, tend to expand in paternal transmission, but are more stable in maternal transmission [5]. Some studies have suggested that an intra- or flanking sequence of the *HTT* gene influences the CAG instability, thus causing the different prevalence rates of the disease [6–8]. A CCG polymorphism is adjacent to the CAG triplet repeat of the *HTT* gene, and is associated with the presence or absence of GAG repeats at codon 2642 (Δ2642) [9]. There is a significant difference in the allele frequencies of CCG polymorphisms among populations of different ancestries [9, 10].

In Caucasian populations, it is thought that a CCG7 polymorphism is associated with expanded CAG alleles [2]. However, in Japanese populations, CCG10 is considered to be associated with the expanded CAG alleles [10]. The different distributions of CCG polymorphisms suggest that they may be a risk factor for CAG instability and cause the varied prevalence. However, only two studies have reported the distribution frequencies of CCG polymorphisms in limited numbers of HD patients in mainland China (32 and 53 cases) [11, 12]. Furthermore, the CCG repeat sizes influencing the CAG instability during germline transmission have never been reported either in Chinese or Caucasian populations. Therefore, we aimed to use parent-child pairs to investigate the correlation between CAG and CCG repeats.

A total of 253 individuals (204 patients manifesting HD and 49 pre-symptomatic mutation carriers) with expanded CAG repeats within the *HTT* gene from 201 HD families were enrolled between February 2008 and May 2019 from three centers located in Southeastern China (the Second Affiliated Hospital of Zhejiang University School of Medicine, Huashan Hospital of Fudan University, and the

First Affiliated Hospital of Fujian Medical University). Among them, 193 cases had already participated in our previous study for a different research purpose [4]. Clinical data were analyzed retrospectively and 52 parent-child pairs were collected: 49 HD parents and 52 offspring. In addition, 248 unrelated control individuals were included. This study was approved by the local Ethics Committees of the above three hospitals. Written consent was given by participants or their legally authorized caregivers. Genomic DNA was extracted from peripheral blood and genetic testing for *HTT* was carried out using the previously reported method [13]. Statistical analysis was conducted using SPSS 20.0 (SPSS Inc., Chicago, IL). A *P*-value < 0.05 was considered statistically significant. To compare two continuous variables, *T* tests, Wilcoxon tests, or Mann-Whitney tests were used. For categorical variables, Pearson or Fisher's exact χ^2 test was used.

The frequency distribution of CCG repeats was determined in 200 unrelated patients manifesting HD (members of one family were all pre-symptomatic mutation carriers) and 248 unrelated normal controls. A total of six different CCG polymorphisms (CCG5, 6, 7, 8, 9, and 10) were detected (Fig. 1). Among the 496 normal chromosomes from 248 normal controls, CCG7 repeat alleles were most frequent (*n* = 270, 54.4%) followed by CCG10 (*n* = 187, 37.7%), and the remaining 39 cases (7.9%) were CCG6,

CCG8, and CCG9 (Fig. 1B). Among the normal alleles of 200 unrelated HD patients (Fig. 1C), 111 (55.5%) were CCG7, 82 (41.0%) were CCG10, and the remaining 7 (3.5%) were CCG6, CCG8, and CCG9. Among the 200 pathogenic alleles, 109 (54.5%) were CCG7, 82 (41.0%) were CCG10, and the remaining 9 (4.5%) were CCG5 and CCG9 (Fig. 1D). We found that the distribution characteristics of CCG polymorphisms in the normal chromosomes were almost same as those of the pathogenic chromosomes.

To explore whether the CCG repeat sizes change during germline transmission, we analyzed the inter-generational changes of CCG repeat sizes in 52 parent–child pairs, including 24 father-child and 28 mother–child pairs. During father–child transmission, inter-generational changes of CCG repeats occurred in 29.2% (7/24) of meiosis, including 20.8% (5/24) expansions and 8.4% (2/24) contractions. The remaining 70.8% (17/24) were not changed. However, in mother-child transmission, only 7.1% (2/28) showed contraction and none shown expansion. The percentage of CCG changes did not differ significantly between paternal and maternal transmission (*P* = 0.06).

As CCG7 and CCG10 were the predominant polymorphisms in both the general and HD populations, we only compared the CAG sizes of the CCG7 and CCG10 groups between the two populations. Among normal controls, the
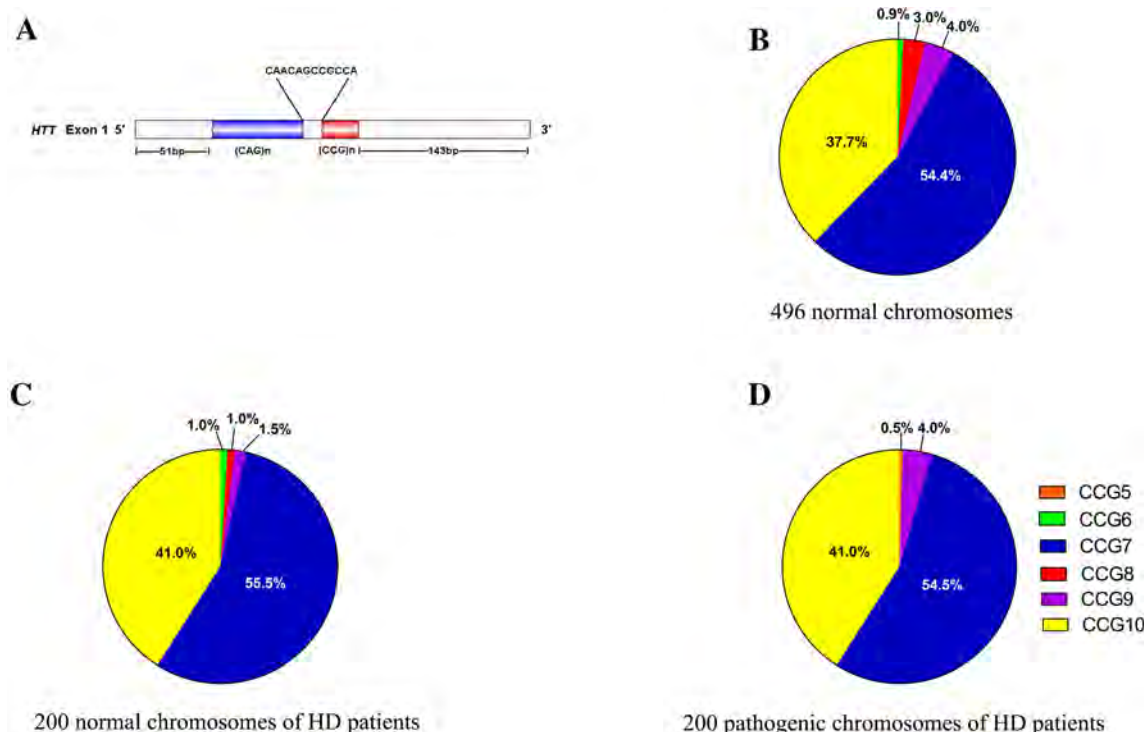
Fig. 1 Frequency distributions of CCG repeat sizes in general and HD populations. **A** Locations of the CAG and CCG polymorphism regions. **B–D** Frequency distribution of CCG repeats on the normal chromosomes from the general population (**B**, *n* = 496), on the normal chromosomes from the HD population (**C**, *n* = 200), and on the pathogenic chromosomes from the HD population (**D**, *n* = 200).

number of CAG repeats was 17.5 ± 2.0 (range 15–31) in the CCG7 group (n = 270) and 17.4 ± 1.7 (range 9–31) in the CCG10 group (n = 187) (P = 0.54). Among the normal alleles of HD patients, the number of CAG repeats was 17.7 ± 1.7 (range 15–26) in the CCG7 group (n = 111) and 17.4 ± 1.6 (range 9–24) in the CCG10 group (n = 82). Although the former was slightly larger than the latter, no significant difference was found (P = 0.19). Among the pathogenic alleles of HD patients, the number of CAG repeats was 45.0 ± 4.4 (range 40–66) in the CCG7 group (n = 109) and 45.0 ± 5.8 (range 39–74) in the CCG10 group (n = 82). No difference was found in the mean CAG repeat size between CCG7 and CCG10 (P = 0.91).

As CAG repeat sizes in the CCG7 and CCG10 groups did not differ at the population level, we tested the relationship at the inter-generational level. Among the 52 parent-child pairs, CCG7 accounted for 48.1% (25/52), CCG10 for 32.7% (17/52), and CCG6, CCG8 and CCG9 for the remaining 19.2% (10/52) (Table 1). Since the parent-child pairs of CCG6, CCG8 and CCG9 were too small, we only compared the CCG7 and CCG10 polymorphisms. In the total of 42 parent-child pairs, no statistical difference of △CAG change was found between the CCG7 (0.8 ± 2.5) and CCG10 (3.5 ± 8.7) groups (P = 0.14). Of note, parents with larger CAGs were more likely to have larger △CAG repeats [5], so we compared the CAG repeats of parents between the CCG7 and CCG10 groups but found no significant difference (P = 0.46). In addition, a previous study reported that the gender of the affected parent is a risk factor for CAG instability [4], so we subdivided the parent-child pairs according to the gender of

the parents to compare the number of △CAG repeats between the CCG7 and CCG10 polymorphisms. In paternal transmission, although the △CAG of the CCG7 group (1.6 ± 3.2) was lower than that of CCG10 (6.6 ± 13.2), it did not reach statistical significance (P = 0.29). In maternal transmission, the △CAG of the CCG7 group (0.3 ± 1.9) was similar to that of the CCG10 group (1.4 ± 2.4) (P = 0.21).

Different populations had different CCG polymorphisms. In Caucasian HD patients, CCG7 polymorphism accounted for 94.4% of the expanded alleles and for 5.6% of the normal alleles (Table S1) [2]. And in the Japanese population, 84.5% of pathogenic alleles were associated with CCG10 but only 15.5% with CCG7 [14]. However, in our current study in mainland China, the CCG7 (54.5%) and CCG10 (41.0%) repeats were similar and the CCG10 repeats had a significantly higher proportion than that reported in the Caucasian populations [2]. The discrepancy between Chinese and Caucasians may be due to the different genetic backgrounds [10]. Many SNPs have been reported to have different distributions between Chinese and Caucasian populations, like the delta 2642 polymorphisms. This may be caused by different founders in the Chinese and Caucasian populations, as supported by haplotype analysis [6–8]. On the other hand, the CCG distributions differ between populations in Japan and mainland of China [2]. A plausible explanation might be the smaller sample size of Japanese.

Here, we first studied the correlation between the inter-generational CCG change and CAG repeats, which have rarely been explored either in Caucasian or Chinese populations. The △CAG of the CCG10 group was higher than that of the CCG7 group, but did not reach a significant level, perhaps because of the small sample size. Therefore, a larger cohort is needed to further support the results.

In summary, to our knowledge, this study is the first to analyze the correlation between CCG polymorphisms and CAG repeats in the *HTT* region at the inter-generational level. We concluded that the distribution of CCG polymorphisms in China differs from that in Caucasians, but CCG polymorphisms did not influence the CAG instability although CCG10 showed a tendency towards CAG expansion during germline transmission. A larger cohort is needed to explore this relationship.

Table 1 Comparisons of inter-generational changes of CAG repeat length between CCG7 and CCG10 groups.

	CCG7	CCG10	P value
Pairs (P/M)	25 (9/16)	17 (7/10)	
Parent	44.6 ± 2.5	43.8 ± 3.8	0.46
Offspring	45.4 ± 3.2	47.4 ± 12.0	0.42
△CAG	0.8 ± 2.5	3.5 ± 8.7	0.14
Paternal	43.4 ± 1.4	44.6 ± 5.7	0.57
Offspring	45.0 ± 3.5	51.1 ± 18.6	0.34
△CAG	1.6 ± 3.2	6.6 ± 13.2	0.29
Maternal	45.2 ± 2.8	43.3 ± 1.9	0.07
Offspring	45.5 ± 3.1	44.7 ± 3.1	0.53
△CAG	0.3 ± 1.9	1.4 ± 2.4	0.21
P value	0.23#	0.34#	

M: maternal inheritance; P: paternal inheritance; △CAG: the inter-generational changes of CAG repeats.

#: Comparison between the △CAG of father-child transmission and mother-child transmission in each CCG group.

Conflict of interest The authors declare that they have no conflict of interest.

References

1. MacDonald ME, Ambrose CM, Duyao MP, Myers RH, Lin C, Srinidhi L, *et al*. A novel gene containing a trinucleotide repeat that is expanded and unstable on Huntington's disease chromosomes. The Huntington's Disease Collaborative Research Group. Cell 1993, 72: 971–983.
2. Squitieri F, Andrew SE, Goldberg YP, Kremer B, Spence N, Zeisler J, *et al*. DNA haplotype analysis of Huntington disease reveals clues to the origins and mechanisms of CAG expansion and reasons for geographic variations of prevalence. Hum Mol Genet 1994, 3: 2103–2114.
3. Li XY, Zhang YB, Xu M, Cheng HR, Dong Y, Ni W, *et al*. Effect of apolipoprotein E genotypes on Huntington's disease phenotypes in a Han Chinese population. Neurosci Bull 2019, 35: 756–762.
4. Li HL, Li XY, Zhang YB, Dong Y, Cheng HR, Gan SR, *et al*. Clinical and genetic profiles in Chinese patients with Huntington's disease: A ten-year multicenter study in China. Aging Dis 2019, 10:1003–1011.
5. Kremer B, Almqvist E, Theilmann J, Spence N, Telenius H, Goldberg YP, *et al*. Sex-dependent mechanisms for expansions and contractions of the CAG repeat on affected Huntington disease chromosomes. Am J Hum Genet 1995, 57: 343–350.
6. Li XY, Li HL, Dong Y, Gao B, Cheng HR, Ni W, *et al*. Haplotype analysis encompassing HTT gene in Chinese patients with Huntington's disease. Eur J Neurol 2020, 27: 273–279.
7. Kay C, Collins J, Skotte JH, Southwell AL, Warby SC, Caron NS, *et al*. Huntingtin Haplotypes provide prioritized target panels for allele-spectic silencing in Huntington disease of European ancestry. Mol Ther 2015, 11: 1759–1771.
8. Warby SC, Montpetit A, Hayden AR, Carroll JB, Butland SL, Visscher H, *et al*. CAG expansion in the Huntington disease gene is associated with a specific and targetable predisposing haplogroup. Am J Hum Genet 2009, 84: 351–366.
9. Hecimovic S, Klepac N, Vlasic J, Vojta A, Janko D, Skarpa-Prpic I, *et al*. Genetic background of Huntington disease in Croatia: Molecular analysis of CAG, CCG, and Delta2642 (E2642del) polymorphisms. Hum Mutat 2002, 20: 233.
10. Morovvati S, Nakagawa M, Osame M, Karami A. Analysis of CCG repeats in Huntingtin gene among HD patients and normal populations in Japan. Arch Med Res 2008, 39: 131–133.
11. Ma M, Yang Y, Shang H, Su D, Zhang H, Ma Y, *et al*. Evidence for a predisposing background for CAG expansion leading to HTT mutation in a Chinese population. J Neurol Sci 2010, 298: 57–60.
12. Zhang BR, Tian J, Yan YP, Yin XZ, Zhao GH, Wu ZY, *et al*. CCG polymorphisms in the huntingtin gene have no effect on the pathogenesis of patients with Huntington's disease in mainland Chinese families. J Neurol Sci 2012, 312: 92–96.
13. Dong Y, Sun YM, Liu ZJ, Ni W, Shi SS, Wu ZY. Chinese patients with Huntington's disease initially presenting with spinocerebellar ataxia. Clin Genet 2013, 83: 380–383.
14. Masuda N, Goto J, Murayama N, Watanabe M, Kondo I, Kanazawa I, *et al*. Analysis of triplet repeats in the huntingtin gene in Japanese families affected with Huntington's disease. J Med Genet 1995, 32: 701–705.

LETTER TO THE EDITOR

Individual Differences in Learning Rate and Fear Response Predict Fear Memory and Recovery in Mice and Human Subjects

Yan Gao[1] · Wei Li[1] · Bo Sui[1] · Nashat Abumaria[1,2]

Dear Editor,

Following an emotionally intensive and fearful traumatic event, some individuals develop anxiety disorders such as post-traumatic stress disorder (PTSD) [1]. Cognitive therapy is used as an effective therapy to suppress fearful and/or traumatic memories; however, it fails in almost half of the anxious patients, resulting in the return of fearful memories [2]. Therefore, intensive research has been conducted to identify genetic, neural, biochemical, behavioral, or computational markers that predict vulnerability to developing PTSD, and/or the response to cognitive therapy [3].

In laboratory settings, Pavlovian fear conditioning and fear extinction represent models of PTSD and cognitive therapy [4]. During fear conditioning, an association between a neutral conditioned stimulus (CS+) and a strong and aversive unconditioned stimulus (US, e.g. electrical shock) occurs. Later on, presentation of the non-aversive CS+ alone is sufficient to elicit a strong conditioned response. During fear extinction, the conditioned fear responses are attenuated by repeated presentation of the

---

Yan Gao and Wei Li have contributed equally to this work.

✉ Nashat Abumaria
Abumaria@fudan.edu.cn

[1]   State Key Laboratory of Medical Neurobiology and MOE Frontiers Center for Brain Science, Institutes of Brain Science, Fudan University, Shanghai 200032, China

[2]   Department of Laboratory Animal Science, Shanghai Medical College, Fudan University, Shanghai 200032, China

CS+ alone. Although extinction can suppress the fear memory *via* different mechanisms, the original fear might recover following extinction [5–7].

Studies in PTSD patients, fear-conditioned human subjects and in experimental animals have identified markers that predict individual differences in terms of the strength of fear memory and/or the recovery of fear [3]. For instance, a higher level of PTSD symptoms before treatment predicts failure of cognitive therapy and recovery of symptoms [8]. A poor response to cognitive therapy in PTSD patients is associated with increases in amygdala activation [9] and decreases in medial prefrontal cortex and hippocampus activation [10]. However, it remains unclear whether such findings reflect predisposing risk factors that predict vulnerability to developing PTSD and resistance to cognitive therapy, or they represent pathological changes induced by the traumatic experience. Furthermore, fear conditioning studies in human subjects show that the degree of recruitment of the amygdala is correlated with the conditioned response during fear learning, memory retrieval, and extinction learning [11]. In mice, brain-derived neurotrophic factor levels in the medial prefrontal cortex predict successful extinction [12]. Fear reactivity predicts the strength of fear memory in rats [13]. Therefore, fear conditioning studies also provide markers that can predict the strength of fear memory and/or recovery of fear. To date, very few studies have attempted to implement computational approaches to identify mathematically-derived predictors of fear memory and recovery. Compared with the above behavioral, biochemical, or imaging approaches, such a mathematical approach would be simpler, less invasive, more cost-effective, and easily validated in experimental animals and human subjects. It has been noted that the quality of learning, as well as response severity, might be among the major determinants

of the strength of fear memory and/or recovery of fear [3]. In support of this hypothesis, a study using mathematical analyses of human fear conditioning datasets found that the quality of extinction learning predicts the spontaneous recovery of fear in individual human subjects [14].

In the current study, we show that individual differences in the rate of fear learning (referred to as S) calculated from prediction error-based (Rescorla-Wagner [15]) or Hebb-based [16, 17] learning models, as well as the maximum unconditioned response during fear conditioning (R_{max}), determine the quality of fear learning. A mathematically-derived value ($S*R_{max}$) was found to correlate with the strength of fear memory, extinction rate, and spontaneous recovery of fear. Furthermore, we established a new computational model to simulate fear learning (the Integrative model). The new model improved the simulation of fear learning curves, reduced variations, and slightly improved the correlations between the $S_{(Integrative)}*R_{max}$ value and fear memory, extinction, and recovery. We tested/validated our mathematical approach as well as our *de novo* Integrative model by using fear conditioning datasets from mice and human subjects (see Fig. 1A for the study design and Supplementary material 1 for the methods and technical details).

We first generated experimental datasets of fear acquisition and recovery in mice ($n = 32$ throughout the study). The mice were given five trials of tone–shock pairings. The freezing behavior increased steadily and significantly over the five trials, indicating successful fear learning (ANOVA repeated measure, $F_{(31, 155)} = 3.05$, $P < 0.0001$, Fig. 1B). During extinction learning (days 2 and 3), the freezing behavior gradually declined over the 10 blocks of training, suggesting successful extinction of fear ($F_{(31, 310)} = 14.0$, $P < 0.0001$; Fig. 1C). To evaluate the recovery of fear, an extinction recall test was conducted on day 4 (Fig. 1D). Following the presentation of a single CS+, some mice exhibited low freezing behavior; others exhibited high percentages of freezing (Fig. 1D; see Supplementary material 2 for detailed behavioral readouts of individual mice), suggesting variations in the recovery of conditioned fear following extinction. To extend our mathematical approach to human subjects, we obtained human fear conditioning (Fig. 1E), extinction (Fig. 1F) and extinction recall (Fig. 1G) datasets that were generated from a cohort of controls ($n = 106$), published by another group of researchers [18]. The same sets of data have also been published in an analytical study of individual differences in extinction learning [14]. We refer the readers to these two studies for detailed methods (see also Supplementary material 1). The data are presented in Fig. 1E–G here as received from the source (see Supplementary material 2 for the differential skin conductance response [SCR] of individuals during each phase).

Next, we applied Rescorla-Wagner (equation 1), Hebb (equation 2), and the Integrative model (equation 3) learning rules, ran simulations of fear learning curves until they reached/approached the asymptotic learning level, corrected them to the minimum error relative to the experimental data (equation 4), and generated representative curves for all the mice (see Supplementary material 1 for explanations of the models/equations).

$$\Delta V = S * (\lambda - V_n) \tag{1}$$

$$W_{ij}(n + 1) = W_{ij}(n) + S * \Delta W_{ij} \tag{2}$$

$$V_{n+1} = (1-k) * (V_n + S^{n+1}) + k * [S * (\lambda - V_n) + V_n] \tag{3}$$

$$\begin{cases} \Delta \bar{V} r_{n+1} - \Delta \bar{V} r_n > 0, & k = 1, \\ \Delta \bar{V} r_{n+1} - \Delta \bar{V} r_n \leq 0, & k = 0 \end{cases}$$

$$Error = \sum\nolimits_{i=1}^{n} (Vr_i - Vs_i)^2 / (n - 1) \tag{4}$$

With the Rescorla-Wagner model, the mice learned the task very rapidly as revealed by the rapid increase in the percentage of freezing during early trials (Fig. 2A, solid line). The mouse curve approached the asymptotic learning level ($\sim 99.99\%$, percentage of freezing) after ~ 140 trials (Fig. 2A). With the Hebb learning rule, the mice also learned the task much faster (Fig. 2B, solid line). However, unlike the Rescorla-Wager simulation curve, the Hebb-derived curve approached the asymptotic level after only ~ 18 trials. Furthermore, the asymptotic level of the Hebb curve was lower ($\sim 50.50\%$; Fig. 2B). In datasets from human subjects, we used the same criteria and derived the learning curves based on the Rescorla-Wagner (Fig. 2C) and Hebb (Fig. 2D) learning models. With the Rescorla-Wagner model, participants learned the task and approached the asymptotic learning level (differential SCR: ~ 1.33) after ~ 173 trials (Fig. 2C, solid line). With the Hebb learning rule, they approached the asymptotic level (~ 0.21) after only ~ 12 trials (Fig. 2D, solid line; see Supplementary material 3 for all simulation data).

Importantly, regardless of the model used, the pattern of the learning curves of individual mice and human subjects differed in terms of speed of learning and maximum responses reached (Fig. 2A–D, dotted lines indicate minimum and maximum learning curves). Therefore, we concluded that S and R_{max} might be among the key determinants shaping the dynamics of fear learning, and hence might provide a certain predictive power to identify individuals with stronger fear memory, slower extinction rate, and/or greater fear recovery.

Based on the above rationale, we calculated S from the simulation curves based on equations 1, 2, and 3 and obtained the value of R_{max} from the fear conditioning data (Supplementary material 4). We defined the maximum unconditioned response during fear conditioning (R_{max}) as
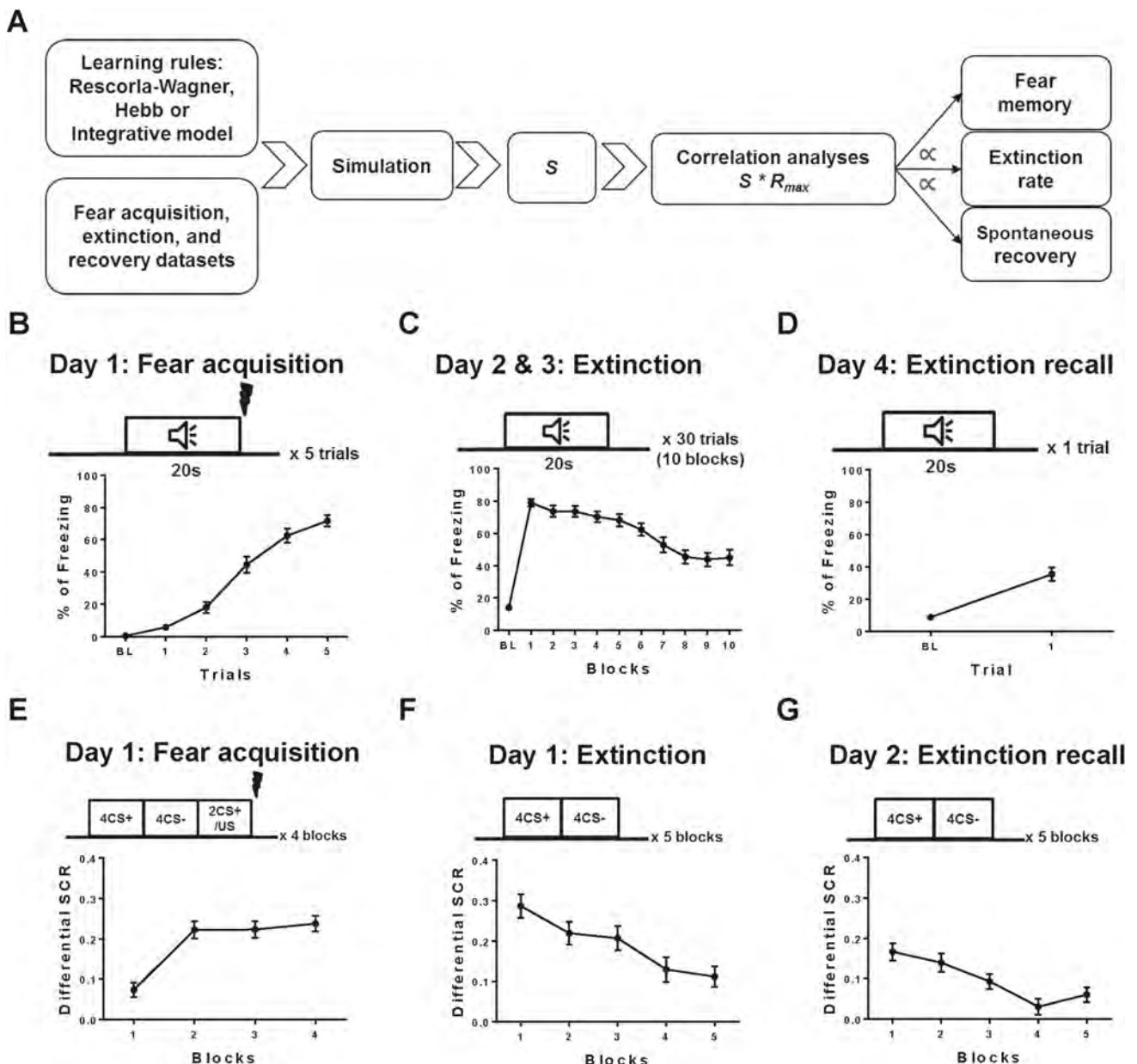
Fig. 1 A Schematic of the design and logical flow of the current study. **B–D** Datasets of fear acquisition (**B**), extinction (**C**), and recovery (**D**) in mice. Behavioral readouts are presented as percentage of freezing (% of freezing). **E–G** Datasets of fear acquisition (**E**), extinction (**F**), and recovery (**G**) in human subjects. Data are presented as the differential skin conductance response (SCR). Mean ± SEM.

the mean of two maximum emotional responses exhibited by individuals in response to presentations of the aversive US during learning in mice (percentage of freezing) and human subjects (SCR). The area under the curve of the extinction curve (AUC$_{extinction}$) was used as an indicator of the extinction rate (a high AUC indicates slow extinction; Supplementary material 2). The conditioned response to the presentation of the first CS+ during extinction learning was used as a measure of fear memory in mice and human subjects. The conditioned response to the presentation of

the first CS+ during the extinction recall test was used as a measure of the spontaneous recovery in mice and human subjects.

We checked the predictive power of *S* and R_{max} by conducting a series of correlation analyses. In the mouse datasets, $S_{(Rescorla-Wagner)}*R_{max}$ correlated with the strength of fear memory (*Pearson's* test, $r = 0.434$, $P = 0.013$; Fig. 2E), extinction rate ($r = 0.590$, $P = 0.0004$; Fig. 2F), and strength of fear recovery ($r = 0.567$, $P = 0.001$; Fig. 2G). Similarly, $S_{(Hebb)}*R_{max}$ correlated with the

818

Neurosci. Bull. July, 2020, 36(7):815–820
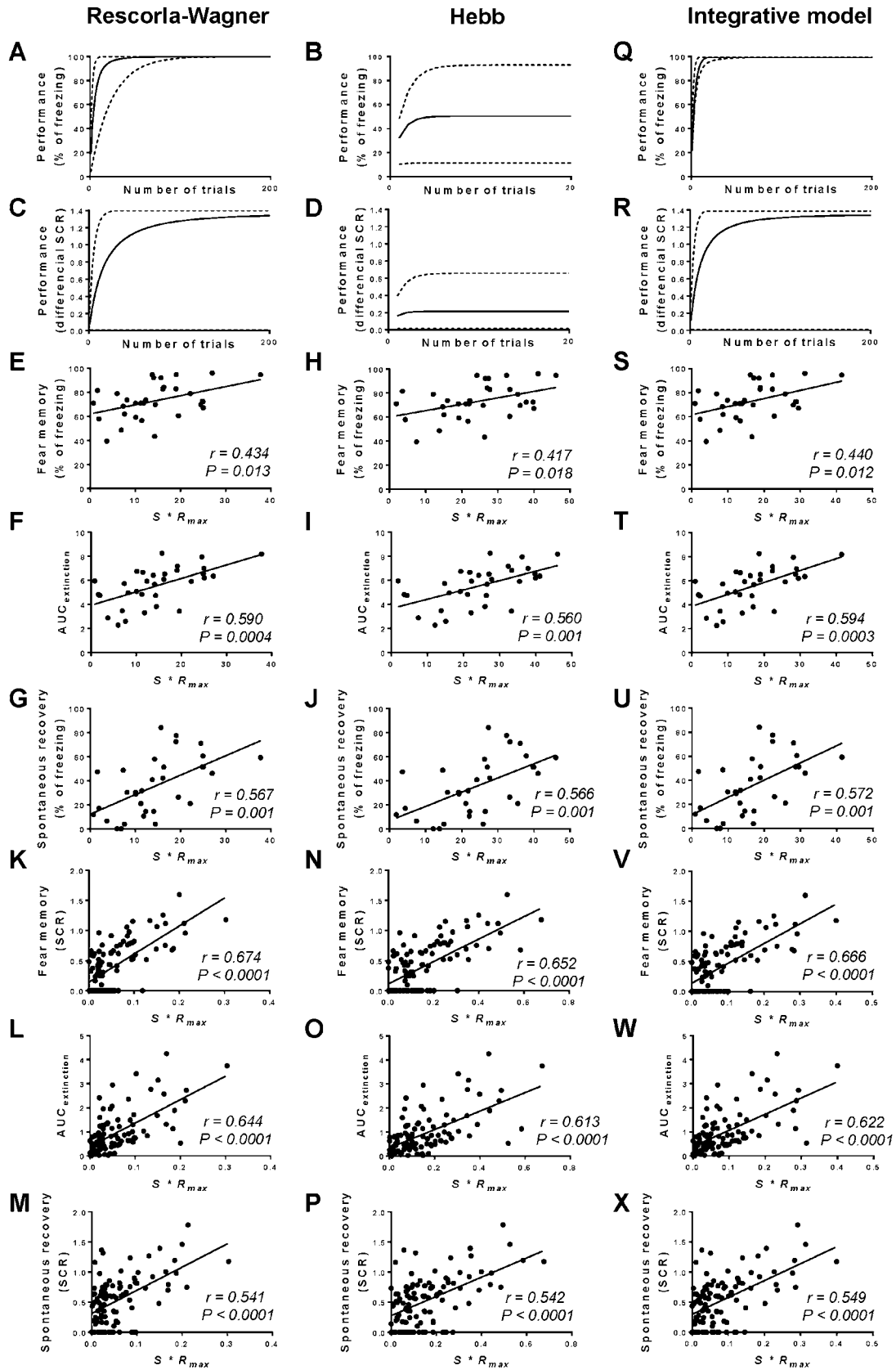
◄**Fig. 2 A–D**, **Q**, and **R** Simulation curves of fear learning in mice (**A, B, Q**) and human subjects (**C, D, R**). Solid lines, average learning curves of individuals; dashed lines, highest (upper) and lowest (lower) learning curves (range). Simulation readouts are presented as the percentage of freezing (% of freezing) for mice, and as differential skin conductance response (SCR) for human subjects. **E–P** and **S–X** Correlations between $S*R_{max}$ and fear memory, extinction rate (AUC$_{extinction}$), and recovery of fear in mice (**E–J** and **S–U**) and human subjects (**K–P** and **V–X**).

strength of fear memory ($r = 0.417$, $P = 0.018$; Fig. 2H), extinction rate ($r = 0.560$, $P = 0.001$; Fig. 2I), and fear recovery ($r = 0.566$, $P = 0.001$; Fig. 2J). In the human datasets, we conducted similar correlation analyses. Strikingly, $S_{(Rescorla-Wagner)}*R_{max}$ positively correlated with the strength of fear memory ($r = 0.674$, $P < 0.0001$; Fig. 2K), extinction rate ($r = 0.644$, $P < 0.0001$; Fig. 2L), and fear recovery ($r = 0.541$, $P < 0.0001$; Fig. 2M). $S_{(Hebb)}*R_{max}$ also correlated with the strength of fear memory ($r = 0.652$, $P < 0.0001$; Fig. 2N), extinction rate ($r = 0.613$, $P < 0.0001$; Fig. 2O), and fear recovery ($r = 0.542$, $P < 0.0001$; Fig. 2P).

Finally, we noted that the Rescorla-Wagner simulation curve required a large number of trials to reach the maximum behavioral readout and/or the asymptotic level of learning. Meanwhile, the Hebb simulation curve reached the asymptotic level too rapidly, and this level was far below the maximum experimental behavioral readout. Thus, we established a new learning model (the Integrative model), in which we integrated both teaching styles. In this model, we hypothesize that during early trials (when the shock is not expected), prediction error learning quickly teaches the circuitry, driving the behavioral readout close to maximum levels. Once the learning gain declines and the shock is anticipated (no discrepancy, no prediction error learning), the Hebb principle of synapse potentiation takes over the circuitry-teaching process (when cells fire together, the circuitry further wires together), leading to a rapid attainment of the target asymptotic level of memory and/or behavioral readout (see equation 3 and Supplementary material 1).

With the Integrative model, the mice learned the task rapidly and the simulation curve approached the asymptotic learning level after ∼90 trials (Fig. 2Q, solid line). The dynamics of the Integrative model curve showed a significantly faster learning rate than that generated by the Rescorla-Wagner model and reached a significantly higher asymptotic level than that generated by the Hebb model (Fig. 2A, B, Q, solid lines). Interestingly, the individual variations were also reduced as indicated by the smaller range in the simulation data generated by the Integrative model than that generated by the other two models (Fig. 2 A, B, Q, dotted lines). We applied the same criteria to the

human datasets and found similar patterns as the curve approached the asymptotic learning level after ∼155 trials (Fig. 2R, solid line; see Supplementary material 3 for simulation data). Furthermore, we checked whether the $S*R_{max}$ value derived from our model using the criteria described above ($S_{(Integrative)}*R_{max}$, Supplementary material 4) retained similar predictive power. In mice, $S_{(Integrative)}*R_{max}$ correlated with the strength of fear memory ($r = 0.440$, $P = 0.012$; Fig. 2S), extinction rate ($r = 0.594$, $P = 0.0003$; Fig. 2T), and strength of fear recovery ($r = 0.572$, $P = 0.001$; Fig. 2U). In the human datasets, $S_{(Integrative)}*R_{max}$ positively correlated with the strength of fear memory ($r = 0.666$, $P < 0.0001$; Fig. 2V), extinction rate ($r = 0.622$, $P < 0.0001$; Fig. 2W), and fear recovery ($r = 0.549$, $P < 0.0001$; Fig. 2X). Thus, by using two well-established learning models and a *de novo* learning model that we established (the Integrative model) we identified two key determinants of the dynamics of fear learning. The mathematically-derived value of these determinants ($S*R_{max}$) can, to a certain extent, predict the strength of fear memories, efficacy of extinction, and recovery of fear in mice and human subjects.

Theoretical studies suggest that associative fear learning follows either prediction error [15] or Hebbian [16] learning theories. The prediction error model views associative learning as a discrepancy between the predicted outcome of the conditioning trial and the actual unexpected outcome of the trial. The unexpected US during early trials is, therefore, more effective in supporting learning than the expected US during later trials [15, 19]. Studies have provided compelling evidence for the involvement of this model in dictating the neuronal circuitry during fear learning [19–21]. On the other hand, the Hebb learning model depends on potentiation of the CS+ synaptic inputs on postsynaptic cells in the lateral amygdala. The potentiation of the weak CS+ inputs is facilitated by postsynaptic depolarization induced by the co-occurring strong US inputs [16]. Studies also provide evidence for the involvement of this model in dictating the neuronal circuitry during fear learning [22, 23]. Thus, it remains debatable which learning model the associative fear learning might follow. Recently, it has been hypothesized that the circuitry and neurotransmitters mediating conditioned fear might be more complex than previously thought, and hence the brain might use both learning models during fear memory encoding [20, 22, 23].

Our results support the latter hypothesis. The simulation studies showed that both learning models successfully generated a fast learning phase during early trials, followed by a slow learning phase and finally reaching an asymptotic level of learning (Fig. 2A–D). Furthermore, $S_{(Rescorla-Wagner)}*R_{max}$ and $S_{(Hebb)}*R_{max}$ had similarly significant correlations with the strength of fear memory and

fear recovery. Thus, both models are equally reliable in reflecting learning curve dynamics as well as in predicting the heterogeneity in the quality of fear learning, retention, and recovery among individuals. However, the Hebb-based simulation curves reached the asymptotic learning levels earlier than the Rescorla-Wagner-based curves. Moreover, the Rescorla-Wagner-based curves approached asymptotic learning levels close to those obtained by real experimental data (100 for mice and 1.4 for human subjects); meanwhile, the Hebb-based curves did not. Thus, there are differences between the models in terms of simulating fear learning processes. Such differences might stem from the different compositions of their equations. For instance, unlike the Rescorla-Wagner equation, the Hebb equation does not include a value for the asymptotic learning level (λ). As mentioned above, it is also possible that both teaching styles are involved in fear memory encoding; however, each style dictates the circuitry at a different phase during the encoding processes (i.e. early *versus* later trials). We established the Integrative model based on this hypothesis. Interestingly, this model resulted in improving dynamics of the simulation curves, reducing variations among individuals, and showing slightly better correlations between $S_{(Integrative)}*R_{max}$ and certain behavioral readouts.

In conclusion, we introduce a mathematical approach to derive a value ($S*R_{max}$) that predicts the strength of fear memory, extinction efficacy, and spontaneous recovery of fear. Our data support the view that individual differences in learning quality and/or response severity might predict vulnerability and resilience in certain psychiatric disorders such as PTSD [3, 14].

References

1. Kessler RC, Chiu WT, Demler O, Merikangas KR, Walters EE. Prevalence, severity, and comorbidity of 12-month DSM-IV disorders in the National Comorbidity Survey Replication. Arch Gen Psychiatry 2005, 62: 617–627.

2. Foa EB. Psychosocial therapy for posttraumatic stress disorder. J Clin Psychiatry 2006, 67 Suppl 2: 40–45.

3. Yehuda R, LeDoux J. Response variation following trauma: a translational neuroscience approach to understanding PTSD. Neuron 2007, 56: 19–32.

4. LeDoux J. The Emotional Brain: The Mysterious Underpinnings of Emotional Life. Simon & Schuster, 1996.

5. Myers KM, Davis M. Behavioral and neural analysis of extinction. Neuron 2002, 36: 567–584.

6. Han SL, Xu TL. Unraveling the mechanisms of memory extinction. Neurosci Bull 2018, 34: 385–388.

7. Guo YC, Yuan T, Guo BY. The secret of fear memory attenuation: facing fears. Neurosci Bull 2019, 35: 775–777.

8. Blanchard EB, Hickling EJ, Malta LS, Jaccard J, Devineni T, Veazey CH, et al. Prediction of response to psychological treatment among motor vehicle accident survivors with PTSD. Behav Therapy 2003, 34: 351–363.

9. Bryant RA, Felmingham K, Kemp A, Das P, Hughes G, Peduto A, et al. Amygdala and ventral anterior cingulate activation predicts treatment response to cognitive behaviour therapy for post-traumatic stress disorder. Psychol Med 2008, 38: 555–561.

10. Rauch SL, Shin LM, Phelps EA. Neurocircuitry models of posttraumatic stress disorder and extinction: human neuroimaging research[mdash]past, present, and future. Biol Psychiatry 2006, 60: 376–382.

11. Phelps EA, Delgado MR, Nearing KI, LeDoux JE. Extinction learning in humans: role of the amygdala and vmPFC. Neuron 2004, 43: 897–905.

12. Peters J, Dieppa-Perea LM, Melendez LM, Quirk GJ. Induction of fear extinction with hippocampal-infralimbic BDNF. Science 2010, 328: 1288–1290.

13. Bush DE, Sotres-Bayon F, LeDoux JE. Individual differences in fear: isolating fear reactivity and fear recovery phenotypes. J Trauma Stress 2007, 20: 413–422.

14. Gershman SJ, Hartley CA. Individual differences in learning predict the return of fear. Learn Behav 2015, 43: 243–250.

15. Rescorla RA, Wagner AR. A theory of Pavlovian conditioning: variations in the effectiveness of reinforcement and nonreinforcement. In: Black AH & Prokasy WF (eds.). Classical Conditioning II: Current Research and Theory. New York: Appleton-Century-Crofts, 1972: 64–99.

16. Hebb DO. The Organization of Behavior. New York: Wiley & Sons, 1949.

17. Cooper RP, Cook R, Dickinson A, Heyes CM. Associative (not Hebbian) learning and the mirror neuron system. Neurosci Lett 2013, 540: 28–36.

18. Hartley CA, McKenna MC, Salman R, Holmes A, Casey BJ, Phelps EA, et al. Serotonin transporter polyadenylation polymorphism modulates the retention of fear extinction memory. Proc Natl Acad Sci U S A 2012, 109: 5493–5498.

19. McNally GP, Johansen JP, Blair HT. Placing prediction into the fear circuit. Trends Neurosci 2011, 34: 283–292.

20. Johansen JP, Tarpley JW, LeDoux JE, Blair HT. Neural substrates for expectation-modulated fear learning in the amygdala and periaqueductal gray. Nat Neurosci 2010, 13: 979–986.

21. Yu K, Ahrens S, Zhang X, Schiff H, Ramakrishnan C, Fenno L, et al. The central amygdala controls learning in the lateral amygdala. Nat Neurosci 2017, 20: 1680–1685.

22. Johansen JP, Diaz-Mataix L, Hamanaka H, Ozawa T, Ycu E, Koivumaa J, et al. Hebbian and neuromodulatory mechanisms interact to trigger associative memory formation. Proc Natl Acad Sci U S A 2014, 111: E5584–5592.

23. Johansen JP, Hamanaka H, Monfils MH, Behnia R, Deisseroth K, Blair HT, et al. Optical activation of lateral amygdala pyramidal cells instructs associative fear learning. Proc Natl Acad Sci U S A 2010, 107: 12692–12697.

www.neurosci.cn
www.springer.com/12264

RESEARCH HIGHLIGHT

Single-Cell RNA Sequencing Reveals Cell-Type-Specific Mechanisms of Neurological Diseases

Zhen-Ge Luo[1] · Jian Peng[1,2,3] · Ting Li[1,3]

Single-cell transcriptomic analysis has provided an unprecedented avenue for the identification of neuronal subtypes that are affected in neurological diseases. However, this strategy is largely hindered by the difficulty of collecting fresh samples of adult human brain. Instead, postmortem brain tissue from both normal and diseased human subjects is more accessible. To reduce sample contamination from other cells or RNA degradation often encountered in whole-cell dissociation and isolation, sequencing of RNA from single nuclei has been developed to reflect whole-cell RNA levels in the human brain [1, 2]. By using single-nucleus RNA sequencing (snRNA-seq), recent studies have identified cell-type-specific molecular changes in the neocortex of patients with autism and Alzheimer's disease [3–5].

Autism spectrum disorders (ASDs) are complex and heterogeneous conditions, with patients showing persistent deficits in social interaction and communication along with stereotyped behavior [6]. Hundreds of genomic loci have been associated with the occurrence of ASDs, including those transmitted from parents and those appearing *de novo* in the germline [7], either as a single penetrant mutation or rare low-risk variants with cumulative effects. Although multifactorial neurodevelopmental defects are believed to underlie ASD etiologies, the cell-type-specific pathology of ASDs is unclear. Recently, Kriegstein's group at the University of California, San Francisco, performed snRNA-seq analysis of 41 postmortem samples of prefrontal cortex and anterior cingulate cortex from 15 ASD patients without intellectual disability and 16 normal controls ranging in age from 4 years to 20 years [8]. They used the prevailing droplet-based 10x Genomics Chromium platform for the analysis and generated 104,559 single-nuclei RNA expression profiles: 52,003 from patients and 52,556 from controls. By annotating cell clusters according to the known markers of specific cell types, they identified cell-type-specific changes in gene expression (see Fig. 1 for the workflow), and intriguingly, established the association of these changes with the clinical severity of disease.

The top differentially-expressed genes (DEGs) were down-regulated in superficial layers 2/3 (L2/3) excitatory neurons and interneurons expressing vasoactive intestinal polypeptide, and up-regulated in astrocytes and microglia. Gene Ontology analysis showed that the dysregulated genes were in pathways involved in chemical synaptic transmission, nervous system processes, postsynaptic membrane potential, axon guidance, neuronal migration, synapse assembly, and γ-aminobutyric acid signaling, across all cell types analyzed. The genes important for synaptic function and some transcription factors critical for brain development were among the top dysregulated genes in L2/3 and 4 excitatory neurons, and notably, genes reflecting activation states were enriched in the microglia and astrocytes of ASD samples. Remarkably, DEGs in L2/3 neurons and microglia were significantly correlated with clinical severity, although the most strongly correlated genes were not among the top DEGs. These results indicate

✉ Zhen-Ge Luo
luozhg@shanghaitech.edu.cn

1   School of Life Science and Technology, ShanghaiTech University, Shanghai 200031, China

2   Institute of Neuroscience, State Key Laboratory of Neuroscience, Center for Excellence in Brain Science and Intelligence Technology, Chinese Academy of Sciences, Shanghai 200031, China

3   University of the Chinese Academy of Sciences, Beijing 100049, China
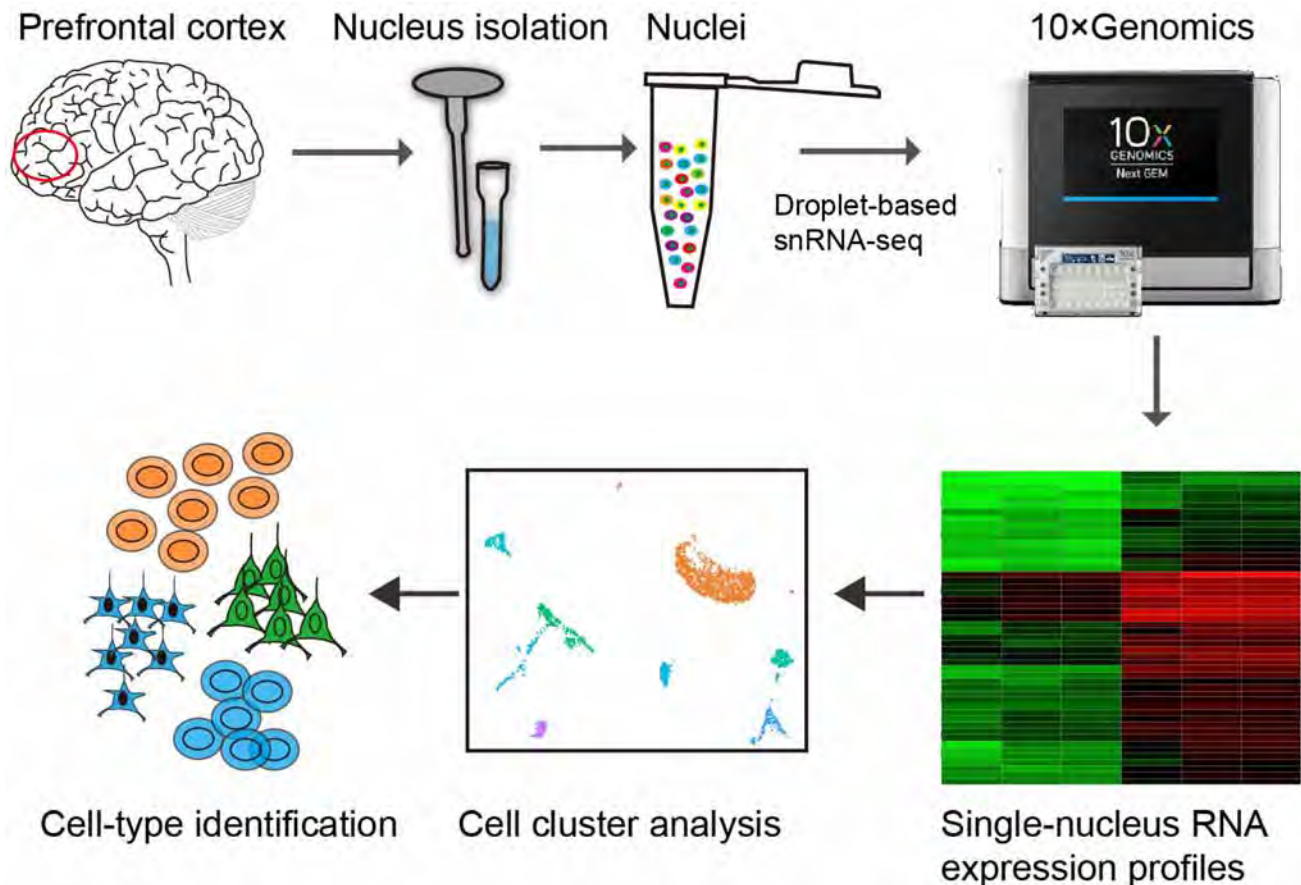
Fig. 1 Schematic of the main technical approach used in snRNA-seq analysis.

that the degree of dysregulation may not be closely correlated with disease symptoms, and instead, disturbance of gene expression networks in specific neuronal cell types represents the molecular pathology of ASD.

This study also compared the molecular changes in ASD and sporadic epilepsy, a comorbidity of ASD, and found minimal overlap of the changes in cell-type-specific gene expression. For example, synaptic transmission, axon guidance, and brain development pathways were among the DEGs detected in ASD, but not in the epilepsy samples. These results suggest that the identified dysregulated pathways are mostly ASD-specific and highlight probable intervention targets and pathways. Because most ASD patients also have intellectual disability, and in particular, various ASD patients exhibit high heterogeneity in clinical symptoms, future studies should include larger cohorts to more precisely associate genetic variants with clinical severity. Considering the male bias in ASD prevalence [9], sex differences should be taken into consideration in future studies of cell-type-specific molecular changes in ASD.

Alzheimer's disease (AD) is one of the major challenge for elder people worldwide. However, current understanding of the molecular and cellular mechanisms of AD

pathogenesis is still in debate; specific markers used for early diagnosis and approaches for diease control are still not available [10]. Using the droplet-based snRNA-seq approach, a recent study performed by Tsai's group at Massachusetts Institute of Technology revealed cell-type-specific changes in AD while considering the degree of pathology and sex differences [4]. They analyzed 80,660 single-nucleus transcriptomes from 48 post-mortem samples of prefrontal cortex (Brodmann area 10) from AD patients with various degrees of pathology. They demonstrated cell-type-specific gene expression changes in the early stages and common changes across major cell types in the later stages. Furthermore, this study revealed sexual dimorphism in transcriptional changes at the cellular level. The resource provided in this study depicts a dynamic trajectory of AD pathology at the single-cell level and reveals heterogeneous responses among cell types.

The samples from 48 individuals were collected from two longitudinal cohort studies of ageing and dementia, the Religious Order Study and the Rush Memory and Aging Project, both of which have detailed clinical records, post-mortem pathological examination, and multiple-omics bulk-tissue profiling [11]. Based on the severity of beta-

amyloid and other AD pathology, the 48 samples were classified into two groups: 24 controls with little or no detectable pathology and 24 age-matched samples with mild to severe AD pathology. The years of education (medians 18 for no pathology and 19.5 for AD pathology), ages (medians 87.1 for no-pathology and 86.7 for AD-pathology), and sexes were balanced. After quality control filtering, a dataset of 17,926 protein-coding genes from 75,060 nuclei with a cut-off value of 200 unique molecular identifiers and at least 200 detected genes in each cell was subjected to further analysis. Based on known cell-type markers, they identified major cell types from 20 transcriptionally-distinct clusters, including excitatory neurons, inhibitory neurons, astrocytes, oligodendrocytes, microglia, oligodendrocyte progenitor cells, endothelial cells, and pericytes. After comparing the gene expression levels between the groups with and without AD pathology, 1,031 DEGs were identified, and interestingly, most DEGs in neurons were down-regulated and most DEGs in oligodendrocytes, astrocytes, and microglia were up-regulated. Notably, some DEGs showed opposite directionality in different cell types, such as *APOE*, which was down-regulated in astrocytes but up-regulated in microglia. The heterogeneous response to AD pathology is difficult to capture using bulk RNA-seq analysis. Although the majority of DEGs were strongly cell type-specific with perturbations only in a particular neuronal or glial cell type, the top DEGs involved in related processes, such as myelination and axonal growth and regeneration, were found across cell types.

Then, the samples with AD pathology were further subdivided into two groups: early-stage with an amyloid burden but modest neurofibrillary tangles and mild cognitive impairment; and late-stage with a higher amyloid burden, more pronounced neurofibrillary tangles, and severe cognitive impairment. Pairwise comparisons of gene expression in distinct cell types were made between early/late pathology and no-pathology groups. Notably, almost all up-regulated and down-regulated DEGs in the no- and early-pathology subgroups were cell-type-specific either in neurons or a single glial cell type. By contrast, up-regulated DEGs in late- *versus* early-pathology were global across cell types, whereas down-regulated DEGs were cell-type-specific. These results reveal dynamic disease progression from the dysregulation of gene expression networks in specific cell types at early stages prior to severe pathological features to global changes due to stress responses at late stages. Furthermore, this study also established associations between gene expression patterns in specific cell types and major pathological traits, including ß-amyloid level, neurofibrillary tangle density, plaque number, and global cognition level, and indicated gene sets responding to AD pathology in specific cell types.

For example, genes positively associated with AD pathology in microglia were enriched in pathways mediating immune and inflammatory responses and β-amyloid clearance, and genes associated with oligodendrocyte pathology were enriched in pathways for oligodendrocyte differentiation and myelination.

To further relate the cell-type heterogeneity to the pathological features of individual samples, this study identified cell subpopulations that might be associated with the pathological status of AD and identified marker genes for each subpopulation. Among these, a subpopulation of excitatory neurons marked by *INGO1*, *RASGEF1B*, and *SLC26A3* and a subpopulation of oligodendrocytes marked by *CADM2, QDPR, NLGN,* and *CRYAB* were over-represented in AD pathology. The study also identified a subpopulation of microglia that was distinct from the microglial state in a mouse model and did not overlap with aged microglia without AD. Genes marking these AD pathology-associated subpopulations encode proteins involved in protein quality control, cell death, and immune responses. Notably, sex differences in the response to AD pathology were identified in some cell subpopulations. Females exhibited pronounced AD pathology-associated cell subpopulations and males exhibited more no-pathology subpopulations. Furthermore, females had higher expression of the marker genes of AD-pathology subpopulations. They also discerned the sex-specific differential responses by cell types to pathological features. The most extreme differences were found in oligodendrocytes and neurons. In males, increased AD pathology correlated with transcriptional activation in oligodendrocytes, and this did not occur in females. In females, increased pathology was correlated with marked down-regulation of gene expression in both excitatory and inhibitory neurons, whereas males showed a less pronounced response in excitatory neurons and little response in inhibitory neurons. Females also showed a significant association between white-matter lesions and decreased cognition. Although these results are inspiring, a larger sample size and large-scale gene-trait association studies, as well as experimental validation, are needed to thoroughly understand sexual dimorphism in the progression of AD.

Using a similar snRNA-seq approach, a recent study provided a single-cell atlas of entorhinal cortex from control and AD brains (6 individuals in each group with a mean age of 77.6 years) [5]. The dataset from 13,214 nuclei was analyzed, leading to the findings of cell-type-specific expression of risk genes and their contributions to disease susceptibility. Specifically, this work has also integrated gene networks and genome-wide association studies, which uncovered genomic loci for AD risk [12] at the single-cell level, revealing cell-type-specific drivers of

824

Neurosci. Bull. July, 2020, 36(7):821–824

disease state transition. Taken together, these analyses have led to novel insights into cell-type-specific changes in AD.

Although numerous studies using bulk RNA-seq analysis have revealed dysfunctions of neurons and/or innate immune responses, they are unable to entangle the heterogeneity of different disease subtypes and distinct responses across cell types. Because many neurological diseases are usually accompanied by multiple systemic comorbidities, scRNA-seq technology will help to disentangle the shared and unique neurological abnormalities among different conditions, which will assist the development of precision medicine. Furthermore, it will also help to determine the dynamic progression of neuronal pathology at the molecular, cellular, and circuit levels, which will deepen the understanding of disease mechanisms and help to develop predictors of disease trajectories. The major limitation at present is the noisy nature of the resulting data, which is primarily due to the technical limitations of working with such small amounts of RNA. This noise makes it difficult to distinguish very similar cell types and identify rare cell types that may contribute to the heterogeneity of disease entities. Another challenge is how to distinguish between neuroprotective responses and neuronal pathology. Future technological improvements will enable a more profound understanding of disease mechanisms at the cell-type level, which will be of help for diagnosis as well as intervention.

References

1. Lake BB, Ai R, Kaeser GE, Salathia NS, Yung YC, Liu R, *et al.* Neuronal subtypes and diversity revealed by single-nucleus RNA sequencing of the human brain. Science 2016, 352: 1586–1590.
2. Lake BB, Chen S, Sos BC, Fan J, Kaeser GE, Yung YC, *et al.* Integrative single-cell analysis of transcriptional and epigenetic states in the human adult brain. Nat Biotechnol 2018, 36: 70–80.
3. Lai M-C, Lombardo MV, Baron-Cohen S. Autism Lancet 2014, 383: 896–910.
4. Mathys H, Davila-Velderrain J, Peng Z, Gao F, Mohammadi S, Young JZ, *et al.* Single-cell transcriptomic analysis of Alzheimer's disease. Nature 2019, 570: 332–337.
5. Grubman A, Chew G, Ouyang JF, Sun G, Choo XY, McLean C, *et al.* A single-cell atlas of entorhinal cortex from individuals with Alzheimer's disease reveals cell-type-specific gene expression regulation. Nat Neurosci 2019, 22: 2087–2097.
6. Qiu Z, Yuan B. Towards the framework of understanding autism spectrum disorders. Neurosci Bull 2019, 35: 1110–1112.
7. Stein JL, Parikshak NN, Geschwind DH. Rare inherited variation in autism: beginning to see the forest and a few trees. Neuron 2013, 77: 209–211.
8. Velmeshev D, Schirmer L, Jung D, Haeussler M, Perez Y, Mayer S, *et al.* Single-cell genomics identifies cell type–specific molecular changes in autism. Science 2019, 364: 685–689.
9. Masi A, DeMayo MM, Glozier N, Guastella AJ. An overview of autism spectrum disorder, heterogeneity and treatment options. Neurosci Bull 2017, 33: 183–193.
10. Sun BL, Li WW, Zhu C, Jin WS, Zeng F, Liu YH, *et al.* Clinical research on Alzheimer's disease: progress and perspectives. Neurosci Bull 2018, 34: 1111–1118.
11. Bennett DA, Buchman AS, Boyle PA, Barnes LL, Wilson RS, Schneider JA. Religious Orders Study and Rush Memory and Aging Project. J Alzheimers Dis 2018, 64: S161–S189.
12. Lambert JC, Ibrahim-Verbaas CA, Harold D, Naj AC, Sims R, Bellenguez C, *et al.* Meta-analysis of 74,046 individuals identifies 11 new susceptibility loci for Alzheimer's disease. Nat Genet 2013, 45: 1452–1458.

www.neurosci.cn
www.springer.com/12264

INSIGHT

An Overview of the Expert Consensus on the Prevention and Treatment of Gaming Disorder in China (2019 Edition)

Yu-Tao Xiang[1,2] · Yu Jin[1,2] · Ling Zhang[3] · Lu Li[4] · Gabor S. Ungvari[5,6] · Chee H. Ng[7] · Min Zhao[8] · Wei Hao[9]

Gaming disorder has gained considerable attention worldwide, including in China [1], where epidemiological surveys have found that its prevalence is as high as 17% [2]. The Bureau of Disease Control and Prevention run by the National Health and Health Commission in China recently released an expert consensus [2] that systematically describes the definition, clinical presentation, assessment, diagnosis, treatment, rehabilitation, and related areas of gaming disorder. As this consensus is published in Chinese, it is not readily accessible by the international readership. For this reason, we present here an overview of the expert consensus on gaming disorder in China.

Definition and Clinical Features

Gaming disorder refers to a behavioral pattern of continuous or repeated use of electronic or video games, manifested as having impaired control and giving priority to gaming over other daily activities, regardless of the adverse consequences of this behavior. This pattern usually persists for at least 12 months [3].

The main clinical presentation of gaming disorder includes loss of control over the occurrence, frequency, and duration of gaming. Gaming takes priority over other interests and daily life, and may continue or even escalate despite its negative consequences. Persons with gaming disorder may be subjectively aware of the desire for games, but may have difficulty in distinguishing between the virtual reality in games and the real world [4].

Yu-Tao Xiang, Yu Jin, Ling Zhang and Lu Li contributed equally to this work.

✉ Yu-Tao Xiang
   xyutly@gmail.com

✉ Wei Hao
   weihao57@csu.edu.cn

1   Unit of Psychiatry, Institute of Translational Medicine, Faculty of Health Sciences, University of Macau, Macao 999078, China

2   Center for Cognition and Brain Sciences, University of Macau, Macao 999078, China

3   The National Clinical Research Center for Mental Disorders & Beijing Key Laboratory of Mental Disorders, Beijing Anding Hospital & the Advanced Innovation Center for Human Brain Protection, Capital Medical University, School of Mental Health, Beijing 100088, China

4   The Affiliated Brain Hospital of Guangzhou Medical University (Guangzhou Huiai Hospital), Guangzhou 510370, China

5   Division of Psychiatry, School of Medicine, University of Western Australia, Perth, Australia

6   University of Notre Dame Australia, Fremantle 6907, Australia

7   Department of Psychiatry, The Melbourne Clinic and St Vincent's Hospital, University of Melbourne, Richmond, VIC 3002, Australia

8   Shanghai Mental Health Center, Shanghai Jiao Tong University School of Medicine, Shanghai 200232, China

9   Department of Psychiatry, National Clinical Research Center on Mental Disorders and National Technology Institute on Mental Disorders, Second Xiangya Hospital, Central South University, Changsha 410011, China

⌂ Springer

Gaming disorder can lead to both physical (such as lack of sleep, circadian rhythm disorders, malnutrition, and seizures) and mental problems (such as irritability, anxiety, aggression, and depression), as well as impairment in social functioning (such as refusal to attend school, avoidance of social activities, family conflict, and impaired academic achievement) [5].

Factors Contributing to Gaming Disorder

The occurrence of gaming disorder is associated with psychological, social, and biological factors. Psychological factors include high impulsivity, high neuroticism, or introverted personality [6]. Some may show aggressive and violent behavior, poor mood regulation, loneliness, low self-esteem, low self-efficacy, poor life satisfaction, vulnerability to sensory overload, depression, and anxiety. Insufficient social support or interpersonal interaction and poor teacher-student or classmate relationships are also risk factors [7]. Brain imaging findings in persons with gaming disorder are similar to those in individuals with substance use or gambling disorders [8] in terms of structural and functional abnormalities in multiple areas of the frontal lobe, ventral striatum, and dorsal striatum, as well as functional abnormalities, such as reduced executive and control function [9].

Diagnosis and Evaluation

Early identification, diagnosis, and intervention are essential for the prevention and treatment of gaming disorder. Prior to the release of the International Classification of Diseases, 11th Revision (ICD-11), some scales had been developed to screen for gaming behaviors. However, these tools have limitations, such as inconsistent core symptoms and insufficient psychometric properties [10, 11]. Consequently, the World Health Organization is developing user-friendly screening assessment tools with satisfactory psychometric properties [12].

For the clinical diagnosis of those with suspected gaming disorder or at a high risk of the disorder, standardized guidelines are needed to ensure the accuracy of diagnosis within the health service. The core features of gaming disorder proposed in ICD-11 are: (1) a continuous or repeated pattern of gaming behavior, characterized by impaired control over gaming (e.g. lack of control over the occurrence, frequency, duration, and cessation of gaming behavior), which has a high priority in daily life, despite having related negative consequences (e.g. impaired rela-

tionships, adverse occupational or academic impact, and damage to health); (2) the pattern persists for at least 12 months (if the symptoms are severe enough and other diagnostic criteria are met, the duration of gaming behavior could be <12 months); and (3) the pattern of behavior leads to significant impairment in personal, family, and occupational functioning, interpersonal relationships, or other important areas. The disorder includes both online and offline gaming behavior [1].

Gaming disorder should be distinguished from normal gaming behavior. If the purpose of the behavior is to promote socialization, relieve boredom, or regulate emotions, and there are no other core features of gaming disorder, then a diagnosis is not warranted [13]. Cultural factors and the impact on an individual's social circle should be considered when diagnosing gaming disorder [14]. In addition, high-intensity gaming may be part of the job of individuals in the gaming industry, so they should not be diagnosed as having the disorder. Gaming disorder is a continuously-evolving process, starting from no gaming, *via* occasional play, to high-frequency gaming, and finally developing into uncontrolled gaming. Therefore, early recognition and prevention in this process are important.

The following differential diagnoses should be excluded when making a diagnosis of gaming disorder: (1) hazardous gaming behavior, which poses a health risk, but the disorder has not yet developed; this state requires further observation or treatment; (2) gambling disorder; the two disorders share certain clinical features, such as the presence of a craving state prior to engagement in addictive behaviors, continued engagement despite negative consequences, and the loss of control over engagement in such behaviors [6]. However, compared to gambling disorder, gaming disorder usually does not involve money. In cases when internet gaming involves gambling content (such as poker, mahjong, and probability sweepstakes), a diagnosis of gambling disorder should be made. In addition, patients with gaming disorder have higher impulsivity levels, while those with gambling disorder have higher compulsivity levels [15]; (3) other psychiatric disorders, such as anxiety disorders, depressive disorders, bipolar disorder, and personality disorders. Excessive gaming behavior may also occur during episodes of the above disorders. If both gaming disorder and other psychiatric disorders exist concurrently, the diagnosis of comorbid gaming disorder with other psychiatric disorders should be considered; and (4) substance use disorders. Gaming behavior often coexists with substance use, especially of alcohol. If the diagnostic criteria of both disorders are met at the same time, comorbid diagnoses can be considered [5, 16].

Comprehensive Intervention Principles and Measures

The general prevention and intervention principles of substance use and addictive behavioral disorders are relevant and needed for those at high risk or with diagnosis of gaming disorder. Gaming disorder is common in children and adolescents, and can evolve from recreational gaming behavior to gaming disorder. Preventive interventions for high-risk groups can significantly reduce the incidence of gaming disorder and the burden of the disorder. To date, there have been no specific effective interventions for gaming disorder. Patients often have comorbid physical and psychiatric disorders, so personalized intervention including psychological and pharmacological treatments and other treatment modalities should be considered. It should be noted that gaming disorder is similar to psychoactive substance use disorder and may recur or become chronic. To provide an integrated management plan, supervision and coordination of medical care, school, family, and society are needed.

In order to reduce the risk factors of gaming disorder, improve mental health, minimize recurrence, and increase the treatment rate, the adoption of a three-level prevention system—universal prevention, targeted prevention, and early detection and treatment—is important. For example, public mental health education to increase knowledge of gaming disorder, improve public mental health status, and reduce the risk factors of gaming disorder is helpful. For groups at high risks of gaming disorder, such as children and adolescents, it is helpful to adopt appropriate psychological interventions at the individual level, particularly in the areas of emotional regulation, cognitive control, and interpersonal communication. Within their family, school, and social environments, public health education on coping skills, improving family relationships and parent-child communication skills, and caring for the psychological needs of children and adolescents are also necessary.

Currently, there are no specific treatment guidelines for gaming disorder, but comprehensive treatments such as psychosocial interventions and medications improve the prognosis. Psychosocial interventions, such as cognitive-behavioral therapy, motivational interviewing, and family therapy are effective in reducing the uncontrolled gaming behaviors and improving the long-term prognosis [17]. At present, there are no medications with specific clinical indications for gaming disorder. Patients with the disorder who have mental, physical, and other comorbidities may require appropriate medications [5]. Researchers have shown that repetitive transcranial magnetic stimulation in patients with gaming disorder enhances brain control and reduces the impulse for gaming, but large-scale studies are lacking [18, 19].

Similar to other substance-use disorders, the treatment goals for gaming disorder are to prevent recurrence and promote social functioning and social reintegration through psychosocial rehabilitation and follow-up management. Patients who are stabilized after treatment should continue receiving maintenance psychological therapy and, if necessary, pharmacotherapy as appropriate. Regular follow-up for stable patients can improve their treatment adherence. Their family members should provide support, participate in the rehabilitation activities of patients, and help to resolve their psychosocial problems in daily life.

Conclusions and Future Perspectives

Considering that the epidemiology, pathogenesis, preventive measures, and treatment strategies of gaming disorder need to be further developed, certain areas should be addressed in future. First, with the amendment of the Law of the Protection of Minors in China, relevant laws and regulations to protect the physical and mental health of children and adolescents that reduce the risk of gaming disorder should be developed. Second, multidisciplinary collaboration involving the health, education, industry and commerce, and culture sectors should be established to regulate and supervise health services for gaming disorder in order to improve access to professional assistance for patients and their families. Third, assessment, and diagnosis system for gaming disorder should be established by relevant academic organizations in China. Fourth, epidemiological surveys and studies to understand the prevalence in different populations, the impact of relevant factors on gaming disorder should be conducted. Fifth, research on medicinal and psychosocial treatments to inform relevant prevention, treatment guidelines, and policies for gaming disorder are warranted. Lastly, all addictive behaviors and problems of social adaptation, including gaming disorder, should be treated as a whole entity. Effective preventive measures and psychosocial interventions for gaming disorder should be developed urgently.

828

Neurosci. Bull. July, 2020, 36(7):825–828

Compliance with Ethical Standards

Conflict of interest Dr. Wei Hao was a member of work group on development of diagnostic guidance of ICD-11 on substance use related disorders, and participated in or organized WHO expert meetings on gaming disorders. Otherwise, the authors declare no conflicts of interest related to the topic of this insight.

References

1. Zhao M, Hao W. Challenges of gaming disorder: suggestions from a public health perspective. Gen Psychiatr 2019, 32: e100086.
2. Disease Prevention and Control Bureau of China. Expert Consensus on the Prevention and Treatment of Gaming Disorders in China released by the Chinese Society of Psychiatry, Chinese Society of Preventive Medicine, Chinese Physicians Association, Chinese Mental Health Association and China Drug Abuse Prevention and Control Association (2019 edition). (in Chinese) 2019. http://www.nhc.gov.cn/jkj/s5889/201907/201844f201291a cff201947efa201900c201906a565844be201906fe.shtml.
3. Snodgrass JG, Zhao W, Lacy MG, Zhang S, Tate R. The cross-cultural expression of internet gaming distress in North America, Europe, and China. Addict Behav Rep 2019, 9: 100146.
4. Gonzalez-Bueso V, Santamaria JJ, Fernandez D, Merino L, Montero E, Jimenez-Murcia S, et al. Internet gaming disorder in adolescents: personality, psychopathology and evaluation of a psychological intervention combined with parent psychoeducation. Front Psychol 2018, 9: 787.
5. Saunders JB, Hao W, Long J, King DL, Mann K, Fauth-Buhler M, et al. Gaming disorder: Its delineation as an important condition for diagnosis, management, and prevention. J Behav Addict 2017, 6: 271–279.
6. Muller KW, Beutel ME, Egloff B, Wolfling K. Investigating risk factors for Internet gaming disorder: a comparison of patients with addictive gaming, pathological gamblers and healthy controls regarding the big five personality traits. Eur Addict Res 2014, 20: 129–136.
7. Rho MJ, Lee H, Lee TH, Cho H, Jung DJ, Kim DJ, et al. Risk factors for internet gaming disorder: psychological factors and internet gaming characteristics. Int J Environ Res Public Health 2017, 15.
8. Zhang JT, Brand M. Editorial: Neural mechanisms underlying internet gaming disorder. Front Psychiatry 2018, 9: 404.
9. Weinstein AM. An update overview on brain imaging studies of internet gaming disorder. Front Psychiatry 2017, 8: 185.
10. Northrup JC, Lapierre C, Kirk J, Rae C. The internet process addiction test: screening for addictions to processes facilitated by the internet. Behav Sci (Basel) 2015, 5: 341–352.
11. Muller KW, Beutel ME, Wolfling K. A contribution to the clinical characterization of Internet addiction in a sample of treatment seekers: validity of assessment, severity of psychopathology and type of co-morbidity. Compr Psychiatry 2014, 55: 770–777.
12. Pontes HM, Schivinski B, Sindermann C, Li M, Becker B, Zhou M, et al. Measurement and conceptualization of gaming disorder according to the world health organization framework: the development of the gaming disorder test. Int J Ment Health Ad 2019: https://doi.org/10.1007/s11469-11019-00088-z.
13. Kiraly O, Demetrovics Z. Inclusion of gaming disorder in ICD has more advantages than disadvantages. J Behav Addict 2017, 6: 280–284.
14. Wichstrom L, Stenseng F, Belsky J, von Soest T, Hygen BW. Symptoms of internet gaming disorder in youth: predictors and comorbidity. J Abnorm Child Psychol 2019, 47: 71–83.
15. Choi SW, Kim HS, Kim GY, Jeon Y, Park SM, Lee JY, et al. Similarities and differences among internet gaming disorder, gambling disorder and alcohol use disorder: a focus on impulsivity and compulsivity. J Behav Addict 2014, 3: 246–253.
16. Griffiths MD, Kuss DJ, Lopez-Fernandez O, Pontes HM. Problematic gaming exists and is an example of disordered gaming. J Behav Addict 2017, 6: 296–301.
17. Sudhir PM. Cognitive behavioural interventions in addictive disorders. Indian J Psychiatry 2018, 60: S479–S484.
18. Kuss DJ, Pontes HM, Griffiths MD. Neurobiological correlates in internet gaming disorder: a systematic literature review. Front Psychiatry 2018, 9: 166.
19. Weinstein A, Livny A, Weizman A. New developments in brain research of internet and gaming disorder. Neurosci Biobehav Rev 2017, 75: 314–330.

Neuroscience Bulletin Copyright Transfer Statement and Submission Form

We submit this type of article (√):
- Original Article
- Review
- Research Highlight
- Insight
- Letter to the Editor
- Method

Title of article:

Words:　　　　　Figures:　　　　　(Color figures:　　　);　　　　　Tables:

A signature below certifies compliance with the following statements

Copyright Transfer Statement: The copyright to this article is transferred to *Neuroscience Bulletin*, Shanghai Institutes for Biological Sciences, CAS and Springer (respective to owner if other than Shanghai Institutes for Biological Sciences, CAS and Springer and for U.S. government employees: to the extent transferable) effective if and when the article is accepted for publication. The author warrants that his/her contribution is original and that he/she has full power to make this grant. The author signs for and accepts responsibility for releasing this material on behalf of any and all co-authors. The copyright transfer covers the exclusive right and license to reproduce, publish, distribute and archive the article in all forms and media of expression now known or developed in the future, including reprints, translations, photographic reproductions, microform, electronic form (offline, online) or any other reproductions of similar nature. An author may self-archive an author-created version of his/her article on his/her own website. He/she may also deposit this version on his/her institution's and funder's (funder designated) repository at the funder's request or as a result of a legal obligation, including his/her final version, provided it is not made publicly available until after 12 months of official publication. He/she may not use the publisher's PDF version which is posted on www.springerlink.com for the purpose of self-archiving or deposit. Furthermore, the author may only post his/her version provided acknowledgement is given to the original source of publication and a link is inserted to the published article on Springer's website. The link must be accompanied by the following text: "The original publication is available at www.springerlink. com". The author is requested to use the appropriate DOI for the article. Articles disseminated *via* www.springerlink.com are indexed, abstracted and referenced by many abstracting and information services, bibliographic networks, subscription agencies, library networks, and consortia.

After submission of this agreement signed by the corresponding author, changes of authorship or in the order of the authors listed will not be accepted by *Neuroscience Bulletin*, Shanghai Institutes for Biological Sciences of Chinese Academy of Sciences and Springer.

Authorship responsibilities

I/We confirm that:

(1) The work described has not been published before in any language or in any journal or media; that it is not under consideration for publication elsewhere; that its publication has been approved by all co-authors, if any, as well as (tacitly or explicitly) by the responsible authorities at the institution where the work was carried out.

(2) We also give an assurance that the material will not be submitted for publication elsewhere until a decision has been made as to its acceptability for *Neuroscience Bulletin* in 2 months, then declare this statement becomes null and void.

(3) I am/We are responsible for obtaining permission for the use of any material in the manuscript that may be under copyright to my/our employer(s) or other party(ies).

(4) I have read the complete manuscript and accept responsibility for the content and completeness.

(5) I have made a significant contribution to this work and am familiar with the contents.

Author (1) signed:　　　　　Date:　　　　　Author (2) signed:　　　　　Date:

Author (3) signed:　　　　　Date:　　　　　Author (4) signed:　　　　　Date:

Author (5) signed:　　　　　Date:　　　　　Author (6) signed:　　　　　Date:

Author (7) signed:　　　　　Date:　　　　　Author (8) signed:　　　　　Date:

Author (9) signed:　　　　　Date:　　　　　Author (10) signed:　　　　　Date:

Corresponding author signed:　　　　　Date:

Corresponding author address:

Tel:　　　　　E-mail:

(Updated on June, 2019)

Neuroscience Bulletin

Neuroscience Bulletin

Impact Factor

4.326

2019 Journal Citation Reports: Q2
(CLARIVATE ANALYTICS, 2020)

OLYMPUS®

转盘共聚焦超分辨显微镜
SpinSR10
IXplore

兼顾分辨率和速度的
转盘共聚焦活细胞超分辨系统 **SpinSR10**

Confocal ◄ ► Super Resolution

5 μm
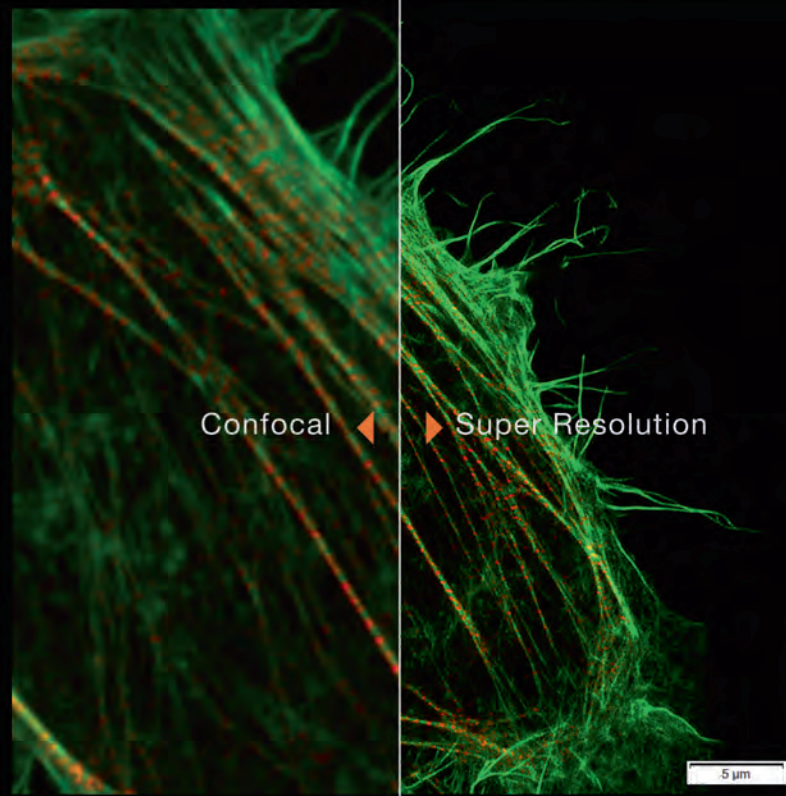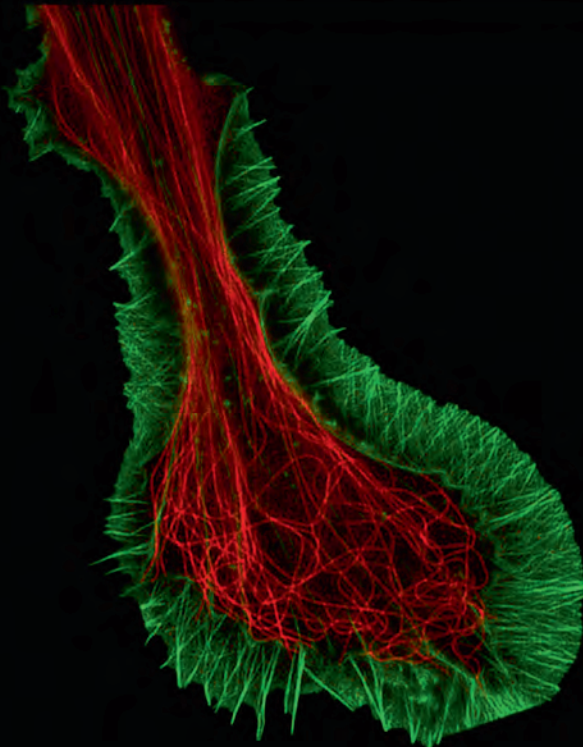
- 分辨率高达110 nm的实时超分辨率成像
- 专有反卷积算法进一步提升图像质量
- 宽视野成像，速度高达 200fps
- 特色硅油物镜可以实现活细胞深层成像
- 宽场、共聚焦、超分辨率模式自由切换
- 功能强大的智能cellSens软件平台

NEW